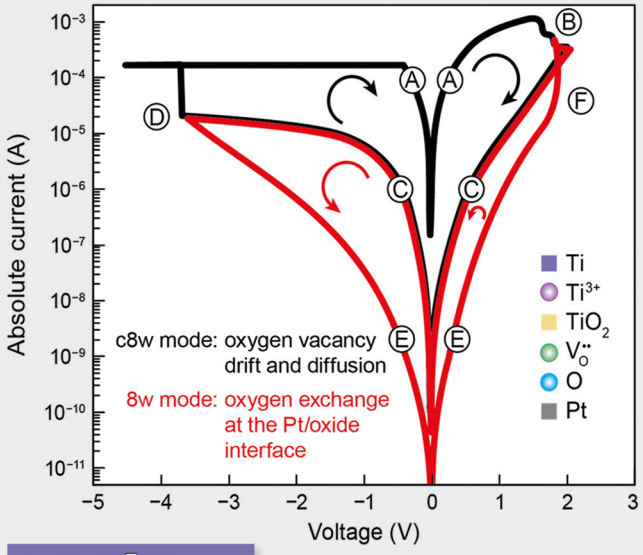

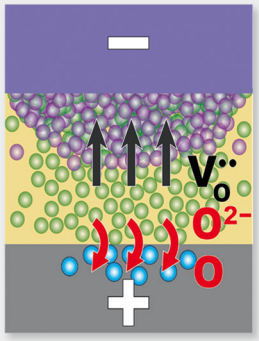

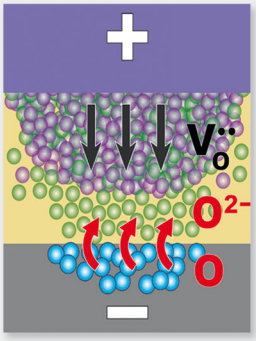

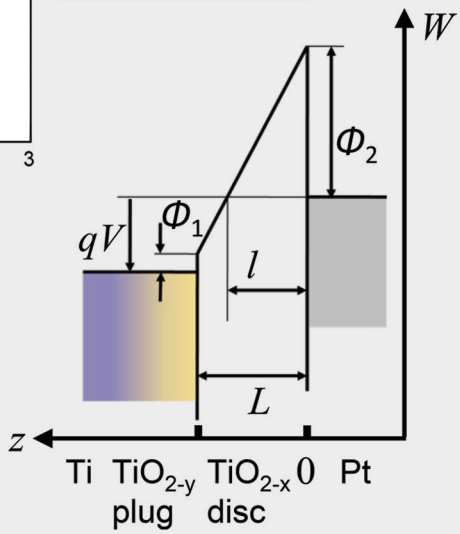

Resistive switching phenomena in stacks of binary transition metal oxides grown by atomic layer deposition

Hehe Zhang

Information
Band / Volume 57
ISBN 978-3-95806-399-0

Mitglied der Helmholtz-Gemeinschaft

JÜLICH
Forschungszentrum

Schriften des Forschungszentrums Jülich
Reihe Information / Information Band / Volume 57

Forschungszentrum Jülich GmbH
Peter Grünberg Institut (PGI)
Elektronische Materialien (PGI-7)

Resistive switching phenomena in stacks of binary transition metal oxides grown by atomic layer deposition

Hehe Zhang

Schriften des Forschungszentrums Jülich
Reihe Information / Information Band / Volume 57

ISSN 1866-1777 ISBN 978-3-95806-399-0

Bibliografische Information der Deutschen Nationalbibliothek.
Die Deutsche Nationalbibliothek verzeichnet diese Publikation in der
Deutschen Nationalbibliografie; detaillierte Bibliografische Daten
sind im Internet über http://dnb.d-nb.de abrufbar.

Herausgeber und Vertrieb:	Forschungszentrum Jülich GmbH Zentralbibliothek, Verlag 52425 Jülich Tel.: +49 2461 61-5368 Fax: +49 2461 61-6103 zb-publikation@fz-juelich.de www.fz-juelich.de/zb
Umschlaggestaltung:	Grafische Medien, Forschungszentrum Jülich GmbH
Druck:	Grafische Medien, Forschungszentrum Jülich GmbH
Copyright:	Forschungszentrum Jülich 2019

Schriften des Forschungszentrums Jülich
Reihe Information / Information, Band / Volume 57

D 82 (Diss., RWTH Aachen University, 2019)

ISSN 1866-1777
ISBN 978-3-95806-399-0

Vollständig frei verfügbar über das Publikationsportal des Forschungszentrums Jülich (JuSER)
unter www.fz-juelich.de/zb/openaccess.

Abstract

Information technology is approaching the era of artificial intelligence. New computing architectures are required to cope with the huge amount of data that has to be processed in all types of cognitive applications. This requires dedicated energy efficient solutions on the level of the computing hardware. The new concepts of neuromorphic computing (NC), like artificial neural networks (ANNs) and computation in memory (CIM), aim to overcome the limitations of classical computers based on von Neumann architecture. Redox-type resistive random access memory (ReRAM) devices are intensively investigated for NC applications due to their non-volatility and energy efficiency, process compatibility with standard complementary metal oxide semiconductor (CMOS) technology, and the ability for device scaling and three-dimensional (3D) integration. The variety of applications requests for different desired properties of the ReRAM devices ranging from an analog-type programmable multilevel behavior to a binary-type switching at high resistance ratio and with linear resistance states.

ReRAM research today focuses on devices built of metal oxide layers with nanometer thickness sandwiched between a chemically inert electrode like Pt or TiN and a chemically reactive electrode. The precise thickness control is achieved by vapor phase deposition techniques, in particular, atomic layer deposition (ALD). However, some basic issues like switching stability and resistance variability are still obstacles on the way towards massive integration. One of the efforts to improve the device performance is the use of combinations of two metal oxides layers, so called bilayer oxide stacks. The two different metal oxide layers are selected regarding their insulation resistance and oxidation enthalpy. Here, especially the bilayer ReRAM stack of TiO_2 and Al_2O_3 has drawn attention of researches worldwide. TiO_2 belongs to the materials integrated into ReRAM devices since the early start in the beginning of this millennium. However, most of the single-layer TiO_2 devices lack stability in the standard valence change mechanism (VCM)-type filamentary switching behavior and suffer from a too high residual leakage current. One approach for improvement is the addition of an Al_2O_3 barrier layer into the TiO_2 ReRAM device. So far, in the scientific literature, there is no clear consensus if this type of Al_2O_3/TiO_2 bilayer cells reveal a standard VCM-type filamentary switching or an area-dependent switching behavior.

The present study aims at a clarification of different phenomena associated with the bipolar resistive switching in bilayer ReRAM devices built from Al_2O_3 and TiO_2 layers. In order to cope with device sizes, which are close to the industrial scale, nano-crossbar ReRAM cells were fabricated with an electrode area of $(60\ \mathrm{nm})^2$ to $(100\ \mathrm{nm})^2$ and oxide layer thickness below 10 nm. Nanometer-thin, dense oxide layers of reproducible quality were grown by means of ALD. Here a Pt bottom electrode was used as the Schottky electrode. In contrast, for the Pt/oxide/metal structures the metal top electrode was

varied between Ti and TiN. A systematic study was performed regarding the effect of the resistive switching oxide comparing single-layers of Al_2O_3 and TiO_2 and bilayers with different stack sequence, this means, Al_2O_3/TiO_2 and TiO_2/Al_2O_3. Study of the electroforming behavior in the various device stacks $Pt/Al_2O_3/Pt$ cells reveals the identical breakdown strength as observed for other reported Al_2O_3 single-layer devices. In contrast, $Pt/Al_2O_3/Ti$ devices show a linear dependence of the electroforming voltage for the Al_2O_3 thickness of 2 to 5 nm. $Pt/TiO_2/Ti$ devices are conductive in their initial state for TiO_2 thickness below 10 nm. In bilayer stacks the electroforming voltage is dominated by the thickness of the Al_2O_3 layer, but the additional TiO_2 layer is not negligible. According to the different oxidation enthalpies, the use of a Ti electrode results in a more reproducible and stable switching compared to TiN.

Pt/metal oxide/Ti nano-crossbar devices with a thin Al_2O_3 layer show filamentary VCM-type counter-eightwise (c8w) bipolar resistive switching after successful electroforming and first RESET step. The resistance ratio is controlled by choosing values of current compliance and RESET stop voltage between high and low resistance state, respectively. Deep RESET behavior is obtained for the Al_2O_3 film thicker than 4 nm. However, effects appear which are attributed to a filling of trap states in the Al_2O_3 layer adjacent to the Pt Schottky electrode. The charge transport behavior of the different cells was systematically analyzed considering the voltage and temperature dependence of the initial state, the high (HRS) and low resistance state (LRS). The current transport in the insulating devices, i.e. Al_2O_3 and the bilayers with Al_2O_3, was successfully simulated by the Simmons' equation for tunneling through a trapezoidal barrier. This also holds for the HRS state with differences in tunneling barrier and tunneling area. The area of 100 nm^2 attributed to the HRS fits well to the physical diameter of the filament of about 10 nm that was determined from the crystallized regime appearing in the cross-section of a switched device via transmission electron microscopy. For all devices the LRS exhibits an almost metallic-type conduction characteristic. Pulse switching analysis leads to a SET kinetic, which is well described by the ion hopping model utilizing Mott-Gurney law for oxygen vacancy drift.

$Pt/TiO_2/Ti$ nano-crossbar devices show an extraordinary behavior of the coexistence of standard filamentary counter-eightwise (c8w) and stable eightwise (8w) switching at significantly reduced currents. The two switching modes with opposite polarity share a common state, this is, the c8w HRS equals the 8w LRS*. A model is proposed which describes this coexistence as a competition between oxygen vacancy drift/diffusion and oxygen incorporation/extraction at the Pt/TiO_{2-x} interface. The reduced/increased amount of oxygen vacancies in the regime of the conductive filament's disc leads to a band bending and a change of the parabolic shaped tunneling barrier at the switching interface. In the $Pt/TiO_2/Ti$ nano-devices the 8w-switching process occurs at switching voltages of about 2 V, but at a significantly reduced current level with resistance values of about Mega- and Giga-Ohm in LRS* and HRS*, respectively.

The deeper understanding of switching phenomena and conduction behavior in the various Al_2O_3 and TiO_2 single-layer and bilayer nano-crossbar devices can be utilized for improvement of existing switching models and for future cell design addressing particular applications.

Kurzfassung

Die Informationstechnologie nähert sich dem Zeitalter der künstlichen Intelligenz. Neue Rechnerarchitekturen sind erforderlich, um die großen Datenmengen zu bewältigen, die für die vielfältigen kognitiven Anwendungen verarbeitet werden müssen. Dies verlangt nach neuen Hardware-Lösungen mit deutlich höherer Energieeffizienz. Die neuen Konzepte des neuromorphen Rechnens, wie z.B. künstliche neuronale Netzwerke und logikfähige Speicher, zielen auf die Überwindung der Beschränkungen klassischer von Neumann-Rechner. Redox-basierte resistive Speicherzellen (redox-based resistive random access memory, ReRAM) werden aufgrund ihrer Nichtflüchtigkeit und Energieeffizienz, sowie der Kompatibilität zu komplementären Metall-Oxid-Halbleiter-Strukturen, der Skalierungsmöglichkeit und der dreidimensionalen Integration intensiv untersucht. Die erforderlichen Eigenschaften von ReRAM-Bauelementen reichen von analog programmierbaren Widerstands-änderungen bis zu binärem Schalten mit einem hohen Widerstandsverhältnis und linearen Zuständen, um die Vielfalt der Anwendungen adressieren zu können.

Die heutige ReRAM-Forschung konzentriert sich auf Bauelemente aus nanometerdünnen Metalloxidschichten, die eingebettet sind zwischen einer chemisch inerten Elektrode wie Pt oder TiN und einer chemisch-reaktiven Elektrode. Die Kontrolle der Schichtdicke wird durch die Gasphasenabscheidungen gewährleistet, z.B. die Atomlagenabscheidung (ALD). Allerdings verhindern noch einige grundlegende Probleme wie Schaltstabilität und Widerstandsverteilung die massive Integration neuartiger ReRAMs. Eine Möglichkeit zur Verbesserung der Bauelemente ist die Kombination von zwei aufeinander folgenden Metalloxidschichten (sog. „Doppeloxid-Stapel“). Die zwei unterschiedlichen Oxidschichten werden gemäß ihrer elektrischen Widerstände sowie ihrer Oxidationsenthalpie gewählt. Hier findet vor allem eine Struktur aus TiO_2 und Al_2O_3 weitreichende Beachtung. Aktuell besteht jedoch noch kein Einvernehmen in der einschlägigen wissenschaftlichen Fachliteratur, ob solche Al_2O_3/TiO_2-Doppelschicht-Bauelemente ein typisches VCM filamentäres Schalten oder ein flächenabhängiges Schalten zeigen.

Ziel der vorliegenden Arbeit ist eine Klärung der unterschiedlichen Phänome, die mit dem bipolaren resistiven Schalten in ReRAM-Bauelementen mit einer Doppelschicht aus Al_2O_3 und TiO_2 verbunden sind. Um mit einer industrienahen Bauelementgröße zu arbeiten, wurden Nano-Kreuzpunkt ReRAM-Zellen mit einer Fläche von $(60\,\mathrm{nm})^2$ bis $(100\,\mathrm{nm})^2$ hergestellt, wobei die gesamte Oxidschichtdicke unter 10 nm bleibt. Es wurden dichte Oxidschichten im Nanometer-Bereich mit reproduzierbarer Qualität per ALD abgeschieden. Die untere Elektrode aus Pt wurde als Schottky-Elektrode eingesetzt. Demgegenüber wurde bei der metallischen Deckschicht der Pt/Oxid/Metall-Strukturen die obere Elektrode zwischen Ti und TiN variiert. Es wurde eine systematische Studie hinsichtlich des Vergleiches zwischen Einzelschichten (TiO_2 und Al_2O_3) und verschiedenen Doppelschichten, nämlich Al_2O_3/TiO_2 und TiO_2/Al_2O_3, durchgeführt. Die Untersuchung

des Elektroformierens zeigt eine mit der Literatur übereinstimmende Durchbruchspannung in Pt/Al_2O_3/Pt Zellen. Im Gegensatz dazu zeigen die Pt/Al_2O_3/Ti-Bauelemente eine lineare Abhängigkeit der Elektroformierungsspannung von der Al_2O_3 Dicke von 2 bis 5 nm. Pt/TiO_2/Ti-Bauelemente besitzen eine hohe Leitfähigkeit im Anfangszustand bei einer Dicke der TiO_2-Schicht unter 10 nm. In den Doppelschichten wird die Elektroformierungsspannung von der Dicke der Al_2O_3-Schicht bestimmt, wobei die TiO_2-Schicht dennoch nicht vernachlässigbar ist. Gemäß ihrer jeweiligen Oxidationsenthalpien führt die Ti-Elektrode zu einem reproduzierbareren und stabileren Schalten im Vergleich zu TiN.

Nach Elektroformieren und RESET zeigen Pt/Metalloxid/Ti-Nano-Kreuzpunkt-Bauelemente mit einer dünnen Al_2O_3-Schicht ein filamentäres VCM-artiges bipolares resistives Schalten, dargestellt durch das entgegengesetzte Schreiben der Ziffer „8“ (eng.: counter-eightwise, c8w). Das Widerstandsverhältnis wird durch die Wahl der Strombegrenzung im SET-Prozess sowie durch den eingestellten Spannungswert im RESET-Prozess geregelt. Für tiefes RESET-Verhalten, wie es für Al_2O_3 dicker als 4 nm gefunden wurde, tauchen Effekte auf, die auf eine Besetzung von Defektzuständen an der Grenzfläche zwischen Al_2O_3 und der Pt Schottky-Elektrode hinweisen. Der Ladungstransport in verschiedenen Zellen wurde systematisch hinsichtlich der Spannungs- sowie Temperaturabhängigkeit der hochohmigen (HRS) und niederohmigen (LRS) Widerstands-zustände analysiert. Der Stromtransport in den isolierenden Bauelementen, Al_2O_3 und den Doppelschichten mit Al_2O_3, konnte mit Hilfe der Simmons' Gleichung für das Tunneln durch eine trapezförmige Barriere erfolgreich simuliert werden. Das Modell gilt auch für die HRS-Zustände mit Unterschieden in Tunnelbarriere sowie Tunnelfläche. Die Fläche von 100 nm^2 für eine Zelle im HRS passt gut zu den Ergebnissen aus Transmissionselektronenmikroskopie-Untersuchungen, die einen kristallinen Bereich mit einer Breite von 10 nm in dem Bauelement zeigen. Für alle Bauelemente zeigt der LRS metallisches Leitfähigkeitsverhalten. Eine Analyse des Schaltverhaltens im Pulsbetrieb führt zu einer SET-Kinetik, die durch Ionenbewegung über das Mott-Gurney-Gesetz erklärt werden kann, wobei nur die Drift der Sauerstoff-leerstellen berücksichtigt wurde.

Pt/TiO_2/Ti-Nano-kreuzpunkt-Bauelemente zeigen eine außergewöhnliche Koexistenz von standardmäßigem filamentärem c8w Schalten und einem stabilen 8w Schalten bei deutlich reduziertem Strom. Die zwei Schaltmoden mit entgegengesetzter Polarität teilen einen gemeinsamen Zustand: der c8w HRS ist gleich dem 8w LRS*. Es wird ein Modell aufgestellt, um diese Koexistenz als eine Konkurrenz zwischen Drift/Diffusion von Sauerstoffleerstellen und dem Ein-/Ausbau von Sauerstoffatomen über die Pt/TiO_{2-x}-Grenzfläche zu beschreiben. Die Erhöhung bzw. Verminderung der Dichte von Sauerstoffleerstellen führt zu einer Bandverbiegung und einer Änderung der parabolischen Tunnelbarriere an der schaltenden Grenzfläche. In den Pt/TiO_2/Ti-Nano-Bauelementen werden die 8w Zyklen bei einer Schaltspannung nahe 2 V beobachtet, jedoch mit einem signifikant reduzierten Stromniveau und Widerstandswerten von im Mega- und Giga-Ohm-Bereich für LRS* bzw. HRS*.

Ein tieferes Verständnis der Schaltphänomene und des Stromtransports in verschiedenden Al_2O_3- und TiO_2-Einzelschicht- und Doppelschicht-Bauelementen hilft bei der Optimierung eines generellen Schaltmodells und bei der Auslegung zukünftiger anwendungsspezifischer Zellkonzepte.

Acknowledgment

I would like to express my gratitude to professors, all colleagues in PGI-7 and in the collaboration and my family. Without their supports this thesis would never be accomplished.

Firstly, I would like to express my sincere gratitude to Prof. Dr. Rainer Waser, who granted me this wonderful chance to carry out my PhD study on ReRAM cells in this institute.

Secondly, I would like to express my heartfelt gratitude to Prof. Dr. Joachim Mayer and Prof. Dr. Regina Dittmann for being the first and second advisor, for agreeing to report this thesis and to participate in hosting the PhD exam. I would like to thank Prof. Jochen M. Schneider very much, who provided a very nice place and supplied a friendly and relaxing atmosphere for the PhD exam.

Thirdly, I owe a lot of thanks to our collaborator, Prof. Cheol Seong Hwang and Sijung Yoo from the Seoul National University, who has supplied a lot of help in the TEM investigation and the discussions.

A sincere appreciation goes to my supervisor, Dr. Susanne Hoffmann-Eifert, who has given the direct help and discussions on many details. Moreover, for the sculpturing of the text in my PhD thesis and papers, she contributed with an immense effort. The special thanks go to Dr. Stefan Menzel and Dr. Dirk Wouters, who have helped me a lot in improving the theory in the right direction.

Also, a lot of thanks to my dear colleagues Carsten Funck, who helps to refine my theoretical model with his expertise in simulation and solid background in physics. Many thanks to Alexander Hardtdegen, who has supplied lots of practical help with his versatility in experiments and wide range of laboratory connections. Special thanks to Felix Cüppers, who has helped me on the software side for pulse experiments with his talent in accomplishing complex tasks. A lot of thanks go to Stephan Aussen for his help in the latex and Astrid Lewalter for her helpful emendation of the German language part. Special thanks to them again for their careful reading of part of my thesis and giving very helpful suggestions for the text.

To Dr. Alexander Schönhals, Camilla La Torre and Andreas Kindsmüller in IWE2, I express my thanks for the discussions about the experimental results. With these discussions, the knowledge exchange is intensified and the scientific rigidity of my work

is improved.

A lot of thanks go to my former college at the early stage of my PhD period, Dr. Marcel Reiners, Dr. Nabeel Aslam, who transferred a lot of knowledge and experience in experimental apparatus and scientific background. Without their help the initiation of my work would be much more difficult.

I also would like to thank the technical staff in our institute with my sincere gratitude. René Borowski, Alfred Steffen, Dr. Stefan Trellenkamp and Mirka Grates have helped me a lot in lithography technologies. Without them the samples will never be smoothly fabricated and be applied in the experiments. Stephan Masberg helped me a lot in machinery issues and always solved the problems from my deposition machines. Dr. Paul Meuffels supplied many inspiring ideas and guaranteed the working of the important XRD machine, which is totally decisive for the sample characterization in the first stage. Marcel Gerst did a lot of work in solving computer problems, which is the basic for any scientific study. Maria Garcia supported the administration issues with her high enthusiasm and warm friendliness.

Finally, my sincere gratitude goes to my parents Yanhua Peng and Yongzhen Zhang for their trust and financial supports during these years. The hurdles and obstacles on the way of my PhD studies that I faced would never be passed without their encouragement. For any high and low moments, they have always been by my side despite the long distance from the home town.

Contents

Chapter 1

Introduction

Resistive switching in metal oxide is not a new phenomenon, since it was firstly discovered about 50 years ago and various materials showing resistive switching have been reported in the 1970s' and 1980s' [1–3]. Due to the technological success of dynamic random access memory (DRAM), the need to explore metal oxide-based resistive switching devices has been suppressed [4]. Around the year 2000, different groups started again to explore this class of materials as a possible candidate for memory devices. Thanks to the high-k metal gate technology introduced into the complementary metal-oxide-semiconductor (CMOS) technology, nowadays, fine structured metal oxides with dimensions down to several tens of nanometers can be fabricated. Transferring the technology, metal oxides showing resistive switching behavior can be integrated into nanometer range metal-insulator-metal (MIM) structures and might in the near furture be introduced into semiconductor memory production lines. Therefore, a new type of memory named resistive switching random access memory (ReRAM) based on the redox processes in oxides can be further explored. Simple sandwiching a thin film oxide between two metal electrodes, oxide-based ReRAM units are proven to have high switching speed (< 5 ns) [5], low power consumption [6] and high scalability [7]. Among other recently developed memory types, oxide-based ReRAM is treated as a prominent candidate for the emerging field of machine learning [8], logic-in-memory concepts [9–11] and neuromorphic computation [12, 13]. Aiming at these applications, the major semiconductor manufacturers are launching their productions of ReRAM. For example, the world's largest semiconductor foundry Taiwan Semiconductor Manufacturing Company announced in 2017 the plan for supplying embedded ReRAM with 22 nm process in the year 2019 [13].

Despite the large number of merits, oxide-based ReRAMs still have several challenges to encounter. Some issues need to be solved by specific cell design. For example the sneak current can be lowered either by addition of a selector (1T1R or 1S1R design) [9, 14–16] or anti-serially arranged ReRAM cells (CRS design) [17]. As pointed out by the international technology roadmap for semiconductors in 2013 [18], due to the fundamental limits of the two-dimensional (2D) scaling, exploration of three-dimensional (3D) vertical architectures

is a necessary issue to increase the package density. Recent studies report on ReRAM cells in the 3D structures showing promising switching behavior [19–21]. Beside the technological issues, the performance of the ReRAM cell itself can also be influenced by choosing different electrode materials [22] and by oxygen vacancy engineering [23]. Still challenges for the material engineering have to be encountered.

1.1 State of the art

Novel bilayer structures are suggested to increase the switching stability and reliability of oxide-based ReRAM devices compared to single-layer structures. Mainly two types of bilayer structures are suggested by different groups. The first type of bilayer structure utilizes metal oxides (MOs) of the same metal element but with the MOs staying in different crystalline phases or with the metal ions exhibiting various oxidation states. For example, Lee et al. [23] found that the system $Pt/TaO_{2-x}/Ta_2O_{5-x}/Pt$ reveals increased endurance and switching stability compared to a $Pt/TaO_{2-x}/Pt$ structure [24]. The second type of bilayer structure is built from metal oxide layers of two different metal ions. One example is the TiO_2/Al_2O_3 bilayer structure that shows a good potential of multilevel states [25]. Furthermore, as reported by the group at IMEC research center, a lower current density ($\leqslant 5$ nA/nm^2) and lower power operation ($\pm$ 4 V/10 ns) have been achieved for $TiN/Al_2O_3/TiO_2/TiN$ cells of 40 nm size [6] compared to other TiO_2 single-layer devices. Recently, the different bilayer stacks containing TiO_2 and Al_2O_3-based bilayer devices are applied in a multibit memory operation [26], which are proved to have a high potential in neuromorphic computing.

However, to obtain a memory product with robust performance that meets industrial standards, a deeper understanding of the resistive switching mechanism is desirable. To this state, different research groups worked on different aspects of bilayer structures and various models for the switching mechanism are under discussion. Taking TiO_2/Al_2O_3 as one example, a consistent understanding of the resistive switching mechanism in this bilayer structure has not yet been established. Kim et al. argue that the switching in TiO_2/Al_2O_3 bilayer structures occurs due to the tunnel barrier height change of Al_2O_3, which is considered as a defective tunnel barrier influenced by the oxygen vacancies via ion movement [27]. Govoreanu et al., however, consider that the oxygen vacancy movement in the TiO_2 layer changes the effective barrier width in the TiO_2/Al_2O_3 bilayer structure and thus influences the resistance state [6]. The role of the Al_2O_3 during the resistive switching is still not clearly proved and a further design based on the functionality of Al_2O_3 is needed. Moreover, the SET and RESET kinetics, which determines the switching speed and retention time, have not been systematically studied in TiO_2/Al_2O_3 bilayer structures. Last, the role of electrodes in TiO_2 and Al_2O_3-based bilayer devices requires further investigation.

1.2 Scope of this work

This work aims at an analysis and understanding of the resistive switching behavior in nano-crossbar ReRAM devices based on nanometer-thin layers of amorphous Al_2O_3, TiO_2, and combinations of the two components. For this study ultra-thin metal oxide layers are grown by atomic layer deposition (ALD) to enable conformal, pinhole-free coverage of the structured Pt bottom electrodes. The ReRAM devices are built from nano-crossbars of 60 to 100 nm wide electrode lines sandwiching the switching oxide layer in the crossing junctions. The first part focuses on the topic, how as-deposited amorphous Al_2O_3 layers of ultra-low thickness between 2 and 5 nm can be utilized for certain oxide-based ReRAM device applications by means of the interfacial engineering. For this purpose, $Pt/Al_2O_3/Pt$, $Pt/Al_2O_3/Ti/Pt$ and $Pt/Al_2O_3/TiO_2/Ti/Pt$ cells are fabricated and characterized. Special view is the effect of the TiO_2 layer, by comparing devices with and without such an artificial film regarding the switching voltage stability as well as of the resistance variability. The second part concentrates on the aim to understand the two types of switching polarities, namely counter-eightwise (c8w) and eightwise (8w), in nanosized oxide-based ReRAM cells based on modified $Pt/TiO_2/Ti/Pt$ structures. In particular, TiO_2 single-layer devices are compared with $Pt/Al_2O_3/TiO_2/Ti/Pt$ cells. To elucidate these points systematically, this thesis is organized into the following chapters:

Chapter 2 shows the application of VCM-type non-volatile memristive devices in emerging energy-efficient concepts for computing (2.1) as well as integration issues of high-density functional arrays (2.2). Section 2.3 introduces basics about two different types of bipolar resistive switching in VCM-type ReRAM devices. The fundamentals are completed by an overview about electronic transport mechanisms controlling the current-voltage characteristics in metal/oxide(s)/metal structures (2.4) and by a summary of the basic material properties of TiO_2 and Al_2O_3 (2.5).

Chapter 3 focuses on the experimental part of this work. Starting with the basics of thermal atomic layer deposition, which has been used to enable conformal growth of a few nanometer-thick oxide films onto the structured bottom electrodes (3.1). The most important film and structure characterization techniques, X-ray reflectivity (XRR) for thickness determination and scanning electron microscopy (SEM) for device inspection are briefly introduced (3.2). The nano-crossbar device fabrication is described through a process flow in section 3.3. To the end, the performed electrical measurements are described together with the utilized setups.

Chapter 4 addresses the characterization of the counter-eightwise bipolar resistive switching (c8w BRS) behavior in various single-layers of TiO_2 or Al_2O_3 and their combinatorial bilayers. The stacks fabricated for this thesis are described and the purpose of the particular variations, like top electrode variation, are presented in section 4.1. The electrical $I(V)$ characteristics of single-layers (4.2) and their combinatorial bilayers (4.3)

with different electrodes and varied layer thicknesses are compared via the sensitivity of high and low resistance values to the switching parameters like current compliance and RESET stop voltage. Section 4.4 compares the resistive switching performance between Al_2O_3-based devices with and without artificial ALD grown 3 nm TiO_2 layer with respect to the resistance states, operation voltages and endurance.

Chapter 5 is about the SET and RESET kinetics in single-layer and bilayer devices through transient pulse measurements. For this purpose, two different stacks, a Pt/5 nm Al_2O_3/Ti/Pt single-layer stack and a Pt/3 nm Al_2O_3/3 nm TiO_2/Ti/Pt bilayer stack with stable c8w BRS behavior are studied. The ion hopping model is applied to explain the relation between SET time and SET pulse voltage with physically meaningful parameters.

Chapter 6 shows a direct structural information of a switched $(100\,\text{nm})^2$ Pt/3 nm Al_2O_3/3 nm TiO_2/Ti/Pt nanosized crossbar cell gained from transmission electron microscopy (TEM) analysis combined with the energy-dispersive X-ray spectroscopy (EDX).

Chapter 7 focuses on the understanding of the electronic transport for different resistance states in the single-layer or bilayer nano-crossbar devices showing c8w BRS. For the initial state and two switching relevant resistance states, namely the high resistance state (HRS) and the low resistance state (LRS), the analysis is carried out through the read-out current-voltage curves obtained in DC mode under varied temperatures. In section 7.1 the impact of the Ti oxygen exchange layer (OEL) on Al_2O_3-based single-layer and bilayer devices is evaluated and the origin for multiple HRS is discussed (7.2). In addition, the low resistance states are characterized by means of the temperature coefficient of the resistance (7.3).

In chapter 8 the phenomena of the coexistence and the transition between the two non-volatile resistive switching modes in TiO_2-based ReRAM devices is analyzed (8.1). Moreover, the characteristics of 8w resistance states and the interface effect by insertion of Al_2O_3 between TiO_2 and two electrodes are studied in this section as well. Section 8.2 discusses the different non-volatile 8w states by means of their temperature and voltage dependence. The analysis is performed by using the Simmons' tunneling model and continuum model simulation. The results are combined and discussed based on mixed electronic-ionic conduction and switching mechanism (8.3).

In chapter 9 the results obtained from this work are summarized and an outlook for the direction of potential investigation is suggested.

Chapter 2

Fundamentals

2.1 Emerging memories

Today's computers are based on the von Neumann concept, which contains three main sub-systems [28]: (1) Input and output interfaces (I/O), (2) central processing unit (CPU) and (3) memory. The memory stores the data and instructions, while CPU processes data and instructions. Since the speed of the processing unit or the processor increases several orders of magnitude higher than of the memory [29], whose improvement in recent years was mainly on the density, the processor needs to wait an amount of time for fetching the data and instructions from memory. This feature of the restricted transfer rate is called "von Neumann bottleneck". To overcome this problem, one of the potential approaches is data processing within the memory, i.e. integration of a computation inside the memory [11]. Such integration requires novel emerging nonvolatile memory technologies [29]. In the following, an overview of the memory types, especially the emerging candidates for this concept are presented.

A categorization of RAM chips is illustrated in Fig. 2.1. Regarding the data retention two classes are distinguished, namely volatile and non-volatile memories. The main two volatile RAM types are static random access memory (SRAM) and dynamic random access memory (DRAM), which are already mature products in the market. Another class of RAM chips that conserve stored data even without voltage supply is non-volatile RAM. Non-volatile RAM can be applied in portable devices, where the energy consumption is a great issue and thus the information has to be stored mostly without applying a voltage. The most widely accepted type of non-volatile RAM is Flash memory, which can be electrically erased and reprogrammed. However, it has several disadvantages: (1) high operation voltage and slow write/erase operation. The voltage amplitude is normally over 6 V in SiO_2-based devices and for a fast writing operation the voltage amplitude can be even over 10 V [30]. The write/erase time is over the microsecond range [31]. (2) High supply voltage (3.3 V or 5 V) during erase/write/read [32, 33] and

(3) low endurance of around 10^5 cycles [30]. Therefore, to develop other types of non-volatile RAM is extraordinarily important. Several kinds of non-volatile RAM chips like phase change memory (PCM) [34], ferroelectric RAM (FeRAM) [35] and magnetic RAM (MRAM) [36], are already on the level of products. Another kind of non-volatile RAM is redox-based resistive random access memory (ReRAM) [37] that involves redox reactions and ion migration processes [4]. The two distinguished types of ReRAM are valence change mechanism (VCM) [38] and conductive bridge RAM (CBRAM) [19, 20]. Beside the intensive investigations of different metal oxide materials for ReRAM, a large amount of research mainly focuses on the switching mechanisms in the resistive switching metal oxides [39–41].

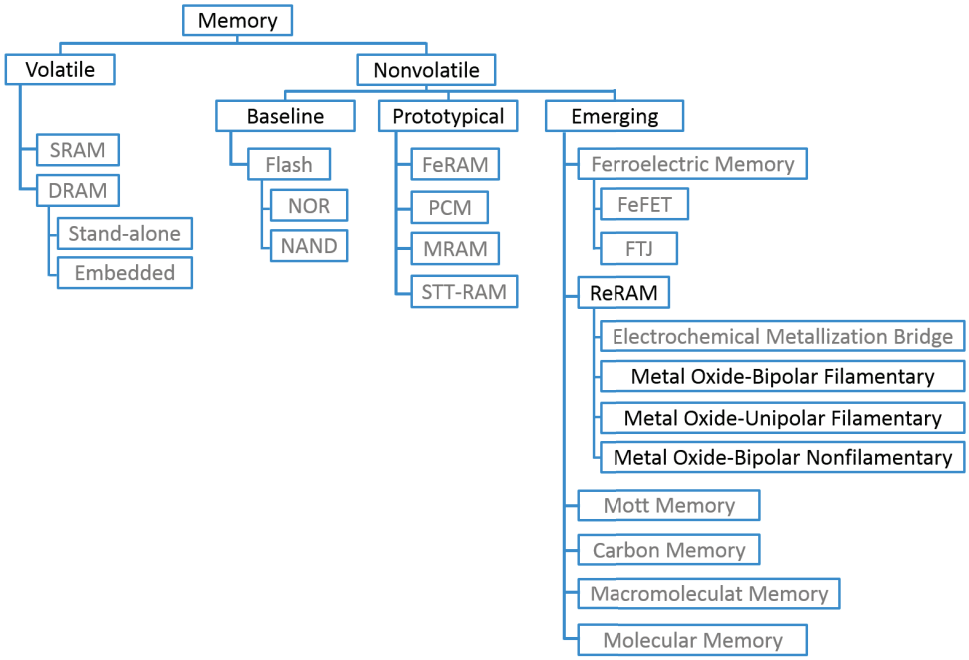

Figure 2.1: *Taxonomy of memory devices. The figure is redrawn from [42].*

2.2 Integration of ReRAM cells

Device design

For the ReRAM integration both conventional two-dimensional (2D) and the developing 3D matrix design are illustrated in Fig. 2.2. In traditional 2D RAM chips the vertical- and horizontal interconnections cross each other and each cross point can be stored one state of either "1" or "0". By accessing the data with two address decoders, namely

row- and column decoder, the states by each cross point can be either read or written through a read/write circuit. To increase the density for the 2D structure, the horizontal miniaturization of cells has been investigated for a long time. However, as the modern lithography technology approaches its limit due to the high developing costs and the resolution limits, 3D stacking of the memory cells is taking the lead. A representative 3D concept is shown in Fig. 2.2 (b). The dark blue pillar is the vertical bit line, while the horizontal blue bars are the word lines. Between the bit line and the word line is the memory cell highlighted by a white frame. With the 3D structure, the device pro volume density should be improved to a great extent in contrast to the traditional 2D designs. However, for the steep vertical structures in 3D matrix, to grow layers with high structural uniformity is a challenge for most of the established deposition techniques. Among others, atomic layer deposition (ALD) is the most suitable method for the growth of thin films on steep structures (the principle will be introduced in section 3.1).

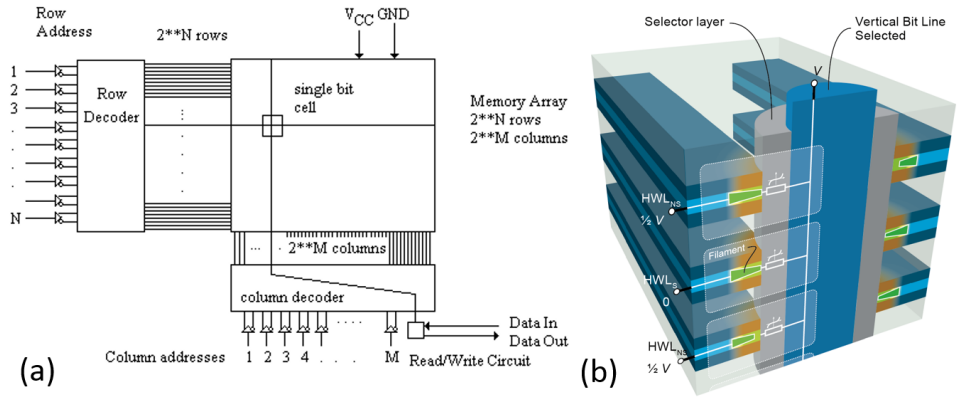

Figure 2.2: *(a) General structure of a RAM chip in 2D concept. (b) One concept of a 3D vertical ReRAM design. The images are taken from [43], and [44], respectively.*

Material research concepts for the VCM-type ReRAM

To obtain the high performance and the low power consumption at the same time, the ReRAM cell has to be optimized through material engineering and device structure designing as well. Different materials are utilized in ReRAM. Among others, three commonly used materials are TiO_2, HfO_2 and TaO_x. The material engineering includes oxide stoichiometry engineering, doping concentration control, crystallography engineering and electrode/oxide interface engineering. Although plenty of papers for each material cover almost every engineering aspect, the following discussion focuses on industrial easily accessible methods. Fitting to the topic in this work, the material engineering in TiO_2-based

ReRAM is illustrated at first, where the oxide chemistry engineering, oxide crystal structure engineering and oxide/electrode interface engineering are introduced separately.

The oxide chemistry engineering comprises stoichiometry engineering and doping with defined impurity elements. The stoichiometry refers to the ratio "x" of oxygen to metal element. Tuning the O/Ti ratio between 1.39 and 1.9 with different oxygen partial pressure during sputtering can significantly influence both SET, RESET voltages and high and low resistance states [45]. Furthermore, the oxide stoichiometry engineering can further extend to the combination of multiple TiO_x layers with different oxygen contents, thereby the switching type can be changed [45] or the switching stability can be improved [46]. Comparing to the non-doped TiO_2 devices, doped cells with impurities, like Co [47, 48], Al, Cu and Cr [49], show an improvement of the general switching performance.

The engineering of the crystal structure is another possible approach to change the switching behavior. However, as reported by [50] and [51], the phases of TiO_2 films show no clear influence of the switching performance. Several groups suggest that an improved switching performance is related to the Magnéli phase (Ti_4O_7) formation in TiO_2-based ReRAM [52, 53]. However, engineering of the crystal structure at local scale in the TiO_2 film is still not fully under control [51].

The engineering of the metal/oxide interface in a TiO_2-based ReRAM can be achieved either by electrode material variation or by inserting another oxide at one metal/oxide interface. The most straightforward method is variation of metal electrode material that is in contact with TiO_2, since the work function of these metals can influence the Schottky barrier height at the oxide/electrode interface and thus influence the switching performance [54]. To reduce the high operation current in TiO_2 single-layer ReRAM cells, which limits its RS applications, a thin insulating layer (e.g. Al_2O_3) that serves as a tunneling barrier [27] is inserted into the active switching interface, i.e. between metal electrode (TiN or Pt) and TiO_2. Al_2O_3 films with the optimal thickness can stabilize the bipolar resistive switching and enhance the switching properties significantly, like resistance ratio between the two states, endurance [25] and operation consumption [6] properties. Oh et al. have proved the oxidation reaction between different metal electrodes and the underlying TiO_2 film during the resistive switching [55]. Furthermore, Bousoulas et al. have reported [56] that the increase of the active Ti electrode thickness can improve the bipolar resistive switching performance via increasing oxygen vacancies in the TiO_2 layer. Therefore, the TiO_2-based ReRAM cell is designed to have one inert metal electrode (like Pt or TiN) and another metal electrode (like Ti) that can react via oxygen exchange with the TiO_2 film.

For HfO_2, one of the focuses lies on the doping and oxide/electrode interface engineering. Compared to the undoped HfO_2-based devices, doped HfO_2 by Al, Si, Gd can improve the retention performance [57–59], provide a faster switching speed [59] and increase the

uniformity with reduced operation voltages and distribution of resistance states [58, 60]. Generally, TiN or Pt is often applied as inert electrode in HfO_2-based ReRAM cells, while the counter reactive electrode like Ti [61–63], Hf [64, 65] or Ta [66], are used to supply a sufficient quantity of oxygen vacancies to support the bipolar resistive switching. By adding highly insulating materials like ZrO_2 [67, 68] and Al_2O_3 films [69] at the interface between inert electrode and HfO_2, the resistance uniformity or endurance can also be enhanced.

For TaO_x-based devices, the similar stoichiometry engineering and oxide/electrode interface engineering are also studied. Ta_2O_5 and TaO_{2-x} are often combined, utilizing their different electronic and ionic conductions to realize high performance devices [23], where the insertion of insulating Al_2O_3 at the interface between inert electrode and TaO_x has been tried as well [70]. Through optimizing the OEL electrodes, TaO_x-based cells with Ta and W show an enhanced switching stability compared to Ti and Hf electodes [22].

Energy efficiency and performance

Both the energy efficiency and the switching performance are important for the application of ReRAM as emerging memory, such as for the Internet of Things (IoT). Mobile applications require low energy consumption due to the limited battery capacity, meanwhile the switching performance like switching speed should be sufficiently enhanced to accomplish requested tasks in time. Resistive switching devices enable low power consumption due to inherent non-volatility and small energy cost for writing bit. As reported by Lee et al. [71], the ReRAM cells can switch as fast as 10 ns within 2 V and prvoide lower power consumption based on 25 µA SET current and $\approx$ 1 V operation voltage amplitude. Besides, many other VCM-type ReRAM cells also show low power consumption [27, 72].

The time for switching, namely SET or RESET time, is defined as the value required for successful changes between the two states during the operation process (Fig. 2.3). Taking the SET time in a VCM-type cell as one example, the reduction of the SET voltage amplitude increases the SET time and thus decreases the switching speed. This general feature is defined as the SET kinetic in VCM-type cells and plays an important role for the optimization of speed and power consumption. Therefore, various studies on the SET and RESET kinetics have been carried out. Several groups report that VCM-type cells, like HfO_x [73, 74] and TaO_x [22, 75], can set within 100 ns. However, the reduction of the switching time is accompanied by the raise of operation voltages. As summarized by Menzel et al. [39], the particular voltage dependence of SET time for VCM-type cells exhibits strong correlation to the oxide materials, whereas other parameters like filament geometry and pre-defined high resistance state could also play important roles.

To increase the energy efficiency, not only switching parameters but also the computing algorithm can be modified. Due to the similar working principle between a synapse

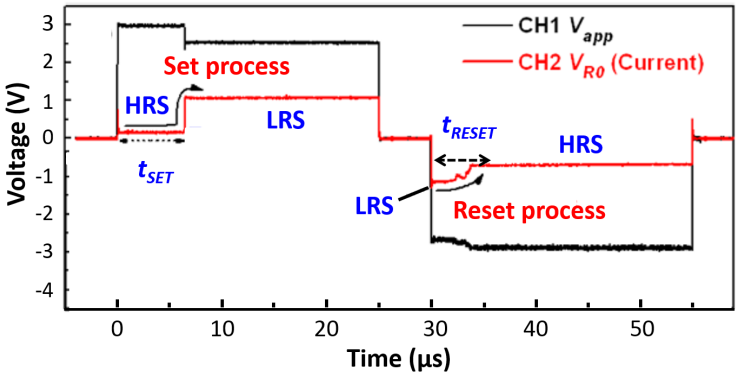

Figure 2.3: *Schematic illustration of SET and RESET process in the pulse measurement. The image is redrawn from [76].*

and a ReRAM cell, the characteristics of the resistance change in VCM-type ReRAM are integrated into the simulation of specific electronic circuits and achieved synapse like behavior [77], which verifies the potential of VCM-type ReRAM for beyond von Neumann computation architectures like neuromorphic computing. In the human brain as shown in Fig. 2.4, the signal transfer between the two neurons is realized through a synapse. By imitating the function principle of a synapse through the VCM-type cells, the propagation of signals in a neuron-based matrix can be reproduced by a VCM-type cell based crossbar matrix [78].

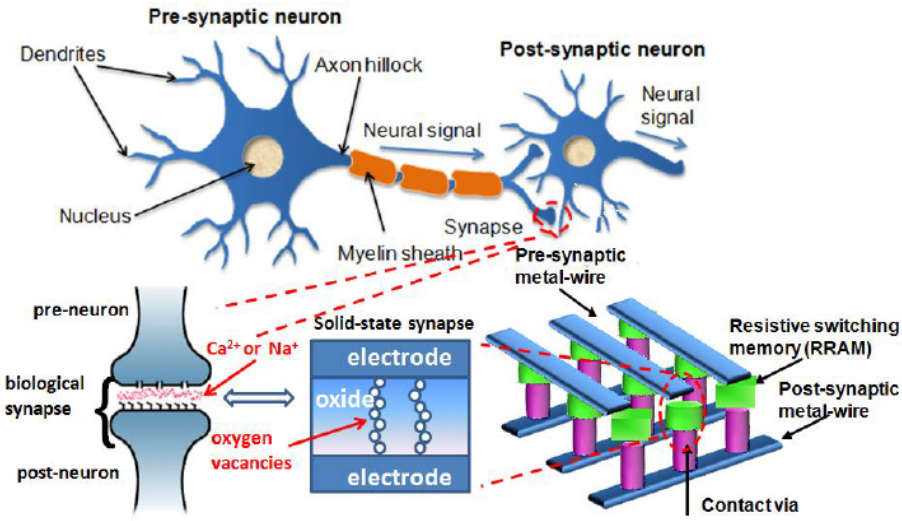

Figure 2.4: *The function of synapses connecting two neurons can be imitated by an oxide-based resistive switching cell in a crossbar structure. The image is taken from [78].*

Besides the pioneering scientific research in this area, first technological approaches aiming to increase the capacity of neuromorphic computing matrices have already been established. Among others, IBM have reported a prototype brain-like chip named as TrueNorth-based PCM devices [79] to emulate the function of the human brain, which could drive 256 Million synapses by < 0.1 W energy cost in year 2014.

2.3 Principle of the VCM-type ReRAM

To introduce the VCM-type ReRAM into the specific hardware requires each cell to meet the defined specification, like switching voltages, resistance values, switching speed, cycling endurance and data retention, within the allowed range of variability. Therefore, the optimization of properties of VCM-type devices is very important. As the dimension of an individual cell is reduced to the tens of nano-meter range, this optimization requires a deep understanding of the switching mechanism focusing on the rearrangement and creation or annihilation of mobile ions. The well accepted understanding of the switching mechanism of VCM-type ReRAM is based on drift/diffusion of oxygen vacancies upon applied electrical field, where a local reduction/oxidation (shortly as redox) process occurs in the typical transition metal oxides [4, 7, 80]. VCM-type cells can be operated in both unipolar and bipolar resistive switching (BRS) modes, referring to the SET and RESET operations accomplished either with one polarity of voltage bias or with two opposite polarities, respectively. The initiation of the two modes is dependent on the switching parameters and the cell stacks. For the unipolar resistive switching the thermal energy plays the most important role, whereas for the bipolar resistive switching the ionic movement is driven by the electrical field and assisted by the thermal energy. Due to the lower demand on the thermal energy, bipolar resistive switching often exhibits relative low operation power [71, 81, 82]. Moreover, the cycling endurance with bipolar operation mode is higher compared to the unipolar mode within the same device [83].

In addition, the VCM-type switching can be divided into filamentary and interface switching, where the resistance values or the corresponding read-out current levels are irrelated [72, 84] or related [6, 85] to the contact area, respectively. The filamentary-type switching happens mainly via one or several conduction paths, while the interface switching involves the whole interface area sandwiched between the electrode and the metal oxide. In this work, the cells switch according to the filamentary-type BRS showing operation ability of two opposite switching polarites. Therefore, the notation introduced by Waser [4], so-called "counter-eightwise (c8w)" and "eightwise (8w)" hysteresis are applied. The c8w BRS is defined by the switching polarity of resistance follows an opposite drawing direction of the handwriting 8, if the the voltage signal is always referred to the electrode that forms the higher barrier (Schottky) contact. In contrast, with the direction along the handwriting 8, it is called 8w BRS. Here the simplified model for c8w switching

mechanism in the filamentary-type VCM cells is discussed and depicted in Fig. 2.5.

A standard VCM-type ReRAM cell consists of an inert high work function metal electrode (e.g. Pt), a metal oxide switching layer (e.g. Ta_2O_5 [87, 88], TiO_2 [89, 90], HfO_2 [91–93]) and an oxygen exchange layer (OEL) (e.g. Hf [94], Ta [22, 95], Ti [61, 63]) as the low work function counter electrode. The extended VCM switching model introduced by Menzel in [96] is used to explain the c8w switching behavior. Prior to the resistive switching behavior, the insulating devices require a "soft breakdown" event, called electroforming. During this step, a conductive filament is formed under the application of electric field and temperature due to Joule heating induced by the current. To take the $Pt/Ta_2O_5/Ta$ stack as one example (see Fig. 2.5), an oxygen vacancy-rich conducting filament forms after electroforming process. The current (I) - voltage (V) hysteresis is started with the cell being in its high resistance state (HRS, "Ⓐ"). The application of a negative voltage to the Pt electrode causes the migration of oxygen vacancies from the Ta_2O_{5-x}/Ta interface towards the Pt/Ta_2O_{5-x} interface. Since the concentration of oxygen vacancies in the filamentary region is higher than in the surrounding oxide film, the electrical conductance of the filamentary region is increased with respect to the surrounding area. Once the conductive part of the filament electrically connects the two electrodes at a sufficient negative voltage bias, the process is defined as SET process ("Ⓑ"). As a consequence, the resistance of the whole cell changes to the low resistance state (LRS, "Ⓒ"). By applying a sufficient positive voltage to the Pt electrode, the positively charged oxygen vacancies (especially the doubly charged oxygen vacancies, i.e. $V_O^{\bullet\bullet}$) close to the

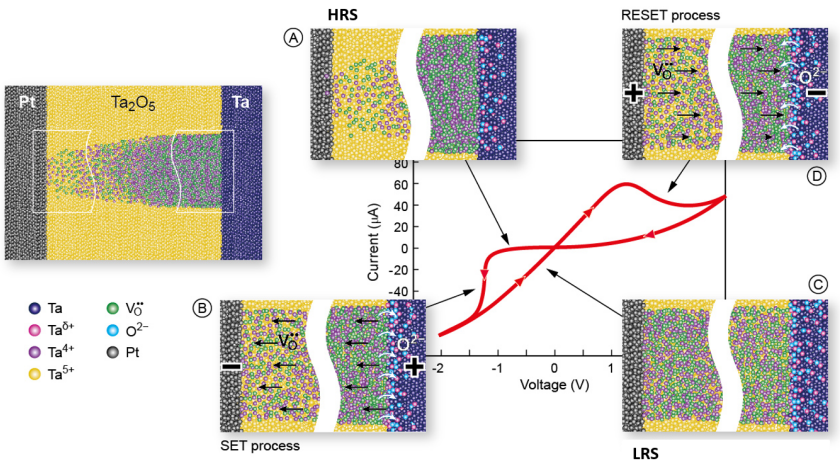

Figure 2.5: *Schematic illustration of the filamentary-type VCM switching model. The switching hysteresis follows the c8w orientation by starting from (a) HRS, undergoing (b) a SET process into (c) LRS and a closing of the loop by (d) a RESET process. The Image is redrawn from [86].*

Pt/Ta_2O_{5-x} interface are repelled from the Pt and migrate towards the Ta electrode. Oxygen vacancies arriving at the Ta_2O_{5-x}/Ta interface can be partly annihilated by oxygen ions that are restored in the Ta electrode [22]. This process is defined as RESET process ("Ⓓ"). As a result, the number of $V_O^{\bullet\bullet}$ close to the Pt/Ta_2O_{5-x} interface are reduced and the conductive filament is ruptured, resulting in an increased total resistance ("Ⓐ"). The ruptured filament can be reconnected by applying the opposite bias. Thereby, the two resistance states can be written and erased by the reversible migration of $V_O^{\bullet\bullet}$ during BRS.

The 8w BRS mode with opposite polarity in contrast to c8w BRS has been obtained in different transition metal oxide-based devices. To take one earliest observation in the $Nb:SrTiO_3/500$ nm $SrTiO_3(Fe)/Pt$ structure as one example, the 8w switching was obtained parallel to c8w switching. By means of the local conductivity atomic force microscopy (LC-AFM) technique, c8w and 8w switching events were addressed to the core and the periphery of the filamentary region, respectively [97]. Reviewing the literature, non-volatile 8w-switching polarity is dominantly reported for $SrTiO_3$-based cells [41, 98] and devices made from TiO_2 [99, 100]. Furthermore, X-ray photoemission spectroscopy (XPS) [101] and electron energy-loss spectroscopy (EELS) studies [41] performed on $SrTiO_3$-based devices provide a strong indication that an interfacial oxygen exchange process should be responsible for the non-volatile 8w switching polarity, which shows persistent LRS by being read out several days later. On the contrary, some switching loops with 8w-polarity were found to be metastable and partially volatile in $TiN/Ta_2O_5/Pt$ [102] and in $Pt/ZrO_x/Ta$ devices [103]. The model for the volatile 8w-switching given by Schönhals et al. [102] is also based on an oxygen exchange reaction at the Pt/Ta_2O_{5-x} interface (see Fig. 2.6). However, this reaction is considered to be volatile and is compensated by the annihilation, due to the slow decay from 8w low to high resistance state within one hour.

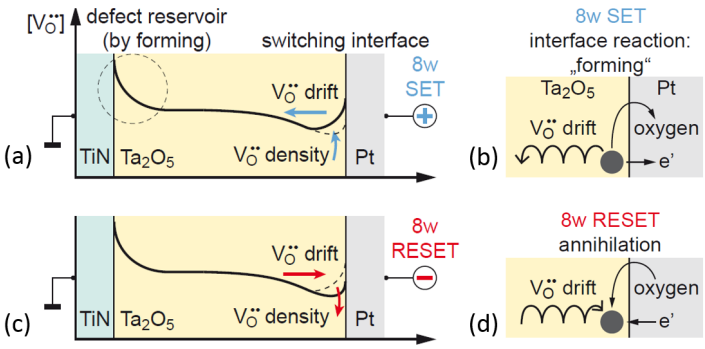

Figure 2.6: *Model of metastable 8w swicthing behavior obtained in $Pt/Ta_2O_5/TiN$ devices. (a,c) Oxygen vacancy profile in the Ta_2O_{5-x} filament. (b,d) Oxygen exchange reaction during 8w SET and RESET process, respectively. Images are adapted from [102].*

As a matter of fact, even in the same material like TiO_2, different VCM-type resistive switching mechanisms can appear in various stacks. After more than ten years of research, TiO_2-based ReRAM devices show their ability of unipolar and bipolar-type of resistive switching (BRS), including standard filamentary-type c8w BRS and 8w BRS [99], the ability of forming-free switching [104] and the potential ability of area-type switching [6, 105]. All these findings make a systematic study on nano-sized TiO_2 ReRAM cells with and without an Al_2O_3 barrier layer very interesting.

2.4 Electronic transport mechanisms

The current transport in a typical ReRAM cell, i.e. a $metal_1$-oxide-$metal_2$ (M_1OM_2) structure, is often complex and comprises multiple mechanisms. However, for defined temperature- and voltage ranges, mostly one transport mechanism can be identified as dominating. Therefore, the determination of the main current conduction mechanism with respect to the character of an M_1OM_2 structure is important. The main transport mechanism in M_1OM_2 structures of almost defect-free oxide layers are considered as the tunneling process (2.4.1) or the thermionic emission (2.4.2). If defects have to be considered as electron traps, the relevant conduction mechanisms that include the influence of defect energy level and defect concentration, such as Poole-Frenkel emission (2.4.3), hopping conduction (2.4.4) and ohmic conduction (2.4.5), should be taken into consideration.

2.4.1 Tunneling

Tunneling without temperature consideration

Figures 2.7 (a-c) represent the schematic band diagrams for electron transport through an M_1OM_2 stack with asymmetric barriers under different applied bias voltages (V). The barrier heights at the two metal oxide interfaces are defined as Φ_1 and Φ_2 with $\Phi_1 < \Phi_2$. The total tunneling length is L.

A generalized formula for the tunneling current through a system with asymmetric barriers was developed by Simmons [106]. According to this theory the current transport in the M_1OM_2 stack is given as:

$$I = A \cdot J_0 \left[\bar{\Phi} \cdot exp(-\alpha \cdot \bar{\Phi}^{\frac{1}{2}}) - (\bar{\Phi} + qV) \cdot exp\Big(-\alpha \cdot (\bar{\Phi} + qV)^{\frac{1}{2}}\Big) \right], \tag{2.1}$$

with $J_0 = \dfrac{q}{2\pi h} \cdot \dfrac{1}{l^2}$ and α is $= \dfrac{4\pi l}{h} \cdot (2m^*)^{\frac{1}{2}}$, A is the tunneling current flux area, m^* is the effective electron mass in the oxide film, $h = 4.13566 \cdot 10^{-15}$ eV·s is the Planck constant and the elementary charge q. The effective tunneling length l and the effective tunneling

barrier $\bar{\Phi}$ are voltage dependent.

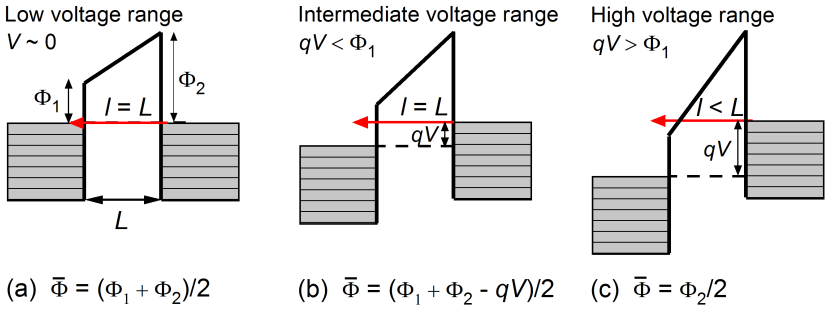

Figure 2.7: *The typical band diagram for an M_1OM_2 structure with asymmetric barriers ($\Phi_1 < \Phi_2$) for: (a) the low voltage range, (b) the intermediate voltage range and (c) the high voltage range. The positive voltage signals are applied to the electrode with low barrier height. The effective tunneling barrier height $\bar{\Phi}$ is listed in each graph. L defines the total tunneling length and l is the effective tunneling length.*

Different expressions for l and $\bar{\Phi}$ can be derived for the three voltage ranges: (a) for the voltage V close to zero (Fig. 2.7 (a)), electrons have to tunnel through the full barrier length ($l = L$) and the tunneling barrier height $\bar{\Phi}$ roughly equals to the average value of the barrier heights from both interfaces. (b) By applying an intermediate positive voltage V ($|qV| < \Phi_1$) to the left electrode (Fig. 2.7 (b)), the direct tunneling process is still through the full barrier length ($l = L$) but with a reduced tunneling barrier height $\bar{\Phi} = \dfrac{\Phi_2 + \Phi_1 - qV}{2}$. (c) Increasing the positive voltage over the left barrier ($|qV| > \Phi_1$), the effective tunneling length is reduced to l, which can be calculated with L, Φ_1, Φ_2 and qV by the similar triangles as: $l = L \cdot \dfrac{\Phi_2}{\Phi_2 - \Phi_1 + qV}$, and the tunneling barrier height $\bar{\Phi}$ equals $\Phi_2/2$. Summarizing the voltage dependent values of l and $\bar{\Phi}$ for the case of a positive voltage applied to the electrode with the lower barrier interface (Φ_2) results in:

$$l = \begin{cases} L, & \text{for } qV \approx 0 \\ L, & \text{for } \Phi_1 > qV > 0 \\ L \cdot \dfrac{\Phi_2}{\Phi_2 - \Phi_1 + qV}, & \text{for } qV > \Phi_1 \end{cases} \tag{2.2}$$

$$\bar{\Phi} = \begin{cases} \dfrac{\Phi_2 + \Phi_1}{2}, & \text{for } qV \approx 0 \\ \dfrac{\Phi_2 + \Phi_1 - qV}{2}, & \text{for } \Phi_1 > qV > 0 \\ \dfrac{\Phi_2}{2}, & \text{for } qV > \Phi_1 \end{cases} \tag{2.3}$$

In contrast, for a negative voltage applied to the left electrode an equivalent set of equations can be derived (for details see [106]). The Simmons' equation is used in chapter 7 and 8 for the discussion of the tunneling current.

Tunneling with temperature consideration

The Simmons' model for the tunneling current through a trapezoidal barrier shown in Fig. 2.7 is derived for a temperature of zero Kelvin (0 K). This means that electrons from the Fermi level can tunnel through a trapezoidal barrier. Regarding the the Fermi-Dirac distribution at 0 K the contribution of thermally activated electrons on the tunneling current is neglected due to the rapid decay of the electron number.

However, the situation changes for a Schottky interface between a metal and an oxide with space charges where the barrier has a nearly parabolic, concave curvature. For this barrier form, the contribution from the thermally activated electrons in the tunneling process becomes non-negligible. The tunneling process through a Schottky-type barrier is schematically shown in Fig. 2.8. According to the ab-initio and continuum simulation [107] the transmission probability of thermally activated electrons through the Schottky barrier is significantly raised in comparison of the electrons tunneling at the Fermi level (W_F) in the low voltage region. Generally, the tunneling current through the Schottky interface is referred to as Schottky tunneling [108].

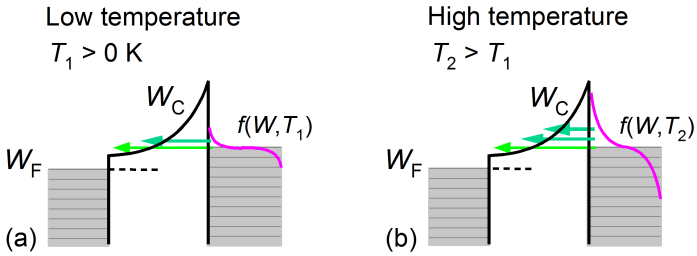

Figure 2.8: *The tunneling of electrons through a Schottky interface in the M_1OM_2 structure (a) with finite temperature and (b) with higher temperature. The number of successfully tunneling electrons is increased due to the wider spread of Fermi-Dirac distribution function f(W,T).*

2.4.2 Thermionic emission

Thermionic emission describes the process of the injection of thermally activated electrons from metal into oxide dielectric (including semiconductor and insulator) by means of overcoming the interface barrier due to their thermal energy. In an M_1OM_2 stack under a high temperature, significant amount of electrons in the metal is activated and can overcome the barrier ($\Phi_B = q\phi_B$) at the metal/dielectric interface (Fig. 2.9 (a)). This

effective interface barrier Φ_B is lower than the interface barrier Φ_{B0}, which is the difference between the metal work function (Φ_M) and the oxide electron affinity (χ). This lowering is due to the image potential generated by the escaping electrons. By applying a negative bias to the right electrode M_2, electrons can be injected into the dielectric with a reduced barrier height ($q\phi_B'$) and then move to the counter electrode further through the conduction band (Fig. 2.9 (b)).

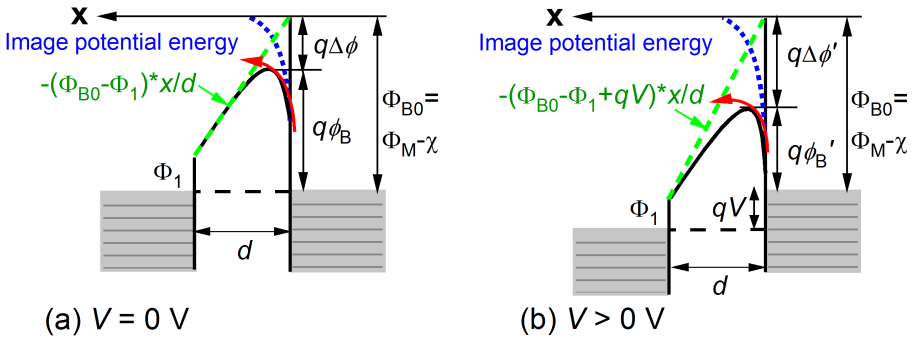

Figure 2.9: *The barrier at a metal/oxide interface for the thermionic emission with the bias to the left electrode for: (a) $V = 0$ V and (b) $V > 0$ V. The dashed blue line represents the image potential energy due to escaping electrons, while the dashed green line represents the potential without image potential in the oxide film (a) without and (b) with external voltage. The black line represents the total potential resulting from blue and green potentials for each situation. d is the thickness of the dielectric.*

The form of this barrier lowering is determined by the combination effect of the total electrical field (the dashed green line in Fig. 2.9) and the image force (the dotted blue line in Fig. 2.9) [109]. The mathematical description fomulated by Schottky [109] of this lowering is expressed as a modified barrier $\phi_B = \phi_{B0} - \sqrt{qE/4\pi\epsilon_r\epsilon_0}$ inserted in the current density (J) - field (E) relation for the thermionic emission [110]:

$$J_S = A^* T^2 \, exp\left(-\frac{q(\phi_{B0} - \sqrt{qE/4\pi\epsilon_r\epsilon_0})}{k_B T}\right), \tag{2.4}$$

where the effective Richardson constant $A^* = \dfrac{4\pi q {k_B}^2 m^*}{h^3} = 1.2{\cdot}10^6$ A/(m^2·K^2) for $m^* = m_0$ [109], the effective electron mass in dielectric m^*, m_0 is the electron rest mass, h is the Planck constant, k_B is the Boltzmann constant, q is the elementary charge, $q\phi_{B0} = \Phi_{B0}$ is the interface barrier height, ϵ_r is the optical permittivity of dielectric and ϵ_0 is the vacuum permittivity. From the intercept of $\ln(J/T^2)$ as the function of $\sqrt{E}$ the interface barrier height $q\phi_B$ can be obtained.

2.4.3 Poole-Frenkel emission

Poole-Frenkel emission describes the internal thermal emission of trapped electrons into the conduction band of an oxide (Fig. 2.10 (a)). In an imperfect oxide film, the positive charged defects, e.g. oxygen vacancies, are combined with trapped electrons to keep the charge-neutrality of the film. Without applying any electrical field, the escape rate of electrons from traps is equal to the capture rate of electrons. In this case the net flux in one direction is statistically zero. Applying an electrical field, the probability of releasing electrons from these traps against the field direction is increased, while in the other direction it is not enhanced. This effect is only obvious for a sufficiently deep defect level, i.e. the trap levels of the defects should be deep in the band gap. After being released from a trap, the electrons should move freely in the conduction band. The re-trapping by neighboring traps is not considered for the Poole-Frenkel emission. To fulfil this condition, the defects should be highly separated from each other and the corresponding defect density should be low.

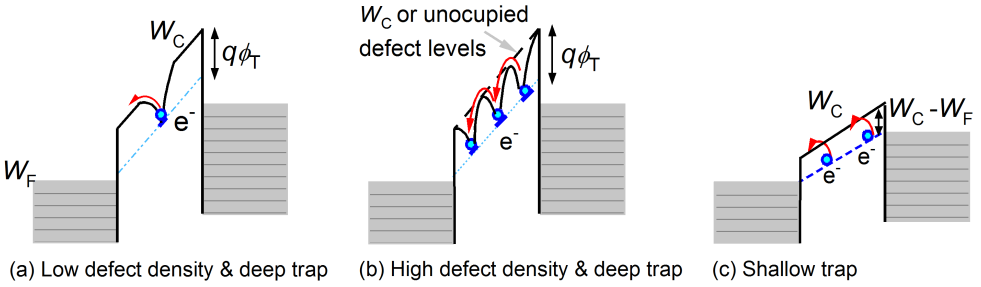

Figure 2.10: *Schematic band diagram of (a) Poole-Frenkel emission, (b) hopping conduction and (c) ohmic conduction in an M_1OM_2 stack.*

The corresponding J vs. E relation is given [110]:

$$J_{\mathrm{PF}} = q\ \mu\ E\ N_{\mathrm{C}}\ exp\left(-\frac{q(\phi_{\mathrm{T}} - \sqrt{qE/\pi\epsilon_{\mathrm{r}}\epsilon_0})}{k_{\mathrm{B}}T}\right), \tag{2.5}$$

where μ is the electron mobility, N_{C} is the effective density of states in conduction band, $q\phi_{\mathrm{T}}$ is the trap energy level. The slope of $\ln(J/E)$ as the function of $1/T$ gives the field dependent transport barrier $W_{\mathrm{a}} = q(\phi_{\mathrm{T}} - \sqrt{qE/\pi\epsilon_{\mathrm{r}}\epsilon_0})$. The intercept of W_{a} vs. $\sqrt{E}$ plot defines the intrinsic Poole-Frenkel barrier $q\phi_{\mathrm{T}}$ under zero bias, which is also the energy distance from the defect trap level to the bottom edge of conduction band W_{C}.

2.4.4 Hopping conduction

In contrast to Poole-Frenkel emission, Hopping conduction describes the release/re-trap process of electrons from/into the neighboring defect levels, which is mostly observed in amorphous solids [111] (Fig. 2.10 (b)). The electron release process that contributes to the current flow is mainly activated by the electrical field instead of the thermal energy. Without external electrical field the barrier ($q\phi_T$) for electrons to be overcome is identical for both directions. By applying the electrical field this barrier can be modified so that the release of electrons in one direction is favored (the red arrows in Fig. 2.10 (b)). To activate the release and re-trap processes, the distance between the neighboring defects has to be short, i.e. the defect density has to be high. Moreover, the defect energy level has to be deep enough in the band gap to hinder the possibility of pure thermal activation of electrons.

The relation of J-E for hopping conduction transport is [112]:

$$J_{\text{hopping}} = q\ n\ a\ \upsilon\ exp\left(-\frac{q\phi_T - \frac{1}{2}qaE}{k_B T}\right), \tag{2.6}$$

where a is the hopping distance, n is the charge carrier concentration, υ is the frequency of the thermal vibration of electrons at trap sites. $q\phi_T$ is the barrier height for hopping conduction, which is not necessarily as high as the distance between the conduction band and the trap energy level, but could also be the difference between unoccupied energy states and occupied states (the black broken line in Fig. 2.10 (b)). Through the analytical method the absolute value of the slope from the ln$I$ vs. $1/T$ plot gives the field dependent transport barrier $q\phi = q(\phi_T - \frac{1}{2}aE)$. By plotting $q\phi$ against the applied voltage V with $E = V/d$, the hopping distance a can be calculated from the slope and film thickness d, i.e. slope $= \frac{a}{2d}$, while the value of the intercept is the activation energy ($q\phi_T$) for field-free case.

Generally, the hopping distance is within several atom spacings. If the hopping distance is too large, the electrons tend to transport in the conduction band and the Poole-Frenkel emission process dominates. If the hopping distance is too small, the electrons tend to tunnel between different trap states. Therefore, the comparison of the hopping distance to the interatomic distance can be used as a signature of the validity of the hopping model. Several studies related to binary oxides in an M_1OM_2 structure applied the electron hopping models, e.g. for LRS in the TaN/SiO_x/n^{++}Si device with $a \approx 1.3$ nm and in the TiW/SiO_x/TiW device with $a \approx 1.6$ nm [112].

2.4.5 Ohmic conduction

Ohmic conduction in an M_1OM_2 structure describes the thermal activation process of electrons from defect levels into the oxide conduction band and the migration of these electrons under the electrical field (Fig. 2.10 (c)).

The relation between the current density J and the electrical field E is [110]:

$$J_{ohmic} = \sigma E = q\, n\, \mu\, E,\ n = N_{\mathrm{C}}\, exp\left(-\frac{W_{\mathrm{C}} - W_{\mathrm{F}}}{k_{\mathrm{B}} T}\right), \tag{2.7}$$

where μ is the electron mobility, $(W_{\mathrm{C}} - W_{\mathrm{F}})$ is the energy difference between the bottom of conduction band and the Fermi-level. Plotting the temperature related $I(V)$ relation as $\ln(I/V)$ against $1/T$, the averaged slope provides the value of $(W_{\mathrm{C}} - W_{\mathrm{F}})$. The plot procedure is illustrated in [110].

2.4.6 Summary for the transport mechanisms

Besides the interface transport, namely thermionic emission (Fig. 2.11 (1)) and tunneling (Fig. 2.11 (2)), other transport mechanisms are all closely related to the traps present in the bulk. In other words, the validity of Poole-Frenkel emission (Fig. 2.11 (3)), hopping conduction (Fig. 2.11 (4)) and ohmic conduction (Fig. 2.11 (5)) depends on the trap density and trap energy level.

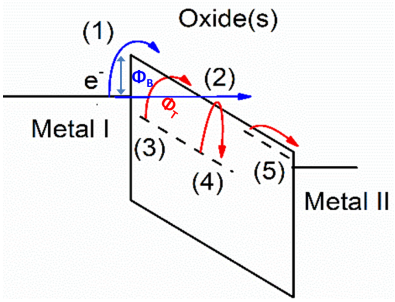

Figure 2.11: *The illustration of possible transport mechanisms in an M_1OM_2 structure: (1) thermionic emission, (2) tunneling process, (3) Poole-Frenkel emission, (4) hopping conduction and (5) ohmic conduction.*

For the ohmic conduction the localized trap energy level should be close to the conduction band. The difference between Poole-Frenkel emission and hopping conduction is mainly defined by the density of traps. For Poole-Frenkel emission, it is assumed that the electrons are emitted from localized traps and mainly move into the delocalized conduction band. To ensure this process, the trap density has to be low. For the hopping conduction, on the contrary, electrons can be emitted and trapped again by the neighbor-

ing localized traps with only a short distance between each other. Therefore, the distance between two localized trap states has to be low, this is, the trap density has to be high.

To analyze the electronic transport mechanism in a given M_1OM_2 structure, three important material parameters of oxide films should be taken into consideration:

1. The effective mass (m^*) of electrons in the oxide, which influences the tunneling current.

2. The electron affinity (χ), which determines the interface barrier height (Φ_{B0}) between the oxide and the metal as: $\Phi_{B0} = \Phi_M$ - χ. This interface barrier height Φ_{B0} ($= q\phi_{B0}$) is important for both tunneling and thermionic emission analysis.

3. The defect level in the oxide film, which is important for separating Poole-Frenkel emission, electron hopping and ohmic conduction from each other.

All the parameters are material specific and are also crystal structure dependent. In the following section, these three parameters are discussed for the materials applied in this thesis.

2.5 Properties of the Materials

2.5.1 Titanium dioxide

As one of the most important valence change materials TiO_2 is extensively studied. Natural TiO_2 minerals exist in three most frequent crystal structures (Fig. 2.12): (a) rutile, (b) anatase and (c) brookite.

Dense and homogeneous TiO_2 thin films with a few nanometers in thickness can be deposited by various techniques, for example sputtering [116, 117], pulsed laser deposition (PLD) [118] and plasma-enhanced atomic layer deposition (PE-ALD) [119]. The crystalline structure of the deposited TiO_2 thin film, however, depends on multiple deposition parameters. For oxide films obtained by thermal liquid injection ALD, which is the technique used in this study, the structure of as-grown TiO_2 thin films is sensitive to the growth temperature and the film thickness [114, 115], even if the deposition temperature for these films was still within the ALD window of the precursors (details see 3.1.1). Figures 2.13 (a) and (c) point out that the as-deposited 3 nm TiO_2 films grown at 200°C or 300°C are still amorphous. Kim et al. [114] found that at 260°C deposition temperature the oxide films for thickness of about 6 nm and 50 nm are amorphous and crystalline, respectively.

The effective mass of electrons in the different TiO_2 phases is summarized in Table 2.1 with the unit of rest electron mass in vacuum (m_0). For the anatase phase most experimental studies suggest the value of around $1 \cdot m_0$, while for the rutile phase the reported

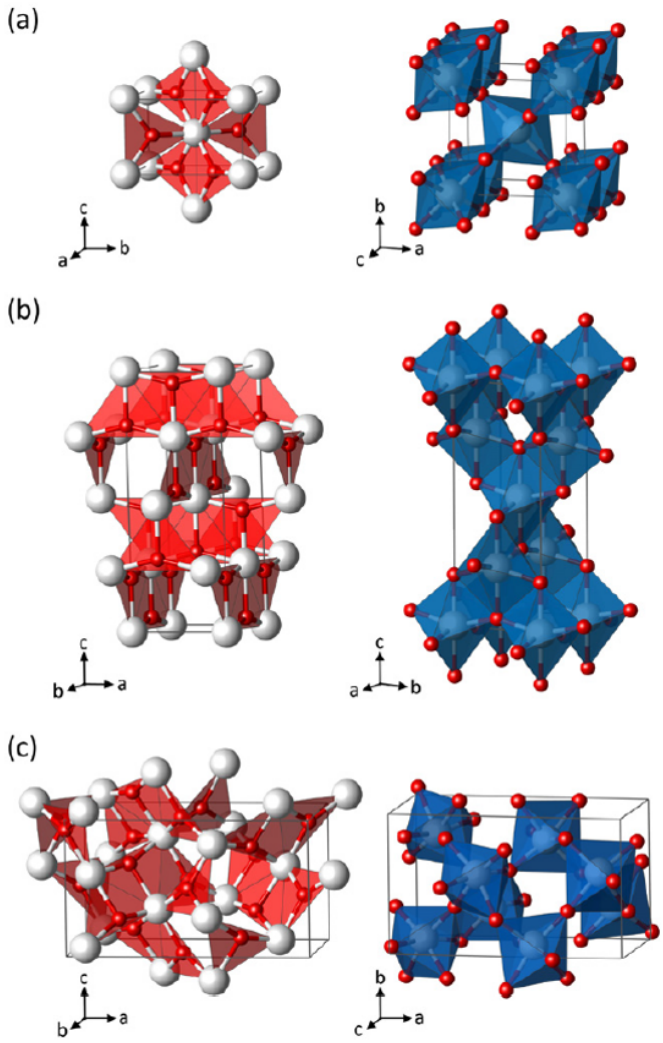

Figure 2.12: *The crystal structures of TiO_2: (a) rutile, (b) anatase and (c) brookite. The left and right columns show the coordination of the Ti^{4+} ions and the O^{2-} ions, respectively. The image is taken from [113].*

values vary to a great extend. The experimental values are above $10{\cdot}m_0$ compared to the value $< 1{\cdot}m_0$ applied in the simulation works. For amorphous related TiO_2 films, only one experimental result has been reported with $m^* = 0.25{\cdot}m_0$.

Besides, the values of the band gap (W_G) and the electron affinity (χ) show the difference between anatase and rutile crystals as well. In anatase phase W_G is around 3.2 eV [120, 127, 128] from experimental results and W_G in rutile phase is slightly reduced to 3.0 eV [120, 129]. Based on the the XPS measurement and theoretical calculations,

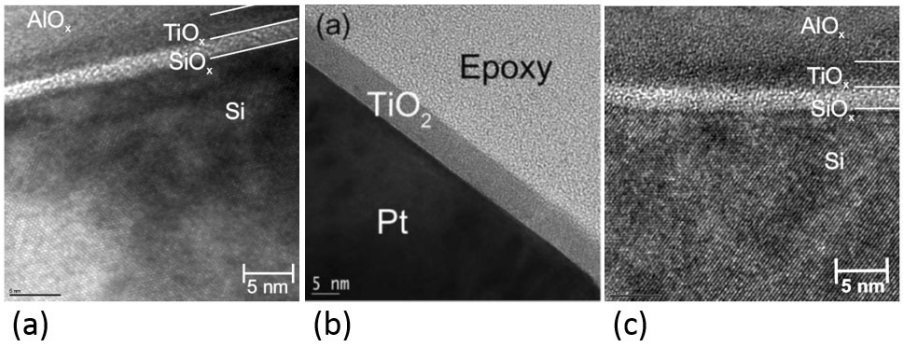

Figure 2.13: *Transmission electron microscopy images of (a) a 3 nm amorphous TiO_x film on Si(100) substrate grown at 200°C, (b) a 6 nm amorphous TiO_2 film on Pt substrate grown at 260°C, (c) a 3 nm amorphous TiO_x film on Si(100) substrate grown at 300°C. Images are taken from [114, 115].*

Crystalline structure	Experimental method	m^* $(\cdot m_0)$
Anatase	Mott transition electron density	1 [120]
	$I(V)$ fitting	≈ 1 [121]
	Optical Absorption coefficient	> 10 [122]
	DFT calculation	0.24 - 0.26 [123]
Amorphous/rutile multilayer	Hall mobility	0.25 [124]
Rutile	Mott transition electron density	20 [120]
	DFT calculation	0.6 - 0.8 or > 1 [125]
	DFT calculation	0.57, 1.11 [123]
	$I(V)$ fitting	≈ 20 [121]
	Hall mobility	37 - 133 [126]

Table 2.1: *The electron effective mass (m^*_{TO}) in different crystal phases of TiO_2 films. The unit is the rest electron mass (m_0) in vacuum. DFT = density functional theory.*

Scanlon et al. point out that the electron affinity of anatase phase should be 5.1 eV, while for rutile it is 4.8 eV [130].

The energy levels from point defects in TiO_2 thin films play an important role for determining the electronic properties. Discovered in the highly application-relevant M_1OM_2 structure, the positively charged oxygen vacancies with different charge states (0, +1 or +2) supply deep traps located around 0.62 eV below the conduction band for rutile phase [126]. Similar deep trap states of 0.5 to 0.8 eV have been observed in thin films of anatase phase [131] and in anatase phase nanoparticles the value has been reported from 0.7 to 1.0 eV [132]. Both values are attributed to the oxygen vacancies. Shallow traps with activation energy around 0.26 eV have been observed in ultra-thin TiO_2-based VCM-type ReRAM structures, where TiO_2 can be amorphous or anatase-type [99, 133]. Besides, shallow traps with 0.1 eV activation energy have been observed in a highly conductive

TiO_2 film [133].

It has to be mentioned that for the Ti-O system in addition to the TiO_2 phases numerous crystal structures exist with compositions of O/Ti < 2. These phases can be formed at high temperature under oxygen poor conditions. The most prominent phases are the class of conductive Magnéli phases Ti_xO_{2x-1} ($4 < x < 9$) [134,135] and corundum phase Ti_2O_3, which typically show an obvious resistance change upon the temperature change [53]. Some authors have successfully identified a Magnéli-type structure in the filament region of TiO_2 films after the hard unipolar switching [136]. However, for the bipolar switching process in rutile-type TiO_2, the observed crystal structure change did not show filamentary geometry [137].

2.5.2 Aluminium oxide

As a mineral in the nature alumina exists as hexoganal α-Al_2O_3 with a corundum structure of the space group R-$\bar{3}$c. α-Al_2O_3 can be treated as a hcp structure with one third of the Al sites being vacant. This phase is the thermodynamically stable phase and has the highest volume density [138].

The schematic structures for a unit cell of α-Al_2O_3 and γ-Al_2O_3 are shown in Fig. 2.14 (a) and (b), respectively. The as-grown amorphous Al_2O_3 thin film can transform into γ-Al_2O_3 and then into α-Al_2O_3 at annealing temperatures above 1000°C [141]. Moreover, γ-Al_2O_3 has lower mass density (3.65 g/cm^3) than α-Al_2O_3 (3.97 g/cm^3) from inorganic crystal structure database (ICSD). Amorphous Al_2O_3 may have even a lower mass density of less than 3 g/cm^3 [142]. With its high band gap Al_2O_3 has been widely applied as gate oxide in CMOS [143], DRAM [144] or tunneling barrier for spintronics [145].

The electron effective mass in different phases of Al_2O_3 is listed in Tab. 2.2. It has

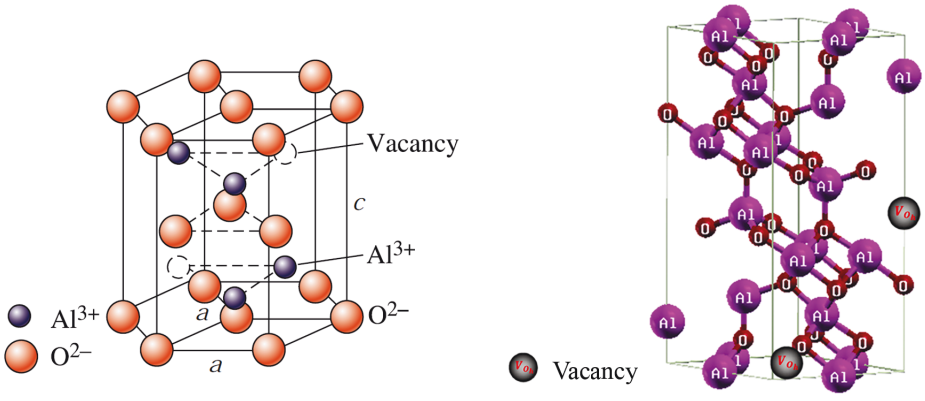

Figure 2.14: *Schematic structures of a unit cell of (a) alpha-alumina (α-Al_2O_3) and (b) gamma-alumina (γ-Al_2O_3). Images are taken from [139,140].*

Crystalline structure	Determination method	m^* ($\cdot m_0$)
α-Al_2O_3	DFT calculation	0.4 [146]
γ-Al_2O_3	DFT calculation	0.4 [146]
Amorphous	$I(V)$ fitting	0.28 ± 0.04 [147]
	$I(V)$ fitting	0.17 - 1.14 [148]
	$I(V)$ fitting (FN tunneling)	0.22, 0.42 [149]
Unknown	Assumption for FN fitting	0.5 [150]
	FN fitting	0.35 [151]
	FN fitting	0.16 [152]
	$I(V)$ fitting (direct tunneling)	0.35 [153]
	Assumption for FN fitting	0.23 [154]
	$I(V)$ simulation	0.2 [155]

Table 2.2: *The electron effective mass in different Al_2O_3 crystal structures. The unit is the rest electron mass (m_0) in vacuum.*

to be mentioned that most effective mass values were obtained from $I(V)$ fitting in the M_1OM_2 or MOS structure based on either direct tunneling or Fowler-Nordheim (FN) tunneling model. Besides the difference from crystalline phases, the deposition methods for the metal electrodes [148] and the voltage polarity [149] can play an important role as well.

As pointed out by different simulation works, the defect levels in Al_2O_3 films could differ greatly with their charge states [156, 157]. Through the comparison between experimental methods and simulation methods, the most acceptable defect energy levels are summarized in Tab. 2.3). Most trap levels in Al_2O_3 film are considered to be deep in the band gap with activation energies larger than 1 eV. In contrast, only one work [158] discussed about shallow trap levels around 0.15 eV in a defect-rich Al_2O_3 film.

Crystalline structure	Determination method	trap level for V_O^X (eV)
α-Al_2O_3	DFT calculation	1.4 [156]
γ-Al_2O_3	XPS	2 - 3 [159]
θ-Al_2O_3	DFT simulation	1.6 - 2.0 [156]
	DFT calculation	2.98 to 3.48 [157]
Amorphous	Thermally stimulated current	0.15 - 1.28 [158]

Table 2.3: *The defect levels in different Al_2O_3 crystal structures. XPS = X-ray photoelectron spectroscopy*

The band gap and electron affinity of different Al_2O_3 crystal phases can be obtained from different analytical methods (see Tab. 2.4), like VUV (vacuum ultraviolet), XES (X-ray emission spectroscopy), UPS (ultraviolet photoemission), IPS (inverse photoemission), REELS (reflection electron energy loss spectroscopy). The band gap for α- and γ-Al_2O_3 are determined as around 8.8 eV, while most amorphous Al_2O_3 films show the values below 7 eV.

Crystalline structure	Determination method	χ (eV)	W_G (eV)
α-Al_2O_3	VUV transimission		8.8 [160]
γ-Al_2O_3	XPS		8.7 [161]
Amorphous	$I(V)$ Fitting and XPS	2.58 ± 0.09	6.65 ± 0.11 [147]
	UPS and IPS	2.5	7 [162]
	XES		6.5 [146]
	REELS		6.77 ± 0.05 [163]
	photoconductivity		6.2 [164]
	XPS		6.7 ± 0.2 [165]
Bulk	estimation from band offset	1	8.8 [166]

Table 2.4: *The electron affinity (χ) and band gaps (W_G) in different Al_2O_3 crystal structures*

Values for the electron affinity suffer from a big variation. The value of electron affinity is reported as around 2.5 eV for amorphous Al_2O_3 from the experimental methods [147, 162], while a theoretical work estimates the χ value at 1 eV [166]. Among others, the electron affinity of 2.58 eV obtained at the chAl2O3/InGaAs interface from the Fowler-Nordheim tunneling fitting [147] is applied in this work, since this determination method is the most closest one for discussion of electron affinity of Al_2O_3 between Al_2O_3 and an electrode material.

Chapter 3

Experimental methods

Chapter 3 starts with the principle and experimental details of the atomic layer deposition of metal oxide thin films in section 3.1, since the oxide deposition method is the core of the device fabrication. The applied methods of structural characterizations are introduced in section 3.2, followed by the fabrication procedure for nano-crossbar structures illustrated in section 3.3. The electrical characterization methods used in this work are described in section 3.4.

3.1 Thermal atomic layer deposition (ALD)

3.1.1 Overview and principle of ALD

Atomic layer deposition (ALD) is applied for growing high-quality thin films based on self-limiting surface chemical reactions between the reactant in the gas phase and reactive surface sites. This deposition technique can yield films with thicknesses from Ångstrom to several µm at growth rates, e.g. for Al_2O_3, from normally about 0.01 to 0.1 nm/s [167, 168] with possible extension to 1.2 nm/s as reported by SoLayTec® in 2010 [169]. The deposition temperature can be tuned in a wide range from room temperature to around 600°C [170] depending on the thermal stability of the precursor [171].

The most known advantages of ALD are a high uniformity of the film quality over large area substrate, Ångstrom-precise thickness control, conformal growth on three-dimensional (3D) structures with high aspect ratio (1:3000 for Al_2O_3 [172]), low impurity content in the films [173, 174], etc. Due to a high potential of a wide variety of thin film materials and good compatibility with semiconductor and photovoltaic materials, ALD has been rapidly accepted not only in microelectronics since the early 2000s [171], but also in many other research and industrial areas depicted in Fig. 3.1.

As aforementioned, the principle of ALD is based on the surface chemical reaction. The reaction sequence of an ALD process is introduced using the example of Al_2O_3. In this work the deposition of Al_2O_3 films was performed via a thermal ALD process

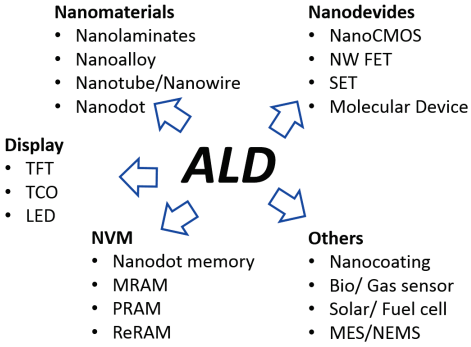

Figure 3.1: *The application fields of atomic layer deposition. The figure is redrawn from [175].*

utilizing dimethylaluminum isopropoxide [DMAI, $(CH_3)_2AlOCH(CH_3)_2$] as Al precursor and water vapor as the oxygen source. The reported reaction of the surface sites [176] will be described in the following. The net chemical reaction of this full ALD cycle can be summarized as:

$$2(CH_3)_2AlOCH(CH_3)_2 + 3H_2O \longrightarrow Al_2O_3 + 4CH_4 + 2HOCH(CH_3)_2, \tag{3.1}$$

with reaction products being the Al_2O_3 film and gaseous byproducts, i.e. CH_4 and $HOCH(CH_3)_2$. The full ALD cycle drawn in Fig. 3.2 is defined by four steps (a-d), which can be understood as two main half reactions. The first half reaction comprises DMAI supply (Fig. 3.2 (a)) and chemisorption to (OH-) surface sites. Then the reaction products and physisorbed DMAI are pumped away during the subsequent DMAI purge step (Fig. 3.2 (b)). This half reaction is summarized as:

$$AlO^{\ddagger}H^{*} + (CH_3)_2AlO^{\dagger}CH(CH_3)_2 \longrightarrow Al\text{-}O^{\ddagger}\text{-}Al[O^{\dagger}CH(CH_3)_2]^{*} + CH_4\uparrow \tag{3.2}$$

In equation (3.2), the crosses at the oxygen note its origin and the stars note surface groups. Excess of precursors and new CH_4 products are removed by carrier gas, Ar as example, in the subsequent purge step (Fig. 3.2 (b)). The second half cycle is the oxidation of the unreacted Al-surface ligands. For this aim, water vapor is fed as the oxygen source and reacts with the -$O^{\dagger}$iPr (isopropoxy) surface group of the incompletely reacted Al-precursor (Fig. 3.2 (c)). A new $AlO^{\ddagger}H^{*}$ surface site is formed and replaces the -$O^{\dagger}$iPr group as indicated by the second half chemical reaction equation:

$$Al[O^{\dagger}CH(CH_3)_2]^{*} + H_2O^{\ddagger} \longrightarrow AlO^{\ddagger}H^{*} + HO^{\dagger}CH(CH_3)_2\uparrow \tag{3.3}$$

Once again a purge step releases new products from the second half reaction and

residual oxidant. The reaction cycles are repeated until the desired film thickness is achieved.

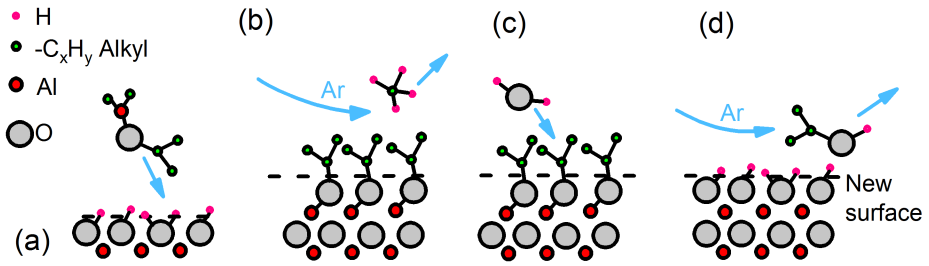

Figure 3.2: *Four steps of one typical ALD period with dimethylaluminum isopropoxide (DMAI) and H_2O vapor as Al and oxygen source, respectively. (a) The supply of metal-organic precursor DMAI and surface reaction. (b) Purge process for residual reaction products from (a). (c) Injection of H_2O as the oxygen source and surface reaction. (d) Purge process for residual reaction products from (c).*

The unique feature of ALD is an alternately surface-controlled, self-limiting chemical reaction during the growth of thin films, which makes the film thickness precisely controlled. Except some processing parameters as investigated in other studies, like absorption effect [177], process pressure [178] and precursor type [179] [171], the significant features of ALD that principally influence the self-limiting chemical reaction, namely (1) the ALD window, (2) the saturation behavior, and (3) the thickness-cycle linearity, will be introduced in the following:

(1) Since the growth rate is correlated with the chance of surface adsorption of precursor molecules and with the possibility of chemical reactions between surface ligands and precursors, which are both temperature relevant, a suitable deposition temperature has to be found out for a stable growth. Aiming at this, the relation between the growth rate and the deposition temperature is summarized in Fig. 3.3. The growth per cycle (GPC) is applied as a measure of growth rate and is defined as the thickness increment divided by cycle number.

If the surface absorption plays a more important role, at low deposition temperatures the precursor condensation on the surface should be taken into consideration. Increasing the temperature will weaken the condensation and thus lead to a decreased GPC (light grey line in the upper-left corner of Fig. 3.3). In contrast, if the temperature is too high, the precursor molecules may desorb from the surface and GPC is reduced as the light grey line in the lower-right corner shown in Fig. 3.3. Alternatively, if the dominating step is the surface reaction, the lower heater temperature can not effectively activate the chemical reaction, and thus GPC decreases with decreasing temperature (dark grey line in the lower-left corner of Fig. 3.3). In contrast, due to the overheating the decomposition of the molecules in the gas phase results in a chemical vapor deposition (CVD)-type process,

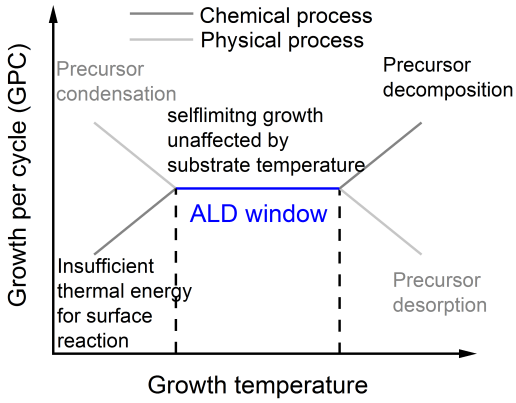

Figure 3.3: *Schematic description of the growth rate as a function of the deposition temperature. This image is redrawn from [180].*

where the increase of temperature makes GPC increase (dark grey line in the upper-right corner shown in Fig. 3.3). Only in a certain temperature regime, which is called the "ALD window", GPC remains stable and independent of the deposition temperature. Therefore, the thickness increment can be precisely controlled.

(2) Another important parameter is the dosage of precursor. To guarantee an effective and saturated growth rate of ALD, a sufficient precursor dose should be supplied (Fig. 3.4 (a)). However, an overdose of precursor will inefficiently increase the precursor consumption and will increase the purge time required for purge saturation, and thus will increase the costs. To achieve a constant growth rate, the purge time has to be long enough to reduce the probability of unwanted CVD reactions arising from residual molecules in the chamber, which can increase the film thickness (Fig. 3.4 (b)).

(3) At the initial ALD cycles the substrate reaction sites can affect the growth type

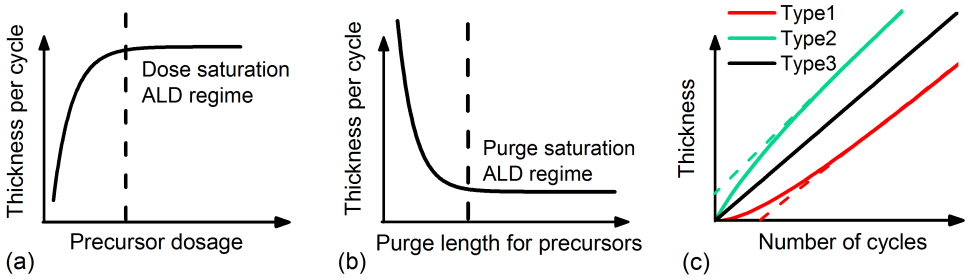

Figure 3.4: *Schematic description of typical characteristics for ALD growth: (a) precursor dosage saturation, (b) purge time saturation for both metal and non-metal precursors, (c) dependency of the GPC on different types of substrates. The dashed lines in red and green are the backward extrapolated ones from the corresponding linear regions.*

(Fig. 3.4 (c)) as reported by Puurunen [177] and by Perros et al. [180]. For type 1, if the substrate adsorbs precursors worse than the oxide itself, the layer growth will be inhibited at the first several cycles and after this initial stage of growth the stable increase of thickness can happen (red curve in Fig. 3.4 (c)). Type 2 shows a better adsorption of precursors on the substrate than it on the oxide, which enhances the initial growth (green curve in Fig. 3.4 (c)). For type 3, the substrate adsorption of precursors is similar to the oxide adsorption and thus makes the growth rate the same both in initial cycles and later cycles (black curve in Fig. 3.4 (c)). The substrate effect on the initial growth behavior can result in a high uncertainty of the film thickness for ultra-thin ALD films. Therefore, the film growth on the selected substrate material has to be carefully controlled, particularly in the very thin thickness regime of about 3 nm and below [181].

3.1.2 Typical precursors for ALD of Al_2O_3 and TiO_2

The choice of metal-organic precursors in ALD processes is of utmost importance, since the optimization process and the optimized ALD parameters are dependent on the properties of the metal-organic precursors, especially their reactivity towards the oxygen source (a detailed overview refers to [171]). Different precursors for deposition of the same oxide can even lead to a great variation of the film quality [182]. An improper choice can result in a low performance of the final films. For the in-situ bilayer or multilayer ALD process, the choice of metal-organic precursors is more complicated, since a suitable parameter range for both precursors, like an overlapped ALD window, has to be found to reduce the process operation complexity and to keep the film quality high.

In this work the precursor DMAI is chosen for growing the Al_2O_3 films because of its relative stability, safety and non-pyrophoricity compared to other common Al alkyl precursors like trimethylaluminium (TMA) [168, 171]. Moreover, the successful Al_2O_3 growth with DMAI has been reported in other studies [176, 183]. For growing TiO_2 films the tetrakis(dimethylamino)titanium precursor [TDMAT, $Ti(N(CH_3)_2)_4$] is utilized. TDMAT does not give rise to any corrosive by-product like HCl formed by $TiCl_4$ precursor [184] and the precursor itself and the corresponding decomposition products are non-toxic [174] as well. In addition, the metal dialkylamide group of TDMAT enables a very low temperature deposition [171], which can be applied for some temperature sensitive processes, like for patterning with photoresist layer that requires the correlated process temperatures below 300°C [185].

3.1.3 Technical parameters of liquid injection thermal ALD

A home-built liquid injection thermal atomic layer deposition system based on an AIXTRON® FE200 reactor is used in this work (Fig. 3.5). The system is equipped with a pulsed liquid injection vaporizer of Jipelec company. Detailed descriptions about this equipment are

reported by Reiners [115]. In this setup the substrates can be heated up to a maximum temperature of 700°C with a resistive heater underneath the sample holder. The precursors are dissolved in a proper solvent. Here, TDMAT (99.99% purity, Strem Chemicals Inc.) dissolved in toluene with a concentration of 0.1 mol/l is used as the Ti source, and DMAI (99.99%-Al, Strem Chemicals Inc.) dissolved in toluene with a concentration of 0.1 mol/l is used as the Al source. Both liquid precursor solutions stored in the steel bubbler cylinder are kept at room temperature. For both processes, ultra-pure deionized water (from ZEA-3 in FZ-Jülich) is used as the oxidant, which is kept in a water bath at 5°C. The high purity argon gas (99.9999%) with a flow rate of 200 sccm (standard cubic centimeters per minute) and of 500 sccm is used as the carrier and purge gas, respectively. With the carrier gas, the liquid precursor is delivered from the bubbler cylinder to a pulsed injection vaporizer. The vaporizer temperature is kept at 150°C and the substrate heater temperature, i.e. the deposition temperature, was set to 250°C, which is within the overlapped ALD window of both metal-organic precursors. The background- and working pressures in the reactor always maintain below 10^{-2} mbar and 10^{-1} mbar, respectively.

As aforementioned in the principle part of ALD, one typical ALD cycle comprises four pulse steps (see Fig. 3.6). With the time pulse train the duration of each step can be described as: (1) the metal-organic precursor "A" (DMAI or TDMAT) supply, (2) the inert gas purge for the 1st step, (3) the second non-metal precursor "B" (H_2O) supply, and (4) the inert gas purge for the 3rd step. For Al_2O_3 growth, the typical step duration for one ALD cycle DMAI/Ar purge/H_2O/Ar purge is 6/7/1/15 s. For the TiO_2 process, namely TDMAT/Ar purge/H_2O/Ar purge, the each step duration is 4.25/7/0.95/20 s.

In Fig. 3.7 the thickness of as-grown thin films is plotted as a function of the number

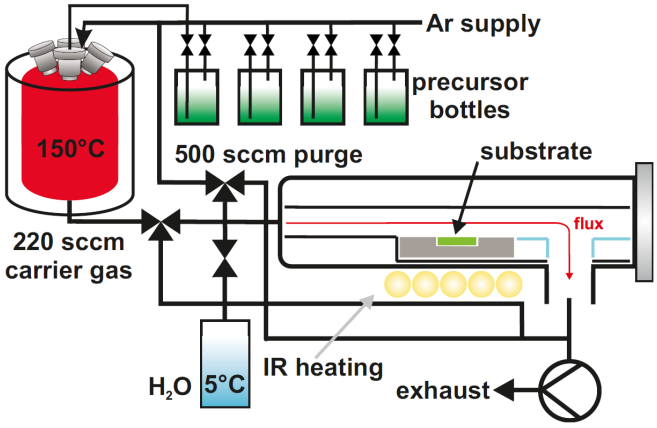

Figure 3.5: *Schematic diagram of the liquid injection thermal atomic layer deposition system in PGI-7, FZ-Jülich. The figure is taken from [115].*

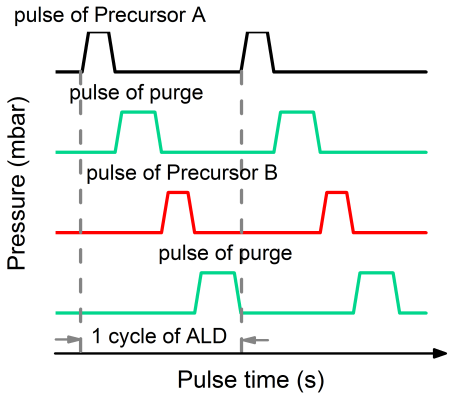

Figure 3.6: *Schematic diagram of a typical pulse train for one ALD cycle*

of ALD cycles. The slope of the plot is the growth rate expressed as GPC. The GPC values for Al_2O_3 and TiO_2 are 0.128 nm/cycle (Fig. 3.7 (a)) and 0.044 nm/cycle (Fig. 3.7 (b)), respectively. Both are accordant with reported values [115, 183]. From the linear fitting of the plots, the back extrapolated dash lines in Fig. 3.7 show negligible intercepts for both oxides. This indicates a negligible inhibition or enhancement of the initial growth of Al_2O_3 and TiO_2 on the Si(100) substrate.

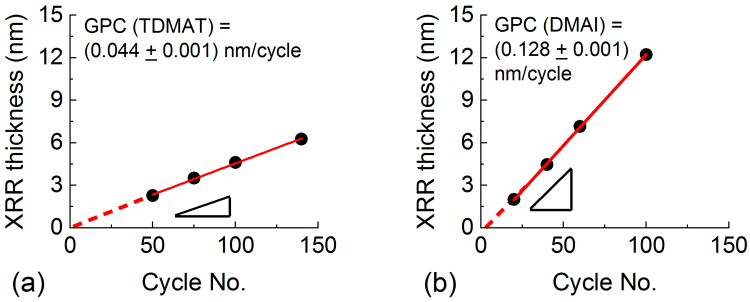

Figure 3.7: *Layer thickness from XRR fits as a function of the ALD cycles for (a) Al_2O_3 deposition with DMAI as Al source and for (b) TiO_2 deposition with TDMAT as Ti source grown at 250°C. From this, the growth per cycle (GPC) was determined by the slope of the linear fitting (red line). The dashed line is backward extrapolated from the red line.*

In this work films were deposited on Si(100) substrates to optimize the ALD process parameters. Besides, it was also applied as the reference sample grown with the nano-crossbar devices in the same batch to estimate the film thickness for the nano-crossbar devices. Pt coated Si substrates (Si/Pt) exhibit a surface roughness of about 2 nm, which does not allow to determine the thickness of nm thin oxide layer by means of X-ray reflectivity (XRR). For this reason, the mass layer densities of Al_2O_3 films grown on two substrates, namely Si(100) substrate and Si/Pt substrate are compared. The mass layer

density of Al_2O_3 films is calculated from the mass layer density of Al element by X-ray fluorescence spectroscopy (XRF) with assumption of the Al to O ratio in the films close to 2:3. The values for both substrates are plotted in Fig. 3.8 (a). A good matching for both data especially for cycles below 150, i.e. layer thickness of $Al_2O_3 \leqslant 20$ nm, indicates that the film thickness obtained from oxide layers grown on Si(100) and on Si/Pt substrate can be considered as the same. Therefore, in the latter chapters the film thickness given for the nano-crossbar devices is determined from the films grown on the Si reference sample in the same ALD batch.

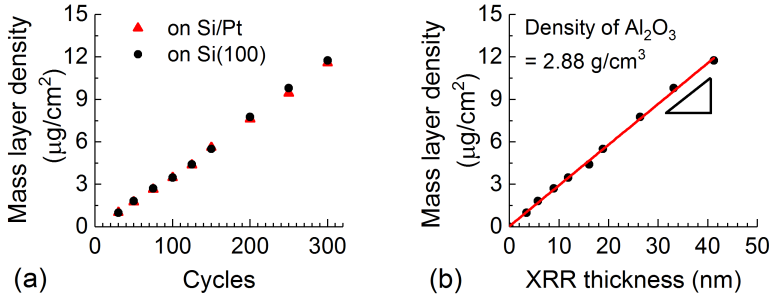

Figure 3.8: *(a) XRF results of as-grown Al_2O_3 layers on planer Si/Pt (circle) and on Si(100) substrates (triangle). The values of mass layer density are derived from XRF (done by ZEA-3 in FZ-Jülich). (b) The mass layer density of Al_2O_3 grown on Si(100) as a function of layer thickness determined by the XRR fitting. The films in (a) and (b) were deposited at 250°C. Figures are taken from the former work [186].*

For a homogeneous film, the mass layer density of the material measured for a defined area on the substrate should be proportional to the layer thickness by a linear relationship as shown in Fig. 3.8 (b). From the slope of the linear fit, an average density of 2.88 g/cm^3 was calculated for the as-grown Al_2O_3 films, which is in good agreement with the layer density estimated from the XRR fitting results of (2.85 ± 0.25) g/cm^3 listed in Tab. 3.1 in the next section.

3.2 Structural characterization methods

3.2.1 X-ray reflectivity

X-ray reflectivity (XRR) can analyze the film thickness from 0.1 nm to 1000 nm [187] with Ångstrom accuracy for single- or multi-layer systems. It uses the interference of the X-rays reflected from the surface and interface(s) near the total reflection angle, i.e. critical angle (θ_c). Due to the total reflection the intensity is very high at the beginning with incident angle lower than the critical angle ($\approx 0.5°$ in Fig. 3.9).

For incident angles slightly higher than the critical angle, the incoming X-ray can penetrate into the film and the intensity of the reflected beam is reduced compared to the incident beam due to absorption events inside the film. From this interaction between the X-rays and the film the critical angle is determined as the first reduction of reflected intensity. The critical angle can be directly linked to the laterally averaged electron density based on $\theta_c \propto \sqrt{\rho}$ [188] and thus confirm the material density of the underlying thin film. The reflection intensity oscillations can be observed due to wave interference. Based on $(\theta_m{}^2 - \theta_c{}^2) = m^2\ (\lambda/2d)^2$ [188], where θ_m is the angle at the maximum of the m^{th} oscillation and λ is the wavelength, the film thickness d can be estimated. Finally, this characterization method can give accurate informations about layer thickness and density [189].

The thickness of metal electrodes (Fig. 3.9) and ALD as-grown oxide films (Fig. 3.10) utilized for nano-crossbar devices were measured via an X'Pert MRD Pro system from

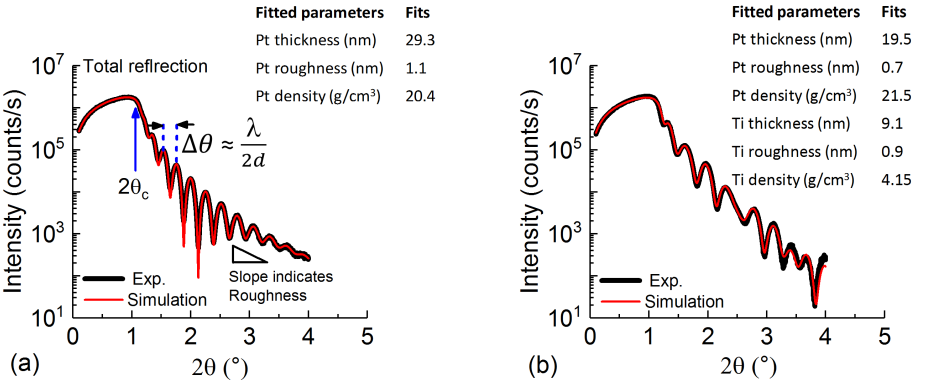

Figure 3.9: *A measured XRR curve (in bold black) and its fitting result (in red) of (a) an expected 30 nm evaporated Pt film and of (b) an expected evaporated 10 nm Ti and 20 nm Pt on Si(100) substrates. The simulation results are listed in the upper-right corner of the graph.*

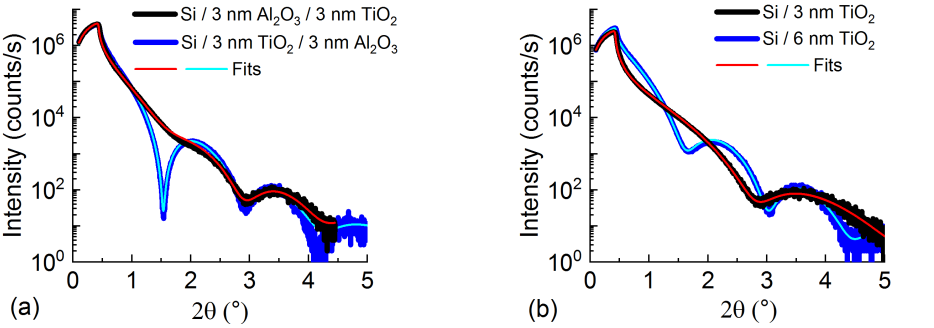

Figure 3.10: *Measured XRR curves and simulation results of (a) two types of bilayers and of (b) TiO_2 single-layers deposited on Si(100) substrates.*

Panalytical® company. The layer thickness was determined via the open source software GenX 2.0 [190]. The experimental data as bold and their best fits as slim lines are illustrated in Fig. 3.9 for two types of top electrodes and in Fig. 3.10 for different oxide layers. The fitting results are listed in the upper-right corner of each graph. Besides these representative curves, the simulation results for other devices used in this work are summarized in Tab. 3.1.

Sample-Nr.	Layer(s)	Density (g/cm^3)	ALD cycles (#)	Mean thickness by XRR (nm)	RMS roughness by AFM (nm)
No.1	5AO	2.8	41	4.8	0.265
No.2	2AO	2.8	23	2.3	
No.3	1AO/3TO	3.1	13	1	
		3.8	66	3.7	
No.4	2AO/3TO	3.1	23	2.3	
		3.8	66	3.0	
No.5	3AO/3TO	2.7	24	2.7	
		3.3	74	3.4	
No.6	3AO/3TO		24	2.7	
			74	3.3	0.248
No.7	3TO/3AO	3.7	74	3	
		2.6	24	3.2	0.256
No.8	3TO	4.15	75	3.2	
No.9	3TO	3.8	66	3.2	
No.10	6TO	3.94	150	6.05	

Table 3.1: *Details for AIXTRON® ALD as-grown oxide layers on Si(100) substrates as the reference sample for the nano-crossbar devices in later chapters. "TO" and "AO" is the abbreviation for TiO_2 and Al_2O_3, respectively. The number in front of "TO" or "AO" is the expected layer thickness in nano-meter (nm).*

Additionally, the layer roughness RMS (Root Mean Square) from atomic force microscopy (AFM) are also listed in Tab. 3.1. The RMS values for 2.6 nm and 5.2 nm thick TiO_2 films deposited on Si(100) substrates are 0.219 nm and 0.232 nm, respectively. Regarding the closed thickness values, the TiO_2 single-layers listed in Tab. 3.1 should have the similar range of roughness as well. Moreover, the RMS value of Si(100) substrate is around 0.2 nm, which supports the homogeneity of the as-grown TiO_2 layers by ALD.

3.2.2 Scanning electron microscopy

The scanning electron microscopy (SEM) can give both morphological contrast and chemical information based on the interaction between the incident electrons and specimen. For this purpose, a typical SEM system is composed of an electron gun, lens systems and detectors. The working principle of SEM is depicted in Fig. 3.11.

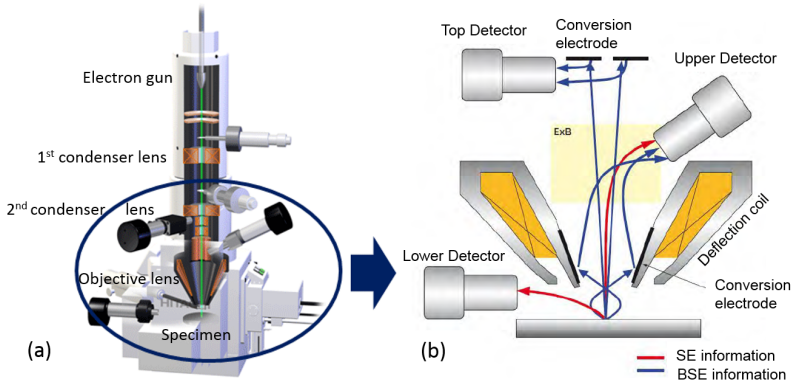

Figure 3.11: *Schematic of (a) section view of Hitachi SU8000 setup and (b) its detection systems. The figures are redrawn from [191, 192].*

The electron gun utilizes commonly an ultra-sharp tungsten tip and a high voltage for emission of electrons. Then electrons with high energy enter into the lens system and start to get focused. The two condenser lenses converge the diverging electron beams by bending their trajectory through the Lorentz force. The spread width of electron beams can be further adjusted by means of the aperture behind the condenser lens. The objective lens focuses the electron beam finally on the sample and thus determines the final resolution. The deflector coils control the electron beam to scan across the specimen surface [193]. During rastering the excited signals are collected by suitable detectors. As Fig. 3.11 (b) shows, the top detector records the high angle backscatter electrons, which comprise mainly chemical contrast. The upper detector (SE(U)) takes both low angle backscatter electrons (LA-BSE) and secondary electrons (SE) signals, whereas the lower detector (SE(L)) takes only SE signals [192]. LA-BSE offer both topographical information and compositional contrast, while the SE signal shows the surface topography [192]. Theoretically the SE(L) supplies the pure topographical image. However, the SE(L) is often operated with long working distance in high magnification mode [194]. Since the long working distance often results in decreased resolution [193–196], the highest topographical resolution achieved is through SE(U) instead of SE(L). Therefore, the SE(U) image obtained from Hitachi SU8200 tool is widely used in this work for the clear surface topography of devices.

3.3 Nano-crossbar device integration

A successful fabrication process for nano-crossbar devices mainly consists of six steps (Fig. 3.12): (1-2) bottom electrode fabrication via metal sputtering, nanoimprint lithography (NIL) and reactive ion beam etching (RIBE), (3) functional oxide layer deposition via ALD; (4-5) top electrode deposition via electron-beam evaporation or DC magnetron sputtering as well as patterning via electron beam lithography (EBL) and back etching process (e.g. RIBE), (6) the device with resulted structure should show the common electrical behavior, like low leakage or no unusual electrical signals due to the unexpected short circuit or destroyed patterns.

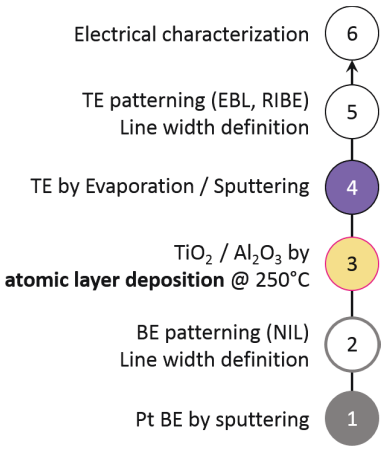

Figure 3.12: *Fabrication procedure of nano-crossbar devices*

Bottom electrode fabrication

Nanoimprint lithography fabricates bottom electrode patterns by mechanical pressing of imprint resist with a quartz mold stamp. This process was applied to a thermal silicon wafer with sputtered 5 nm Ti as adhesion layer and 30 nm Pt layers as electrode metal on top. In the next etching step the residual resist layer and metal layers beside the patterning strucuture are removed. The final line width of bottom electrode is obtained from 100 nm down to 40 nm (for details see [197]). The nano-crossbar substrates were supplied by N. Aslam and A. Steffen and the metal layers were deposited by R. Borowski from PGI-7, FZ-Jülich.

Crossbar cell fabrication

Then the patterning of top electrode structures was performed. After the deposition of thin oxide layer(s) and metal top electrodes, the full surface of samples was coated with

special photo resist (see Fig. 3.13 (a)). To achieve the smaller device size, this resist AZ® nLof 2020 (diluted with AZ® EBR as 1:2 in volume) was spin coated on the sample surface with spin speed of 3000 rps for 1 min. Then the sample was baked at 110°C for 1 min.

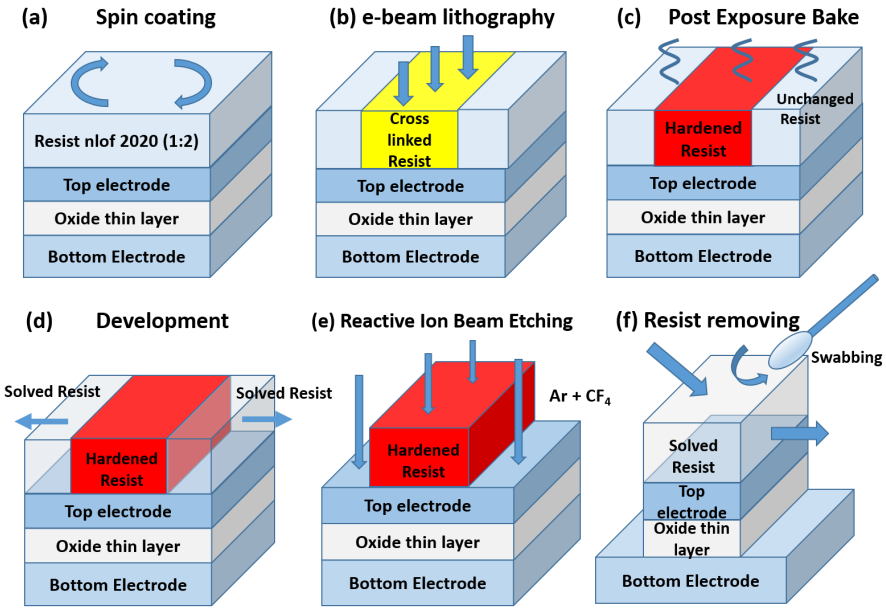

Figure 3.13: *Process flow for the crossbar patterning*

Then, a focused electron beam (Fig. 3.13 (b)) is applied to transfer the top electrode patterns onto the resist coated samples with standard e-beam dose of 23 $\mu C/cm^2$ (done by S. Trellenkamp in HNF). After cross-linking the resist by post exposure bake (Fig. 3.13 (c)), the negative resist without e-beam exposure can be dissolved in the developer AZ® 726 MIF (Fig. 3.13 (d)). Since the patterned resist protects the layers underneath including the top electrode and the underlying oxides, during the subsequent etching step, the layers without resist are etched down to the bottom electrode or the substrate (Fig. 3.13 (e)). The RIBE parameters for all devices processed in this work are listed in Tab. 3.2.

After dissolving the protective resist in the stripper TechniStrip® NI555 at 80°C for at least one hour, the residual resist can be removed by swabbing (Fig. 3.13 (f)) or placing in an ultrasonic bath (results see Fig. 3.14 (b)). The final pattern of the top electrode and the cross point are thereby fabricated and inspected by SEM (see Fig. 3.14 (c)).

An overview of the nano-crossbar layout is shown in Fig. 3.15. There are 6 rows (from Y01 to Y06) and 12 columns (from X01 to X12) of blocks for each sample. Every block, e.g. X01Y01, comprises of 25 cells. In the same block, for each column the five cells are with the same cell size, while for each row the cell size varies from 100 nm to 20 nm

from right to left with 20 nm decrement. Ideally, 12·6·5 = 360 cells with one cell size are available on one sample.

Layers to be etched	Etchants and etching time
Residual nLof resist	O_2 @ 0° (low), t=15 s
20 nm Pt capping layer	Ar @ 0°, t=1 min
10 nm Ti top electrode and 5-6 nm oxide(s)	CF_4 @ 0°, t=1 min 40 s
10 nm TiN top electrode and 5-6 nm oxide(s)	CF_4 @ 0°, t=40 s
Etching rate for TiO_2 layer	CF_4 @ 0°, 20.4 nm/s
Etching rate for Al_2O_3 layer	CF_4 @ 0°, 13 nm/s

Table 3.2: *Etching parameters utilized in the nano-crossbar fabrication (see Fig. 3.13 (e)). This etching process is done by R. Borowski.*

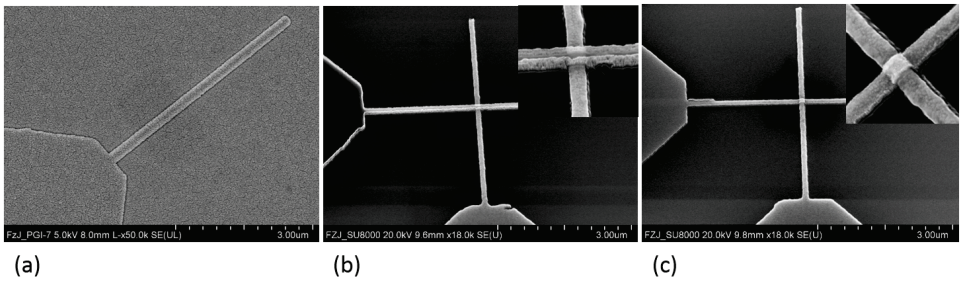

Figure 3.14: *SEM images for nano-crossbar devices (a) after oxide layer and top electrode deposition, (b) after development, (c) after removing residual resist.*

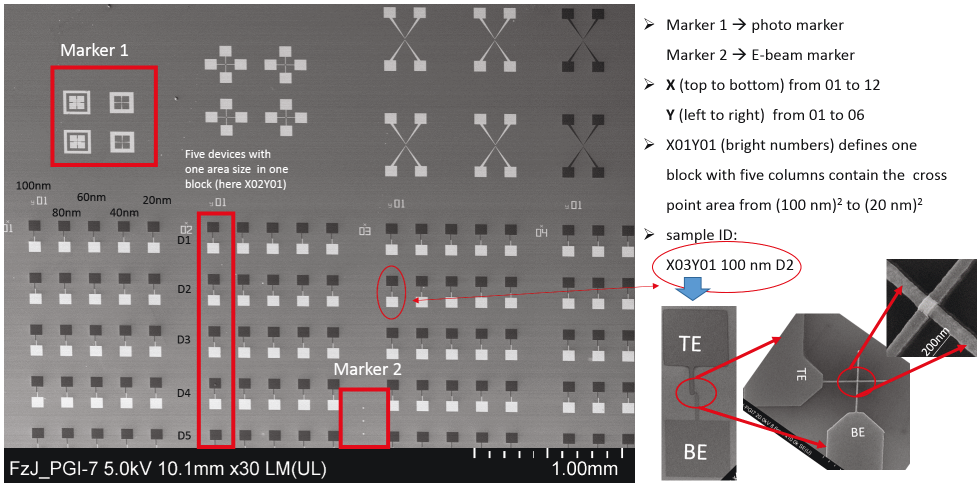

Figure 3.15: *Overview of the arrangement of the nano-crossbar structures in blocks*

3.4 Electrical characterization

3.4.1 Continuous $I(V)$ hysteresis curves

In this work, the $I(V)$ characterizations were performed on a B1500A Semiconductor Parameter Analyzer from Agilent Technologies Inc. combined with a Semi-automatic probe station SÜSS MicroTec PA-200. Agilent B1500A supports different measurement modules [198]. In this work, the staircase voltage sweep is chosen as the input and the current response for each sweep step is recorded, i.e. the data is in $I(V)$ illustration. For this purpose, one source/monitor unit (SMU) that can supply and measure the DC voltage or current and one ground unit (GNDU) as the reference of measurement ground are utilized [198]. During the $I(V)$ sweep measurements, several sweep parameters can be selected, like the sweep direction as single or double, the start- and stop value of the sweep, and the compliance current value of the source. In the following chapters, the variations of these parameters are performed to characterize the cell's electrical features. In addition, to obtain a high resolution of the current, the high resolution SMU is equipped with 73CT-APTA replaceable coaxial probe (American Probe & Technologies, Inc.) and thus provides the current resolution of 5 fA [198].

Temperature measurement

DC $I(V)$ characteristics can also be carried out at a certain temperature in the same SÜSS MicroTec equipment. By means of an integrated heating unit from ATT (Advanced Temperature Test Systems GmbH) that is equipped under the substrate holder, the holder can be heated up or cooled down between 10°C and 205°C.

The low temperature measurement is carried out in a home-built system, which comprises a Lake Shore's cryogenic probe station with model 332 temperature controller, an HP34401A multimeter, a pump system combining a scroll SC 5D and turbomolecular pump (TURBOVAC SL 80) [199,200]. The TTP4 mode of the cryogenic probe station can offer a temperature range from 4.2 K to 475 K with a helium or nitrogen cylinder [201].

3.4.2 Voltage pulse measurements

The pulse measurements were carried out on two different setup systems, namely 4200 SCS (semiconductor characterization system) from Keithley Instruments and Agilent B1110A in home-made Mark II system. With the first one, the response of transient currents, i.e. the time-varying currents, are measured by utilizing a single voltage pulse performed by 4225-PMU pulse/measurement units. By equipped with model 4225-RPM (remote amplifier/switch) [202] the attainable current level can be ranging from 100 nA to 200 mA at a minimal pulse length varying from 134 µs to 70 ns [203]. In this system the current resolution is strictly dependent on the pulse width. To take the current lower

than 1 µA as one example, the pulse length should be not less than 20.4 µs. The possible reason could be signal level and Johnson noise [204]. The detailed relation between the current limitation and the pulse length can be obtained from [203].

Generally, a pulse signal is defined by five parameters, namely pulse delay, pulse length, rise- and fall time and pulse period (see Fig. 3.16). The pulse delay is the time difference between the end of the previous voltage pulse and the start of the subsequent voltage signal in the ongoing pulse. For each pulse, the voltage increases abruptly to achieve the setting value (V_{pulse}) within the rise time, keeps constant for a pulse length, i.e. the width or duration, and decreases to zero again within the fall time. The rise and fall times are normally within a certain percentage of the pulse length. The period is the full width of the pulse. By defining timing (Table in Fig. 3.16) and voltage amplitude, the pulse measurement can be programmed with the repeated SET, READ, RESET and READ pulse steps.

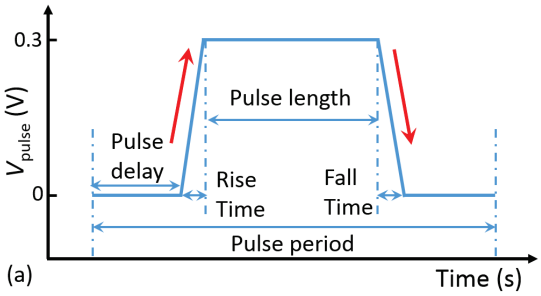

Timing parameters	
Period	1.50e-4 s
Length	1.00e-4 s
Rise time	5.00e-8 s
Fall time	5.00e-8 s
Pulse delay	2.00e-5 s

(b)

Figure 3.16: *(a) Illustration of the pulse signal and (b) its timing parameters for a read step applied in the Keithley 4200 SCS setup.*

The alternative measument for the transient current response upon fast voltage pulses is performed via Agilent B1110A pulse-/pattern generator in Mark II system (for details see [203]). The pulse length (t_{pulse}) can be varied in a larger range from 10 ns to 10 s. In addition, a sinusoidal read signal of 25 mV bias [205] over the tested device is applied to record the read-out resistance value.

SET/RESET pulse variation performed by Keithley 4200 SCS

To get an overview of the switching possibility of a memory cell, the SET and RESET kinetic studies were firstly performed in Keithley 4200 SCS system. In order to make the influence from each parameter variation less interfered by the previous operations, "precycling" is always applied to keep the read-out value of resistance states within a predefined range. For this purpose, the precycling was repeated until the predefined read-out resistance value is achieved. The parameters of the precycling are normally optimized through the endurance test or obtained from the parameters for stable DC

switching cycles. Once the read-out value was within the defined range, SET or RESET cycle initiates. The parameters during SET or RESET cycling, like timing and the voltage amplitude, can be varied and be tested with several repetitions for the statistical analysis.

For the SET kinetic study (see Fig. 3.17 (a)), for instance, the read-out resistance for HRS is $R_{\mathrm{pre,OFF}} = 200\ \mathrm{k\Omega} - 500\ \mathrm{k\Omega}$ after the precycling. Once the required $R_{\mathrm{pre,OFF}}$ is reached, the SET cycle starts. The read-out pulse is always kept constant as 0.3 V applied to the Pt bottom electrode with the pulse length of 0.1 ms. Then the read-out resistance after SET pulse, i.e. R_{read} at 0.3 V, will be recorded. This kind of data recording procedure is defined as pulse/read mode, where the read-out resistance values were recorded after the SET or RESET pulse and plotted as the matrix of the operation voltages and pulse lengths.

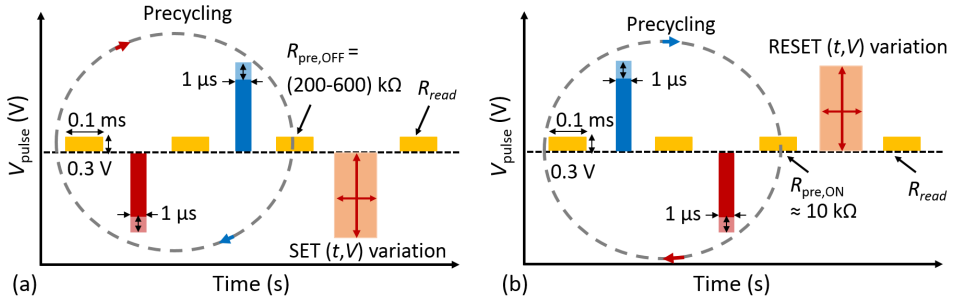

Figure 3.17: *Schematic illustration of (a) the SET pulse and (b) the RESET pulse measurement via Keithley 4200 SCS system. The precycling is emphasized by circles.*

The RESET pulse measurement was carried out in two different ways via the same setup systems. One is the pulse/read mode, where the defined read-out resistance of LRS after precycling is $R_{\mathrm{pre,ON}}$ = 10-12 kΩ (Fig. 3.17 (b)) and the read-out resistance after RESET pulse is recorded. The similar "heat graphs" can be obtained. Another is the transient pulse measurement of RESET events. By decreasing the RESET pulse length, once the cell shows no RESET, i.e. the read-out resistance after RESET is less than 50 kΩ, the RESET pulse length, namely the RESET time (t_{RESET}) can be confirmed. In this way, the relation between t_{RESET} and the applied RESET voltage pulse can be studied.

Pulse pattern generator Agilent B1110A

The abrupt SET event is observed in many VCM-type c8w BRS devices. In order to understand the SET kinetic study with the physical model, like ion hopping model, the SET time (t_{SET}) for a given SET pulse voltage ($V_{\mathrm{SET,pulse}}$) should be confirmed and their relation should be explained. Therefore, this measurement of the transient current response upon fast pulse was performed via an Agilent B1110A pulse pattern generator in

setup "Mark II". The pulse train and the recorded transient current response are shown in Fig. 3.18 (a) and (b), respectively.

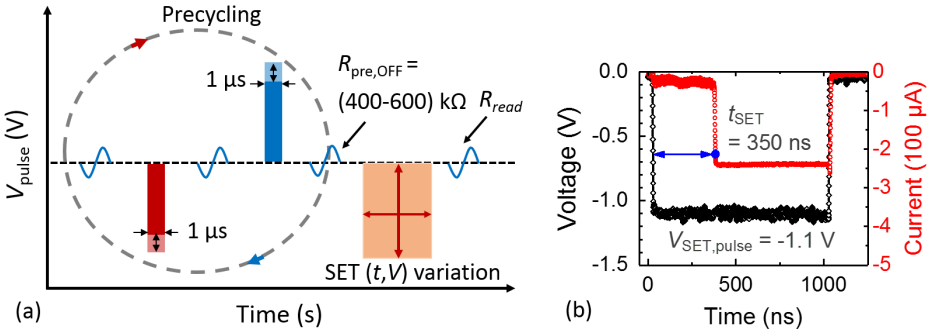

Figure 3.18: *(a) Schematic illustration of the SET pulse flow for the SET kinetic study performed by Agilent B1110A in Mark II. The precycling is emphasized by circles. (b) The transient current responses upon the pulse driven SET events for a (100 nm)² Pt/5 nm Al_2O_3/Ti cell. The SET pulse signal $V(t)$ is drawn in black and the current responses $I(t)$ are given in red. The experimental data is gathered from F. Cüppers.*

A similar "precycling" step was performed to guarantee the device stayed in a defined high resistance state (HRS) prior to the application of the SET pulse operation, i.e. $R_{\text{read}} \leqslant 10\,\text{k}\Omega$. Upon the application of the constant voltage signal (see Fig. 3.18), the device shows firstly a low pre-SET current amplitude ($|I_{\text{pre-SET}}|$), which represents the current through the cell in HRS at the corresponding voltage ($V_{\text{SET,pulse}}$ = -1.1 V). Within a certain delay time (here 350 ns as an example) the current abruptly increases directly to the level of low resistance state. To quantitatively describe the abrupt SET events, the t_{SET} is defined as the time difference between 90% of the abrupt drop of voltage signal and 90% of the medium saturation current. In addition, for the statistical analysis, a large amount of SET operations for each pulse group were carried out by F. Cüppers.

Chapter 4

Counter-eightwise resistive switching in the nano-structures

In this chapter the counter-eightwise (c8w) type current-voltage ($I(V)$) characteristics of Pt/oxide(s)/metal/Pt (capping layer) nano-crossbar devices are investigated. The layer sequence written from left to right always corresponds to the layer stack sequence from the bottom electrode (BE) to the top electrode (TE). In order to focus on the "active" M_1OM_2 cells the topmost Pt capping layer and the layers below the Pt bottom electrode are not mentioned as a part of the stack in the following chapters. The oxides comprise TiO_2 and Al_2O_3 single-layers as well as bilayers, which are either built from Al_2O_3/TiO_2 or from the reversed stacking order TiO_2/Al_2O_3. Beside a pure Pt top electrode, two different top electrodes containing Ti element are used: (a) a reactive 10 nm Ti electrode deposited by evaporation or sputtering; (b) a moderate reactive 10 nm sputtered TiN electrode. For consistency with the switching model (cf. [4]), the voltage polarity is always referred to the high work function Pt BE with the top electrode set to ground. All cells to be discussed in sections 4.1 to 4.3 were structured to $(100\ \text{nm})^2$.

In section 4.1, the fabricated stacks are described and the purpose of the particular variations is explained. In 4.2, the $I(V)$ characteristics of single-layers, TiO_2 and Al_2O_3, with varied thicknesses and different electrodes are discussed. The $I(V)$ characteristics of bilayers in different modifications are investigated in 4.3. In the last section 4.4 the performance of Al_2O_3-based devices with and without 3 nm TiO_2 is compared with $(100\ \text{nm})^2$ and $(80\ \text{nm})^2$ cell size.

4.1 Overview of the nano-crossbar devices

4.1.1 Single-layer oxide cells

The single-layer stacks discussed in this chapter are summarized in Fig. 4.1. The top electrodes were obtained from evaporated 10 nm Ti, sputtered 10 nm Ti*, 10 nm TiN, and

evaporated 30 nm Pt. The ALD oxide layers were grown in two different systems. The standard process (see section 3.1.3) utilized pulsed liquid injection in an AIXTRON® reactor feeding the metal-organic precursors, DMAI and TDMAT, as solutions with toluene as solvent. Alternatively, TiO_2 films were grown by thermal ALD from TDMAT and H_2O, feeding the TDMAT in bubbler-type mode, into Oxford Instruments FlexAL ALD reactor [206]. The thickness of TiO_2 and Al_2O_3 single-layers was varied from 3 nm to 11 nm and from 2 nm to 5 nm, respectively. Details about oxide layers are listed in Tab. 3.1 and in "Appendix C".

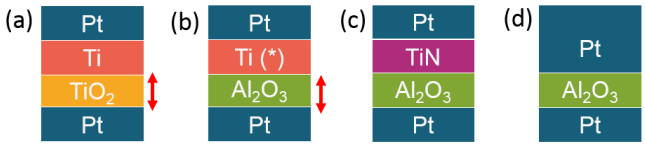

Figure 4.1: *Stacks of oxide single-layers with varied layer thickness in nano-crossbar structures: (a) Pt/3 nm to 11 nm TiO_2/evaporated Ti, (b) Pt/2 nm or 5 nm Al_2O_3/evaporated Ti or sputtered Ti*, (c) Pt/5 nm Al_2O_3/sputtered TiN, (d) Pt/5 nm Al_2O_3/10 nm evaporated Pt. The bottom electrode for all stacks was 30 nm sputtered Pt and all 10 nm top electrodes linked with 20 nm Pt capping layer that was deposited by the same system without breaking the vacuum.*

The VCM-type devices are built in an asymmetric structure, where the high work function Pt BE forms the Schottky contact, the ALD oxide is the switching layer and the low work function TE metal forms the ohmic contact and the oxygen exchange layer (OEL). The oxygen scavenging abilities of different electrodes are studied for the Al_2O_3-based single-layer devices (Fig. 4.1 (b-d)). Here, in particular, the Al_2O_3 single-layer sandwiched in two inert Pt electrodes are tested as reference. Two types of titanium electrodes obtained from evaporation and sputtering are differentiated to account for a possible surface damage effect included by the high energetic particles from the sputtering process.

4.1.2 Bilayer oxide cells

The stack variations for Al_2O_3-TiO_2-based bilayer cells are summarized in Fig. 4.2. The layer thickness of Al_2O_3 is chosen as 1 nm, 2 nm and 3 nm in Pt/Al_2O_3/TiO_2/Ti stack, while the TiO_2 layer in this stack remains 3 nm (see Fig. 4.2 (a)). In other bilayer stacks the thickness for both TiO_2 and Al_2O_3 films is kept constant at 3 nm (Fig. 4.2 (b-d).

It has to be mentioned that (1) the oxide bilayers are processed in-situ by subsequent ALD processes; (2) the top electrodes with 20 nm Pt capping layer are differentiated into: 10 nm evaporated Ti, 10 nm sputtered Ti* (Fig. 4.2 (a,c)) and 10 nm sputtered TiN (Fig. 4.2 (b,d)). (3) To make the TE comparison most reliable, the respective stacks for

the same oxide order were processed in the same batch.

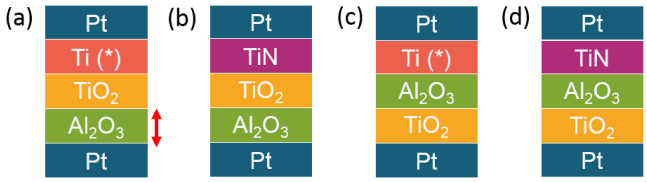

Figure 4.2: *Bilayer stacks in Pt/bilayer/TE nano-crossbar structures: (a) Al_2O_3/TiO_2 with 10 nm evaporated Ti or sputtered Ti* as TE. For evaporated Ti the Al_2O_3 layer thickness was 1 nm, 2 nm and 3 nm with 3 nm TiO_2. (b) Pt/3 nm Al_2O_3/3 nm TiO_2/10 nm TiN. Structures in (c) and (d) correspond to (a) and (b), respectively, with the bilayer being 3 nm TiO_2/3 nm Al_2O_3.*

4.2 $I(V)$ characteristics of the single-layer devices

For a typical c8w bipolar resistive switching (BRS) cycle, the negative voltage is first applied on Pt BE with stepwise (10-20 mV with a delay time of 10 ms) increasing amplitude from 0 V to the stop voltage ($V_{-,\max}$) that exceeds the threshold voltage. Through this operation cells are electroformed or SET from an initial state or a high resistance state (HRS) to a low resistance state (LRS) with a proper current compliance that protects the device from a permanent breakdown. The positive voltage sweep initiates the RESET process at a certain RESET voltage where the cell's state starts changing from LRS to HRS. A full RESET loop starts from 0 V to the maximal positive stop voltage ($V_{+,\max}$) and ends by sweeping back to 0 V. The influence of two switching parameters during the voltage sweep are investigated, namely the current compliance (I_{CC}) during the SET process and the RESET stop voltage ($V_{+,\max}$) during the RESET process. The $I(V)$ characteristics between different stacks are analyzed with respect to the defined switching parameters. The statistical results on the SET, RESET voltages and the read-out resistance values for HRS and LRS, are summarized in the form of cumulative distribution function (CDF) plots or box plots to address the variability in respect of cycle-to-cycle (C2C) and device-to-device (D2D) feature.

4.2.1 TiO_2

The Pt/TiO_2/Ti devices are initially conductive for layer thickness from 3 nm* to 6 nm resulting in read-out resistance for the initial state (R_{initial}) increasing from about 1 to 5 kΩ by 50% CDF (see Fig. 4.3). The CDF plots are gathered from about 25 to 40 devices each. The "*" symbols make samples which were grown in the FlexAL reactor, while the others are prepared in the AIXTRON® system. The deviations are in an acceptable

range. By applying 2 V the cells can be reset to the Megaohm (MΩ) range, and thus the initially existing conductive paths are closed or annihilated. However, for a thicker TiO_2 layer of 11 nm, R_{initial} normally exceeds 100 kΩ (pink triangle in Fig. 4.3).

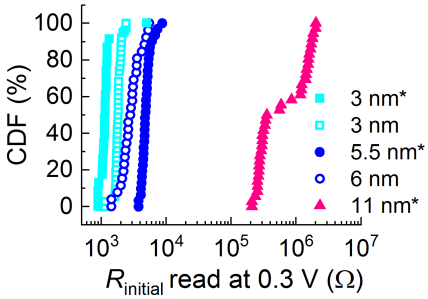

Figure 4.3: *CDF plots of the read-out initial resistance ($R_{initial}$) in Pt/TiO_2/Ti cells with XRR fitting thickness ranging from 3 nm* to 11 nm*. The star ("*") marks the TiO_2 layers deposited in the FlexAL ALD system (see "Appendix C"), while others were fabricated by the standard ALD process with AIXTRON® reactor (see Tab. 3.1). The statistics are gathered from 23, 38, 26, 31, 36 cells (from left to right), respectively.*

Applying $V_{+,\max} = 2$ V and $|I_{CC}| \approx 50$ µA to 150 µA for the RESET and the SET, respectively, the three TiO_2 cells exhibit the similar asymmetric c8w switching behavior, i.e. the required c8w SET voltage amplitude ($|V_{c8w,SET}|$) is higher than the c8w RESET voltage ($V_{c8w,RESET}$) that is the required voltage starting to rupture the conducting filament (see Fig. 4.4). To repeat the c8w switching, the applied stop voltage amplitude $|V_{-,\max}|$ has to exceed the required $|V_{c8w,SET}|$ for each cycle. Otherwise, in the case of $|V_{-,\max}| < |V_{c8w,SET}|$, the cells will reverse the switching polarity, and the 8w BRS will appear. This is the topic of chapter 8.

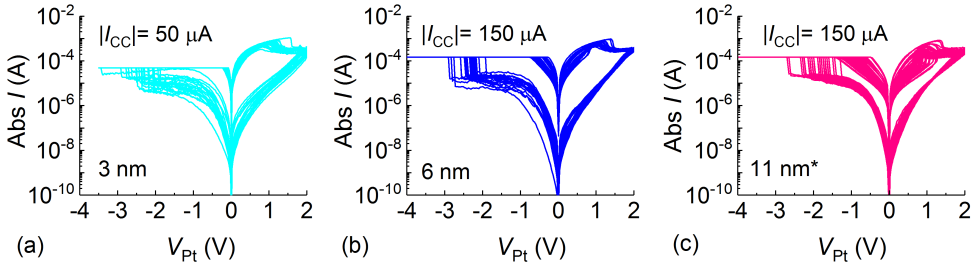

Figure 4.4: *Overview of $I(V)$ characteristics during c8w BRS cycles of Pt/TiO_2/Ti stacks for (a) 3 nm TiO_2, (b) 6 nm TiO_2 and (c) 11 nm* TiO_2. The $I(V)$ curves are given for (a) 20 cycles, (b) 20 cycles and (c) 42 cycles.*

Comparing devices from 6 nm and 11 nm* TiO_2 layers as examples, the CDF plots in Fig. 4.5 (a) indicate that the median values of $V_{c8w,SET}$ and $V_{c8w,RESET}$ are not affected by the TiO_2 layer thickness. Additionally, cells of both stacks show a similar read-out

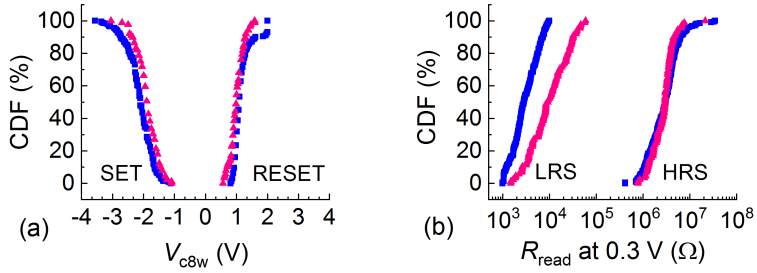

Figure 4.5: *(a) CDF plots of $V_{c8w,SET}$ and $V_{c8w,RESET}$ in two $Pt/TiO_2/Ti$ stacks with 6 nm oxide layer (blue square) and 11 nm* oxide layer (pink triangle). The statistical ensembles comprise 11 cells and 220 cycles (6 nm) and 3 cells and 89 cycles (11 nm*). (b) The corresponding CDF plots of read-out resistance of HRS (open dots) and of LRS (solid dots).*

resistance of the HRS, i.e. $R_{c8w,OFF}$ = 2-3 MΩ at 0.3 V (see Fig. 4.5 (b)). However, for the sample with 11 nm* TiO_2 out of 30 devices only 3 cells reveal over 20 BRS cyles with c8w polarity, while other 27 cells rather show stable 8w BRS. This indicates that the thicker TiO_2 layers can not improve the reproducibility and stability of c8w BRS.

4.2.2 Al_2O_3

Unlike for typical binary transition metal oxides like TiO_2 [207, 208], HfO_2 [209] and VO_x [44], no successful resistive switching phenomena have been reported for Al_2O_3 single-layers integrated in the symmetric $Pt/Al_2O_3/Pt$ structures. One possible reason is the difficulty for incorporation of a certain amount of oxygen vacancies into the as-grown Al_2O_3 layer sufficient for enabling resistive switching. However, the deposition of an oxygen exchange layer (OEL), i.e. an electrode with high oxygen scavenging ability like Ti, enhances the tendency for formation of an oxygen-vacancy-rich layer through interface reactions [22, 94, 210]. This layer serving as a buffer layer can take up and release oxygen ions from the memristive oxide layer during the switching cycle. Therefore, a qualitative classification can be made for the $Pt/Al_2O_3/TE$ devices in this work: (1) Al_2O_3 with an OEL, i.e. the TE is from evaporated Ti or sputtered Ti*. (2) Al_2O_3 without an OEL, i.e. the TE is from TiN or Pt.

Electroforming in Al_2O_3 single-layer devices

$I(V)$ characteristics of the electroforming process in Al_2O_3-based devices are shown in Fig. 4.6. Due to the different conduction of the initial state, the $|I_{CC}|$ was set to 5 µA for the highly insulating Pt/5AO/TE devices and to 500 µA for the relative conductive Pt/2AO/TE devices. The colored curves represent one typical electroforming and subsequent RESET loop for each stack. The pink arrows in Fig. 4.6 (b) indicate the switching

direction of the c8w electroforming and 1st RESET step valid for all four stacks shown. Since the current increases suddenly over several orders of magnitude, the absolute voltage value, where the current reaches 80% of the $|I_{CC}|$ value, is defined as the electroforming voltage amplitude ($|V_{Fr}|$). The mean value of $|V_{Fr}|$ and the number of the tested cells are listed in each graph and caption, respectively.

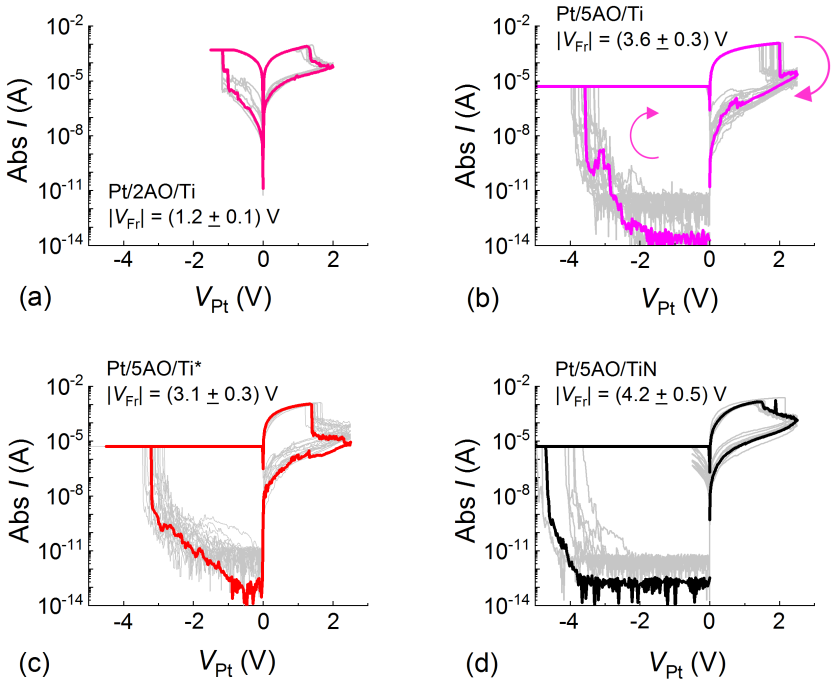

Figure 4.6: *Electroforming process in $Pt/Al_2O_3/TE$ devices: (a) 2AO/Ti (from 69 cells), (b) 5AO/Ti (from 83 cells), (c) 5AO/Ti* (from 48 cells), (d) 5AO/TiN (from 9 cells). "AO" is the abbreviation for Al_2O_3. The number in front of "AO" is the nearest positive integer of the layer thickness in nanometer (nm).*

As shown in Fig. 4.6 (a), the absolute value of initial current in Pt/2AO/Ti cells reads between 10^{-7} A and 10^{-5} A at -0.3 V. These devices show instantaneous resistive switching, and the electroforming votlage value is very comparable to the SET voltage. The current level in 5AO-based devices at -0.3 V is still below the measurement resolution of 10^{-13} A (see Fig. 4.6 (b-d)). From the statistical results of the electroforming process, the yield of electroforming events in cells obtained from the same 5 nm Al_2O_3 is dependent on the TE materials. In cells with Ti or Ti* as TE a highly reproducible and successful electroforming process is obtained, which is featured through the well-behaved RESET process after electroforming and the following switching cycles. However, most Pt/5AO/TiN cells show "stuck-LRS" failure as defined in [209], i.e. no successful RESET operation after

the electroforming process due to the permanent conductive state. The further RESET operation leads to only electrical breakdown. Therefore, the yield in these cells is only 5% (= 9 cells/180 tested cells) as shown in Fig. 4.6 (d). The rare switchable Pt/5AO/TiN cells can be explained by a chemically modified TiN TE as TiN_xO_y due to the reaction with the oxide in contact [159, 211]. In addition, electroforming the Pt/5AO/TiN cells with the opposite polarity, i.e. the negative voltage applied on TiN TE, brings the same electrical breakdown events. As a symmetric structure, the Pt/5AO/Pt cells show no possible switching but only electrical breakdown. The breakdown phenomena in both Pt/5AO/Pt and in Pt/5AO/TiN devices are accompanied with the disrupture of the electrode lines, which was verified by SEM.

To compare the electroforming and breakdown events more statistically, the cumulative distribution function (CDF) plots of the electroforming voltage amplitude ($|V_{\mathrm{Fr}}|$) for different single-layer stacks are summarized in Fig. 4.7 (a). The y-axis of the CDF plot shows the probability of a variable that takes the value smaller than or equal to a certain number on x-axis. In Fig. 4.7 (a) the 50% CDF value stands for the median value of $|V_{\mathrm{Fr}}|$ and the spread of CDF plot represents the cell to cell variability. In case of the hard breakdown of Pt/5AO/Pt cells the electroforming voltage is defined as the value at an absolute current of 0.1 µA nearby the breakdown point. The data for the CDF plot of the Pt/5AO/TiN cells are collected from both successfully electroformed cells, and cells with the hard breakdown. The small tail of the CDF plot in Pt/5AO/TiN cells (solid black diamond) in Fig. 4.7 (a) coincides with the cells with regular RESET process. To compare the material specific dielectric character of Al_2O_3 films, the breakdown field (E_{BR}) is introduced, which can be described as the ratio of the electrical breakdown voltage divided by the total dielectric film thickness. This is done for "hard" breakdown events and for "soft" breakdown (= electroforming) [213]. E_{BR} is calculated as $E_{\mathrm{BR}} = \dfrac{|V_{\mathrm{Fr}}|}{d_{\mathrm{AO}}}$, where d_{AO} is the as-deposited Al_2O_3 layer thickness obtained from the XRR fitting (see

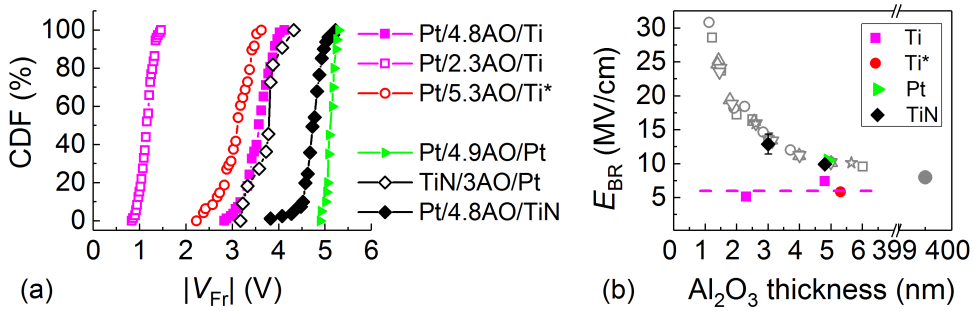

Figure 4.7: *(a) CDF plots of $|V_{Fr}|$ in Al_2O_3-based devices. (b) The corresponding mean value of E_{BR} as a function of Al_2O_3 layer thickness. The grey dots are redrawn from [154] (open dots) and from [212] (solid dot). Other colored dots are from this work.*

Tab. 3.1). The mean values of E_{BR} with available error bars are displayed as a function of Al_2O_3 thickness in Fig. 4.7 (b). The color defines the different stacks. It has to be mentioned that for a simplified description in the later sections and chapters the Al_2O_3 thickness will be given as a positive integer except in Fig. 4.7.

For Al_2O_3 single-layers sandwiched between Pt and TiN or Pt and Pt, the median electroforming voltage amplitudes are of around 3.9 V for 3 nm Al_2O_3 (open black diamond), of around 4.8 V for 4.8 nm Al_2O_3 (solid black diamond) and of around 5.1 V for 4.9 nm Al_2O_3 (solid green triangle) in Fig. 4.7 (a). The corresponding E_{BR} values of cells without OEL in Fig. 4.7 (b) is accordant with the reported data from comparably thick Al_2O_3 films that are deposited on the GaAs substrate [154]. However, the devices with an OEL, namely Pt/Al_2O_3/Ti (pink square) and Pt/Al_2O_3/Ti* (red circle), show lower values of $|V_{Fr}|$. This reveals a different influence of d_{AO} on E_{BR} for the two types of devices. For those without an OEL (triangle and diamonds in Fig. 4.7 (b)), E_{BR} increases with the decreasing Al_2O_3 thickness, while in cells with an OEL (square and circle in Fig. 4.7 (b)) E_{BR} remains almost constant at around 7 MV/cm, which is consistent with the reported E_{BR} in cells with same OEL, like Au/Ti/59 nm ALD Al_2O_3/Ti/Au stack [214].

The difference of $|V_{Fr}|$ and E_{BR} between Al_2O_3-based devices with an Ti(*) OEL and with metals like TiN or Pt electrodes can be explained from the different oxygen chemical potential of these metals. In VCM cells the functional oxide is reduced during the electroforming process and the filament is formed thus making the MOM stack conducting [215]. Since the electroforming or soft breakdown requires incorporation of oxygen vacancies into the thin film [216,217], the oxygen chemical potential of the metal electrode is correlated with the formation energy of oxygen vacancies in the oxide thin film [22]. For the metal with higher, i.e. less negative, oxygen chemical potential, the metal is hard to be oxidized and thus the introduction of oxygen vacancies into the pristine oxide thin film needs a high energy for formation of oxygen vacancies [218].

Cells with more negative oxygen chemical potential electrodes like Ti(*) show the reduced $|V_{Fr}|$ and show a frequently successful RESET process. On the contrary, cells with high oxygen chemical potential electrodes like TiN or Pt exhibit mostly hard breakdown, which leads to rarely stable c8w BRS. A more detailed and quantitative comparison is placed in 4.3.3.

c8w BRS in 5 nm Al_2O_3 single-layer devices

Comparing the typical $I(V)$ curves in Fig. 4.8, the c8w BRS behavior in two Pt/5AO/Ti(*) samples are remarkably similar. The cells switch to a linear LRS, and then during RESET a clear reduction of current level by over one order of magnitude is observed (Fig. 4.8 (a,b)). In contrast, Pt/5AO/TiN cells show a more unstable LRS and small resistance ratio (see Fig. 4.8 (c)). HRS can be around 10 times higher in Pt/5AO/Ti(*) cells than

in Pt/5AO/TiN cells.

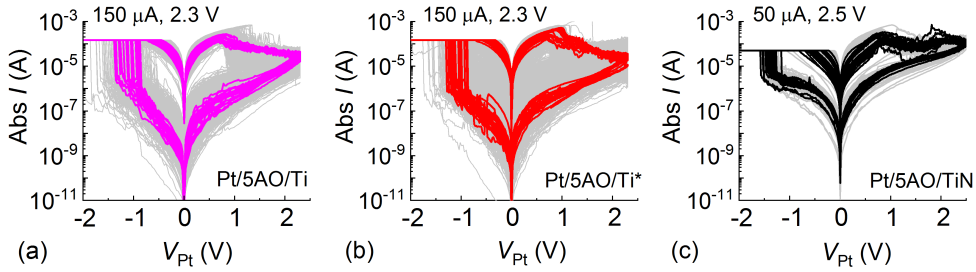

Figure 4.8: *$I(V)$ characteristics of c8w BRS in Pt/5AO/TE cells with different top electrodes: (a) evaporated Ti, (b) sputtered Ti* and (c) sputtered TiN. The most typical curves of each stack are drawn in pink, red, and black, while the grey curves given in the background represent statistical ensembles of 70, 48, and 5 cells, respectively. The sweeping parameters $|I_{CC}|$ and $V_{+,max}$ are given in the upper-left corner of each graph.*

Fig. 4.9 shows a statistical comparison of the SET ($V_{\mathrm{c8w,SET}}$) and RESET voltages ($V_{\mathrm{c8w,RESET}}$), and the read-out resistance values for LRS and HRS obtained for the three samples. The black CDF plots are obtained from all tested cells of one sample, which represent device-to-device (D2D) variations in comparison to the cycle-to-cycle (C2C) variation given in color. The cells with Ti and Ti* TE share the similarly median SET

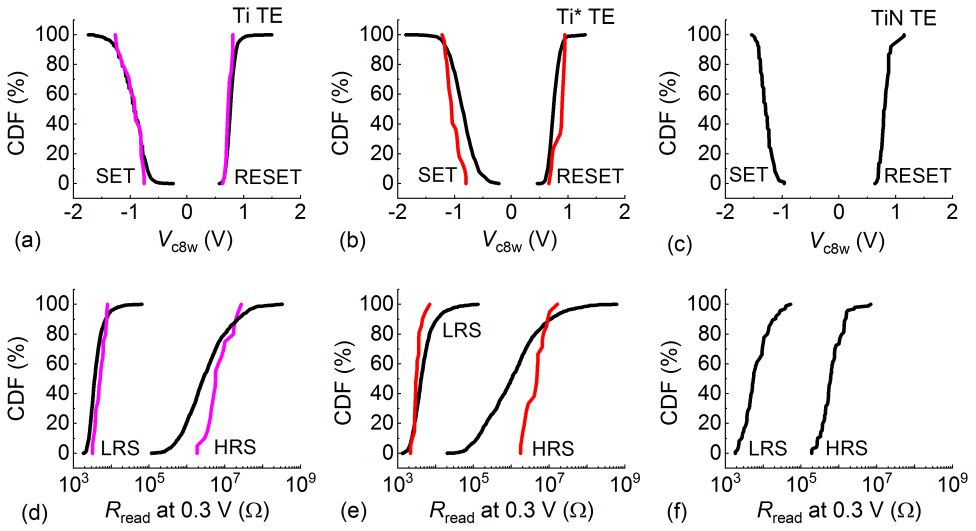

Figure 4.9: *CDF plots of $V_{c8w,SET}$ and of $V_{c8w,RESET}$ in a Pt/5AO/TE stack with (a) evaporated Ti for 70 cells, (b) sputtered Ti* for 48 cells, (c) sputtered TiN for 5 cells. The corresponding CDF plots of read-out resistance for HRS and LRS are shown in (d) to (f). The black lines are the statistics in all tested cells, colored lines represent the 20 cycles in the representative cell from Fig. 4.8.*

voltage value of around -1 V (see Fig. 4.9 (a,b). Comparing to this, cells with TiN TE have a more negative median SET voltage of about -1.5 V (see Fig. 4.9 (c)). The RESET voltage, however, remains at almost 1 V for all the cells independent of the TE. In Fig. 4.9 (d,e) a higher spread of $R_{\mathrm{c8w,OFF}}$ for cells with Ti and Ti* TE indicates an increased cell to cell variability. In addition, the ratio between median $R_{\mathrm{c8w,OFF}}$ and $R_{\mathrm{c8w,ON}}$ can reach 3-4 orders of magnitude in Pt/5AO/Ti(*) cells. The colored CDF plots reveal the C2C variability in the typical cell for twenty cycles. From Fig. 4.9 (d,e) the most striking difference between the distributions of D2D and C2C is found for the $R_{\mathrm{c8w,OFF}}$ values. Furthermore, the spread between the devices (D2D, black curves) is larger for the sample with sputtered Ti* TE compared to the evaporated Ti TE. Due to the low yield of switchable Pt/5AO/TiN cells, the narrow spread of CDF plots in Fig. 4.9 (f) can not suggest the higher uniformity between cells. In addition, the median resistance ratio in CDF of around 2 orders of magnitude in Pt/5AO/TiN cells is lower than in cells with Ti(*) OEL.

RESET stop voltage influence on c8w BRS

As shown in Fig. 4.10 the 5AO-based devices reveal the common VCM-type BRS behavior, this is, the current level in HRS decreases for increasing RESET stop voltage $V_{+,\mathrm{max}}$ [22]. The $V_{+,\mathrm{max}}$ dependent SET voltages are a consequence of the increased HRS values. In addition, no major difference is found between cells with two types of titanium electrodes obtained from evaporation or sputtering. Therefore, the curves for Ti* electrode are not explicitly shown here.

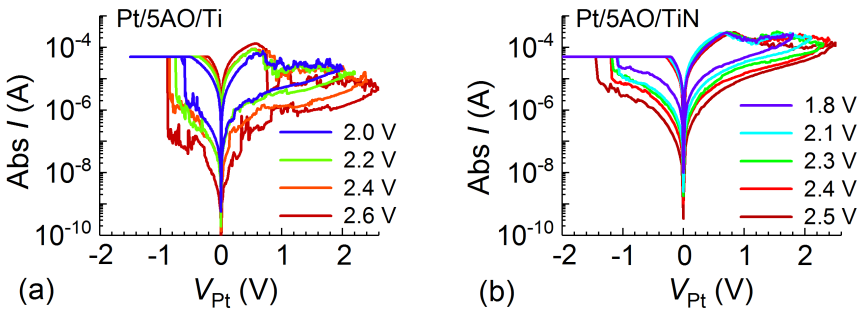

Figure 4.10: *$V_{+,max}$ influence on the c8w BRS in Pt/5AO/TE cells with different top electrodes: (a) evaporated Ti and (b) sputtered TiN. $|I_{CC}|$ is kept as 50 μA.*

The change of characteristic switching properties of the 5AO-based memristive devices, namely, $V_{\mathrm{c8w,SET}}$, $V_{\mathrm{c8w,RESET}}$, $R_{\mathrm{c8w,ON}}$ and $R_{\mathrm{c8w,OFF}}$, under RESET stop voltage variation are summarized in Fig. 4.11. The box plot displays the median value (horizontal line in the box), which represents the 50% probability value, while the lower and upper boundaries of the box correspond to 25% to 75% probability, respectively. Similarly, the

error bars cover the 10% and 90% probability. With this definition, the median value in the box plot becomes the same as the 50% value in the CDF plot. The length of the quadratic box is defined as interquartile range (IQR) and represents the variability of a quantity, which is similar to the spread in CDF plot.

Fig. 4.11 (a-b) show a weak change of median $V_{\mathrm{c8w,RESET}}$ and a slight increment of median $V_{\mathrm{c8w,SET}}$ of around 0.4 V with $\Delta V_{+,\mathrm{max}} \geqslant 0.6$ V in both samples. In Fig. 4.11 (c-d) the median value of $R_{\mathrm{c8w,ON}}$ stays almost unchanged within several kΩ for both devices, while the $R_{\mathrm{c8w,OFF}}$ values increase by several orders of magnitude with increasing $V_{+,\mathrm{max}}$. Pt/5AO/TiN cells show a limitation in their RESET capability through a less sensitive change in median $R_{\mathrm{c8w,OFF}}$ values towards the RESET stop voltage. As a result, the increase of resistance ratio induced by the same voltage increment is only around 10 in Pt/5AO/TiN, while in Pt/5AO/Ti cells it can achieve over 10^2.

As reported by Kim et al. [22], the metal electrode with a less negative oxygen chemical potential should induce a larger change in $R_{\mathrm{c8w,OFF}}$ upon RESET stop voltage variation. The possible explanation is that the less negative oxygen chemical potential of metallic electrode should release the oxygen ions back into the oxide layers easier and thus partially

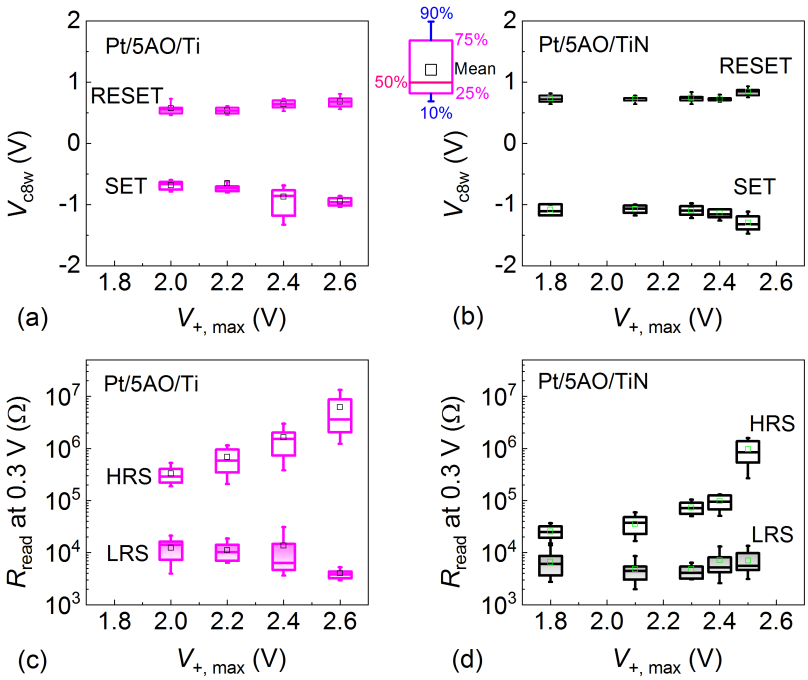

Figure 4.11: *Dependency of the characteristic switching parameters from $V_{+,max}$ in the form of box plots for $V_{c8w,SET}$, $V_{c8w,RESET}$ and for $R_{c8w,ON}$, $R_{c8w,OFF}$ in Pt/5AO/TE cells with Ti (a,c) and TiN (b,d) electrode, respectively. The data for each varied parameter is taken from Fig. 4.10 for 20 cycles.*

annihilate the conductive oxygen vacancy filament [22]. As a consequence the cells with an electrode having a less negative oxygen chemical potential should reach more insulating HRS under the same $V_{+,\max}$.

The oxygen chemical potential of TiN per oxygen atom is tabulated as -2.91 eV [219], which is higher than the value of Ti of about -5 eV [218]. Therefore, the cells with TiN TE should reveal stable and more insulating HRS. However, the experimental results contradict the prediction for Pt/5AO/Ti and Pt/5AO/TiN stacks. Due to the low yield of successfully electroformed and then still switchable Pt/5AO/TiN cells, the cells showing c8w BRS should have chemically modified electrode part in form of TiN_xO_y during the deposition process [159]. Accompanying with Joule heating during the electroforming, it is reasonable to postulate that TiN_xO_y tends to stay unstable and reacts further with oxygen ions. The oxygen chemical potential for TiN_xO_y may be even lower than the Ti electrode. In this way, the TiN_xO_y can release oxygen ions less efficiently than Ti OEL.

Current compliance influence on c8w BRS

The current compliance is generally used to control the electroforming or SET process in order to prevent current overshoot and to protect the cell from hard breakdown. In addition, it could define the achieved LRS resistance and thus the required RESET voltage [80]. As was experimentally observed, the $I(V)$ characteristic by increasing $|I_{CC}|$ reveals an increase of the current level in LRS, or in another words, a decrease of $R_{c8w,ON}$. In the meanwhile, a larger RESET voltage is required. This trend is observed in the Pt/5AO/Ti cell for a large $|I_{CC}|$ range shown in Fig. 4.12 (a) and is also observed in the HfO_x-based devices reported by Hardtdegen [220]. Oppositely, the Pt/5AO/TiN cell exhibits a weaker $|I_{CC}|$ dependent $V_{c8w,RESET}$ and an opposite $|I_{CC}|$ dependence of the LRS (see Fig. 4.12 (b)).

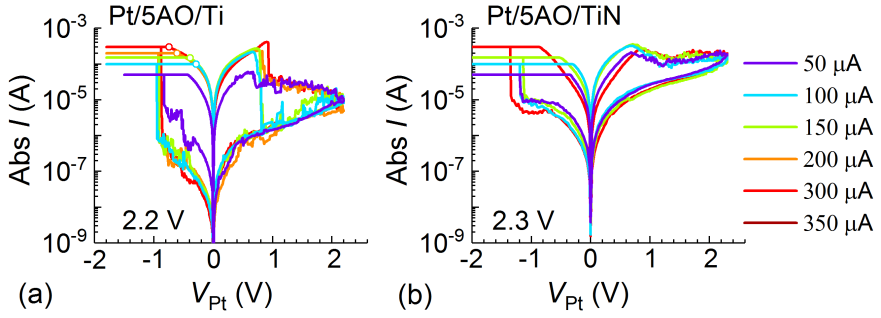

Figure 4.12: *Current compliance influence on the c8w BRS in Pt/5AO/TE cells with (a) evaporated Ti and with (b) sputtered TiN. The tested $|I_{CC}|$ values are listed on the right and the applied $V_{+,max}$ are given in the lower-left corner of each graph.*

Fig. 4.13 shows the constant median value of the SET voltage for both devices accompanied with the almost unchanged $R_{\mathrm{c8w,OFF}}$ values during the $|I_{\mathrm{CC}}|$ variation. A prominent $|I_{\mathrm{CC}}|$ dependent $R_{\mathrm{c8w,ON}}$ and $V_{\mathrm{c8w,RESET}}$ behavior is seen in the Pt/5AO/Ti cell, while it is absent in the Pt/5AO/TiN cell. Therefore, the increase of resistance ratio is more effective in the Pt/5AO/Ti cell through the higher and stable $R_{\mathrm{c8w,OFF}}$ and through the decreasing $R_{\mathrm{c8w,ON}}$ before this saturates at around 2-3 kΩ. The maximum achieved resistance ratio exceeds 10^2. The resistance ratio in the Pt/5AO/TiN cell, however, is limited to about 10.

Besides the phenomenological description, the current compliance, LRS and $V_{\mathrm{c8w,RESET}}$, could also be related in a mathematical way. Due to the nanometer scale metallic interconnects (60 nm to 100 nm width) applied in this work, the resistance arising from the interconnects can reach over 800 Ω to about 1.3 kΩ [197]. This is comparable to the readout values for LRS from the switching layer. Therefore, the total measured resistance for LRS should include both resistance contributions from the switching layer and the series resistance.

As reported by Hardtdegen et al. [220], for a same asymmetric Pt/oxide(s)/Ti stack

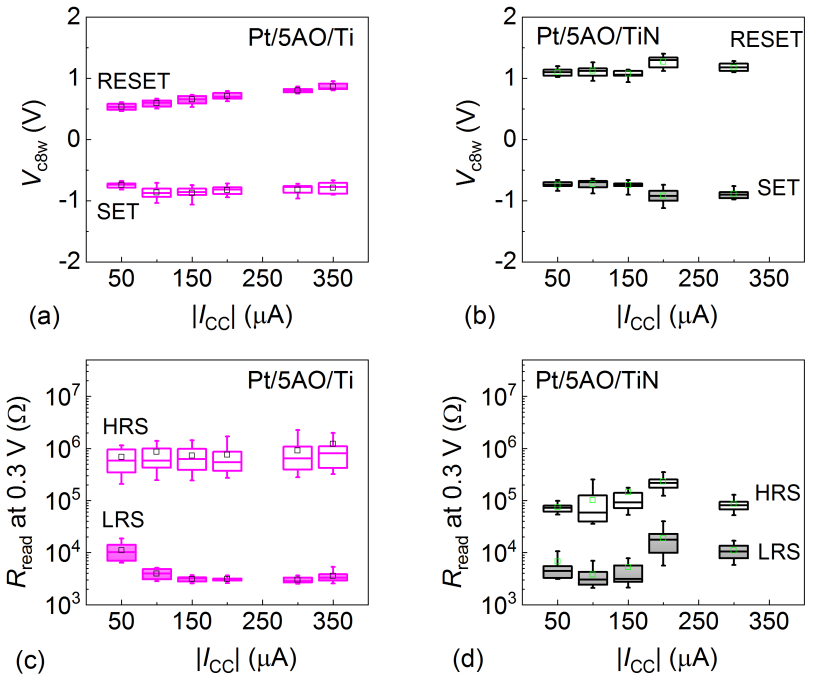

Figure 4.13: *Dependency of the characteristic switching parameters from the $|I_{CC}|$ variation in the form of box plots for $V_{c8w,SET}$, $V_{c8w,RESET}$ and for $R_{c8w,ON}$, $R_{c8w,OFF}$ in Pt/5AO/TE cells with Ti (a,c) and TiN (b,d) electrode, respectively. The data for each varied parameter is taken from Fig. 4.12 for 20 cycles.*

the total resistance for LRS ($R_{\mathrm{c8w,ON}}$) in the VCM-type ReRAM cell can be described as:

$$R_{\mathrm{c8w,ON}} = R_{\mathrm{ON,cell}} + R_{\mathrm{S}}, \tag{4.1}$$

where $R_{\mathrm{ON,cell}}$ is the resistance of the switching layer in LRS and R_{S} is the series resistance.

As suggested by Ielmini et al. [80], during the SET process the resistance for LRS in the cell ($R_{\mathrm{ON,cell}}$) should be controlled by the current compliance. Once the cell is switched to the LRS, the voltage across the cell is reduced and limited by the current compliance. During the DC voltage sweep with the duration of each sweeping step in second region, a stable LRS in the cell should be reached with a constant voltage on the cell ($V_{\mathrm{ON,\ cell}}$) and constant current flux ($\approx \mathrm{I_{CC}}$). Therefore, the resistance in the cell for LRS can be described by the division of $V_{\mathrm{ON,\ cell}}$ through the given current compliance value:

$$R_{\mathrm{ON,cell}} = |\frac{V_{\mathrm{ON,cell}}}{I_{\mathrm{CC}}}|, \tag{4.2}$$

then the total resistance can be expressed as:

$$R_{\mathrm{c8w,ON}} = |\frac{V_{\mathrm{ON,cell}}}{I_{\mathrm{CC}}}| + R_{\mathrm{S}}. \tag{4.3}$$

If a cell shows linear dependence of $R_{\mathrm{c8w,ON}}$ against the reciprocal of $|I_{\mathrm{CC}}|$, the series resistance as well as the $|V_{\mathrm{ON,cell}}|$ can be determined through a linear fitting. However, to verify the validity of this model, two restrictions for the measured data should be discussed prior to the fitting. After SET the current maintains the given value of current compliance until the applied voltage amplitude is reduced to a certain voltage ($|V_0|$) (see colored circles in Fig. 4.12 (a)). Since for voltage amplitude lower than this value, the response current amplitude is smaller than $|I_{\mathrm{CC}}|$, it should show a relation in a serial circuit as:

$$|V_0| = |V_{\mathrm{ON,cell}}| + |I_{\mathrm{CC}}| \cdot R_{\mathrm{S}} \tag{4.4}$$

The first restriction is: the amplitude of the defined voltage should be smaller than the SET voltage. i.e. $|V_0| < |V_{\mathrm{SET}}|$. The second confinement is that the maximum current (I_{RESET}) in the RESET process should be similar to $|I_{\mathrm{CC}}|$, since the SET and RESET processes in the cell should be initiated symmetrically, i.e. the current level for two processes should be similar. In practise, it is necessary to take the measurement noise of around 10% into consideration, i.e. I_{RESET} - $|I_{\mathrm{CC}}| < 0.1 \cdot |I_{\mathrm{CC}}|$.

By fulfilling the two restrictions, Fig. 4.14 (a) not only verifies the linear dependence but also gives a hint to the actual values of the series resistance $R_{\mathrm{S}} \approx 1.5$ kΩ and $|V_{\mathrm{ON,cell}}|$ ≈ 0.30 V. From the best fitting line in Fig. 4.14 (b) the values of R_{S} and $|V_{\mathrm{ON,cell}}|$ can be varied with a tiny increase of R_{S} in the $R_{\mathrm{c8w,ON}}$ - $|I_{\mathrm{CC}}|$ relation. It has to be mentioned that the $V_{\mathrm{ON,cell}}$ value should be a characteristic constant in the cell, which represents the

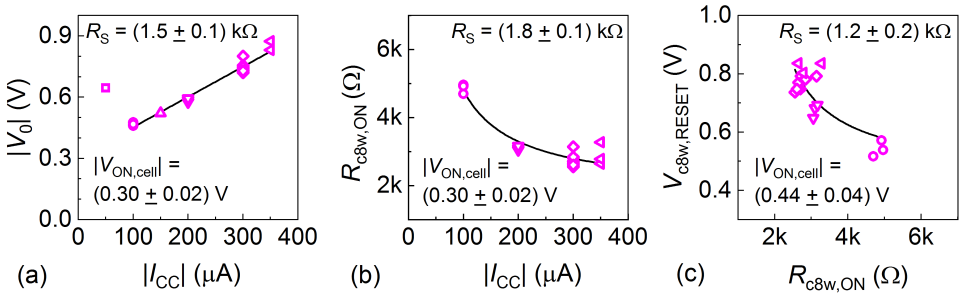

Figure 4.14: *(a) The filtered value of $|V_0|$ extracted from the $I(V)$ curves as the function of $|I_{CC}|$ for a Pt/5AO/Ti cell from Fig. 4.12 (a). The data point for $|I_{CC}| = 50\ \mu A$ is excluded from the linear fitting. (b) The filtered value of $R_{c8w,ON}$ as the function of $|I_{CC}|$ from Fig. 4.13 (a). (c) The filtered value of $V_{c8w,RESET}$ as the function of $R_{c8w,ON}$. The $R_{c8w,ON}$ value is read out at 0.3 V.*

stable voltage on the cell during DC voltage sweeping at current compliance. A similar idea is suggested by Ielmini et al. [221]. The reason is the following: in the normal DC mode the switching time stays in the second range. From the SET kinetics based on the pulse measurement with ns to 100 µs pulse length, the required SET voltage for DC switching mode in second range can be estimated [215, 222]. For example, a constant SET voltage required for operation within one second can be thus extrapolated. A SET voltage amplitude of 0.4 V for HfO_x-based cells is reported for DC mode with one second operation time in [221]. It has to be mentioned that in DC mode, the applied voltage ramps up and down with triangular form [223], which is different from the constant voltage amplitude during pulse measurement. However, in DC mode after I_{CC} is reached, the voltage really applied on the cell ($V_{ON,cell}$) is reduced to be exactly lower than the voltage required for oxygen vacancy migration. Therefore, the voltage amplitude on the cell effectively stays at $|V_{ON,cell}|$ shortly after the moment when I_{CC} is reached, until the start of current reduction (see colored circles in Fig. 4.12 (a)). Based on the fittings from Fig. 4.14 (a-b), $|V_{ON,cell}|$ is 0.3 V for the 5AO cell.

As suggested by Larentis [224] and observed by other experiments [80,220], the RESET transition requires both Joule heating and electrical field to make oxygen vacancies move away from the electrode. As the LRS has been defined by $|I_{CC}|$ and the voltage on the cell $|V_{ON,cell}|$ during the SET, the linearity of the $I(V)$ relation sustains even by reversion of voltage polarity. The LRS can remain by the symmetric voltage amplitude, and thus the turning point, namely $|V_{RESET,cell}|$, leads to the start of RESET process. Therefore, $|V_{RESET,cell}| \approx |V_{ON,cell}|$. Taking a series resistance R_S into consideration, the required RESET voltage $V_{c8w,RESET}$ from the $I(V)$ curves should follow the rule as:

$$|V_{c8w,RESET}| = |V_{RESET,cell}| + R_S \cdot |I_{RESET}|, \tag{4.5}$$

where the maximal RESET current value $|I_{\mathrm{RESET}}|$ can be calculated as:

$$|I_{\mathrm{RESET}}| = \frac{|V_{\mathrm{RESET,cell}}|}{R_{\mathrm{ON,cell}}} = \frac{|V_{\mathrm{ON,cell}}|}{R_{\mathrm{ON,cell}}}, \tag{4.6}$$

Combining equations (4.3), (4.5) and (4.6), the relation between RESET voltage and the LRS resistance can be expressed as:

$$|V_{\mathrm{c8w,RESET}}| = |V_{\mathrm{RESET,cell}}| \cdot (1 + \frac{R_{\mathrm{S}}}{R_{\mathrm{ON,cell}}}) = |V_{\mathrm{ON,cell}}| \cdot \frac{R_{\mathrm{c8w,ON}}}{R_{\mathrm{c8w,ON}} - R_{\mathrm{S}}}. \tag{4.7}$$

Based on equation (4.7), the plot of the median RESET voltage as a function of the total LRS resistance is given in Fig. 4.14 (c). An inverse proportionality is observed. This is similar to the relation between RESET voltage and LRS resistance observed by Ielmini et al. [80]. From the best calculated curve for the Pt/5AO/Ti cell, $|V_{\mathrm{RESET,cell}}| = 0.44$ V and $R_{\mathrm{S}} = 1.2$ kΩ are determined, suggesting a higher $|V_{\mathrm{ON,cell}}|$ and a lower R_{S} than the values acquired from Fig. 4.14 (b). Regarding the significant data variation in Fig. 4.14 (c), the relation $|V_{\mathrm{RESET,cell}}| \approx |V_{\mathrm{ON,cell}}|$ should hold. The same plots of $R_{\mathrm{c8w,ON}}$ as the function of $|I_{\mathrm{CC}}|$ and of $|V_{\mathrm{c8w,RESET}}|$ in the Pt/5AO/TiN cell show no dependence that fits equation (4.3) and equation (4.7).

Endurance in Pt/5 nm Al_2O_3/Ti cells

To verify the potential of the devices for the industrial application, a stable cycling endurance is of pivotal importance. By repeating the pulse cycles (for details see section 3.4.2), the endurance test for a typical Pt/5AO/Ti cell is shown in Fig. 4.15. The SET and RESET pulse values, i.e. $V_{\mathrm{RESET,pulse}}$ and $V_{\mathrm{SET,pulse}}$, are given in each graph. The pulse length (t_{pulse}) is kept as 1 µs. $R_{\mathrm{c8w,ON}}$ and $R_{\mathrm{c8w,OFF}}$ were read at -0.3 V applied to Pt BE.

In pulsed mode, the Pt/5AO/Ti nano-crossbar device reveals a reasonable stable

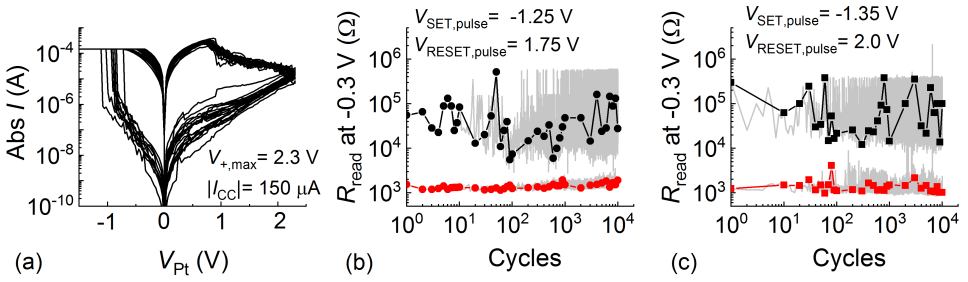

Figure 4.15: *(a) The $I(V)$ sweep test before endurance test for a Pt/5AO/Ti cell. (b,c) Two endurance tests performed with different voltage pulse amplitudes. The pulse length is kept as 1 µs.*

switching behavior up to 10^4 cycles. For the applied switching parameters, the total resistance in LRS turns out to be affected by the line resistance of the nano-crossbars. This explains the almost saturated $R_{\mathrm{c8w,ON}}$ values of about 2 kΩ obtained for SET pulses of -1.25 V and -1.35 V. The larger voltage amplitude yields a more reliable $R_{\mathrm{c8w,OFF}}$ to $R_{\mathrm{c8w,ON}}$ window of about a factor of 10.

4.2.3 Summary for single-layer devices

Unlike the rarely stable c8w BRS in TiO_2-based single-layer devices, Al_2O_3-based single-layer devices show a successful electroforming process and reproducible c8w BRS behavior. The systematic study has been performed in cells sandwiched between chemically modified electrodes (like Ti or TiN) and the active switching electrode like Pt. Distinct features of $I(V)$ characteristics obtained in both single-layer devices can be summarized as follows:

1. Comparing the cells with the same Ti TE but with different oxide layers, TiO_2 single-layer devices show an initially conductive nature for layer thickness $\leqslant$ 6 nm. On the contrary, the Al_2O_3-based cells showing highly insulating initial states require electroforming voltages.

2. Comparing the initial states and electroforming processes, the difference between Al_2O_3 single-layer devices with Ti and TiN electrode is obvious: a high level of the initial current and a reduced electroforming voltage amplitude is found in $Pt/Al_2O_3/Ti$ cells. This can be explained by the lower (or more negative) oxygen chemical potential of Ti of -5 eV [218] compared to this of TiN of -2.91 eV [219]. As the oxygen vacancies should be induced in the oxide layer during the electroforming process, the Ti electrode with the lower formation energy of oxygen vacancies can introduce more oxygen vacancies in the Al_2O_3 layer compared to the TiN. Therefore, the Al_2O_3 layers in the $Pt/Al_2O_3/Ti$ structure reveal a less insulating character and 1 V lower electroforming voltage amplitude compared to the $Pt/Al_2O_3/TiN$ devices.

3. An increment in the RESET stop voltage of around 0.6 V can increase the read-out resistance from LRS to HRS by a factor of 10^3 in the Pt/5AO/Ti cell and by 10^2 in the Pt/5AO/TiN cell. Additionally, at the same $V_{+,\mathrm{max}}$ the read-out value of HRS in cells with TiN TE does not reach comparable high resistance states as it does in cells with Ti TE. This phenomenon indicates a formation of TiN_xO_y at the Al_2O_3/TiN interface, which should have more negative oxygen chemical potential than the Ti OEL.

4. The increase of $|I_{\mathrm{CC}}|$ during the SET process decreases $R_{\mathrm{c8w,ON}}$ from several 10 kΩ to stable 2-3 kΩ in cells with Ti TE. However, the further decrease of $R_{\mathrm{c8w,ON}}$ is

not possible due to the limitation caused by resistive elements in series with the switchable filament resistance. Moreover, the relation between $|I_{CC}|$ and $R_{c8w,ON}$ as well as the relation between $R_{c8w,ON}$ and $|V_{c8w,RESET}|$ similar to the observation made by Larentis and Ielmini et al. [80, 224] is also observed for the Pt/5AO/Ti cell. However, Pt/5AO/TiN cells do not reveal any comparable relation.

4.3 $I(V)$ characteristics of the bilayer devices

4.3.1 Effect of the layer sequence and the redox active electrode

Electroforming

Figure 4.16 shows the electroforming behavior of two bilayer stacks of reverse order with Ti or TiN TE: namely, Pt/Al_2O_3/TiO_2/TE and Pt/TiO_2/Al_2O_3/TE. The grey curves in this figure show the electroforming and the subsequent successful RESET process from

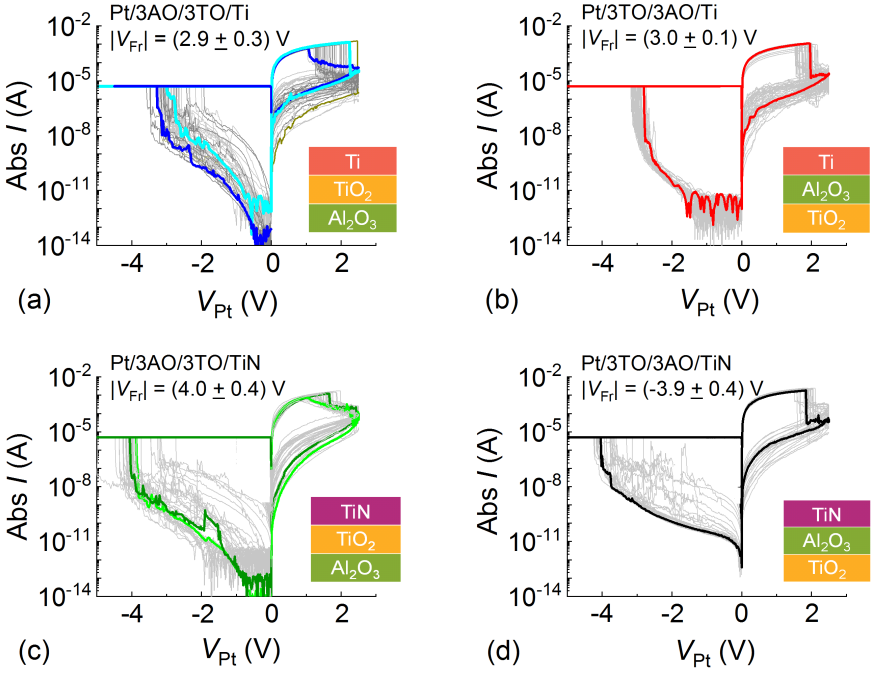

Figure 4.16: *Electroforming behavior in four stacks: (a) Pt/3AO/3TO/Ti, (b) Pt/3TO/3AO/Ti, (c) Pt/3AO/3TO/TiN and (d) Pt/3TO/3AO/TiN. The most typical curves of each stack are drawn in color, while the grey curves given in the background represent statistical ensembles of 46 successfully electroformed of all tested 63 cells, 51 (of 245), 37 (of 119) and 27 (of 166) cells, respectively. "TO" and "AO" are the abbreviations for TiO_2 and Al_2O_3, respectively. The numbers in front of "TO" and "AO" are the integer value of the layer thickness in nanometer (nm).*

multiple cells, from which the mean value of electroforming voltage with error bar and the yield of the successful switched cells are obtained and are given in each graph and caption, respectively. The colored curves show the representative behavior.

The main differences between the four stacks can be summarized as follows:

(1) For different top electrodes, Pt/bilayer/Ti cells reveal an electroforming voltage amplitude, which is by about 1 V lower than in Pt/bilayer/TiN cells.

(2) For the same type of oxygen exchange electrode, the different bilayer stacks reveal almost identical $|V_{\mathrm{Fr}}|$ values independent of the oxide stack: Pt/3AO/3TO/TiN and Pt/3TO/3AO/TiN samples show the same mean $|V_{\mathrm{Fr}}|$ of about 4 V (see Fig. 4.16| (c,d)). Interestingly, the TiN/3AO/Pt cells in Fig. 4.7 (a) also have the same value of $|V_{\mathrm{Fr}}|$. It could be concluded that the electroforming process in cells with TiN electrode is controlled by a soft breakdown in the Al_2O_3 layer.

(3) Both the oxide stack and the electrode material have a strong impact on the yield of the switchable cells. In contrast to a high yield of 73% in Pt/3AO/3TO/Ti cells, less than 21% Pt/3TO/3AO/Ti cells show successful RESET process after electroforming. Most Pt/3TO/3AO/Ti cells show hard breakdown. This difference repeats also for bilayer cells with TiN as TE. Comparing the same bilayer stack, cells with Ti TE supply higher yield than cells with TiN TE.

c8w BRS in TiO_2 and Al_2O_3-based bilayer devices

Reproducible c8w BRS behavior in the four bilayer stacks performed with similar control parameters is shown in Fig. 4.17. The colored lines show 20 representative cycles in one device, while the D2D variability is represented by the $I(V)$ curves plotted in grey. The discussion on the $I(V)$ characteristics is focused on the colored lines.

Generally, cells with the same electrode materials show more similar switching behavior than the cells with the same oxide stack. Cells with Ti as TE show a linear behavior in LRS and moderate SET voltages of around -1 V, whereas most of the TiN-based cells reveal a significant non-linear LRS and a more negative SET voltage of around -1.5 V. Although the RESET voltage in four stacks remains around 0.8 V to 1.0 V, the same oxide stack with different top electrodes shows the different RESET behavior varying from abrupt to gradual (Fig. 4.17 (a) vs. (c) and (b) vs. (d)).

The CDF plots in Fig. 4.18 and in Fig. 4.19 are acquired from 220 to 920 measured $I(V)$ loops. Several features show up from the statistical analysis:

(1) for bilayer cells with Ti TE the median values of SET and RESET voltages share the same absolute value of around 0.8 V (blue triangle and red circle in Fig. 4.18) and thus reveals a symmetric c8w BRS. On the contrary, a significant asymmetry of the median SET and RESET voltage values can be observed in the Pt/bilayer/TiN stacks (green square, black diamond in Fig. 4.18).

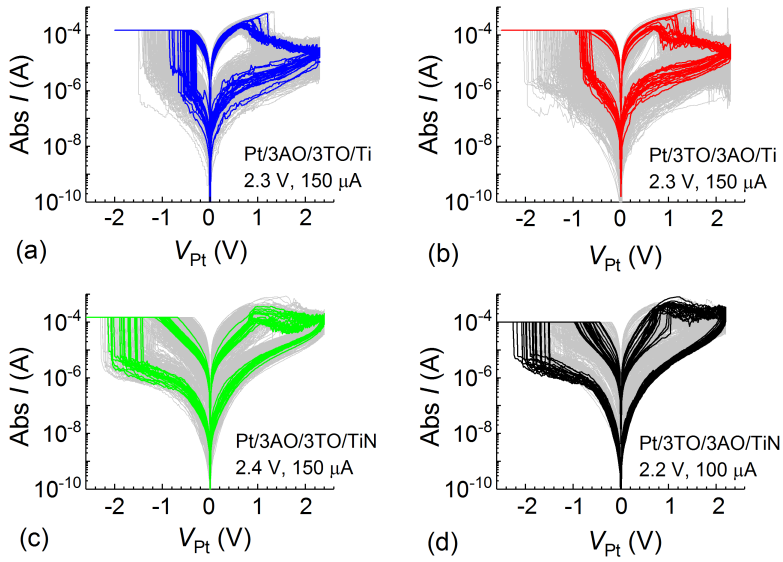

Figure 4.17: *(a-d) $I(V)$ characteristics of c8w BRS in bilayer Pt/oxides/TE stacks. The represented curves are drawn in color. The grey curves in the background from (a) to (d) represent statistical ensembles of 26, 41, 15 and 11 cells, respectively. $V_{+,max}$ and $|I_{CC}|$ are given in the lower-right corner of each graph.*

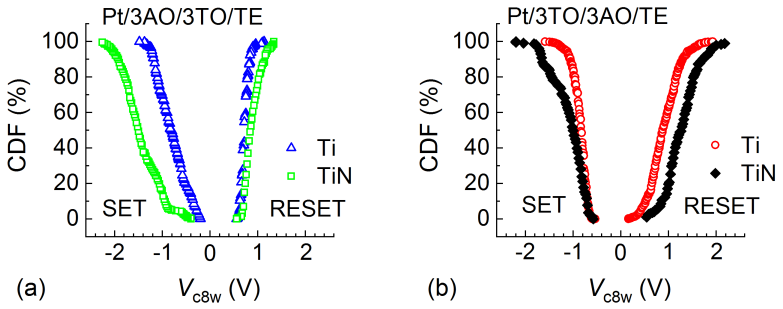

Figure 4.18: *CDF plots of $V_{c8w,SET}$ and of $V_{c8w,RESET}$ determined from Fig. 4.17: (a) Pt/3AO/3TO/Ti (blue triangle) and Pt/3AO/3TO/TiN (green square), (b) Pt/3TO/3AO/Ti (red circle) and Pt/3TO/3AO/TiN (black diamond).*

(2) Additionally, the Pt/bilayer/Ti cells show a RESET from a moderately low median $R_{\mathrm{c8w,ON}}$ of ≈ 4 kΩ to a median $R_{\mathrm{c8w,OFF}}$ value of about 500 kΩ, which leads to a resistance ratio of around 10^2 (see Fig. 4.19 (a,b)). However, the bilayer cells with TiN TE in Fig. 4.19 (c,d) show a resistance ratio of only about 10. Although the $R_{\mathrm{c8w,ON}}$ values of Pt/bilayer/Ti cells show a good uniformity, the large spread of $R_{\mathrm{c8w,OFF}}$ in CDF of around two orders of magnitude reveals a high D2D variability in all stacks. In cells with TiN as TE, the larger spread of $R_{\mathrm{c8w,ON}}$ in CDF (see Fig. 4.19 (c,d)) indicates a non-negligible part of the non-linear $I(V)$ characteristics of the LRS.

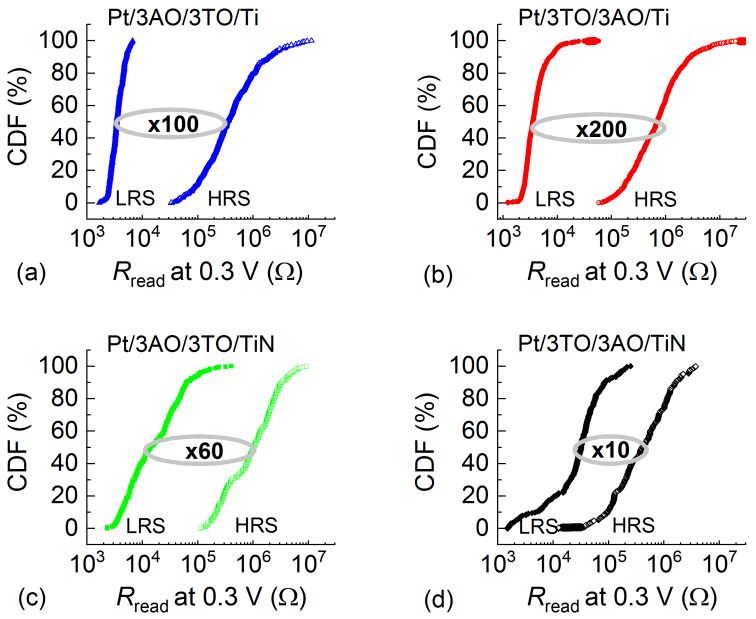

Figure 4.19: *CDF plots of read-out resistance for HRS and LRS extracted from the $I(V)$ curves in Fig. 4.17: (a) Pt/3AO/3TO/Ti, (b) Pt/3TO/3AO/Ti, (c) Pt/3AO/3TO/TiN and (d) Pt/3TO/3AO/TiN. The resistance ratio at 50% CDF is marked with grey ellipse.*

RESET stop voltage influence on c8w BRS

The influence of the RESET stop voltage ($V_{+,\max}$) on c8w BRS derived from the $I(V)$ characteristics of the four stacks are shown in Fig. 4.20. Representative $I(V)$ characteristics in 20 cycles show common trends: (1) by increasing $V_{+,\max}$, the current level for HRS decreases in all bilayer stacks; (2) due to the different RESET behavior between cells with the same oxide sequence but different TE, the impacts of $V_{+,\max}$ variation on HRS enhancement are obviously different. These features can be statistically described by the box plot in Fig. 4.21.

Comparing the Pt/bilayer/Ti cells in Fig. 4.21 (a), the median values (black square in the box) of the SET voltage amplitude increase slightly with increasing the $V_{+,\max}$ values. This trend can be observed in two Pt/bilayer/TiN cells in Fig. 4.21 (b) as well. For the four stacks the RESET voltages stay unchanged during the $V_{+,\max}$ variation.

As Fig. 4.21 (c) shows, the $V_{+,\max}$ dependence on $R_{\mathrm{c8w,ON}}$ and $R_{\mathrm{c8w,OFF}}$ for the two Pt/bilayer/Ti samples is similar. Comparing the median value of read-out resistance for LRS and HRS, $R_{\mathrm{c8w,ON}}$ remains almost unchanged, while $R_{\mathrm{c8w,OFF}}$ increases around one order of magnitude with $V_{+,\max}$ increased from 1.8 V to 2.4 V. In Fig. 4.21 (c,d) by keeping the switching parameters the same, Pt/3TO/3AO/TE cells with Ti (red box) or TiN (black box) show almost the same trend, but a larger variability of $R_{\mathrm{c8w,ON}}$ is observed

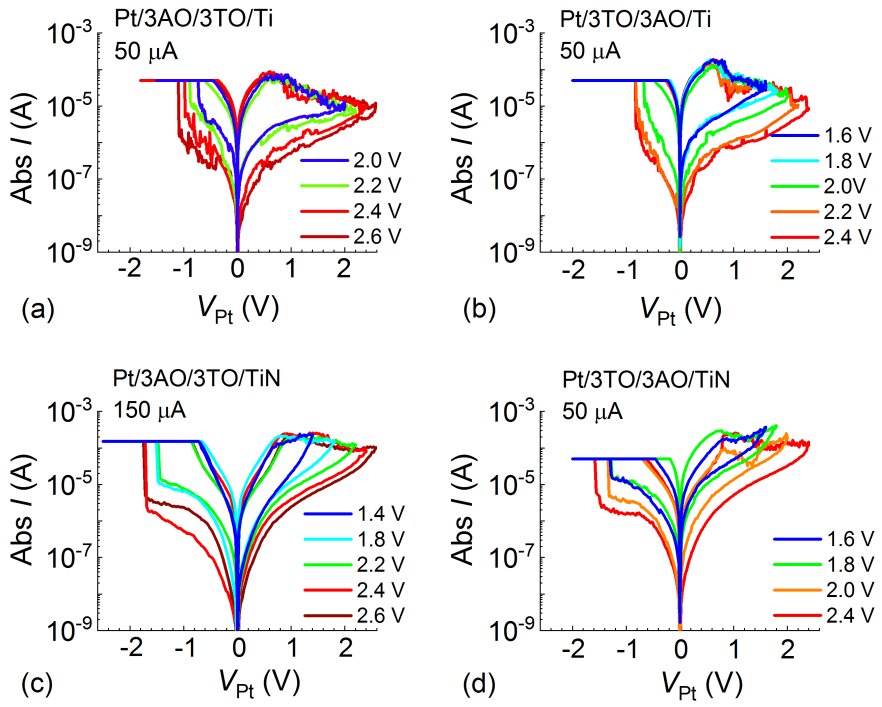

Figure 4.20: *$V_{+,max}$ influence on the c8w BRS in (a) Pt/3AO/3TO/Ti, (b) Pt/3TO/3AO/Ti, (c) Pt/3AO/3TO/TiN, (d) Pt/3TO/3AO/TiN stacks. The applied $|I_{CC}|$ are given under the stack and the $V_{+,max}$ variation are listed in the lower-right corner of each graph.*

in the Pt/3TO/3AO/TiN cell. Although the Pt/3AO/3TO/TiN cell was switched with a slightly higher $|I_{CC}|$ of 150 µA (green box in Fig. 4.21 (d)), it reveals a similar trend like others: an almost constant $R_{c8w,ON}$ and an increase of $R_{c8w,OFF}$ within one order of magnitude from 1.8 V to 2.4 V.

The median value of $|V_{c8w,SET}|$ as a function of the median value of $R_{c8w,OFF}$ is plotted in Fig. 4.22. All the bilayer devices show almost a linear dependence of $|V_{c8w,SET}|$ on $\log(R_{c8w,OFF})$. As suggested by Larentis, such a correlation between $|V_{c8w,SET}|$ and $\log(R_{c8w,OFF})$ can be modeled by a field driven ion hopping model [224]. That means the increase of $V_{+,max}$ leads to an increased insulating gap length, which results in an enhancement of $R_{c8w,OFF}$ and $|V_{c8w,SET}|$. As Fig. 4.21 (c,d) shows, the same $V_{+,max}$ can lead to similar values of $R_{c8w,OFF}$ in cells with Ti or TiN TE. This indicates that the insulating gap length that dominates the electronic transport should be similar. In addition, for the same $R_{c8w,OFF}$ value shown in Fig. 4.22, the cells with TiN TE (green square and black diamond) require more $|V_{c8w,SET}|$ than cells with Ti TE (blue triangle and red circle). This could originate from the different SET mechanisms between the two types.

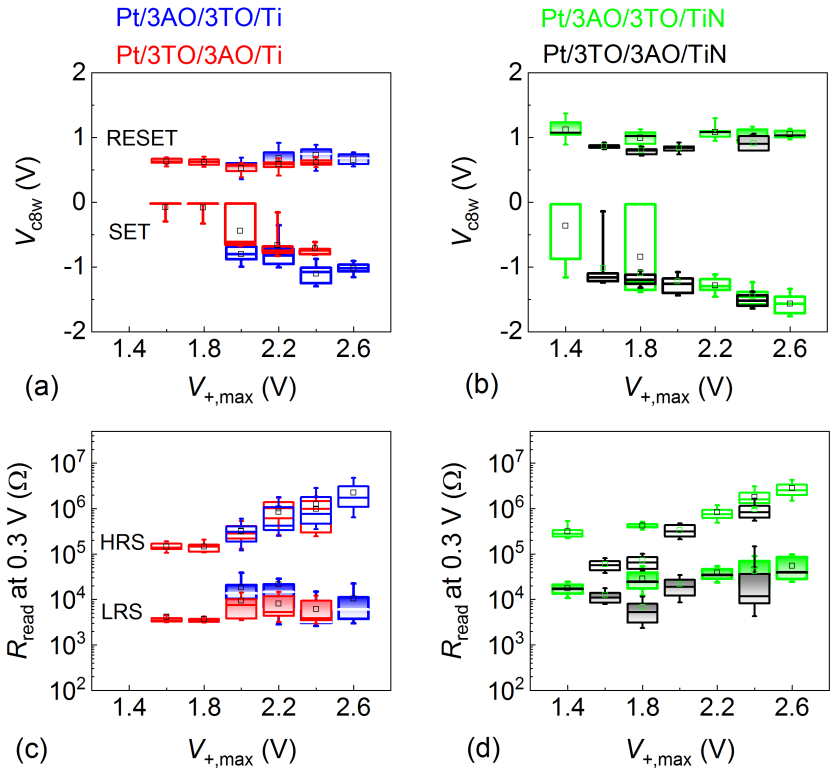

Figure 4.21: *Dependency of the characteristic switching parameters from $V_{+,max}$ in the form of box plots for (a,b) $V_{c8w,SET}$, $V_{c8w,RESET}$ and (c,d) $R_{c8w,ON}$, $R_{c8w,OFF}$ in Pt/3AO/3TO/Ti (blue) and Pt/3TO/3AO/Ti (red), Pt/3TO/3AO/TiN (black) and Pt/3AO/3TO/TiN (green) stacks, respectively. The data for each varied parameter is taken from Fig. 4.20 for 20 cycles.*

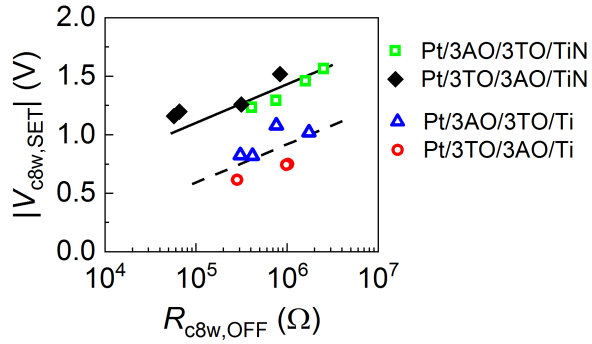

Figure 4.22: *$|V_{c8w,SET}|$ as a function of of $log(R_{c8w,OFF})$ obtained from the median values in Fig. 4.21.*

Current compliance influence on c8w BRS

To describe the influence of current compliance amplitude ($|I_{CC}|$) on c8w BRS, the representative $I(V)$ curves of the two bilayer stacks with Ti or TiN TE are summarized in Fig. 4.23.

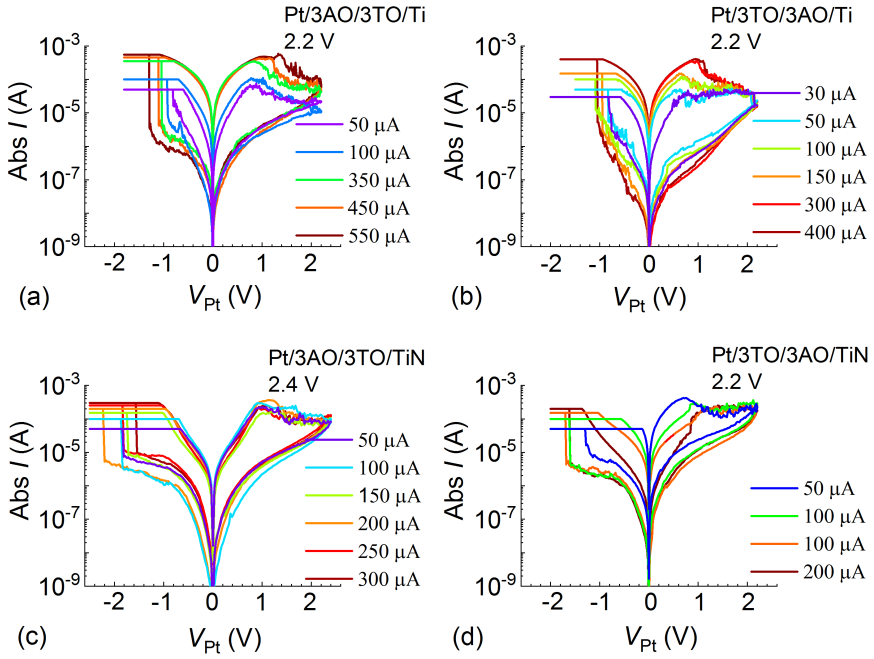

Figure 4.23: *The influence of $|I_{CC}|$ on $I(V)$ behavior in (a) Pt/3AO/3TO/Ti, (b) Pt/3TO/3AO/Ti, (c) Pt/3AO/3TO/TiN, (d) Pt/3TO/3AO/TiN stacks. The applied $V_{+,max}$ are given under the stack and the $|I_{CC}|$ variation is listed in the lower-right corner of each graph.*

Bilayer cells with Ti top electrode show a similar $|I_{CC}|$ dependence. As $|I_{CC}|$ increases, the current level for LRS increases and the required RESET voltage increases as well (see Fig. 4.23 (a-b)). On the contrary, the influence of $|I_{CC}|$ differs in Pt/bilayer/TiN cells. In Fig. 4.23 (c) the Pt/3AO/3TO/TiN cell shows an $|I_{CC}|$ independent LRS, and no visible changes on the RESET curves. The Pt/3TO/3AO/TiN cell in Fig. 4.23 (d), however, has an opposite effect, i.e. the higher the $|I_{CC}|$ values, the lower the current level for LRS.

The box plots in Fig. 4.24 (a,b) describe the statistical influence of the current compliance on SET and RESET voltages in the four stacks. Regarding the $|I_{CC}|$ dependence of SET and RESET voltages, the variation of the oxide stack from 3AO/3TO to 3TO/3AO results in minor changes of the trend for both bilayer cells with Ti TE (red and blue in Fig. 4.24 (a)) and TiN TE (green and black in Fig. 4.24 (b)). However, the influence of $|I_{CC}|$ on the read-out resistance for LRS and HRS differs between two different electrodes.

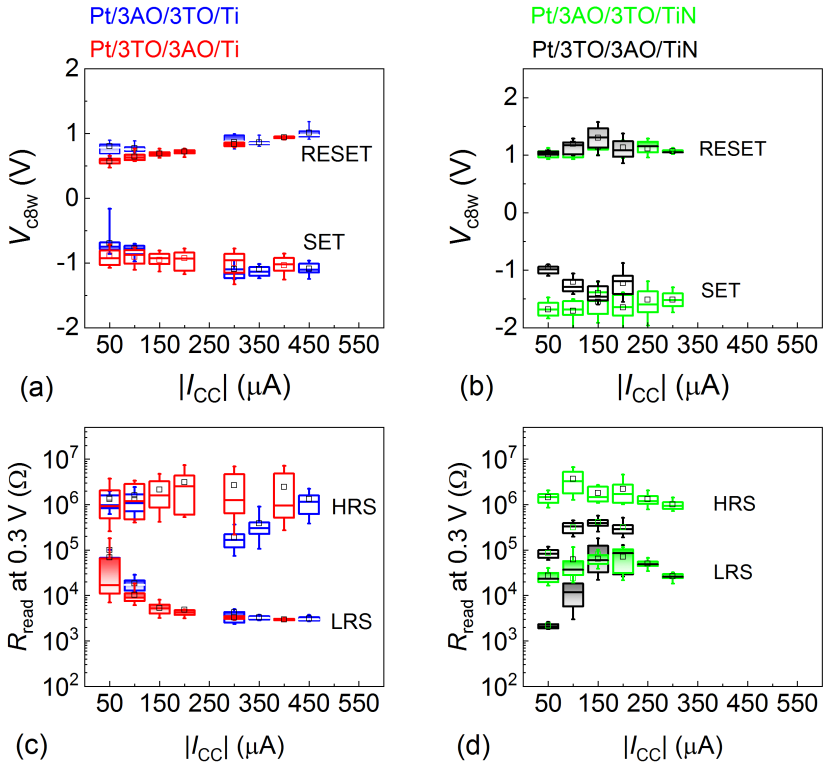

Figure 4.24: *(a,b) Box plots of $V_{c8w,SET}$ and of $V_{c8w,RESET}$ from Fig. 4.23 in Pt/3AO/3TO/Ti (blue), Pt/3TO/3AO/Ti (red), Pt/3AO/3TO/TiN (green), Pt/3TO/3AO/TiN (black) stacks. (c,d) The corresponding box plots of $R_{c8w,OFF}$ and of $R_{c8w,ON}$ for these four stacks.*

As the increase of $|I_{CC}|$ mainly reduces the LRS in bilayers with Ti electrode, the devices with TiN electrodes show either $|I_{CC}|$ independence on LRS (green box in Fig. 4.24 (d)) or no stable influence on both HRS and LRS (black box in Fig. 4.24 (d)).

Similar to Fig. 4.14, the $|V_{ON,cell}|$ and R_S values in the Pt/3TO/3AO/Ti cell can be estimated from fitting based on equations (4.3), (4.4) and (4.7). The plots of $|I_{CC}|$ against $|V_0|$, $|I_{CC}|$ against $R_{c8w,ON}$ and $V_{c8w,RESET}$ against $R_{c8w,ON}$ are illustrated in Fig. 4.25 (a) to (c), respectively. Firstly, a linear dependence in Fig. 4.25 (a) is observed and indicates the validity of equation (4.3), considering the series resistance and current compliance effect on the switching behavior. Furthermore, these fittings in Fig. 4.25 (a) to (c) suggest consistently that both $|V_{ON,cell}|$ and $|V_{c8w,RESET}|$ are around 0.5 V and R_S is around 1.3 kΩ, since the variation from the three fits are in the range of error. However, for other bilayer cells with either Ti or TiN as TE, the trend does not fit the model. The validity of the model shown in Pt/3TO/3AO/Ti and Pt/5AO/Ti cells indicates a symmetric c8w BRS process in these cells.

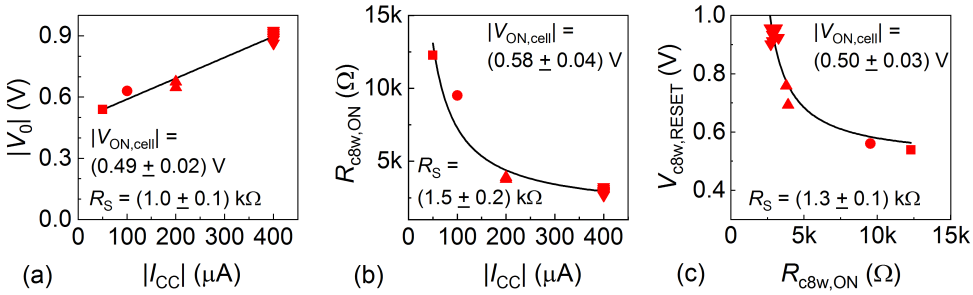

Figure 4.25: *(a) The filtered value of $|V_0|$ as the function of $|I_{CC}|$ for a Pt/3TO/3AO/Ti cell from Fig. 4.23 (b). (b) The filtered value of $R_{c8w,ON}$ as the function of $|I_{CC}|$ from Fig. 4.23 (a). (c) The filtered value of $V_{c8w,RESET}$ as the function of $R_{c8w,ON}$.*

Endurance in bilayer cells

Endurance tests for c8w BRS in two Pt/bilayer/Ti cells reveal the influence of oxide orders on the switching stability. Fig. 4.26 (a) shows the representative endurance result for one Pt/3AO/3TO/Ti cell, while the endurance results with similar voltage pulse amplitudes but different pulse lengths in one Pt/3TO/3AO/Ti cell are summarized in Fig. 4.26 (b,c). The black and red dots represent the $R_{\mathrm{c8w,ON}}$ and $R_{\mathrm{c8w,OFF}}$ values at a read pulse of -0.3 V with cycle numbers on logarithmic scale, respectively. The grey lines in Fig. 4.26 (b,c) illustrate the read-out values during each pulse cycle. The black- and red dots are chosen from grey curves within a certain interval to make the trends clear.

As Fig. 4.26 (a) shows, switching the Pt/3AO/3TO/Ti cell at SET pulse of -1.3 V and at RESET pulse of 1.75 V enables stable c8w BRS cycles up to at least 10^5. The resistance ratio can be sustained at around ten. In Fig. 4.26 (b,c) the Pt/3TO/3AO/Ti cell shows an influence of both $V_{\mathrm{SET,pulse}}$ and pulse length (t_{pulse}) on the resistance ratio. However, neither of these control parameters can enhance its endurance over 10^4 cycles.

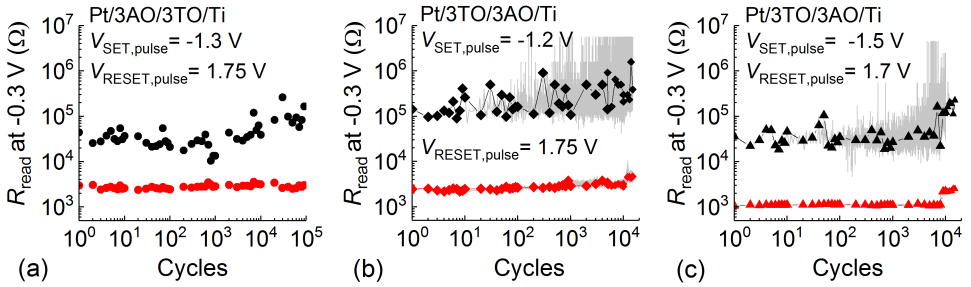

Figure 4.26: *The endurance test was applied (a) in a Pt/3AO/3TO/Ti cell with pulse length $t_{pulse} = 1\ \mu s$. (b) and (c) represent the endurance test in a Pt/3TO/3AO/Ti cell with $t_{pulse} = 100\ \mu s$ and $t_{pulse} = 1\ \mu s$, respectively. The applied SET and RESET pulses are listed in each graph.*

Compared to the cells with 10^4 endurance cycles, like Pt/5AO/Ti and Pt/3TO/3AO/Ti, Pt/3AO/3TO/Ti shows a 10 times higher endurance. As the first two stacks have naturally formed interfacial TiO_x layer at the Al_2O_3/Ti interface, the Pt/3AO/3TO/Ti cell has an artificial ALD grown 3 nm TiO_x layer between Al_2O_3 and Ti electrode. The higher endurance in cells with artificial TiO_x layer might indicate the stabilizing effect of TiO_x for the performance optimization.

4.3.2 Effect of Al_2O_3 thickness

Besides the order of the oxide layers and the electrode material, the thickness of each oxide layer should also play an important role for the c8w BRS behavior. In this section the initial state and the $I(V)$ characteristics of c8w BRS in the Pt/Al_2O_3/3 nm TiO_2/Ti stack with different Al_2O_3 layer thicknesses is studied and compared (see Fig. 4.27).

The red curves in Fig. 4.27 (a-c) represent the 1st cycle. In detail, the 1st negative branch describes the initial leakage and a possible electroforming behavior. The Pt/1AO/3TO/Ti cells show a relatively high conductivity at the initial state (Fig. 4.27 (a)). Therefore, this structure does not require an extra electroforming step. In contrast,

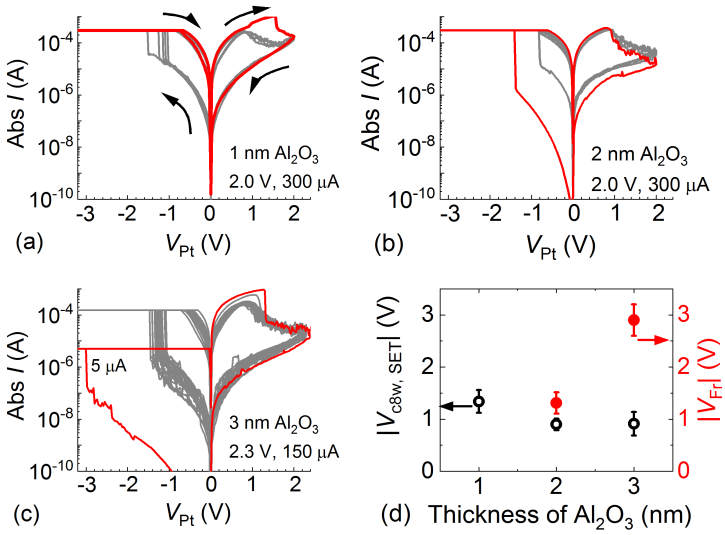

Figure 4.27: *Characteristic $I(V)$ curves of the in Pt/AO/3TO/Ti structures with (a) 1 nm Al_2O_3, (b) 2 nm Al_2O_3 and (c) 3 nm Al_2O_3 layer. The red curves in (a-c) represent the 1st cycle including the initial state, a possible electroforming and the subsequent RESET process. The grey curves show the next c8w BRS. The electrical parameters are given in each graph. (d) The dependence of $|V_{Fr}|$ and $|V_{c8w,SET}|$ as a function of the Al_2O_3 layer thickness. The median values of $|V_{Fr}|/|V_{c8w,SET}|$ in (d) are gathered from 10/9, 39/10, 46/26 cells for 1 nm, 2 nm, 3 nm Al_2O_3 respectively. The data from SET-free process are excluded.*

the insulating initial state in Pt/2AO/3TO/Ti and Pt/3AO/3TO/Ti cells requires an electroforming step at a voltage that exceeds the SET voltage of c8w BRS (Fig. 4.27 (b,c)). The corresponding electroforming and SET voltage amplitudes are summarized in Fig. 4.27 (d) as red dots and black circles, respectively. Comparing the two red dots, the $|V_{\mathrm{Fr}}|$ is enhanced from 1 V to 3 V by increasing the thickness of the Al_2O_3 layer from 2 nm to 3 nm. On the contrary, the $|V_{\mathrm{c8w,SET}}|$ shows an opposite dependence on the Al_2O_3 layer thickness. Without the Al_2O_3 layer, the $|V_{\mathrm{c8w,SET}}|$ value in Pt/TiO_2/Ti cells is more than 2 V. For 1AO3TO stack, this value is reduced to 1.5 V, whereas for 2AO3TO and 3AO3TO the $|V_{\mathrm{c8w,SET}}|$ saturates around 1 V. This clear difference of Al_2O_3 thickness dependence between $|V_{\mathrm{Fr}}|$ and $|V_{\mathrm{c8w,SET}}|$ indicates different mechanisms of electroforming and c8w SET process in these stacks.

4.3.3 Dicussion of redox reactions

In summary, the former sections discussed both electroforming and c8w BRS characteristics investigated in the bilayer devices to clarify the influence of the electrode variation and oxide stack variation. Focusing on the yield of successfully electroformed devices, the required voltage for the c8w SET and RESET operation as well as the resistance ratio between HRS and LRS, the cells with Ti electrode show a better performance than the cells with TiN electrode, and the oxide stack variation shows a slight influence. Additionally, all the bilayer devices show an increased HRS by increasing $V_{+,\mathrm{max}}$. Among them, cells with Ti electrode show a more stable multilevel type resistive switching, which show a good potential to produce electronic neurons and synapses for neuromorphic computing applications [225, 226]. Moreover, regarding the $|I_{\mathrm{CC}}|$ dependence, bilayer devices with Ti electrode reveal a clear LRS reduction by arising $|I_{\mathrm{CC}}|$, while the devices with TiN show neither clear nor stable $|I_{\mathrm{CC}}|$ dependence. These observations indicate that the electrode plays a more dominant role in the switching behavior.

The effect of the two top electrodes can be explained considering the oxygen vacancy formation energy in various material systems. For an asymmetric Pt/oxide/TE system, the oxygen vacancy can be generated by the following reaction [22] between the chemical active metal electrode (M*) and the switching metal oxide (MO) layer:

$$2\mathrm{O}^{\mathrm{X}}_{\mathrm{O(MO)}} + 4\mathrm{M}^{\mathrm{X}}_{\mathrm{M(MO)}} + \mathrm{M}^{*X}_{\mathrm{M^*(M^*)}} \leftrightarrow 2\mathrm{V}^{\bullet\bullet}_{\mathrm{O(MO)}} + 4\mathrm{M}'_{\mathrm{M(MO)}} + \mathrm{M^*O_2} + V''''_{\mathrm{M^*(M^*)}} + 4\mathrm{h}^{\bullet}, \quad (4.8)$$

where $\mathrm{M_{M(MO)}}$ means an M atom on an M-metal site in the MO metal oxide given by a Kröger-Vink notation, "X" stands for the neutral state, " $'$ " and " $''''$ " stand for one and four negative charges, respectively. $\mathrm{h}^{\bullet}$ is the hole with one positive charge.

Hence, the oxygen vacancies are formed in the metal oxide (MO) layer, which could contribute to the filament formation process. Since the formation process of oxygen vacancies in the oxide is accompanied by the simultaneous oxidation of the employed

electrode, the oxygen vacancy formation energy $E_{\mathrm{Vo}}(\mu(\mathrm{O}))$ in an arbitrary oxide can be correlated with the oxygen chemical potential ($\mu(\mathrm{O})$) in the metal electrode by the following equation [218]:

$$E_{\mathrm{Vo}}(\mu(\mathrm{O})) = E_{\mathrm{Vo}}(0) + \mu(\mathrm{O}), \tag{4.9}$$

where $E_{\mathrm{Vo}}(0)$ is the reference value for $\mu(\mathrm{O}) = 0$ eV, that is equivalent to the oxygen-rich limit, i.e. contacting with oxygen molecules [156, 227].

The oxygen vacancy formation energy in the oxygen-rich limit ($E_{\mathrm{Vo}}(0)$) for TiO_2 is around 6 eV [227], and for Al_2O_3 this value is around 7 eV [156]. The chemical potential of oxygen ($\mu(\mathrm{O})$) in Ti is around -5 eV, which is also described as the oxide heat of formation per O atom in Ti. Based on equation (4.9), the oxygen vacancy formation energy at the Al_2O_3/Ti or TiO_2/Ti interface can be estimated as ≈ 2 eV and ≈ 1 eV, respectively [218]. However, this difference can not directly explain the difference of electroforming voltage between the two Pt/Al_2O_3/Ti and Pt/TiO_2/Ti single-layer stack, since the oxides might be not completely stoichiometric in their initial states. Moreover, as Fig. 4.28 shows, the oxygen vacancy formation energy in Al_2O_3 contacted with TiN electrode is higher than in Al_2O_3 contacted with Ti electrode. This explains well the lower $|V_{\mathrm{Fr}}|$ in Pt/3TO/3AO/Ti cells than in Pt/3TO/3AO/TiN cells.

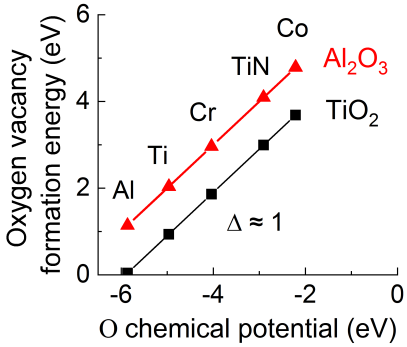

Figure 4.28: *Oxygen vacancy formation energy in Al_2O_3 and TiO_2 layers connecting with different metals. The data used to calculate the relation of oxygen vacancy formation energy and O chemical potential are gathered from [218, 219].*

By considering the oxygen vacancy formation energy during c8w BRS processes, the endurance behavior can be understood. Since the OEL has been oxidized particially through the electroforming process and previous c8w cycles, the reaction between oxidized OEL and underlying oxide reads [22]:

$$\mathrm{O}^{X}_{\mathrm{O(MO)}} + 2\mathrm{M}^{X}_{\mathrm{M(MO)}} + \mathrm{V}^{\bullet\bullet}_{\mathrm{O(M^*O)}} + 2\mathrm{M}^{*'}_{\mathrm{M^*(M^*O)}} \leftrightarrow \mathrm{V}^{\bullet\bullet}_{\mathrm{O(MO)}} + 2\mathrm{M}^{'}_{\mathrm{M(MO)}} + 2\mathrm{M}^{*X}_{\mathrm{M^*(M^*O)}} + \mathrm{O}^{X}_{\mathrm{O(M^*O)}} \tag{4.10}$$

Here the oxygen vacancies in the partially oxidized OEL could migrate into the adjacent metal oxide, which only results in the metal ion valence change. For the OEL in contact with its own oxide, i.e. TiO_2/Ti contact, the oxygen vacancy formation energy on two sides are equal, which renders an unexpected migration of oxygen vacancies ($V_O^{\bullet\bullet}$). However, for cells with an Al_2O_3/Ti interface, the oxygen vacancy formation energy in Al_2O_3 (MO) is higher than in the interfacial TiO_x layer (M*O) at the Al_2O_3/Ti interface, which means the oxygen vacancy is preferred to form in the TiO_x and the Al_2O_3 layer is simultaneously reoxidized. This oxygen vacancy exchange leads to an unexpected breaking of oxygen vacancy filament in the Al_2O_3 layer, which could be the origin of low endurance cycles in cells with Al_2O_3/Ti interface, namely Pt/3TO/3AO/Ti, Pt/2AO/Ti and Pt/5AO/Ti in comparison to Pt/3AO/3TO/Ti cells, which have a thicker artificial TiO_2 layer deposited by ALD to avoid direct oxygen vacancy exchange between Al_2O_3 and Ti.

For the Al_2O_3 thickness dependence of electroforming voltage in Pt/2AO/3TO/Ti and Pt/3AO/3TO/Ti devices, both the interface of TiO_2/Ti and Pt/Al_2O_3 are important. Since the oxygen vacancy formation energy at the Pt/Al_2O_3 interface (≈ 7 eV) is higher than at the Pt/TiO_2 interface (≈ 6 eV) [218], the thicker Al_2O_3 would inhibit the introduction of oxygen vacancies from the Pt interface. Therefore the increased Al_2O_3 thickness raises the required amount of oxygen vacancies for constructing the conductive path from the TiO_2/Ti interface, which requires a electroforming step and a higher electroforming voltage amplitude.

4.4 Comparison of the BRS performance in single-layer and bilayer devices

As revealed in the previous sections, the interface between OEL electrode and oxide plays a notable role for c8w BRS in single-layer and bilayer devices. With a more detailed comparison between single-layer and bilayer devices in the following, the understanding of the impact from the interfacial layer could be improved. As discussed in section 4.2.2 a metal with a low oxidation enthalpy like Ti, Hf or Ta enables the switching in the oxide layer by the exchange of oxygen ions. Several works reveal the importance of engineering the metal OEL by variation of the material [22] or the thickness [228]. By means of the interfacial engineering, a thin interfacial TiO_x layer can be formed due to an oxygen exchange reaction between Al_2O_3 and Ti. In this way, the Pt/Al_2O_3/Ti stacks are defined as the devices without (w/o) 3 nm TiO_2 artificial layer. Otherwise, if a 3 nm TiO_2 layer is intentionally added, namely the Pt/Al_2O_3/3 nm TiO_2/Ti stacks, devices are defined as the ones with an artificial ALD TiO_2 layer. Here, the integer value is used as the layer thickness.

2 nm Al_2O_3 with and without artificial TiO_2 layer

The cumulative distribution functions of the initial state and the electroforming voltage (V_{Fr}) for 2 nm Al_2O_3-based devices are listed in Fig. 4.29 to provide an overview on the functionality of an artificial TiO_2 layer between the Al_2O_3 and Ti top electrode. As Fig. 4.7 shows, the CDF of $|V_{Fr}|$ and the resulting E_{BR} of Al_2O_3 films sandwiched between a Pt and a Ti electrode or between symmetric Pt electrodes show distinct features. The reduced median value of $|V_{Fr}|$ provides an evidence of a local reduction of the Al_2O_3 layer by means of an oxidation of the Ti OEL. By intentionally adding a 3 nm artificial TiO_2 layer between 2 nm Al_2O_3 layer and Ti OEL, the initial resistance ($R_{initial}$) of the pristine cells increases by a factor of 10 and reduces the spread of the CDF (see claret-red solid circles in Fig. 4.29 (a)). Although the Pt/2AO/3TO/Ti cells are more insulating, the median value of V_{Fr} is only slightly lower than the value for the cells without the artificial layer (Fig. 4.29 (b)). Since the Pt/3 nm TiO_2/Ti cells show a highly conductive nature, this increase of $|V_{Fr}|$ in the Pt/2AO/3TO/Ti devices is attributed to a suppression of the oxygen exchange reaction between Ti OEL and Al_2O_3 by insertion of the artificial layer. Additionally, for the same stack no significant area dependence of $|V_{Fr}|$ between $(100\ nm)^2$ and $(80\ nm)^2$ is observed (Fig. 4.29 (b,c)), which indicates a filamentary-type switching.

Al_2O_3-based devices with or w/o artificial TiO_2 layer show stable c8w BRS behavior with minor variations. Switching at the same electrical parameters, namely RESET stop voltage of 2.0 V and current compliance amplitude of 50 µA, the two stacks show

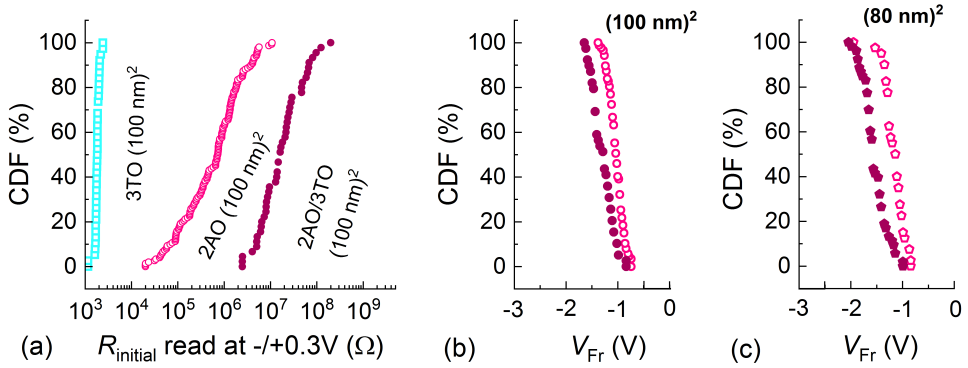

Figure 4.29: *Comparison of the three Pt/oxide(s)/Ti stacks: 3 nm TiO_2 (blue open square), 2 nm Al_2O_3 with (claret-red solid circle) and without (pink open circle) an additional 3 nm TiO_2 artificial layer. (a) The read-out initial resistance ($R_{initial}$) of the pristine cells measured at -/+0.3 V, (b) V_{Fr} of cells from (a). The CDF plots comprise measurements of 38, 45 and 88 cells with $(100\ nm)^2$ cells, respectively. (c) CDF plots of V_{Fr} for about 50 cells with $(80\ nm)^2$ size for each stack. Solid and open pentagon stand for 2 nm Al_2O_3-based cells with and without 3 nm TiO_2 artificial layer, respectively.*

similar statistics of SET and RESET voltages with median values of -1.0 V and +1.0 V, respectively (Fig. 4.30 (a)) as well as the two read-out resistance states with median values of ≈ 6 kΩ and ≈ 250 kΩ, respectively (Fig. 4.30 (b)). Especially, the spread of CDF plots for the LRS is reduced in devices with the artificial layer. Based on these statistical results, the effect of the artificial TiO_2 at the interface between the thin insulating Al_2O_3 layer and Ti OEL can be summarized as follows: first, the initial resistance and electroforming voltage are increased due to an inhibited oxygen ion exchange between Al_2O_3 and Ti OEL. Second, once the device is electroformed, the artificial TiO_2 layer will not disturb the c8w BRS behavior, but can enhance the switching stability to a certain extend. However, the 2 nm Al_2O_3-based devices even with artificial layer show no RESET stop voltage influence on the HRS. Keeping I_{CC} = 150 µA, $V_{-,max}$ = -1.5 V and repeating 20 cycles for each RESET stop voltage, the Pt/2AO/3TO cell with $(100\ nm)^2$ cell size show an almost unchanged median value of read-out resistance for LRS of ≈ 6 kΩ and for HRS of ≈ 70 kΩ, although the $V_{+,max}$ varies from 1.4 V to 2.6 V with 0.2 V increment. The endurance test for the ultra-thin 2 nm Al_2O_3 layer is shown in Fig. 4.30 (c). The memory window is limited to about several tens, and the endurance is limited to about 10^4 cycles.

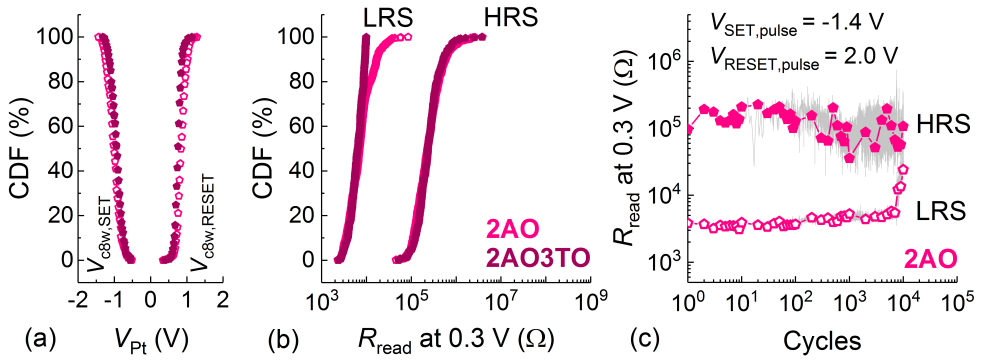

Figure 4.30: *Comparison of the switching characteristics of $(80\ nm)^2$ Pt/2 nm Al_2O_3/Ti cells without (pink open pentagon) and with a 3 nm TiO_2 artificial layer (claret-red solid pentagon). (a) SET and RESET voltage distributions, (b) the read-out resistance for LRS and HRS. The CDF plots comprise measurements of 32 and 21 cells, respectively. (c) Endurance test for a $(80\ nm)^2$ Pt/2 nm Al_2O_3/Ti cell. The operation pulses are listed in the graph.*

5 nm Al_2O_3 compared to 3 nm Al_2O_3/3 nm TiO_2

To enlarge the memory window a Pt/oxide(s)/Ti stack including a thicker Al_2O_3 layer with and without the same 3 nm TiO_2 artificial layer is compared and discussed here. The Pt/5 nm Al_2O_3/Ti stack can be considered as the cells without an artificial layer and Pt/3 nm Al_2O_3/3 nm TiO_2/Ti as the cells with an artificial layer.

For a similar total layer thickness, Pt/5AO/Ti cells require a higher electroforming voltage amplitude in comparison to the Pt/3AO/3TO/Ti devices (see Fig. 4.31 (a)). This increase of $|V_{\mathrm{Fr}}|$ should originate from the thicker insulating Al_2O_3 layer in Pt/5AO/Ti cells. Reproducible c8w BRS loops are observed in both stacks (Fig. 4.31 (b,c)), showing not only the similar operation voltages (Fig. 4.31 (d)), but also the same stable read-out resistance ratio over 10^2 (Fig. 4.31 (e)). Due to the larger spread of CDF for LRS in cells without an artificial layer, Pt/3AO/3TO/Ti cells show a more stable LRS. This trend is in good agreement with the thinner 2 nm Al_2O_3-based cells. Although for the same switching parameters, a higher read-out resistance value for HRS can be seen in Pt/5AO/Ti devices than in Pt/3AO/3TO/Ti devices (Fig. 4.31 (d)), but also the same stable read-out resistance ratio over 10^2 (Fig. 4.31 (e)), the endurance characteristics for 1 µs pulses with relative low pulse amplitudes, namely $|V_{\mathrm{SET,pulse}}| = 1.25$ V to 1.3 V, $|V_{\mathrm{RESET,pulse}}| = 1.75$ V, reveals a 10 times higher cycling stability for the cells with artificial layer than cells without artificial layer (Fig. 4.31 (f)).

As a conclusion, the artificial TiO_2 layer can strongly improve the endurance through suppressed interfacial reaction between Al_2O_3 and Ti OEL. Therefore an artificial TiO_2 layer is recommended for a stable c8w BRS in Al_2O_3-based devices.

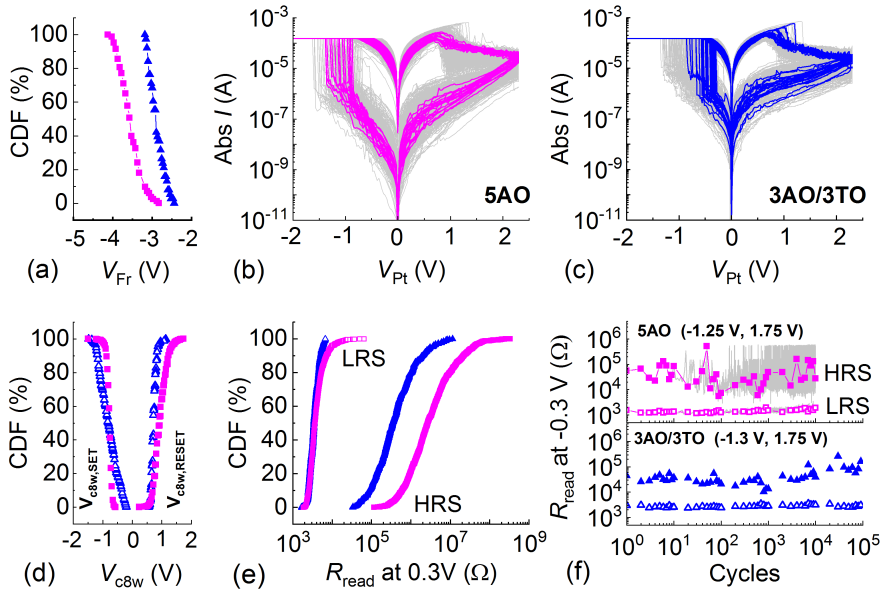

Figure 4.31: *Comparison of the statistics of Pt/5 nm Al_2O_3/Ti (magenta square) and Pt/3 nm Al_2O_3/3 nm TiO_2/Ti (blue triangle) with (100 nm)^2 cell size: (a) CDF plots of V_{Fr}, (b,c) $I(V)$ characteristics with the same electrical parameters, (d) SET voltage and RESET voltage, (e) read-out resistance for HRS and LRS and (f) endurance performed under 1 µs pulse. Figures are collected from the former sections.*

Chapter 5

Counter-eightwise switching characteristics in pulse mode

To approach the industrial application, how fast the memory cell can switch is an important criterion. In general, the write speed for VCM-type ReRAM devices can be reduced several orders of magnitude from second to nanosecond accomplished by a slightly increased operation voltage amplitude within one order of magnitude [39]. This strongly non-linear voltage-time behavior of the SET kinetics originates from the ReRAM switching mechanism, which is related to the electric field and temperature dependent oxygen vacancy motion. In this chapter, the SET (5.2 to 5.3) and RESET kinetics (5.4) was studied in Pt/5 nm Al_2O_3/Ti single-layer cells and Pt/3 nm Al_2O_3/3 nm TiO_2/Ti bilayer cells showing stable c8w BRS behavior. The pulse measurements were performed through pulse/read and transient pulse modes.

5.1 Overview of measurement schemes

For SET and RESET kinetic studies two different pulse measurements were carried out. One is the pulse/read mode via Keithley 4200 SCS setup. The general pulse train for SET and RESET pulse measurements with the corresponding initiation conditions is drawn in Fig. 5.1 (a) and (b), respectively. Details of the setup and the schematic description of the pulse train are introduced in chapter 3 section 3.4.2.

The read-out resistance values (R_{read}) were recorded after the SET ($V_{\mathrm{SET,pulse}}$) or RESET pulse ($V_{\mathrm{RESET,pulse}}$) was applied. The switching behavior in this pulse/read mode was analyzed from the matrix of R_{read} as a function of operation pulse amplitudes and the corresponding pulse length (t_{pulse}), i.e. "heat graphs" (see sections 5.2.1 and 5.4).

For the SET kinetic study the transient current response upon fast voltage pulses was performed by Agilent B1110A setup. The transient current was monitored continuously during SET pulse. The SET time determined by the abrupt increase of the voltage signal

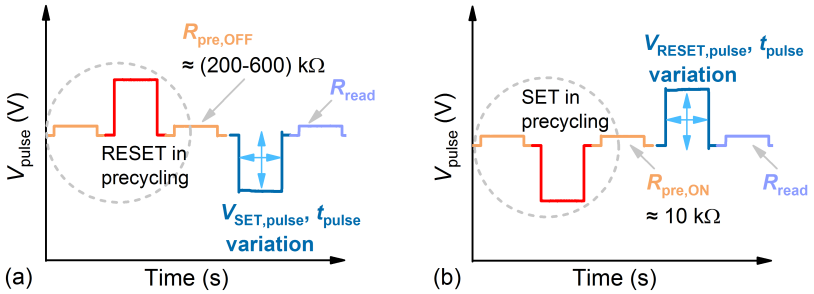

Figure 5.1: *Schematic illustration of (a) the SET pulse and (b) the RESET pulse measurements with Keithley 4200 SCS system. The precycling is emphasized by circles.*

and current signal was read out as well (for details see section 3.4.2). If no increase of the current amplitude is observed during the SET pulse, this process is defined as non-SET. The relation between t_{SET} and the applied SET pulse amplitudes ($|V_{SET,pulse}|$) are investigated in section 5.2.2 and will be compared with the "heat graph" from the pulse/read mode.

5.2 SET pulse variation

5.2.1 Pulse/read measurement

Two cells of single-layer and bilayer stacks showing typical $I(V)$ characteristics are chosen. Based on the former voltage sweep measurements in section 4.4 the Pt/5 nm Al_2O_3/Ti cells can generally reset to a more insulating HRS than the Pt/3 nm Al_2O_3/3 nm TiO_2/Ti cells by applying the same RESET stop voltage. For the two pulsed cells with the same electrical parameters, namely $V_{-,max}$ = -1.75 V, $V_{+,max}$ = 2.3 V, $|I_{CC}|$ = 300 µA, R_{read} = 33 MΩ and 3 MΩ were obtained for the single-layer and bilayer devices, respectively. Therefore, the pre-conditions for a comparable SET process study of both cells were adjusted to achieve $R_{pre,OFF}$ values between 300 kΩ and 600 kΩ for the Pt/5 nm Al_2O_3/Ti cell and between 240 kΩ and 490 kΩ for the Pt/3 nm Al_2O_3/3 nm TiO_2/Ti cell (see Fig. 5.1 (a)). For the SET process study, two parameters, i.e. the amplitude of the SET pulse voltage ($|V_{SET,pulse}|$) and the pulse length (t_{pulse}) of the SET pulse were changed in turn. In order to get a rough statistic, each variation was repeated for five times.

Fig. 5.2 shows the change of R_{read} values obtained after application of increased pulse voltage amplitude. Starting from the same HRS, the single-layer cell shows a gradual increase of the read-out resistance for LRS starting at $|V_{SET,pulse}|$ = 0.95 V. The LRS value stagnates at around 7-8 kΩ for $|V_{SET,pulse}| > 1.05$ V (Fig. 5.2 (a)). In contrast, the bilayer device shows a more abrupt onset of the SET event (Fig. 5.2 (b)). In addition,

for $|V_{\mathrm{SET,pulse}}| \geqslant 0.95$ V the read-out values for LRS stay the same at 3-4 kΩ.

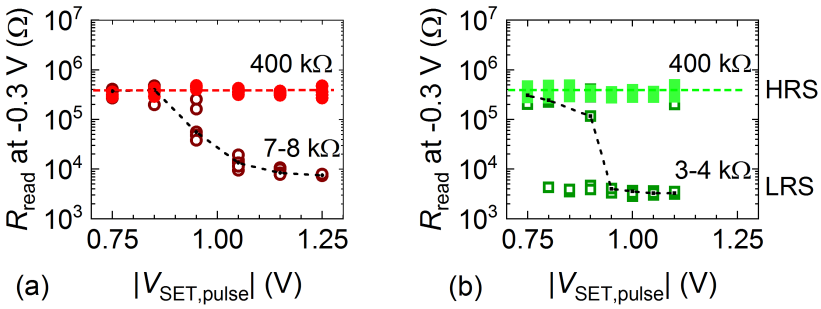

Figure 5.2: *The SET behavior obtained for SET pulses length of 1 µs of (a) a Pt/5 nm Al_2O_3/Ti cell with (80 nm)^2 cell size and (b) a Pt/3 nm Al_2O_3/3 nm TiO_2/Ti cell with (100 nm)^2 cell size. The values for HRS (solid dots) and for LRS (open dots) are read out before and after SET pulse, respectively. The colored dash lines represent the almost constant HRS of ≈ 400 kΩ. The black dash lines link the median value of LRS.*

To give a better illustration, the read-out resistance values after the SET pulses are shown in the form of "heat-graphs" in Fig. 5.3. The color codes the read-out resistance values. The maps confirm the observation of Fig. 5.2 that the SET process is more abrupt in the bilayer cell than in the single-layer cell. Take $R_{\mathrm{read}} \leqslant 10$ kΩ as the criterion for a successful SET process, the events with such resistances in the Pt/5 nm Al_2O_3/Ti cell lie on a line with the slope of roughly 1 dec/0.075 V (Fig. 5.3 (a)). The corresponding slope for the Pt/3 nm Al_2O_3/3 nm TiO_2/Ti cell is approximated as 1 dec/0.05 V (see Fig. 5.3 (b)). These slope values describe the required voltage increment for a reduction of SET

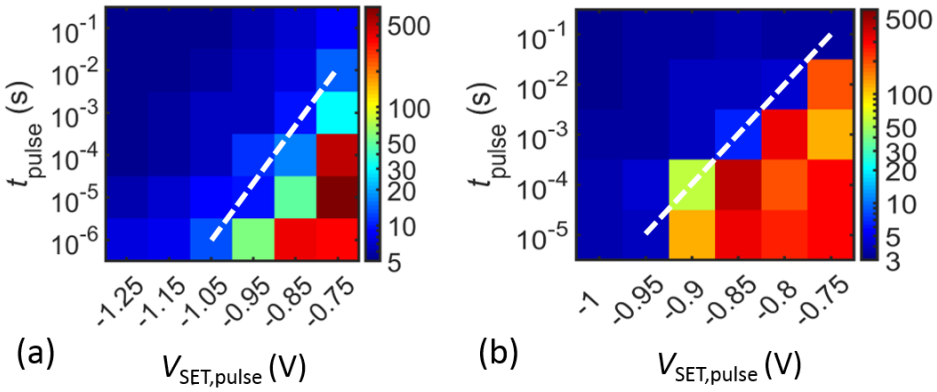

Figure 5.3: *Illustration of the read-out resistance against pulse length and SET pulse voltage in (a) one Pt/5 nm Al_2O_3/Ti cell with (80 nm)^2 cell size and (b) one Pt/3 nm Al_2O_3/3 nm TiO_2/Ti cell with (100 nm)^2 cell size. The white dash lines mark the boundary for the read-out resistance of ≈ 10 kΩ.*

pulse length by one decade and reveal quantitatively that the Pt/5 nm Al_2O_3/Ti cell requires a higher increment of $|V_{SET,pulse}|$ than the Pt/3 nm Al_2O_3/3 nm TiO_2/Ti device for the same acceleration of the SET event.

5.2.2 Transient pulse measurement

To further investigate the SET kinetics, the relation between SET time and the voltage amplitude of SET pulse should be discussed. Two Pt/5 nm Al_2O_3/Ti cells were tested and the results are plotted in Fig. 5.4. Regarding a considerable overlap between the data points from the two cells, to distinguish them, the plots are drawn in two graphs. The SET time expands from 20 ns to 0.1 s with voltage amplitude ranging from 1.1 V to 0.8 V. In addition, to compare the results between pulse/read mode and transient pulse mode, a black line being equal to the white dash line in Fig. 5.3 (a) is added to Fig. 5.4 (a), which marks the boundary between the successful SET and the failed SET events.

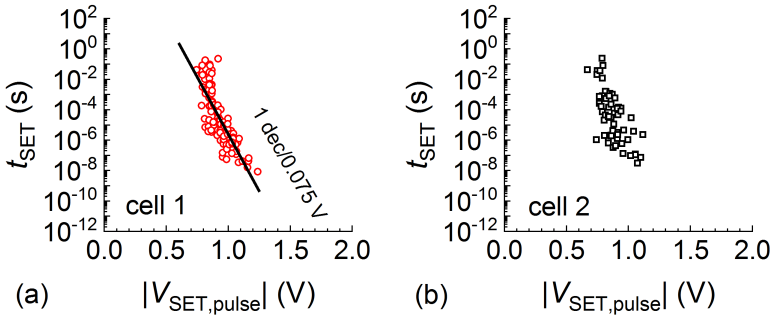

Figure 5.4: *(a) and (b) SET time as a function of the applied SET pulse amplitude in two (100 nm)² Pt/5 nm Al_2O_3/Ti cells. The black line in (a) with the estimated slope 1 dec/0.075 V is taken from Fig. 5.3 (a).*

Although the data for t_{SET} - $|V_{SET,pulse}|$ relation in Fig. 5.4 (a) can match the black line in a certain range, it has to be mentioned that the SET pulse length (t_{pulse}) and SET time (t_{SET}) are still different from each other and this limited correspondence can only indicate a qualitative consistent SET kinetics between different Pt/5 nm Al_2O_3/Ti cells. As revealed by simulation studies [39], the SET process in VCM cells is a field accelerated and Joule heating-assisted drift/diffusion process of oxygen vacancies. To exactly describe and undestand the non-linearity of the switching kinetics, an analytical method, namely ion hopping model that shows an s-shaped $\log(t_{SET})$ - $V_{SET,pulse}$ relation [229], prevails more over the straight line. Therefore, for a more exact interpretation of the SET kinetics, the ion hopping model is applied and the results are presented in the next section.

5.3 SET kinetic modelling

Before applying the ion hopping model to the experimental data shown in Fig. 5.4, some constant parameters used in the model can be firstly extracted from the non-SET pulses. Since the two Pt/5 nm Al_2O_3/Ti cells have the similar read-out resistance values for HRS under the same voltage pulse, to refine the resistance range, the read-out value of (500 ± 100) kΩ are chosen. The applied pulse voltages and the corresponding read-out current values, namely the cyan dots, reveal in good accordance with the black $I(V)$ curves from DC voltage sweep experiments (see Fig. 5.5). It has to be mentioned that the cyan dots with higher voltage amplitudes showing non-SET event, like -1 V in cell 1 (Fig. 5.5 (a)), always have a shorter pulse length, e.g. 10^{-6} s. On the contrary, the $I(V)$ curves from DC voltage sweep operated by a stepwise increment of 20 mV after a 10 ms delay time show a lower required SET voltage amplitude in second time scale (black curves in Fig. 5.5 (a)). The behavior corresponds with the non-linearity of the SET kinetics.

Assuming a diode-like character of the disc region and a serially connected resistance for the plug [230], the voltage (V_{disc}) applied on the disc region controls the current ($I_{\text{pre-SET}}$) before SET. To describe the current-voltage relation of the HRS and considering the possible contribution of the series resistance (R_{S}), the equation suggested by Ortiz-Conde [231] is applied:

$$I_{\text{pre-SET}} = I_0 \cdot \left[\exp\left(q \cdot \frac{V_{\text{SET,pulse}} - I_{\text{pre-SET}} \cdot R_{\text{S}}}{\eta k_{\text{B}} T_0} \right) - 1 \right], \tag{5.1}$$

where $V_{\text{disc}} = V_{\text{SET,pulse}}$ - $I_{\text{pre-SET}} \cdot R_{\text{S}}$, I_0 is the saturation current, η is the ideality factor, k_{B} the Boltzmann constant, q is the elementary charge, T_0 the temperature in the cell,

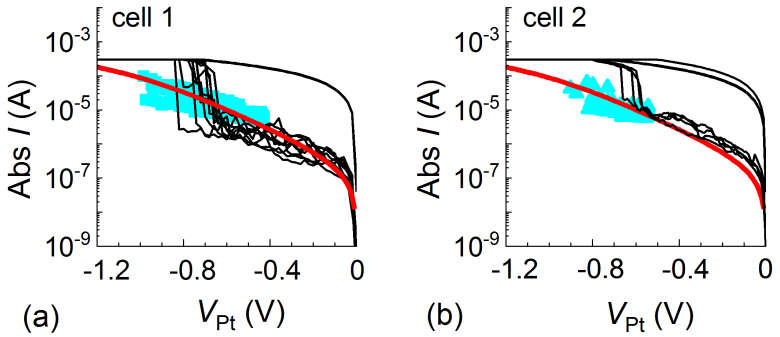

Figure 5.5: *$I(V)$ curves measured at different modes: black lines represent the DC voltage sweep cycles, cyan dots are the plots of read-out current as a function of applied SET pulses obtained from non-SET process. The red lines are fits. Curves in (a) and (b) were performed in two Pt/5 nm Al_2O_3/Ti cells with $(100\ \text{nm})^2$ cell size. The resistance range for cyan dots and the simulation parameters by MATLAB are listed in Tab. 5.1.*

which should be constant at about 300 K guaranteeing the absence of ionic mobility. As suggested by Sze, η close to unity indicates thermionic emission, while $\eta > 1$ hints on a tunneling process [109].

However, to solve such a transcendental equation (5.1), numerical solutions are given based on Lambert's function $W(x)$, which satisfies $W(x) \cdot \exp(W(x)) = x$ [232]. The calculation of this function is supplied by the commercial MATLAB® software (academic license from RWTH Aachen). The solution of the equation (5.1) is described as:

$$I_{\text{pre-SET}} = -I_0 + \frac{\eta k_B T_0}{q R_S} \cdot W\left(\frac{q I_0 R_S}{\eta k_B T_0} \cdot \exp\left(q \cdot \frac{V_{\text{SET,pulse}} + I_0 R_S}{\eta k_B T_0}\right)\right). \tag{5.2}$$

By applying $\eta = 6$, $I_0 = 0.2$ µA and $R_S = 1$ kΩ, the extended cyan dots for HRS in Fig. 5.5 can be fitted well with red lines. These three parameters obtained from fitting will be set as constant and be applied in the following ion hopping model.

In the ion hopping model, the SET process is described as the drift of oxygen vacancies through an oxygen depleted region under the voltage (V_{disc}) applied on this region. The drift velocity (v_{drift}) is described by the Mott-Gurney law:

$$\nu_{\text{drift}} = af \cdot \exp\left(-\frac{W_A}{k_B T_{\text{disc}}}\right) \cdot \sinh\left(\frac{2q \cdot a}{2k_B T_{\text{disc}}} \cdot \frac{V_{\text{disc}}}{l_{\text{disc}}}\right), \tag{5.3}$$

where a is the hopping distance, f is the ion hopping attempt frequency, W_A is ion hopping barrier for oxygen vacancies at zero field, $2q$ is the charge of the hopping ions and l_{disc} is the depletion region length. Since the $\sinh(x)$ can be expanded as $sinh(x) = \frac{\exp(x) - \exp(-x)}{2}$, the term "$\exp(x)$" describes the lowering effect of the hopping barrier along the direction of the electric field and the term "$\exp(-x)$" is dedicated to the barrier increase effect against the electrical field. In consequence, the term "$sinh(x)$" describes the resultant effect induced by the applied field.

Assuming a homogeneous and steady drift process of oxygen vacancies and the hopping barrier lowering effect is mainly considered across the disc region, the time needed for the SET process is described as [230]:

$$t_{\text{SET}} = \frac{l_{\text{disc}}}{\nu_{\text{drift}}} = \frac{l_{\text{disc}}}{af} \cdot \exp\left(\frac{W_A}{k_B T_{\text{disc}}}\right) \cdot \left[\sinh\left(\frac{2q \cdot a}{2k_B T_{\text{disc}}} \cdot \frac{V_{\text{disc}}}{l_{\text{disc}}}\right)\right]^{-1} \tag{5.4}$$

The local temperature T_{disc} is approximated as follows [233]:

$$T_{\text{disc}} = T_0 + R_{\text{th}} \cdot V_{\text{disc}} \cdot I_{\text{pre-SET}}, \tag{5.5}$$

where T_0 is the ambient temperature assumed as 300 K afore the SET process, R_{th} is the effective thermal resistance, which is dependent on both the thermal property and the geometry of the filament [39]. The term "$R_{\text{th}} \cdot V_{\text{SET,pulse}} \cdot I_{\text{pre-SET}}$" accounts for the temperature increase regarding the Joule heating [39].

Although the estimated R_S of 1 kΩ is much lower than the total resistance for HRS ($R_{read} \geqslant 100$ kΩ), the voltage drop on R_S was still taken into consideration. Combining equations (5.4), (5.5) and $V_{disc} = V_{SET,pulse}$ - $I_{pre\text{-}SET} \cdot R_S$, the SET time can be expressed as:

$$t_{SET} = \frac{l_{disc}}{af} \cdot \exp\left(\frac{W_A}{k_B\left(T_0 + R_{th} \cdot V_{SET,pulse} \cdot I_{pre\text{-}SET}\right)}\right) \cdot \left[\sinh\left(\frac{2q \cdot a}{2k_B\left(T_0 + R_{th} \cdot V_{SET,pulse} \cdot I_{pre\text{-}SET}\right)} \cdot \frac{V_{SET,pulse} - I_{pre\text{-}SET} \cdot R_S}{l_{disc}}\right)\right]^{-1}, \quad (5.6)$$

Beside the predefined values for I_0, R_S and η, several other constants and restrictions should be discussed as well. The hopping frequency in the range of 10^{12} Hz is assumed to be constant and takes the value of $6.67 \cdot 10^{12}$ Hz as suggested by other SET kinetic studies [230]. As suggested by Menzel [39], the a/l_{disc} ratio should be $\leqslant 1/5$, regarding the physically reasonable values of a and l_{disc}. The remaining parameters are obtained by applying equation (5.6) to simulate the t_{SET} - $|V_{SET,pulse}|$ relation. The best matching simulation result and the optimized parameter values are summarized in Fig. 5.6 and Tab. 5.1.

Although the simulation parameters are optimal for the matching to the experimental data, their validity in the sense of physics should be discussed as well. As W_A and R_{th} can strengtheningly influence the final form of simulated curves, the influence of each parameter will be discussed separately. The effect on the curve shift of changing these parameters can be found in [203] or in "Appendix B" in this work.

The simulated value W_A of 1.1 eV for both Pt/5 nm Al_2O_3/Ti cells is close to the acti-

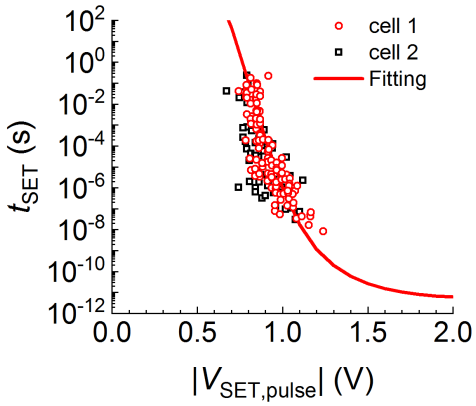

Figure 5.6: *SET time as a function of the applied SET pulse amplitude in two Pt/5 nm Al_2O_3/Ti cells from Fig. 5.5. The experimental data are depicted as dots and the model calculation as the red line. The resistance range for dots and the best simulation parameters are summarized in Tab. 5.1.*

Parameters	Values
R_{read} for HRS (kΩ)	400 - 600
R_{read} for LRS (kΩ)	$\leqslant 10$
R_{s} (kΩ)	1
I_0 (μA)	0.2
η (-)	6
W_A (eV)	1.1
R_{th} (K/W)	$6{\cdot}10^6$
f (Hz)	$6.67{\cdot}10^{12}$ [233]
T_0 (K)	300
l_{disc}/a	5

Table 5.1: *The resistance range for dots and the simulation parameters applied for the red line in Fig. 5.6.*

vation energy of $V_O^{\bullet\bullet}$ diffusion of 1.26 eV in the 2 nm Al_2O_3 film suggested by a simulation work [234].

For the effective thermal resistance R_{th}, the best suitable value is $6{\cdot}10^6$ K/W obtained from the simulation. As suggested by Russo et al. [235], for a homogeneous thermal conductive filament with two electrodes as thermal sinks, the effective thermal resistance can be described as:

$$R_{\mathrm{th}} = \frac{1}{8\kappa} \cdot \frac{l_{\mathrm{filament}}}{A_{\mathrm{filament}}}, \tag{5.7}$$

where l_{filament} is the length of the whole filament, which is equivalent to the oxide layer thickness, A_{filament} is the cross-sectional area of filament and κ is the thermal conductivity of the filament. For Pt/5 nm Al_2O_3/Ti cells, $l_{\mathrm{filament}} = 5$ nm, $R_{\mathrm{th}} = 6{\cdot}10^6$ K/W and A_{filament} is assumed to be 100 nm^2 regarding the high-resolution TEM result in chapter 6, κ is calculated to be 1.04 W/(K·m). This value is close to the reported value of 1.4 W/(K·m) for room temperature [236]. Generally, a higher R_{th} value can lead to an enhancement of the Joule heating effect and strengthen the temperature increase by a slight voltage increment. This contributes to a drastic change of the SET time.

5.4 RESET pulse variation

The RESET behavior of the cells was performed in a pulse/read mode (see Fig. 5.1 (b)). Details for the pulse train and conditions to initiate the RESET pulse are given in section 3.4.2.

Figures 5.7 (a) and (c) show the typical $I(V)$ characteristics for Pt/5 nm Al_2O_3/Ti and Pt/3 nm Al_2O_3/3 nm TiO_2/Ti cells, respectively. To minimize the probable voltage divider effect, $R_{\mathrm{pre,ON}}$ should be ≈ 10 kΩ. For the single-layer device the $R_{\mathrm{pre,ON}}$ value can be well defined as 10-17 kΩ, however, due to the abrupt SET process for the bilayer device, $R_{\mathrm{pre,ON}}$ value is always ranging from 3 to 12 kΩ.

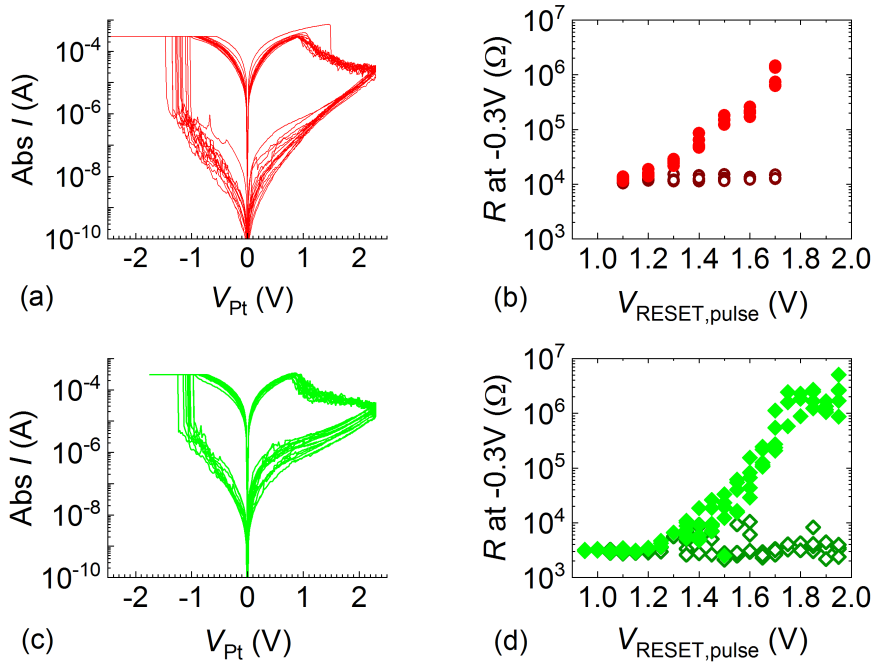

Figure 5.7: *Typical $I(V)$ curves obtained from $V_{+,max} = 2.3$ V and $|I_{CC}| = 300\,\mu A$ for (a) one Pt/5 nm Al_2O_3/Ti cell with (80 nm)^2 cell size and (c) one Pt/3 nm Al_2O_3/3 nm TiO_2/Ti cell with (100 nm)^2 cell size. (b) and (d) show the $V_{RESET,pulse}$ dependent R_{read} for HRS (solid dots) and LRS (open dots) in two (80 nm)^2 single-layer and bilayer cells, respectively. The RESET pulse length is kept as 1 µs.*

After reaching the defined $R_{\mathrm{pre,ON}}$ value the RESET pulse is applied. The read-out resistance values (R_{read}) are recorded after the RESET operation and are plotted as the function of RESET pulse voltage ($V_{\mathrm{RESET,pulse}}$) for a pulse length of 1 µs (see Fig. 5.7 (b,d)). The read-out resistance values before and after RESET pulse shows a higher statistical variance in the bilayer cell (Fig. 5.7 (d)) than in the single-layer cell (Fig. 5.7 (b)). To reset the cell to at least 100 kΩ, the RESET pulse should exceed 1.4 V for the single-layer cell and 1.6 V for the bilayer cell.

To give a better illustration, the "heat-graphs" are applied (see Fig. 5.8). Taking the resistance of 100 kΩ as a criterion for a successful RESET event (cyan box in Fig. 5.8 (a) and green box in Fig. 5.8 (b)), the white guide line separate the cells with and without the defined RESET event. The slope of around 1 dec/0.1 V for both Pt/5 nm Al_2O_3/Ti and Pt/3 nm Al_2O_3/3 nm TiO_2/Ti cells indicates a similar RESET non-linearity. However, the required $V_{\mathrm{RESET,pulse}}$ value to obtain the same read-out HRS value differs significantly. Taking 100 kΩ by a pulse length of 1 µs as one example, the $V_{\mathrm{RESET,pulse}}$ value should exceed 1.5 V for the single-layer cell compared to about 1.75 V for the bilayer cell.

As reported by Lentz, the line resistance of 5 Ti/15 nm Pt in (100 nm)^2 sized nano-

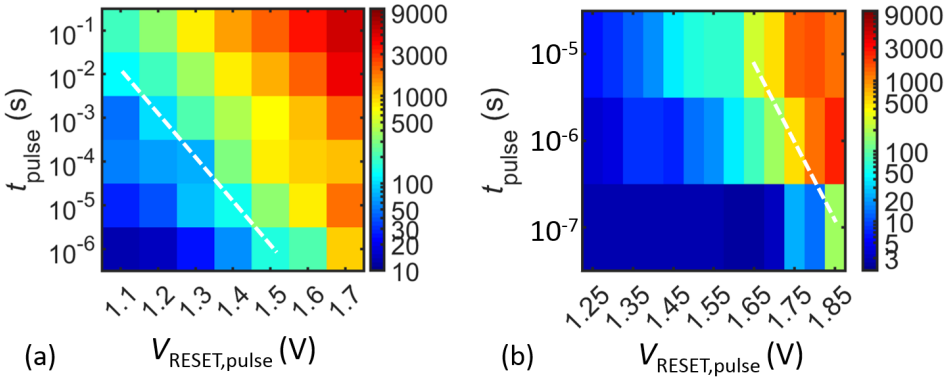

Figure 5.8: *Illustration of the read-out resistance against pulse length and RESET pulse voltage in (a) one Pt/5 nm Al_2O_3/Ti cell and in (b) one Pt/3 nm Al_2O_3/3 nm TiO_2/Ti cell with the same (80 nm)^2 cell size. The white dash lines mark the boundary for the read-out resistance of* $\approx$ *100 k*Ω.

structure is around 1.3 kΩ measured at room temperature [197]. Therefore, it is reasonable to considered the series resistance R_S to be within the range of 1.3 kΩ. For an abrupt and successful SET event in the bilayer cells, the LRS can reduce to $\approx$ 2 kΩ that is closed to the series resistance. This leads to a non-negligible partial voltages due to the series resistance R_S. The applied voltage ($V_{\mathrm{RESET,pulse}}$) should be divided into two parts: the voltage ($V_{\mathrm{RESET,cell}}$) across the switching oxide layer and the voltage on the series resistance. This voltage divider-effect can cause a larger required $V_{\mathrm{RESET,pulse}}$ in the bilayer cell.

To further support the voltage divider-effect, here, a Pt/5 nm Al_2O_3/Ti cell is taken as one example, whose RESET transient current behavior was obtained from $R_{\mathrm{pre,ON}}$ of about 2 kΩ. Fig. 5.9 (a) shows that for the same $V_{\mathrm{RESET,pulse}}$ value the applied RESET pulse length (t_{pulse}) can approach the required RESET time (t_{RESET}). The read-out resistance values support the determination of the approached value. Plotting the t_{RESET} (black square) as a function of applied $V_{\mathrm{RESET,pulse}}$ in Fig. 5.9 (b), the linear fit gives a slope of 1 dec/0.16 V. Comparing the RESET behavior from cells with $R_{\mathrm{pre,ON}}$ of $\approx$ 2 kΩ (cyan dash line) and $\geqslant$10 kΩ (black dash line), a clear shift to higher voltage amplitudes accompanying with a difference in the slope can be seen in this plot.

An interpretation of the RESET behavior can be more meaningful, if a complete simulation of the actual cell can be applied with proper identification of different elements. However, for a analytical method, starting the RESET study from a higher resistance state, like for example 10 kΩ for the nano-crossbar cells in this work, can help to make the voltage divider effect marginal.

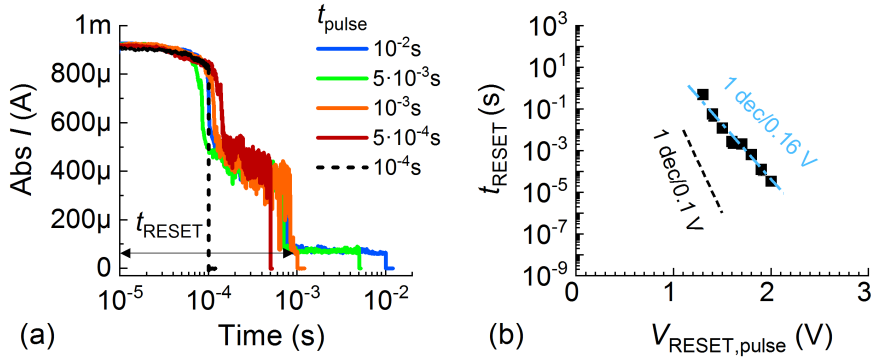

Figure 5.9: *(a) The transient current response with the applied $V_{RESET,pulse}$ of 1.8 V in one (100 nm)^2 Pt/5 nm Al_2O_3/Ti cell with $R_{pre,ON} \approx 2$ kΩ for LRS. The tested pulse lengths were listed as legend. (b) The plot of t_{RESET} against $V_{RESET,pulse}$ for two Pt/5 nm Al_2O_3/Ti cells. The black dash line is taken from cell with $R_{pre,ON}$ = 10-17 kΩ. The cyan dash line is the slope of the black square obtained from cells with $R_{pre,ON}$ of around 2 kΩ.*

5.5 Summary and discussion

In this chapter the SET and RESET kinetics are compared in two different stacks, namely the single-layer Pt/5 nm Al_2O_3/Ti and the bilayer Pt/3 nm Al_2O_3/3 nm TiO_2/Ti stacks. A direct overview of the SET and RESET behavior in pulse mode was performed by the pulse/read measurements expressed as "heat-graphs" in Fig. 5.3 and Fig. 5.8, respectively. A more abrupt SET event was observed in the bilayer cell and comparable RESET events in both single-layer and bilayer cells. Comparing the SET and RESET events, the non-linearity of kinetics in both single-layer (1 dec/0.075 V vs. 1 dec/0.1 V) and bilayer cells (1 dec/0.05 V vs. 1 dec/0.1 V) are slightly asymmetric.

A deeper understanding of the SET kinetics for Pt/5 nm Al_2O_3/Ti cells is obtained through a detailed analysis via transient pulse measurement. The ion hopping model based on Mott-Gurney law for ionic drift of oxygen vacancies is applied to explain the correlation between $\log(t_{\mathrm{SET}})$ and $|V_{\mathrm{SET,pulse}}|$. Physically meaningful parameters fit the experimental data well. As the characteristic material parameters, both the ion hopping barrier (W_{A}) of oxygen vacancies of 1.1 eV and the thermal conductivity (κ) of 1.04 W/(K·m) are in a range suggested by the literature. Other geometrical parameters like the disc length (l_{disc}) of around 1.5 nm and filament area (A_{filament}) assumed as 100 nm^2 are supported by the tunneling fitting and high-resolution TEM in the next two chapters. Moreover, the read-out $I(V)$ relation for HRS can also influence the kinetics through the energy dissipation.

Under the frame of the ion hopping model, the involved parameters related to the switching material, cell structure and electrical behavior could give a hint for device engineering:

1. Obtained either from experimental studies or from simulations, material related parameters, like W_{A} and κ can influence SET kinetics and thus could impact the choice of oxide material for a ReRAM cell. According to the literature, κ of TiO_2 and Al_2O_3 films is reported as 7.5 W/(K·m) [237] and 1.5-3 W/(K·m) [236], respectively. Concerning the cells with similar filamentary geometry and showing similar $I(V)$ characteristics, this difference of κ can lead to a larger R_{th} value in Al_2O_3 single-layer cells than in the cells comprising Al_2O_3 and TiO_2. The impact of R_{th} on the non-linearity of SET kinetics is listed in "Appendix B (a)". Similarly, W_{A} can supply the positive impact on the non-linearity of SET kinetic, i.e. the higher W_{A} leads to a higher non-linearity of SET kinetic.

2. The device structure could partially restrict the filament geometry, like $A_{\mathrm{filament}} < A_{\mathrm{cell}}$ and the filament length ($l_{\mathrm{filament}} = l_{\mathrm{disc}} + l_{\mathrm{plug}}$) that limits the disc region. In addition, the effective thermal resistance R_{th} is determined by A_{filament}, l_{filament} and κ, which strongly influences the ion hopping process through T_{disc}.

3. The device structure and behavior could also partially restrict the power input during the SET process, which has significant influence on the non-linearity of SET kinetic. Therefore, a good description of the relation between the response current $I_{\text{pre-SET}}$ and applied voltage $V_{\mathrm{SET,pulse}}$ is simulated through optimization of series resistance (R_{S}) from filament plug and interconnects, saturation current (I_0) and ideality factor (η).

Chapter 6

Nanostructural analysis of a switched nano-crossbar cell

Nanostructural analysis of a ReRAM device is of the utmost importance. First of all, as revealed by many studies, the switching mechanism can be identified by the high-resolution transmission electron microscopy (HRTEM). Take TiO_2-based devices as one example, a filament found in such a switched cell should be related to the filamentary type switching mechanism [136]. Second, the geometry of the switching area can help verifying the filament area [238]. In addition, direct structural informations can be used to check the reasonability of electronic transport analysis and switching models. Moreover, the chemical information from the energy-dispersive X-ray spectroscopy (EDX) can contribute to further refine the proposed microscopic models. In this chapter a systematic study on a switched 30 nm Pt (BE)/3 nm Al_2O_3/3 nm TiO_2/10 nm Ti (TE)/20 nm Pt (capping) ReRAM cell with a $(100\,\text{nm})^2$ cross-point area is analyzed by HRTEM. The TEM sample was prepared by means of focused ion beam (FIB) cutting parallel to the direction of the top electrode. The preparation and TEM analysis were done by S. Yoo from Seoul National University in a project collaboration. The fabrication details are comparable to the description in [239].

A typical nano-crossbar structure shows a well-defined lateral metal interconnect (Fig. 6.1 (a)). As the vertical cut for the cross-section is illustrated by a black dash window in Fig. 6.1 (b), the investigated area via TEM method is circled by the red dash line as shown in Fig. 6.1 (c). The Pt capping layer and Pt bottom electrode appear dark, while Al_2O_3, TiO_2 oxide layers and Ti top electrode appear bright. For clarity a 3D drawing picture in Fig. 6.1 (d) describes the stack order from Fig. 6.1 (c).

Prior to the TEM analysis the Pt/3 nm Al_2O_3/3 nm TiO_2/Ti/Pt cell was electroformed and switched at room temperature for several c8w cycles with $V_{+,\text{max}} = 2.35$ V and $|I_{CC}| = 200$ µA. To evaluate a possibility of intermixing of Al_2O_3 and TiO_2 layers during the c8w BRS cycles, a chemical analysis across the cross-section in a vertical

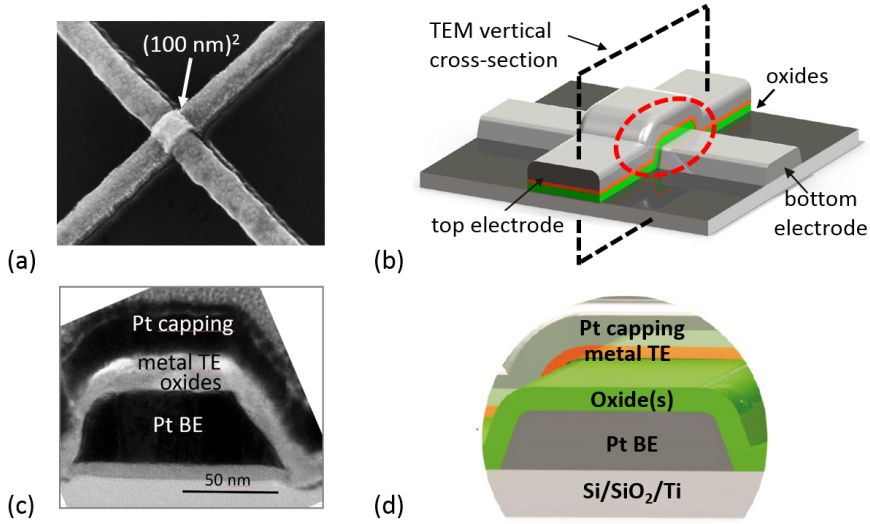

Figure 6.1: *(a) Top view of a (100 nm)² cross-point ReRAM cell obtained by SEM and its (b) 3D illustration image with vertically cutting window marked as black dash line. The vertical cross-sectional structure marked as red dash line is illustrated by both (c) a TEM image of the BE/oxide(s)/TE/Pt (capping) layer stack and (d) a sectional 3D drawing picture. Image in (b,d) are redrawn from [115].*

direction was performed and the result is shown in Fig. 6.2.

From the overview scan of its zoomed region, a large amorphous matrix of TiO_2 and Al_2O_3 sandwiched between two metal electrodes can be seen (Fig. 6.2 (a)). The white guild lines mark the interface between different layers. In addition, an energy dispersive X-ray spectroscopy (EDX) line performed in scanning TEM mode scans perpendicularly to the layer stack. This nano-chemical analysis with EDX line profiles (colored signals in Fig. 6.2 (b)) shows the averaged distribution signal from the four different elements, namely O, Ti, Al and Pt. A clear drop of Al signal and a clear increase of Ti signal by around 3 nm from Pt electrode confirm that the bilayer structure retained after switching.

Fig. 6.3 shows the edge region of the same cell in TEM and HRTEM, respectively. The bright part reveals a dominating amorphous layer of roughly 6 nm thickness and a crystalline layer of about 10 nm on top, which are identified as the metal oxide bilayer (3 nm Al_2O_3 and 3 nm TiO_2) and the Ti top electrode, respectively. A careful investigation of the full cross-section was performed tilting HRTEM pictures every 25 nm along the full cross-section region. Among the amorphous matrix of the Al_2O_3 and TiO_2 layers only one small region close to the edge of the cross-point structure reveals a crystalline structure with around 10 nm width as shown in Fig. 6.3 (b). Regarding the local Joule heating [39], the large amorphous matrix can be considered as the non-switched region that sustains the pristine state, while the crystallized structure should be the filament

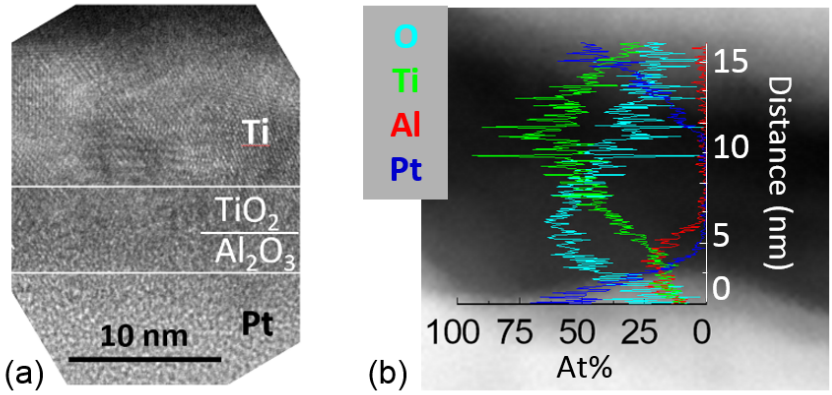

Figure 6.2: *Nano-chemical analysis for the cross-section in a switched 30 nm Pt (BE)/3 nm Al_2O_3/3 nm TiO_2/10 nm Ti (TE)/20 nm Pt (capping) device: (a) an overview TEM scan and (b) the corresponding element distributions vertical to the two electrodes from EDX line profiles. The element distribution profiles are O (cyan), Ti (green), Al (red) and Pt (blue). The vertical axis is the distance from the Pt/Al_2O_3 interface in the unit of nanometer, while the horizontal axis is the normalized atomic fraction of each species in the unit of At%, meaning atom percentage.*

involved in the switching process. This result is in good agreement with the VCM-type filamentary model of the switching process. Therefore, it is reasonable to assume that the current flux is mainly through the switching area of the filament (A_{filament}), which can be roughly estimated as 100 nm^2 based on the width of crystallized region of $\approx$ 10 nm.

Through further zooming in the crystalline region (Fig. 6.3 (c)) and a careful investigation of the lattice planes with fast Fourier transform (FFT) analysis, a clear rutile pattern in the upper marked TiO_2 region can be recognized (Fig. 6.3 (d)). The lower marked crystalline region shows a cubic structure with a lattice parameter of 0.193 nm (Fig. 6.3 (c)), which hints towards γ-Al_2O_3. However, the FFT in this region (not shown here) could not suggest a concrete conclusion about the crystal phase of Al_2O_3.

In summary, the nano-structure of a Pt/3 nm Al_2O_3/3 nm TiO_2/Ti/Pt device reveals a crystalline filament region surrounded by the amorphous matrix. The cross-section TEM image at the cross-point reveals homogeneous thicknesses for metal electrodes and metal oxide layers. The nano-chemical analysis for the lateral structure (Fig. 6.2) and the atomic structure related to the switching event (Fig. 6.3) are summarized to supply a detailed structural analysis for a switched bilayer cell. The element distribution profiles exclude the intermixing between Al_2O_3 and TiO_2 layers regarding the resolution limit of EDX analysis. In addition, a nano-scaled filament containing crystalline Al_2O_3 and TiO_2 with a diameter of around 10 nm is observed after c8w switching, which verifies the filamentary-type switching mechanism for c8w BRS and supplies a concrete filament area

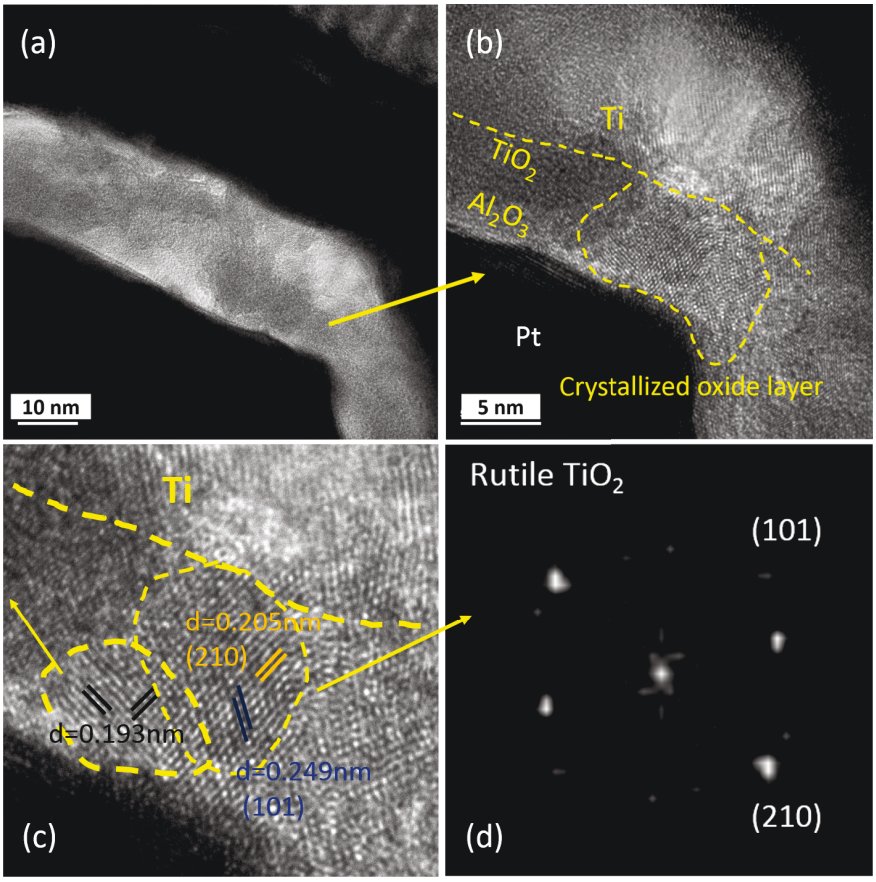

Figure 6.3: *The TEM analysis of the filament region in an active switched Pt/3 nm Al_2O_3/3 nm TiO_2/Ti/Pt ReRAM cell: (a) overview of the cross-section with the active region for resistive switching, (b) region with the crystallized filament, (c) high-resolution TEM of the two marked crystallized regions with atomic resolution, (d) the fast Fourier transform (FFT) of the upper selected region in (c), which shows a rutile structure.*

of 100 nm^2 for the estimation of thermal resistance for ion hopping model in chapter 5 and a further modelling of electronic transport in the following two chapters. The existence of two crystalline phases indicates the appearance of the high temperature during the switching event, which serves as a proof for significant Joule heating during c8w BRS cycles.

Chapter 7

Electronic transport in counter-eightwise BRS states

Electronic transport properties of VCM-type ReRAM devices strongly affect the switching characteristics due to the non-linearity of the current-voltage behavior and the corresponding local heating of the filament. In the nano-crossbar cells of this study, the total current through the devices is controlled by the electronic contribution. The ionic motion is detected as a change of the conduction paths or space charge configuration rather than being measurable as a significant contribution to the net current. Therefore, this chapter focuses on the characterization and description of the electronic transport in the $(100\,\mathrm{nm})^2$ Pt/oxide(s)/Ti crossbar devices for the different resistance states.

For the analysis of the initial state in single-layer and bilayer stacks comprised of TiO_2 and Al_2O_3 with evaporated Ti electrode, the impact of the Ti oxygen exchange layer (OEL) on different oxide layer thicknesses (see 7.1.1 and 7.1.2) and on different oxide orders (sections 7.1.3 and 7.1.4) are investigated. The study for the initial state includes the field and temperature dependent analysis and discussions on tunneling phenomena by using Simmons' tunneling model.

The $I(V)$ characteristics of c8w BRS behavior has been studied in chapter 4 through a statistical approach for single-layer and bilayer stacks. The high resistance state (HRS) showing a significant dependence of RESET stop voltage ($V_{+,\mathrm{max}}$) is analyzed in the same way as for the initial state. Especially, the interpretation of the HRS based on Simmons' tunneling model is described in section 7.2.

The linearity of current-voltage relation of the low resistance state (LRS) indicates a metallic conductive character of the devices with Ti electrode. This metallic-like state is characterized by the temperature coefficient of resistance in section 7.3.

Finally, section 7.4 discusses and concludes the aforementioned points for the different resistance switches between initial, HRS and LRS during c8w BRS.

7.1 Conduction behavior in the initial state

Based on the characteristics of the initial state for TiO_2 and Al_2O_3 single-layers in chapter 4, the following assumptions are made and applied in this section:

- as-grown Al_2O_3 films are insulators with high band-gap of ≈ 6.5-8.8 eV.
- as-grown TiO_2 films are described as n-type semiconductor with band-gap of ≈ 3.2 eV and oxygen vacancies as shallow donors.
- interface charges as well as space charges are not negligible.

Four different stacks are discussed for their initial states, namely 4.8 nm Al_2O_3 (abbreviated as 5AO), 2.3 nm Al_2O_3 (abbreviated to 2AO), 3 nm Al_2O_3/3 nm TiO_2 (3AO/3TO) and 3 nm TiO_2/3 nm Al_2O_3 (3TO/3AO) sandwiched between Pt bottom electrode and Ti top electrode.

7.1.1 Initial current in the Pt/4.8 nm Al_2O_3/Ti device

Regarding the high band-gap, Al_2O_3 is always applied as tunneling barrier and the main current contribution in Al_2O_3-based cells is considered and proofed as tunneling in many papers [6, 154]. Therefore, an analytical method, the Simmons' tunneling model with a trapezoidal barrier [106], is first used to describe the electronic transport of the highly insulating initial state in Pt/4.8 nm Al_2O_3/Ti devices (Pt/5AO/Ti for short).

To interpret this state, a band diagram with reported material values is suggested. The barrier at the Pt/Al_2O_3 interface can be calculated by the difference between the work function of Pt and electron affinity of Al_2O_3 as Φ_2 = 5.65 eV - 2.58 eV = 3.07 eV [147,240]. Similarly, the barrier for the Al_2O_3/Ti interface is Φ_1 = 4.33 eV - 2.58 eV = 1.75 eV [241]. The band diagram derived from these values is shown in Fig. 7.1 (a). Besides, the electron effective mass m^* is assumed as $0.23 \cdot m_0$ in the Al_2O_3 film (see Tab. 2.2 in chapter 2). For the highly insulating initial state of Pt/5AO/Ti single-layer cells, the current flux is assumed to be homogeneously flowing through the nano-crossbar cell with cross-point area. Therefore, the tunneling area A is assumed as 10^4 nm^2. By applying the Simmons' equation with these parameters and by calibrating the layer thickness around 5 nm, the tunneling current can be calculated and the best fitting curve is illustrated in Fig. 7.1 (b).

The initial current before electroforming in the Pt/5AO/Ti cell can be fitted well in the voltage range from -1.7 V to -2.3 V (Fig. 7.1 (b)). Above -1.7 V the current signal is just noise caused by the limitation of the measurement setup. Below -2.4 V the amplitude of current response starts to increase abruptly, which indicates a change of the local structure due to ion movement and the beginning of the electroforming process. From the

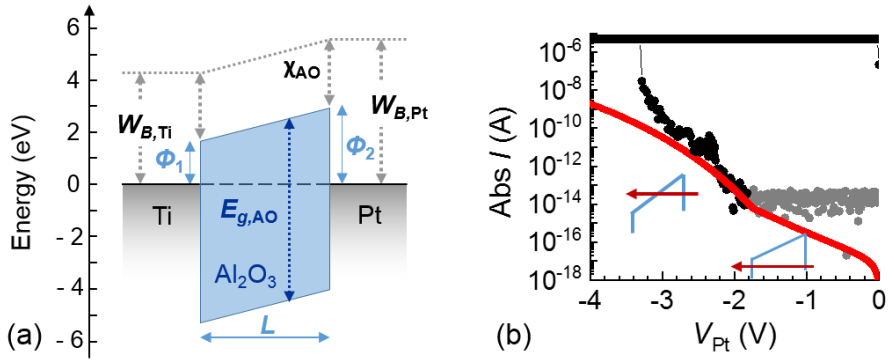

Figure 7.1: *(a) The description of simulation parameters in a band diagram for $Pt/Al_2O_3/Ti$ stack. (b) The best simulation result (red line) for the $I(V)$ characteristics (black dots) in a Pt/4.8 nm Al_2O_3/Ti cell from the initial state to the electroformed state. The data plotted in grey is limited by the equipment resolution. The calculated parameters applied in the red line are $\Phi_1 = 1.75$ eV, $\Phi_2 = 3.07$ eV, $m^* = 0.23 \cdot m_0$, tunneling current area $A = (100\ nm)^2$, tunneling length $L = 4.5$ nm.*

calculation result, the tunneling length of 4.5 nm is slightly smaller than the XRR fitting thickness of 4.8 nm. The difference of about 0.3 nm could be attributed to experimental uncertainty caused by surface and interface roughness effects for example. In addition, due to Φ_1 of 1.75 eV, the clear bend on the red line gives a hint that at around -1.9 V the electronic transport should turn from direct tunneling to Fowler-Nordheim tunneling, as the insets show in Fig. 7.1 (b). Additionally, as the current flux area A is equal to the cross-point area of $(100\ nm)^2$, the whole cell should be involved in the tunneling process. Therefore, the high insulating nature of the initial state in the 5AO cell supports the first assumption at the beginning of this section.

7.1.2 Initial current in the Pt/2.3 nm Al_2O_3/Ti device

In contrast to the Pt/5AO/Ti device, applying the same theoretical barrier heights and XRR fitting Al_2O_3 thickness of 2.3 nm for the Pt/2AO/Ti device results in no suitable calculated tunneling current that fits the experimental data (see the light green curve in Fig. 7.2 (a)). Since the calculated current is 10^3 times lower than the measured initial current (black dots), the electronic transport for this state should not originate from tunneling through a homogeneous, highly insulating 2.3 nm Al_2O_3 film.

However, the best simulation result is shown as pink line in Fig. 7.2 (b) with lower tunneling barrier heights (Φ_2 and Φ_1), a smaller tunneling area of 100 nm^2 and a significant reduced tunneling length $L \leqslant 1.4$ nm. Regarding the good overlap between $I(V)$ curves of the initial state and the c8w HRS during BRS cycling, it implies that some filaments might already exist in the oxide layer even in its pristine state. In this case, the

effective tunneling area A in equation (2.1) in chapter 2 corresponds to the "disc" area, while itself is defined by the spot size of the conductive filament "plug". A 3D image depicted for initial state is drawn in Fig. 7.2 (c). This indicates the 10 nm Ti OEL effect on the thin 2.3 nm Al_2O_3 layer. Another support is the tunneling area value, which is staying compatible with both the HRTEM result from this work and other studies [94]. A filament area (A_{filament}) of $\approx 100\ \text{nm}^2$ is observed in a $(100\ \text{nm})^2$ Pt/3AO/3TO/Ti cell (see section 7.2.3). As a direct determination of the disc diameter with structural analysis is not accessible for each electrically tested cells, a reasonable value of tunneling current area A can be assumed based on the HRTEM for other $(100\ \text{nm})^2$ crossbar cells and verified through the optimization of the fitting results. Other typical values reported for the filament's spot size in VCM-type switching devices range from 10 nm^2 to 500 nm^2 [136, 242, 243]. Recently, Du et al. [238] reported a very careful study on the nature of conductive filaments in Nb:$SrTiO_3$/Fe:$SrTiO_3$/(Au)Pt epitaxial devices. The authors identified a multi-filamentary switching process with the maximal filament

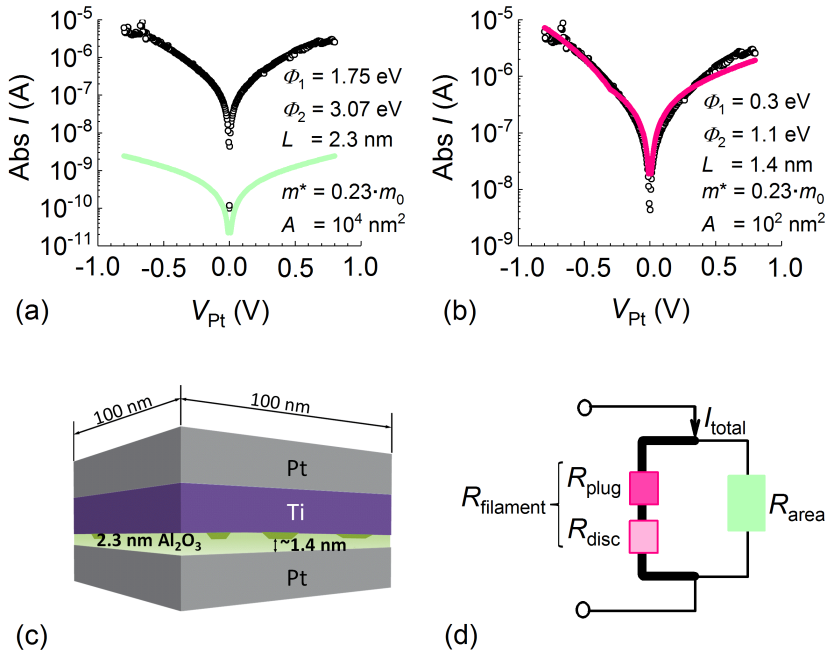

Figure 7.2: *(a) Experimental $I(V)$ characteristic for the initial state measured at 60°C (black dots) in a $(100\ \text{nm})^2$ Pt/2.3 nm Al_2O_3/Ti cell. The light green curve is the calculation result based on the theoretical value applied in Fig. 7.1. (b) The best simulation result (pink line). The corresponding simulation parameters are listed in the lower-right corner of each graph. (c) Proposed initial state based on the best calculation parameters for this cell. (d) Suggested equivalent circuit with proposed existed conduction filament with a tunneling area of 100 nm^2.*

diameter around 10 nm at the front of a conical filament.

Based on the results from Fig. 7.2 (a-c), an equivalent circuit is suggested for initial state in Pt/2AO/Ti cell (see Fig. 7.2 (d)): a parallel connection of resistors representing the conductive filament region (R_{filament}) and the surrounding non-conductive region (R_{area}). In the conductive region the structure of the filament can be divided further into two serial resistance contributions: a highly conductive part ("plug") and a current restricting part ("disc") that forms a tunneling barrier with a length of about 1.4 nm. The current contribution from the surrounding area and the filament region correspond to the green curve in Fig. 7.2 (a) and pink curve in Fig. 7.2 (c), respectively. As the current contribution from the surrounding area plays a minor role in the absolute value, the sum of the green and pink curve will not lead to a strong deviation from the pink curve and the current transport should be mainly through the filament.

To check the validity of the tunneling model, the $I(V)$ behavior of initial state was investigated for different temperatures (Fig. 7.3 (a)). By setting the substrate temperature from 30°C to 160°C, the consecutive $I(V)$ curves were measured at each predefined temperature. The $I(V)$ characteristics of the initial state show an almost negligible tem-

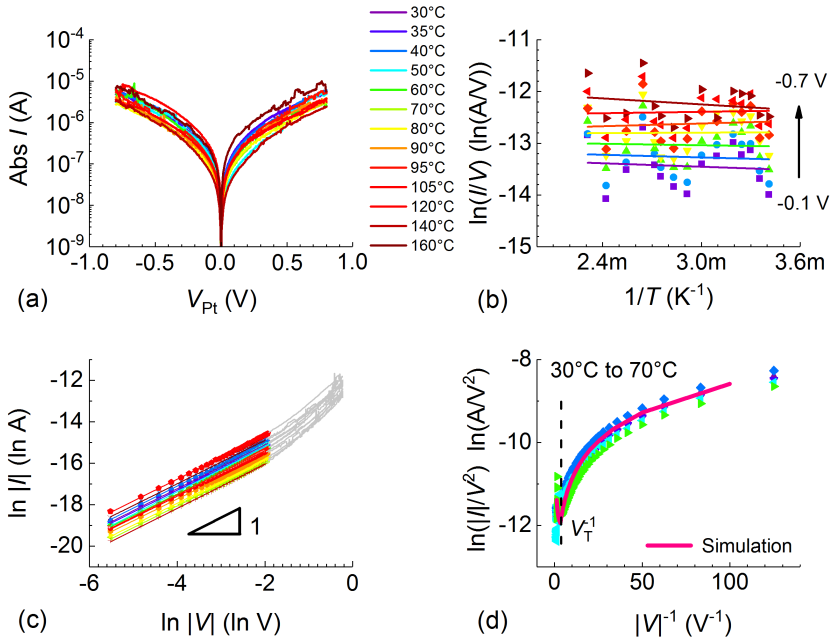

Figure 7.3: *(a) The $I(V)$ characteristics of initial state in a Pt/2AO/Ti cell measured at different temperatures. The data from (a) plotted in the form of (b) $ln(I/V)$ vs. $1/T$ and (c) $ln|I|$ vs. $ln|V|$ for the negative voltage branch with the temperature ranging from 30°C to 160°C. (d) The plots of $ln(|I|/V^2)$ vs. $|V|^{-1}$ for the negative branch from (a) as dots and from the simulation result from Fig. 7.2 (b) as the pink line.*

perature dependence based on the data analysis in Fig. 7.3 (b). This weak temperature dependence is reproducible in 7 of 9 tested cells. From the plot of $\ln|I|$ vs. $\ln|V|$ for low voltage amplitudes (Fig. 7.3 (c)), a good linearity and overlap of the curves are observed. The slope of 1 supports the assumption of direct tunneling transport. Fig. 7.3 (d) further supports a high tunneling possibility with the characteristic plot of $\ln(|I|/V^2)$ vs. $|V|^{-1}$. The measured data (colored dots) and the simulated pink line show the characteristic minimum, the so-called reciprocal value of transition voltage (V_T), which describes a superposition of temperature assisted tunneling (or direct tunneling) dominating at the low voltage amplitudes and field-assisted tunneling (or Fowler-Nordheim tunneling) showing up for the higher voltage amplitudes.

In this subsection, the temperature related $I(V)$ characteristics for the initial state in Pt/2.3 nm Al_2O_3/Ti and Pt/4.8 nm Al_2O_3/Ti devices are studied. For cells with a thinner Al_2O_3 film, the initial state shows higher current level than the calculated tunneling current for 2.3 nm insulating film. Regarding the 10 nm thick Ti OEL effect and the probably existing filament based on the tunneling simulation results, the oxygen vacancies introduced in the thinner Al_2O_3 layer can be reasonably proposed and the conductive paths of 1.4 nm length in maximum can consequently form in the initial state as well. In contrast, the OEL effect in the thicker 4.8 nm Al_2O_3 layer shows just up in a slightly lowered tunneling barrier length of 4.5 nm.

7.1.3 Initial current in the Pt/3 nm Al_2O_3/3 nm TiO_2/Ti device

The $I(V,T)$ characterization of the initial state is also performed in several bilayer cells and the experimental results of one typical cell are summarized in Fig. 7.4. Different from the single-layer devices, the $I(V)$ curves in the Pt/3 nm Al_2O_3/3 nm TiO_2/Ti bilayer cell show a significant temperature dependence.

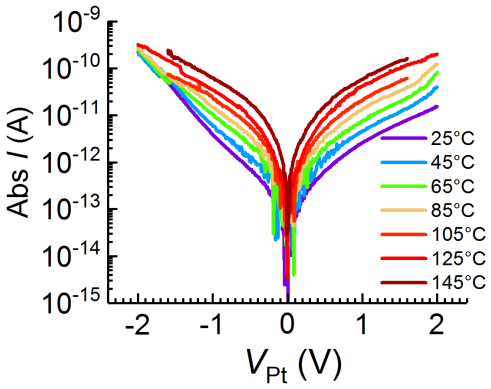

Figure 7.4: *The temperature dependent $I(V)$ characteristics of the initial state in a Pt/3AO/3TO/Ti cell.*

In the same way, the Pt/Al_2O_3 barrier height Φ_2 in this bilayer cell is postulated as 3.07 eV. According to the assumptions in section 7.1, the Pt/3AO/3TO can be treated as a metal/insulator/semiconductor junction. Due to a tiny difference between the work function of Ti (4.33 eV) and the electron affinity of TiO_2 (4.2-4.8 eV) [130, 244, 245], the contact between TiO_{2-y} layer and the Ti electrode is considered as an ohmic contact, where "2-y" represents the sub-stoichiometric titanium dioxide caused by the Ti OEL effect. As a starting approach, the possible space charge region formed between Al_2O_3 and TiO_2 layers will firstly not be taken into account, but will be discussed later. As a result, the barrier height between the Al_2O_3 and the TiO_2 layer can be assumed as around 1.75 eV. Due to the highly insulating nature of the initial state in this bilayer cell, the current transport is considered homogeneous across the cross-section area of the cell, i.e. $A = A_{cell}$ of 10^4 nm^2.

By applying $m^* = 0.23{\cdot}m_0$, tunneling area $A = (100\text{ nm})^2$, $\Phi_2 = 3.07$ eV, $\Phi_1 = 1.75$ eV in Simmons' tunneling equation and adjusting the tunneling length, the calculated current-voltage curve (open dots) can fit each experimental $I(V)$ curve measured at a defined temperature quite well (see Fig. 7.5). The increased current levels by increasing the substrate temperature from 45°C to 145°C can be well explained with a reduction of the tunneling length (L) from 3.2 nm to 2.85 nm, respectively.

Regarding the XRR fitted Al_2O_3 layer thickness of 2.7 nm in the bilayer cells, the smallest values of the calculated barrier length of 2.85 nm and 2.93 nm show a small

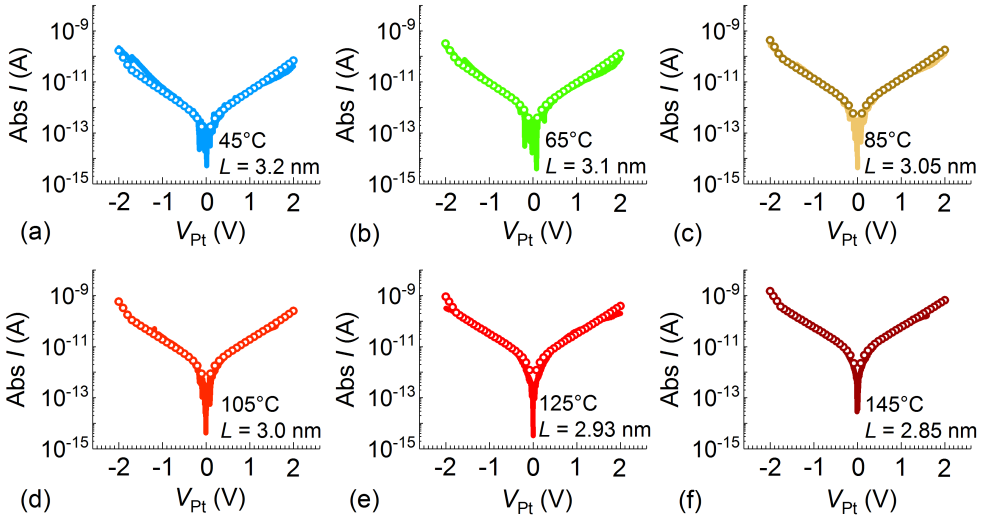

Figure 7.5: *(a) to (f) The best calculation result (dots) on the $I(V)$ characteristics (colored lines) of the initial state in a Pt/3AO/3TO/Ti cell measured from 45°C to 145°C. Some parameters are kept constant: $\Phi_1 = 1.75$ eV, $\Phi_2 = 3.07$ eV, $m^* = 0.23{\cdot}m_0$, tunneling area $A = (100\text{ nm})^2$. The substrate temperature and the optimized tunneling length are listed in the lower-right corner of each graph.*

deviation, which is still in the range of the film's and substrate's roughness of around 0.3 nm (for details see Tab. 3.1). However, $L \geqslant 3.0$ nm is out of the deviation range. The larger tunneling lengths observed for the low temperature range can only originate from a very thin layer of TiO_2 involved in the tunneling process. As suggested by the continuum model described in chapter 8 section 8.2.2, the interfacial TiO_2 close to Al_2O_3/TiO_2 interface can form a space charge region or a depletion region, which enables the thermally activated electrons to contribute to the total tunneling current. This proposal is depicted in Fig. 7.6 (b). The band bending in the space charge region of TiO_{2-y} layer increases the contribution of thermally activated electrons to total tunneling current, which leads to a slightly temperature dependent tunneling length. The details of the tunneling through the Schottky barrier is reported in [107].

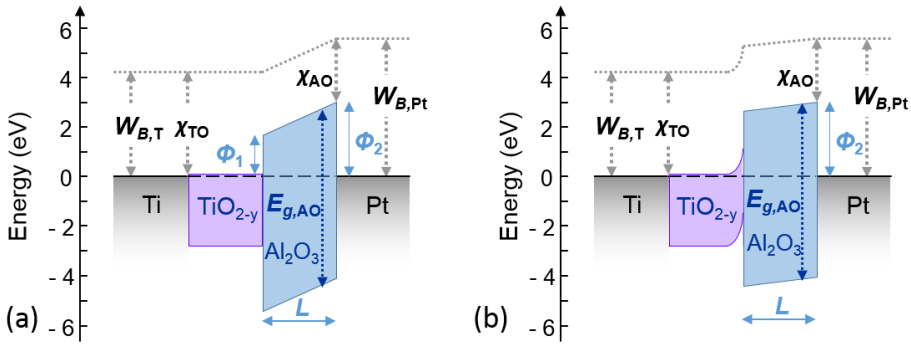

Figure 7.6: *The suggested band diagram for initial state in the Pt/3AO/3TO/Ti cell based on (a) the Simmons' tunneling model with trapezoidal barrier and (b) Schottky tunneling through an extra TiO_2 depletion region and insulating Al_2O_3 layer.*

Other electronic transport possibilities like Poole-Frenkel emission, ohmic conduction and hopping conduction were also discussed. Some analytical results are listed in "Appendix A". However, the low barrier heights obtained from these transport mechanisms are not compatible with the low current level of the highly insulating initial state in the Pt/3AO/3TO/Ti device.

7.1.4 Initial current in the Pt/3 nm TiO_2/3 nm Al_2O_3/Ti device

A similar temperature dependence of the $I(V)$ characteristics of the initial state is also observed in one typical Pt/3 nm TiO_2/3 nm Al_2O_3/Ti device as well (see Fig. 7.7 (a)).

For this "reverse stack", three different interfaces should be taken into consideration: (1) the possible Schottky barrier at the Pt/TiO_2 interface, the theoretical interface barrier should be 5.65 eV - 4.3 eV = 1.25 eV. (2) The TiO_2/Al_2O_3 interface. The difference between the two electron affinities is 4.2 eV - 2.58 eV = 1.62 eV. (3) The barrier at

Al_2O_3/Ti interface, which show the theoretical value of 1.75 eV. Although the character of pure TiO_2 in this reverse stack is not clear, regarding the similar electroforming voltage in both Pt/3TO/3AO/Ti and of Pt/3AO/3TO/Ti devices, the dominating insulating layer should be still the Al_2O_3 layer, where the tunneling transport mainly happens. Taking values for the barrier heights around the theoretical values and keeping the tunneling length in the range of (3.3 ± 0.3) nm obtained from the XRR fitted Al_2O_3 layer thickness and AFM measured RMS roughness, the comparison of the best simulation dots with the experimental curves are shown in Fig. 7.7 (b-f).

A consistent, well matching simulation result can be obtained for a barrier height

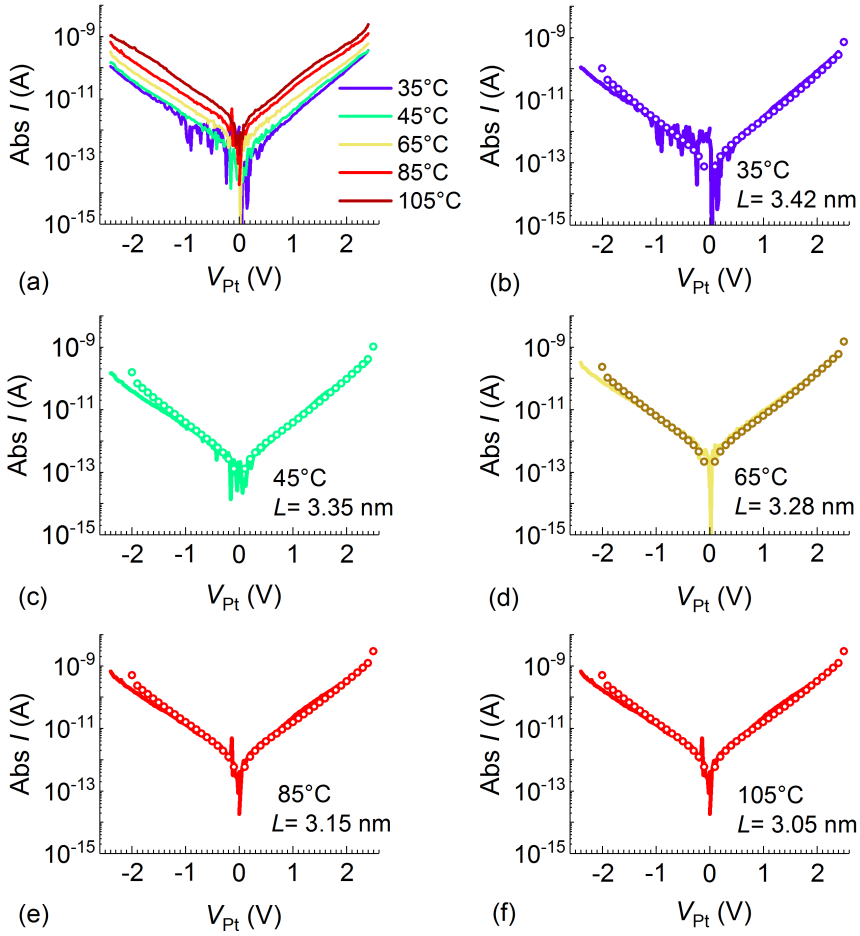

Figure 7.7: *(a) The temperature dependent $I(V)$ characteristics of initial state in a Pt/3TO/3AO/Ti cell. (b) to (f) are experimental curves (colored lines) and the corresponding best simulation result (dots). Some parameters are kept constant: $\Phi_1 = 1.9$ eV, $\Phi_2 = 2.4$ eV, $m^* = 0.24 \cdot m_0$, tunneling area $A = (100\ \text{nm})^2$, the tunneling length L and the substrate temperature are listed in the lower-right corner of (b-f).*

Φ_1 at Al_2O_3/Ti interface of 1.9 eV, which is close to the value of 1.75 eV used for the Pt/5AO/Ti devices. The second barrier Φ_2 of 2.4 eV should be most possibly placed at the TiO_2/Al_2O_3 interface. Although the affinity difference between two oxides should be theoretical around 1.62 eV, the larger barrier height obtained from the simulations might originate from a band bending in the TiO_2 layer. The slightly varied electron effective mass of $0.24{\cdot}m_0$ is still acceptable for the Al_2O_3 layer [147, 246].

The increase of initial current from 35°C to 105°C in the reverse bilayer stack can be explained by the reduction of tunneling length from 3.42 nm to 3.05 nm. The changed barrier heights indicates an existence of depletion region and resulted band bending. In contrast to the relative simple metal/oxide/semiconductor band diagram assumed for Pt/3AO/3TO/Ti in Fig. 7.6, the band diagram in Pt/3TO/3AO/Ti is hard to determine due to the two possible depletion regions.

7.1.5 Summary for the initial state

The $I(V)$ characteristics for the initial state show almost no temperature dependence in Pt/2.3 nm Al_2O_3/Ti single-layer devices. Based on this observation, tunneling of electrons should be the most probable transport mechanism among others in Al_2O_3-based cells. Regarding the asymmetric electrodes with respect to their work functions, a trapezoidal tunneling barrier is assumed. For thicker Al_2O_3-based devices showing low initial current, the initial state can be well explained by the Simmons' tunneling model with comparable barrier heights to the theoretical values and a slightly reduced tunneling thickness. In contrast, for thinner Al_2O_3-based cells, the conductive paths have to be taken into the tunneling model. This result indicates that an interface reaction between Ti OEL and the adjacent Al_2O_3 can be more significant for thinner Al_2O_3 layer.

Applying the simple trapezoidal barrier to the bilayer stacks faces difficulties. The first obstacle is the temperature dependent $I(V)$ behavior for initial state. Regarding the ohmic contact between TiO_2 and Ti electrode, the barrier heights of trapezoidal barrier in Pt/3AO/3TO/Ti stack can sustain the same value as assumed for the Pt/5AO/Ti stack. Based on the Simmons' equation, although the increased current level upon the increase of substrate temperature can be well depicted by the tunneling length shrink, a more reasonable explanation for this temperature dependent effect should be postulated as a depletion region between Al_2O_3 and TiO_2 layer.

For the reverse stack, Pt/3TO/3AO/Ti, however, the situation is more complex. First, the barrier Φ_1 at Al_2O_3/Ti is 1.9 eV, which is slightly higher compared to 1.75 eV at the same interface in the Pt/5AO/Ti cell. Second, the barrier Φ_2 for this trapezoidal barrier model is possibly placed at TiO_2/Al_2O_3 interface. However, the good matching value of 2.4 eV is much higher than the affinity difference between two oxides. Due to the unknown quality of TiO_2 without the OEL influence, the barrier between TiO_2 and Pt

bottom electrode is different from the $Pt/TiO_2/Ti$ device and thus not clear. Both make the physical meaning of barrier Φ_2 ambiguous. Third, the temperature dependent $I(V)$ curves can be well explained phenomenally by a similar tunneling length reduction based on the Simmons' model. All three features indicate an existence of depletion region(s) in the Pt/3TO/3AO/Ti cell, which makes it improper to describe $I(V)$ with a simple tunneling through the trapezoidal barrier.

Other transport mechanisms related to either bulk, e.g. Poole-Frenkel emission, or interface properties, e.g. Schottky emission, are also possible candidates but show less significance since they can not supply suitable physical parameters to explain observed currents. Therefore, the efforts with analysing the data under these mechanisms are listed in the "Appendix A".

7.2 Conduction behavior in the high resistance state

The current response of a defined resistance state in the nano-sized devices is strongly dominated by the electronic contribution. To discuss the charge transport behavior in the single-layer or bilayer devices, continuous $I(V)$ hysteresis loops executed at room temperature are applied to program the cells into HRS or LRS. Subsequently, the defined resistance states are analyzed with respect to the voltage- and temperature related current response, i.e. $I(V,T)$.

7.2.1 HRS in the Pt/2.3 nm Al_2O_3/Ti device

After 20 stable c8w BRS cycles (grey curves in Fig. 7.8 (a)) the high resistance state (HRS) was defined by 2.0 V in the last half loop. Subsequently, the read-out $I(V)$ curves for this written state were performed between -0.8 V and 0.8 V at each setting temperature. The temperature range of the sample stage is from room temperature to 140°C. No clear temperature dependence from these $I(V,T)$ curves coded by different colors can be observed, even in a higher magnification in Fig. 7.8 (b). This is further confirmed by the temperature related plot shown in Fig. 7.8 (c). Instead, the linear behavior with a slope of 1 in the $\ln|I|$ vs. $\ln|V|$ plot supports a direct tunneling process in the low voltage range (Fig. 7.8 (d)).

A simulation on the $I(V,T)$ characteristics is performed assuming a trapezoidal shaped barrier according to the Simmons' model. In Fig. 7.9 the best simulation result matching both the voltage dependence and the temperature independence is shown for the semi-logarithmic $I(V)$ curve (Fig. 7.9 (a)) and for the characteristic tunneling plot (Fig. 7.9 (b)), respectively. The tunneling current area (A) is taken as the filament area A_{filament} of 100 nm^2, which is supported by the former simulation results and the HRTEM study (see section 7.2.3). Regarding the almost same $I(V)$ behavior for both initial state and

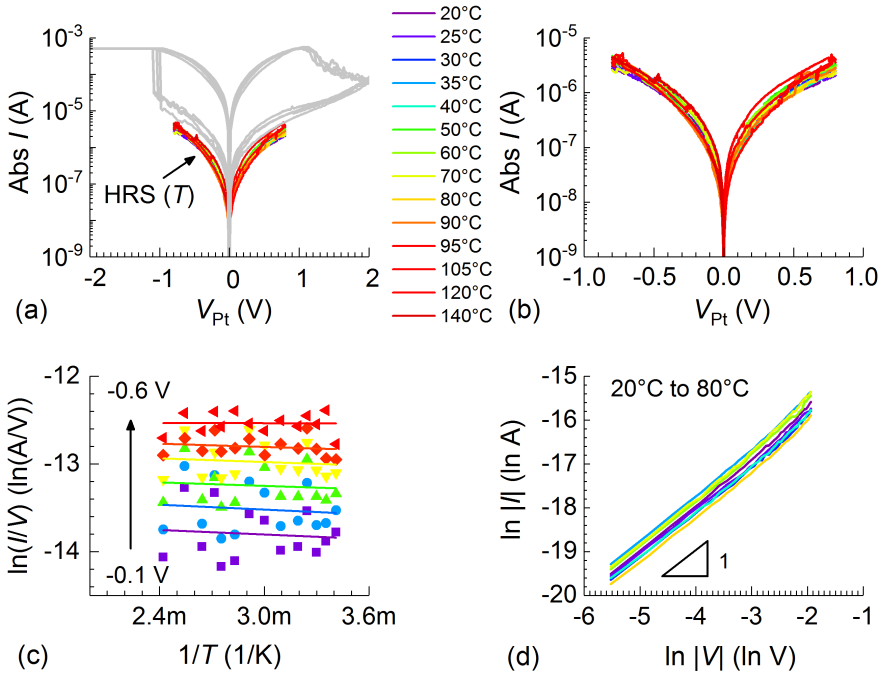

Figure 7.8: *(a) The $I(V)$ characteristics of a Pt/2AO/Ti cell in 20 cycles (grey curves) measured at room temperature with $V_{+,max} = 2.0$ V and $|I_{CC}| = 150\,\mu A$. The read-out $I(V)$ loops for HRS were measured from 20°C to 140°C as rainbow lines. (b) The zoomed $I(V,T)$ curves. (c) The plots of $ln(I/V)$ vs. $1/T$ and (d) of $ln|I|$ vs. $ln|V|$ from (b) for the negative voltage branch.*

the written HRS in the 2.3 nm Al_2O_3 single-layer cells, the barrier heights and tunneling length can be assumed to be the same. In addition, the barrier height Φ_1 is limited to 0.3 eV due to the small transition voltage (V_T) obtained from Fig. 7.9 (b).

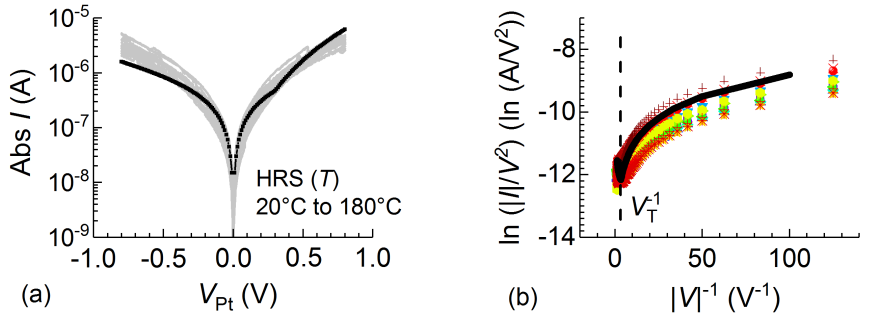

Figure 7.9: *(a) Temperature related read-out $I(V)$ loops (grey lines) and (b) its corresponding plots in form of $ln(|I|/V^2)$ vs. $|V|^{-1}$ for the negative voltage branch from Fig. 7.8 (b). The best simulation lines in (a) and (b) are drawn in black. The calculated parameters are $\Phi_1 = 0.3$ eV, $\Phi_2 = 1.1$ eV, $m^* = 0.23 \cdot m_0$, $A = 100$ nm^2, $L = 1.4$ nm.*

In standard VCM-type c8w filamentary switching, the reversible switching state depends on both the highly conductive filament part, so-called plug, that is described by an oxide area with high oxygen vacancy concentration, and the relative insulating filament part, disc with the average oxygen vacancy concentration. Based on the former simulation results of the Pt/2AO/Ti devices, the filament should consist of plug region near to Ti electrode and the disc close to the Pt bottom electrode (see Fig. 7.2 (c)). Similar to the situation in $Pt/TiO_2/Ti$ (see chapter 8), the space charge region, which is caused by the oxygen vacancies in the disc and placed close to the Pt/Al_2O_3 interface, can lead to the strongly reduced interface barrier height Φ_2, i.e. from the expected value of 3.07 eV for Pt/stoichiometric Al_2O_3 to 1.1 eV. At the interface between conductive plug and the disc region a barrier of around 0.3 eV arises due to the difference in defect concentration, here predominately oxygen vacancy concentration, in the oxide layer.

7.2.2 HRS in the Pt/4.8 nm Al_2O_3/Ti device

The multiple high resistance states upon RESET stop voltage ($V_{+,\max}$) can be obtained in single-layer and bilayer cells (see 4). Firstly, for the Pt/5AO/Ti cell, the different HRS written by different $V_{+,\max}$ during 20 cycles are discussed. One typical $I(V)$ curve for the same HRS is extracted and curves for each $V_{+,\max}$ value are compared in Fig. 7.10 (a). The enhancement of the read-out resistance for HRS is around 1 dec/0.6 V as shown in Fig. 7.10 (b).

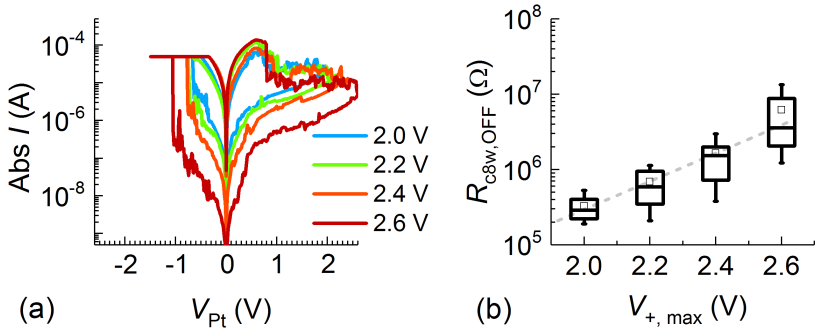

Figure 7.10: *(a) Comparison of typical $I(V)$ curves with different $V_{+,max}$ values in a Pt/5AO/Ti cell. (b) The corresponding read-out resistance value for HRS as a function of RESET stop voltage.*

Applying the similar simulation parameters used for HRS in the Pt/2AO/Ti cell, the simulation curves shown in black in Fig. 7.11 (a-d) fit the experimental $I(V)$ curves for negative bias branch quite well. The reduction of the current level for HRS can be explained by the increase of the tunneling barrier length. However, the simulation curves do not fit precisely the experimental data in the higher positive voltage range, like $V_{+,\max}$

$\geqslant$ 2.4 V (see Fig. 7.11 (c,d)).

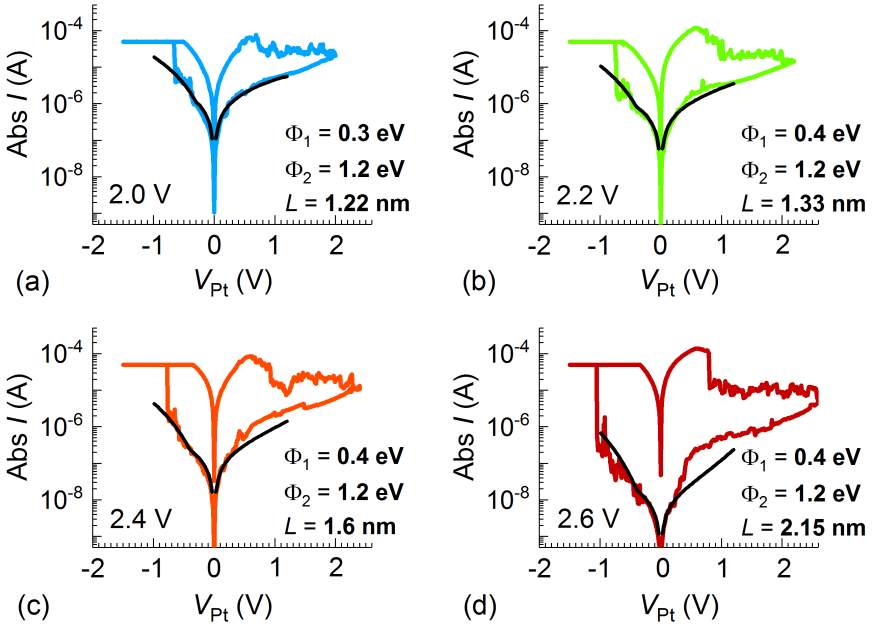

Figure 7.11: *The best simulation results on $I(V)$ characteristics from Fig. 7.10 with $V_{+,max}$ of: (a) 2.0 V, (b) 2.2 V, (c) 2.4 V, (d) 2.6 V. The barrier heights and lengths are listed in the lower-right corner of each graph. $m^* = 0.23 \cdot m_0$ and $A = 100\ nm^2$ are kept constant.*

To explain this phenomenon, 9 cells were switched for 21 cycles with the same $V_{+,\max}$ of 2.6 V and the same $|I_{CC}|$ of 50 µA. Two typical cells were chosen to show their first 20 cycles (grey lines) and the last RESET cycle (blue loop) (Fig. 7.12). Then the read-out loops were first performed within 1.5 V (green line) and subsequently stopped at the negative branch within -0.5 V (red line).

As Fig. 7.12 (a) and (b) show, the read-out green and red curves for both polarities can be well simulated with one set of parameters (black line). However, the more frequent RESET behavior (blue curve in Fig. 7.12 (b)) shows a volatile relaxation phenomenon compared to the green read-out line and a large deviation from the black simulated $I(V)$ line. Volatile switching phenomena have been observed for Ta_2O_5 and ZrO_x-based devices as well [103]. A proposed theorem considers interface defects of the Pt/oxide interface with a continuously distributed energy range. Positively charged traps residing at the interface after application of high positive RESET voltage cause an increase of conductance by modifying the barrier height. Structural relaxation may lead to an energy level shift when the defects change the charge state. Localized defect states in ALD Al_2O_3 films have been characterized by synchrotron based spectroscopic technique, especially

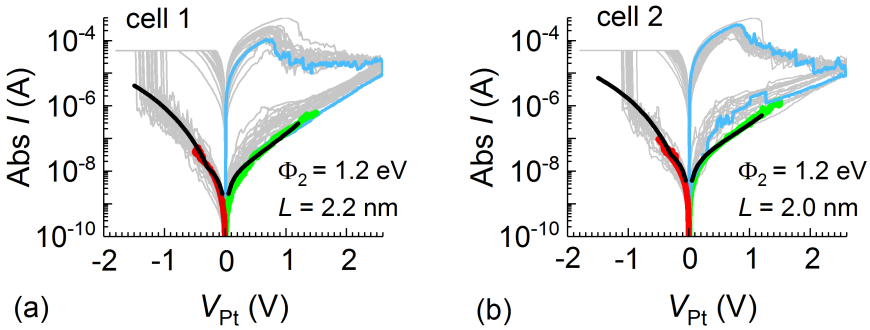

Figure 7.12: *(a) and (b) represent two typical $I(V)$ characteristics for $V_{+,max}$ = 2.6 V in two Pt/5AO/Ti cells. 20 c8w BRS cycles are drawn in grey. The blue curve is the last RESET loop and subsequently, the green and red read-out loops are measured one after the other. The best simulation results are in pink. The adjusted parameters are listed in lower-right corner of each graph, whereas $m^* = 0.23 \cdot m_0$, $A = 100\ nm^2$ and $\Phi_1 = 0.3\ eV$ are kept constant.*

resonant photoemission spectroscopy. From the results a band scheme has been derived, which is replotted in Fig.11 in [247]. In ALD Al_2O_3 films the charge transfer band has a width of about 3 eV and is located $\approx$ 3.5 eV above Fermi level.

7.2.3 HRS in the Pt/3 nm Al_2O_3/3 nm TiO_2/Ti device

For the Pt/3AO/3TO/Ti cell, the high resistance state was defined by 2.2 V RESET stop voltage and stabilized by 20 c8w BRS cycles at room temperature (grey curves in Fig. 7.13 (a)). Then the read-out $I(V)$ loops for HRS are measured at a certain setting temperature ranging from 25°C to 200°C (colored curves in Fig. 7.13 (a)). These read-out curves show almost no temperature dependence even in the zoomed magnification in Fig. 7.13 (b). Moreover, the lack of valid analytical results from Fig. 7.13 (c) and (d) can further confirm this temperature independence and exclude any significance of temperature activated mechanisms like Poole-Frenkel, ohmic conduction mechanisms and hopping conduction. The plots for both polarities share the same trend, therefore, the data for the positive voltage branch are not explicitly shown.

Closer analysis of the HRS in the Pt/3AO/3TO/Ti cell, which is programmed by a RESET voltage sweep up to 2.2 V, is performed by means of the introduced tunneling model into the filament area with a conductive plug and an insulating disc as the tunneling barrier. The slope of $\ln|I|$ vs. $\ln|V|$ plots is 1 for the low voltage amplitude, which indicates a direct tunneling transport (Fig. 7.14 (a)). By adjusting the barrier heights Φ_2 at the Pt/Al_2O_3 interface and Φ_1 between plug and disc, the simulation curve can fit the read-out $I(V)$ curves for HRS well, here take the curve measured at 45°C as one example

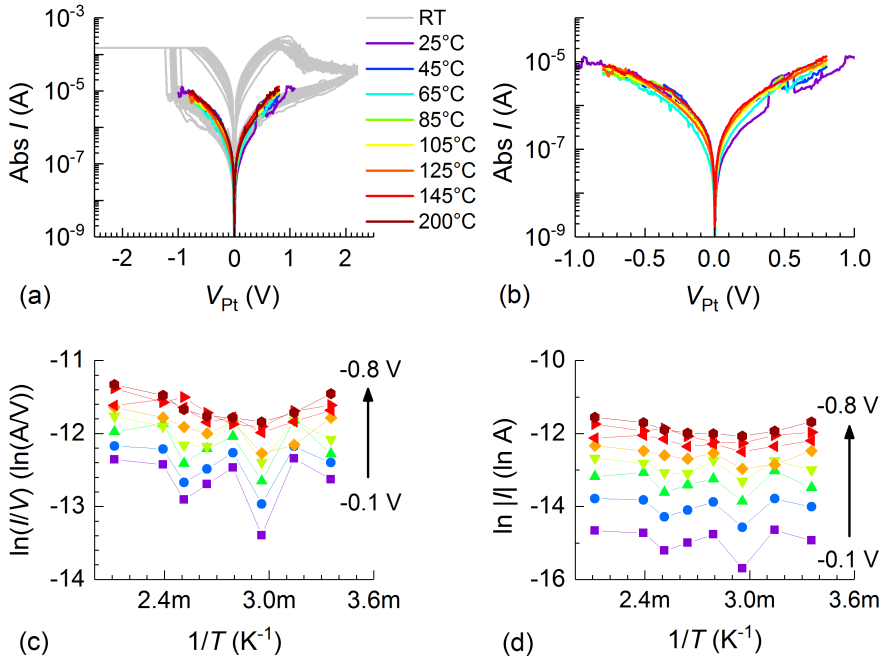

Figure 7.13: *(a) The $I(V)$ characteristics in 20 c8w BRS cycles (grey curves) of a Pt/3AO/3TO/Ti cell measured at room temperature with $V_{+,max} = 2.2$ V and $|I_{CC}| = 150\,\mu$A. The read-out $I(V)$ curves for HRS measured from 25°C to 200°C as rainbow lines. (b) The zoomed $I(V,T)$ curves. The data from (b) in the negative voltage branch are plotted as (c) $ln(I/V)$ vs. $1/T$ and as (d) $ln|I|$ vs. $1/T$.*

(see Fig. 7.14 (b)). The simulation parameters, namely $\Phi_1 = 0.3$ eV, $\Phi_2 = 1.1$ eV and $L = 1.25$ nm, are very comparable to the HRS value with the same RESET stop voltage in other cells. Plotting the simulated data into the $\ln(|I|/V^2)$ vs. $1/V$ relation, a good agreement between simulation (black line) and experimental data can be demonstrated for the whole voltage range (Fig. 7.14 (c)).

The ability of writing multiple HRS in a Pt/3AO/3TO/Ti cell through changing the $V_{+,\max}$ values is summarized in Fig. 7.15 (a). For each $V_{+,\max}$ value, 20 c8w BRS cycles are carried out and one typical $I(V)$ curve is shown. Simulations are performed by keeping $m^* = 0.23{\cdot}m_0$, $A = 100$ nm^2 and $\Phi_2 = 1.1$ eV as optimized from Fig. 7.14 (b) and by allowing a variation of Φ_1 and the tunneling barrier length. The $I(V)$ characteristics for multiple HRS are clearly correlated with an increasing barrier length from 1.3 nm to 1.95 nm (see Fig. 7.15 (b-d)). For a higher $V_{+,\max}$ value of 2.6 V, a slight deviation of the simulation curve from the experimental data for $V > 0.5$ V is observed as well. This can be attributed to a volatile switching region (0.5 V to 1 V) discussed for deep RESET in the Pt/5AO/Ti device.

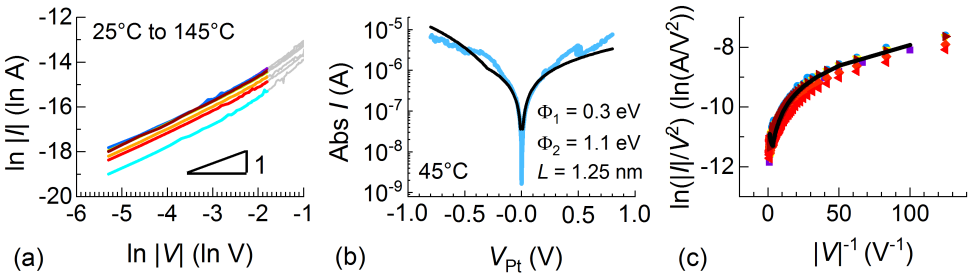

Figure 7.14: *(a) The plots of ln|I| vs. ln|V| from Fig. 7.13 (b) for negative bias. (b) The read-out $I(V)$ curve (blue line) for HRS measured at 45°C from Fig. 7.13 (b). The best simulation result is drawn in black with $m^* = 0.23 \cdot m_0$ and $A = 100\ nm^2$, whereas the changeable parameters are listed in the lower-right corner. (c) The read-out $I(V,T)$ curves from Fig. 7.13 (b) and the simulation result from (b) are plotted into $ln(|I|/V^2)$ vs. $|V|^{-1}$ as color dots and as black line, respectively.*

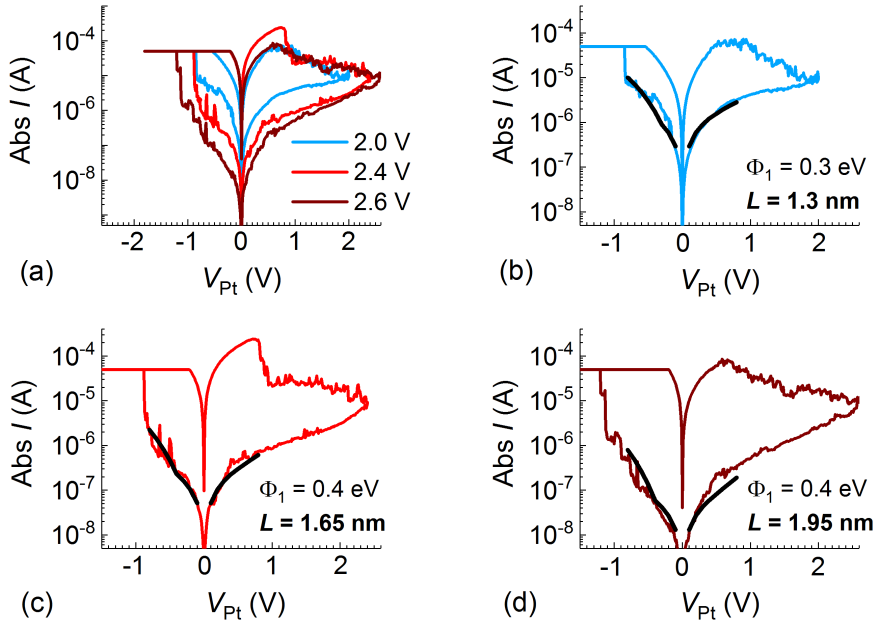

Figure 7.15: *(a) Comparison of one typical $I(V)$ curve with different $V_{+,max}$ values in a Pt/3AO/3TO/Ti cell. The best simulation result on $I(V)$ characteristics with $V_{+,max}$ of (b) 2.0 V, (c) 2.4 V, (d) 2.6 V. The simulation parameters are listed in each graph, whereas $m^* = 0.23 \cdot m_0$, $A = 100\ nm^2$ and $\Phi_2 = 1.1\ eV$ are kept constant.*

7.2.4 HRS in the Pt/3 nm TiO_2/3 nm Al_2O_3/Ti device

Similarly, the temperature related $I(V)$ characteristics for HRS were also performed in the reverse stack (see Fig. 7.16 (a)). The read-out $I(V)$ curves for HRS show a slight temperature dependence (Fig. 7.16 (b)). The plot of $\ln(I/V)$ vs. $1/T$ for a certain voltage

value reveals a negative slope (Fig. 7.16 (c)). From these slopes the derived values show no voltage dependence and the corresponding barrier height is only about 0.1 eV. This analytical result indicates that neither Poole-Frenkel nor ohmic conduction transport is the dominating mechanism for this high resistance state. The similar analytical result obtained from positive bias is not repeated here.

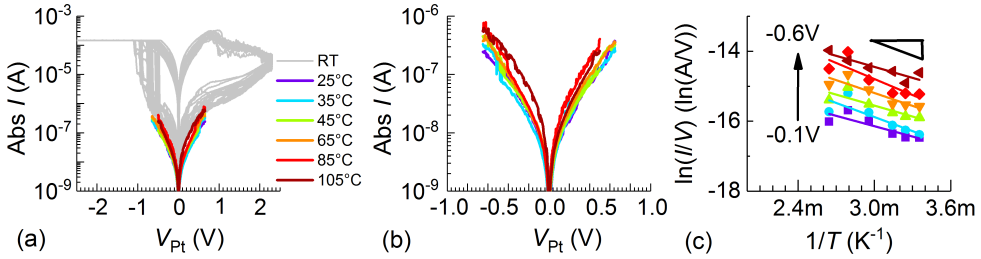

Figure 7.16: *(a) The $I(V)$ characteristics of a Pt/3TO/3AO/Ti cell in 20 cycles (grey curves) measured at room temperature with $V_{+,max}$ = 2.3 V and $|I_{CC}|$ = 150 µA. The read-out $I(V)$ loops for HRS measured from 25°C to 105°C as rainbow lines. (b) The zoomed $I(V,T)$ curves. (c) The plots of ln(I/V) vs. 1/T from (b) for the negative voltage branch.*

Plotting the current against voltage in the semi-logarithmic scale (Fig. 7.17 (a)), the slope of ≈ 1 for the low voltage range indicates a direct tunneling process. Applying the afore optimized tunneling parameters a good matching between simulation and the $I(V)$ curves is observed (Fig. 7.17 (b)).

For the Pt/3TO/3AO/Ti device the similar comparison of multiple HRS written by varied $V_{+,\mathrm{max}}$ values is shown in Fig. 7.18 (a). By applying the barrier values from Fig. 7.17 (b) and slightly tuning the tunneling barrier length L, the different HRS written by increasing $V_{+,\mathrm{max}}$ values can be well explained by the corresponding tunneling length

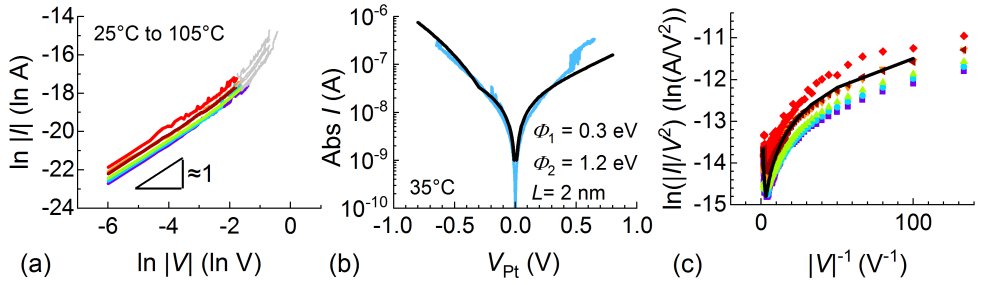

Figure 7.17: *(a) The plots of ln|I| vs. ln|V| from Fig. 7.16 (b) for the negative voltage branch. (b) Comparison of the read-out loop (blue line) measured at 35°C from Fig. 7.16 (b) and the best simulation curve (black line) with $m^* = 0.23 \cdot m_0$ and $A = 100\ \mathrm{nm}^2$. Other optimized parameters are listed in the lower-right corner. (c) Comparison between the read-out loops (color dots) and simulation result (black line) in form of ln(|I|/V^2) vs. $|V|^{-1}$.*

change from 1.35 nm to 1.85 nm in Fig. 7.18 (b) to (d).

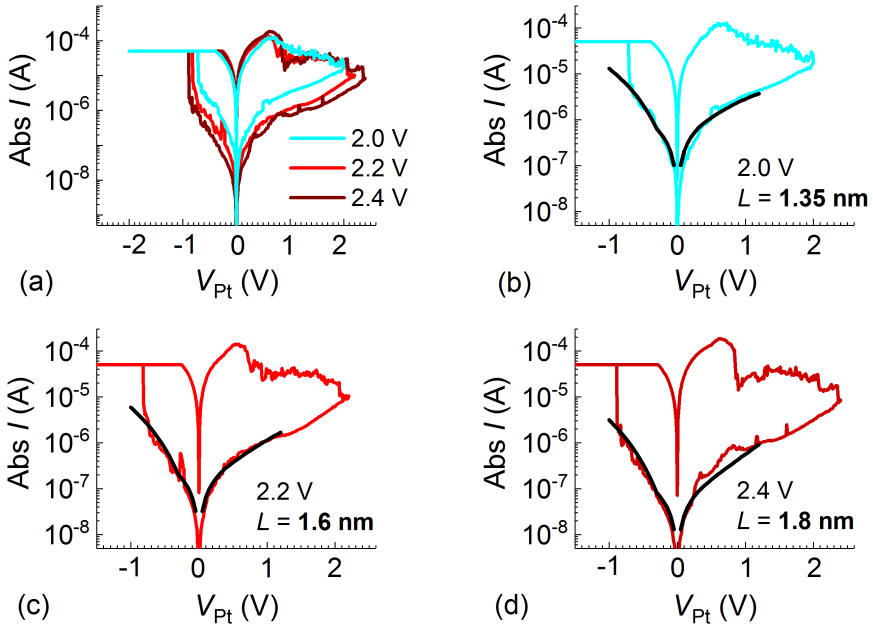

Figure 7.18: *(a) Comparison of one typical $I(V)$ curve with different $V_{+,max}$ values in a Pt/3TO/3AO/Ti cell. The best simulation result on $I(V)$ characteristics with $V_{+,max}$ of (b) 2.0 V, (c) 2.4 V, (d) 2.6 V. The optimized tunneling length is listed in each graph, whereas $m^* = 0.23 \cdot m_0$, $A = 100\ nm^2$, $\Phi_1 = 0.3\ eV$ and $\Phi_2 = 1.2\ eV$ are kept constant.*

7.2.5 Summary for HRS

In this section, the electronic transport in HRS is investigated for different single-layer and bilayer devices, namely Pt/2 nm Al_2O_3/Ti, Pt/5 nm Al_2O_3/Ti, Pt/3 nm Al_2O_3/3 nm TiO_2/Ti and Pt/3 nm TiO_2/3 nm Al_2O_3/Ti. As the filamentary-type BRS switching is confirmed by HRTEM in the Pt/3 nm Al_2O_3/3 nm TiO_2/Ti cell (see chapter 6), the other stacks like Pt/2 nm Al_2O_3/Ti, Pt/2 nm Al_2O_3/3 nm TiO_2/Ti showing no significant area-dependence in chapter 4, can be considered as filamentary-type BRS switching as well. Therefore, the electronic transport through a filament placed in an amorphous and insulating matrix is assumed. Based on this and aforementioned results, several points can be summarized as follows:

(1) Firstly, the analysis on the temperature related read-out $I(V)$ loops for HRS point out that the dominating process should be determined as tunneling among the other transport mechanisms. Especially, both read-out $I(V,T)$ loops for HRS and the represented $I(V)$ curves caused by RESET stop voltage variation can be well matched by the calculated tunneling current obtained from the Simmons' equation with trapezoidal

barrier. Interestingly, the area of tunneling current flux A for HRS analysis can be kept as 100 nm^2 for all the stacks. This supports the filamentary-type c8w BRS occurring in these stacks and the filament area equals to the tunneling area.

(2) For all the different stacks, HRS written by the same RESET stop voltage, take 2.0 V as one example, can be well explained by the same tunneling barrier heights, i.e. $\Phi_1 = 0.3$ eV and $\Phi_2 \approx (1.15 \pm 0.05)$ eV. The lower barrier values could originate from the high oxygen vacancy density in the filament and a formed depletion region, respectively. The optimized barrier length is limited in the range of (1.3 ± 0.1) nm. Combining with the unchanged effective mass of $0.23 \cdot m_0$ for all stacks, the tunneling process should happen rather in the Al_2O_3 layer.

(3) The multiple HRS that show RESET stop voltage dependence in cells like Pt/5AO/Ti and Pt/3AO/3TO/Ti can be well explained by the change of the tunneling barrier length. As the tunneling barrier length is still within the range of the Al_2O_3 film thickness, the depletion region or "disc" is most probably close to the Pt/Al_2O_3 interface and this part of Al_2O_3 should be resistively tunable and be responsible for the multiple HRS.

(4) For thicker Al_2O_3-based cells, a volatile RESET loop is observed at RESET stop voltage $\geqslant 2.4$ V. This leads to a contradiction between the non-volatile read-out loop for HRS and the RESET loop back to 0 V. The volatile phenomenon can be explained by the positive charged immobile defects at the Pt/Al_2O_3 interface, which are discharged by positive voltage on Pt and shift the Fermi level in Al_2O_3 upwards. This shift leads to a decrease of interface barrier and the corresponding increase of current.

7.3 Conduction behavior in the low resistance state

For a filamentary-type c8w SET process, the accompanying Joule heating enhances the ion mobility in the switching regime and thus enables the switching time as short as 10 ns [229, 248–250]. In order to accurately understand the c8w BRS process, the conduction behavior in LRS is of considerable importance. For this purpose, after programming the cells into LRS at the room temperature, the continuous $I(V)$ hysteresis loops are applied as read-out curves for LRS and measured from room temperature to around 200°C. In this work, the c8w LRS in different stacks reveal an almost linear $I(V)$ behavior with minor temperature dependence. In the following discussion the $I(V)$ characteristics are plotted in the linear scale and magnified within the voltage range from 0.18 V to 0.3 V.

7.3.1 LRS in single-layer devices

For 2 nm Al_2O_3 and 3 nm TiO_2 single-layer devices, the current response of LRS decreases monotonically with increased temperature (see Fig. 7.19). Regarding the good linear $I(V)$ relation for both single-layer devices, the LRS can be characterized by means of the temperature coefficient of the resistance (TCR) determined at $V_{\text{read}} = 0.3$ V applied to the Pt bottom electrode.

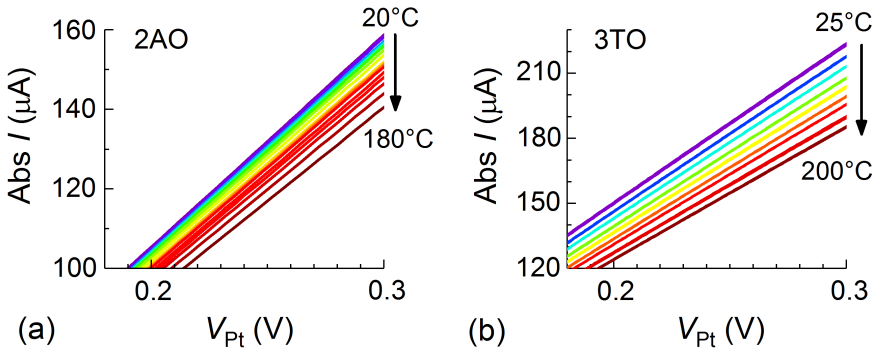

Figure 7.19: *The temperature dependent $I(V)$ behavior in LRS for two single-layer devices, namely, (a) Pt/2 nm Al_2O_3/Ti, (b) Pt/3 nm TiO_2/Ti.*

The temperature dependence of a linear resistance element can be expressed as follows:

$$R = R_0[1 + \alpha_0(T - T_0)], \tag{7.1}$$

where R_0 is the resistance measured at the reference temperature (T_0), for example $T_0 \approx 300$ K, and α_0 is the temperature coefficient of resistance (TCR, in K^{-1}) defined from the following relationship [124]:

$$\alpha_0 = TCR = \left(\frac{1}{R_0}\right)\left(\frac{\partial R}{\partial T}\right)|_{T=T_0} \tag{7.2}$$

Since the total resistance comprises not only the oxide material but also the electrode materials including Ti and Pt, only comparative conclusions on the TCR values can be drawn. Fig. 7.20 shows the normalized resistance change, $(R - R_0)/R_0$, as a function of the change in temperature, $(T - T_0)$. The reference value $R_0 = R(T_0)$ is the read-out resistance in LRS at 298 K. The linear fitting in Fig. 7.20 (a) and (b) provides a TCR value of $(0.76 \pm 0.02)\cdot10^{-3}K^{-1}$ for the Pt/2AO/Ti cell and of $(1.18 \pm 0.01)\cdot10^{-3}K^{-1}$ for the Pt/3TO/Ti device.

For pure Al metal, the TCR value is (3.8 - 4.3)·10^{-3}K^{-1} [251,252]. The reported TCR values of 50 - 200 nm Ti and 50 nm Pt thin films are (1.74 - 2.07)·10^{-3}K^{-1} and 1.04·10^{-3}K^{-1}, respectively [253]. The TCR value of metall films is dependent on the film thickness, expecially when the film thickness is reduced to the nanometer range [254]. Therefore, the precise contribution of the Ti top electrode of 10 nm with 20 nm Pt capping layer and Pt bottom electrode of 30 nm used in this work to the total TCR value is hard to estimate. From the comparison of the TCR values between the metal-oxide films and metal electrodes, it's difficult to exclude the possibility of the metal filament. Still such positive values obtained from the two stacks can give a hint that the filament can be described as almost metallic. Regarding the findings of Magnéli-type phases forming conductive filaments in VCM-type switching TiO_2 devices [136,255,256] that leads to a metallic filament and as confirmed by high-resolution TEM, only the crystallized metal-oxide filament was observed in a switched Pt/3AO/3TO/Ti cell. Moreover, highly conductive Al_2O_3 with high density of defects has been experimentaly observed as well [158]. It could be concluded that the positive TCR values obtained in the both single-layer devices should originate from the metal-oxide phase showing high conductivity.

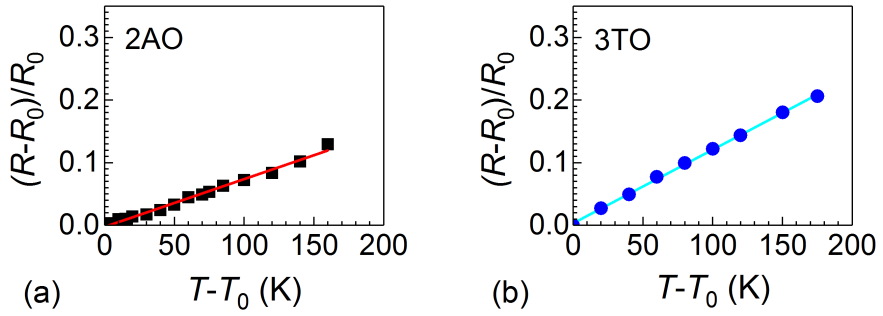

Figure 7.20: *Temperature dependency of the resistance of (a) one Pt/2AO/Ti cell and of (b) one Pt/3TO/Ti cell set into the c8w LRS normalized to the resistance value R_0 at T_0 = 298 K. The TCR values of $(0.76 \pm 0.02)\cdot10^{-3}K^{-1}$ and of $(1.18 \pm 0.01)\cdot10^{-3}K^{-1}$ are obtained from the linear fitting in (a) and (b), respectively.*

7.3.2 LRS in bilayer devices

The similar temperature dependency of LRS in bilayer devices is observed within a certain range: for the Pt/3AO/3TO/Ti cell a gradually reduced current level of LRS by increasing temperature is observed within 175°C in Fig. 7.21 (a) and for the Pt/3TO/3AO/Ti cell the decrease of current level by LRS is more significant with temperature lower than 125°C (Fig. 7.21 (b)).

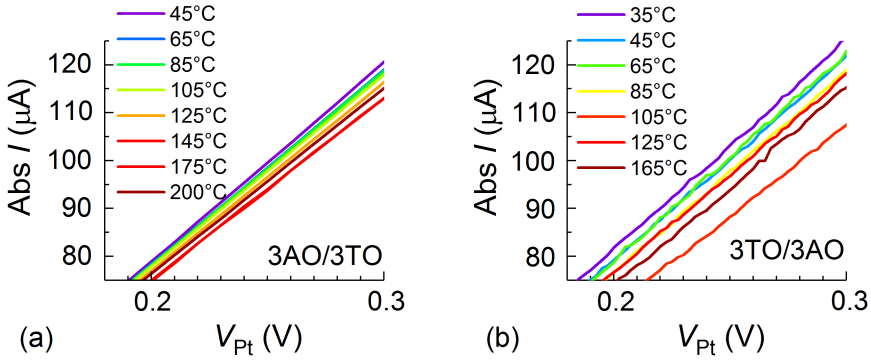

Figure 7.21: *The temperature dependent $I(V)$ behavior in LRS for two bilayer devices, namely, (a) Pt/3 nm Al_2O_3/3 nm TiO_2/Ti, (b) Pt/3 nm TiO_2/3 nm Al_2O_3/Ti.*

Due to the high noise in the $I(V,T)$ curves as shown in Fig. 7.21 (b), the resistance values for TCR are not directly read out at 0.3 V, but are the reverse slope values of I against V in the linear scale within voltage rang from -0.3 V to 0.3 V. In this way, the statistical noise is minimized. From the fitting in the two bilayer stacks, the TCR value is $(0.54 \pm 0.06)\cdot 10^{-3}K^{-1}$ for Pt/3AO/3TO/Ti device (Fig. 7.22 (a)) and is $(2.54 \pm 0.26)\cdot 10^{-3}K^{-1}$ for Pt/3TO/3AO/Ti device (Fig. 7.22 (b)).

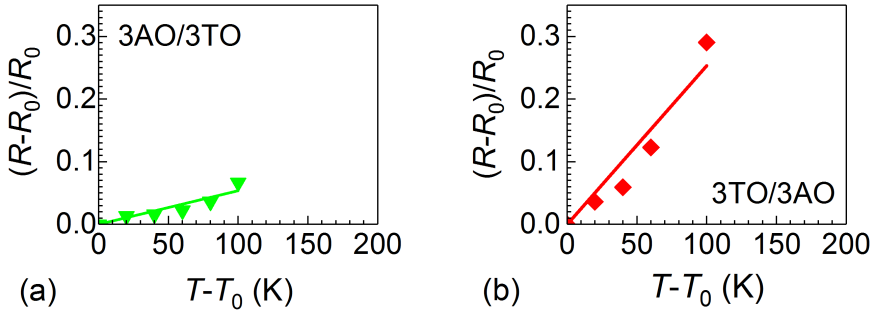

Figure 7.22: *Temperature dependency of the resistance of (a) one Pt/3AO/3TO/Ti and of (b) one Pt/3TO/3AO/Ti cell in the c8w LRS normalized to the resistance value R_0 at T_0 = 318 K. The TCR value of $(0.54 \pm 0.06)\cdot 10^{-3}K^{-1}$ and of $(2.54 \pm 0.26)\cdot 10^{-3}K^{-1}$ are obtained from the linear fitting from (a) and from (b), respectively.*

Similar to the discussion in single-layer cells, solely the positive values of TCR in bilayer stacks can not determine the contribution from the oxide layers to the LRS. However, related to the HRTEM findings in Pt/3AO/3TO/Ti, a highly conductive oxide part should be existed in both bilayer devices.

To sum up the transport mechanism of LRS, two conclusions can be made for single-layer and bilayer stacks. Firstly, due to the low resistance of the LRS (≈ 2 kΩ) and high linearity, the conductive filament should connect the top and bottom electrodes in all cells. Secondly, in the conductive filament for LRS, sufficient defects should exist in the highly conductive oxide.

7.4 Summary and discussion

With Simmons' model for an asymmetric trapezoidal tunneling barrier, the electronic charge transport in the initial state and in the high resistance state (HRS) of Al_2O_3-based single-layers and Al_2O_3-TiO_2-based bilayer stacks sandwiched between a Pt bottom electrode and a Ti top electrode can be well described. The major tunneling parameters, like tunneling barrier heights (Φ_1 and Φ_2), tunneling barrier length (L), electron effective mass (m^*) and tunneling area (A) are summarized in Tab. 7.1.

Pt/oxide(s)/Ti	States	Φ_1 (eV)	Φ_2 (eV)	L (nm)	$m^*(\cdot m_0)$	A ($\cdot 10^2$ nm)
2AO	initial	0.3	1.1	1.4	0.23	1
	HRS	0.3	1.1	1.4	0.23	1
5AO	initial	1.75	3.07	4.5	0.23	100
	HRS	0.3	1.2	1.22	0.23	1
3AO/3TO	initial	1.75	3.07	3.2	0.23	100
	HRS	0.3	1.1	1.3	0.23	1
3TO/3AO	initial	1.9	2.4	3.45	0.24	100
	HRS	0.3	1.2	1.35	0.23	1

Table 7.1: *The simulation parameters for resistance states in different stacks: initial states measured at room temperature and HRS written by 2.0 V are chosen to be compared with each other.*

Several statements can be concluded from the analysis:

1. The tunneling current flux area (A) is varied from the cell cross-point area $A_{\text{cell}} = 10^4$ nm^2 to an assumed filament front area $A_{\text{filament}} = 10^2$ nm^2 in different cases. For understanding of the highly insulating initial state in thicker single-layer and bilayer cells, like, Pt/5AO/Ti, Pt/3AO/3TO/Ti and Pt/3TO/3AO/Ti, the current flux should go through the whole area of the electrode crossing due to the absence of the conductive path. However, for the thinner 2 nm Al_2O_3 film investigated into a Pt/2AO/Ti stack, the formation of a conductive path has already happened

after the fabrication due to the Ti OEL impact. Correspondingly, the A should be reduced to A_{filament} of 100 nm^2. For the HRS, a filamentary-type VCM switching with the same area for these cells can be concluded regarding the best simulation results and the HRTEM results in this work.

2. The electron effective mass (m^*) of about $0.23{\cdot}m_0$ can be used for all stacks to get the best simulation results. This value lies in the range of $(0.16 - 0.4){\cdot}m_0$ reported for Al_2O_3 films [147–149, 152]. In contrast, trying to apply the frequently reported effective electron mass in TiO_2 films, i.e. $1{\cdot}m_0$ for anatase phase [120] and several ten m_0 for rutile phase [126], no good matching can be obtained for a physically reasonable tunneling barrier length. Therefore, it can be concluded that tunneling process should be mainly controlled by the Al_2O_3 layer and the corresponding interfaces.

3. The tunneling length (L) optimized for simulation of the $I(V)$ curve varies in the different cases. For the initial state in the thicker devices, L is almost consistent with the physical thickness of the Al_2O_3 layer determined from XRR fitting. Only for the thinner Al_2O_3 devices, i.e. Pt/2AO/Ti, L is much smaller than the physical thickness of the Al_2O_3 layer of 2.3 nm, which can be explained by the impact of Ti OEL in direct contact to Al_2O_3 layer during the fabrication process.

   For the switched cells, the filament is created during the electroforming process and consists of conductive plug and insulting dics parts. As only the disc region should be responsible for the reversible switching phenomenon, the tunneling length should represent this region. Here take HRS written by 2.0 V as one example (see Tab. 7.1), compared to the initial state, the values of L are reduced to around 1.3 nm, which indicates that the disc region is still a part of the Al_2O_3 layer. The possibility of high conductivity in Al_2O_3 films was proved by Nigo et al. [158] experimentally and the reason was assumed to be the delocalized electronic states close to conduction band formed by sufficient oxygen vacancies in the films.

4. For the initial states, the tunneling barrier heights are in good accordance with values derived from comparison of the theoretical band offset for the oxide-metal interfaces in Pt/5AO/Ti and Pt/3AO/3TO/Ti stacks.

   For the HRS, the simulation results indicate that an asymmetric barrier with similar barrier heights of $\Phi_1 \approx (0.35 \pm 0.05)$ eV and $\Phi_2 \approx (1.15 \pm 0.05)$ eV can be valid for all single-layer and bilayer cells. Specific for Pt/5AO/Ti and Pt/3AO/3TO/Ti, the disc region should be in the Al_2O_3 layer close to Pt/Al_2O_3 interface. The lower barrier Φ_1 describes the contact between insulating disc and conductive layer and can be roughly limited by the transition voltage, while the higher barrier Φ_2 denotes

the barrier at the Pt/Al_2O_3 interface. Compared to the initial states, this barrier height in HRS is reduced from 3.07 eV to around 1.3 V.

Two possible physical mechanisms could be responsible for this effect. First, the high oxygen vacancy density in the filament region leads to the formation of depletion region, which results in band bending close to Pt/Al_2O_3 interface as for Pt/TiO_2 interface (for details see chapter 8). Therefore the interface barrier is reduced. Second, the defect states at the interface between Al_2O_3 and Pt from switching processes could results in pinning of the Fermi-level in Al_2O_3. As the interface defect states could be filled and emptied by the charging process, volatile states could be observed as well. As evidenced in Fig. 7.12, in Pt/5AO/Ti, volatile RESET loop suggests the effect of immobile charges at the Pt/Al_2O_3 interface.

5. The LRS in single-layer and bilayer stacks show a good linearity of $I(V)$ relation. From the plots of $(R\text{-}R_0)/R_0$ against $T\text{-}T_0$ the positive TCR values for all single-layer and bilayer stacks are obtained and indicate a metallic conducting character of the oxide-based filament. Regarding the low value for the LRS that is closed to the metal line resistance, the filament should be connecting the top and bottom electrode after the c8w SET process.

Summing up the different resistances in the single-layer and bilayer stacks, the c8w BRS in the tested stacks can be undestood as follows, which is compatible with the well-known understanding for the resistive switching behavior reported in [4]: During the SET process by negative bias to Pt electrode a conductive filament bridging the two electrodes of the cell can be built and switch the cell to LRS, while the RESET process breaks the conductive filament and leaves a certain insulating disc region close to the Pt electrode, which converts the total resistance state of the whole cell to HRS.

Chapter 8

Eightwise resistive switching in TiO_2-based nano-structures

In this chapter, the coexistence of two opposite bipolar resistive switching polarities, namely, the filamentary VCM-type counter eightwise (c8w) switching and the opposite eightwise (8w) switching, as it was mainly observed in 30 nm Pt (BE)/3 nm to 11 nm TiO_2/10 nm Ti (TE)/20 nm Pt (capping layer) nano-crossbar devices of $(60\ nm)^2$ to $(100\ nm)^2$ size, is discussed. In order to focus on the asymmetry of the VCM devices the topmost Pt capping layer is not mentioned in this chapter.

The phenomenon of the coexistence and the transition between the two switching modes is firstly depicted in sections 8.1.1 and 8.1.2. The characteristics of 8w resistance states are studied by the hysteresis curves obtained from DC voltage sweep and pulse voltage operation in sections 8.1.3 and 8.1.4. In addition, the interface effect by insertion of Al_2O_3 between TiO_2 and two electrodes are investigated in section 8.1.5 and 8.1.6, respectively.

Section 8.2 discusses the different non-volatile 8w states by means of its temperature and voltage dependence. The analysis using the Simmons' tunneling model [106] provides first results on the electrical characteristics of the states in the switching regime. In order to further understand the switching mechanims, the two resistance states are linked to the ion configuration via a recently established continuum model simulation [107].

Combining all the results, a switching mechanism based on the mixed electronic-ionic conduction nature in TiO_2 proposed in section 8.3, which properly describes the coexistence of c8w BRS and 8w BRS sharing a common state. The model mainly describes the competition between the migration of oxygen vacancies in the oxide and oxygen exchange across the Pt/TiO_{2-x} interface at the local position of the filament end.

8.1 Characteristic phenomena in 8w BRS devices

8.1.1 Coexistence of c8w and 8w BRS

The metal$_1$/oxide/metal$_2$ (M_1OM_2) structure utilized in this chapter is shown in Fig. 8.1 (a). Based on the absence of area dependence of shared state c8w HRS (= 8w LRS*) (in the latter section 8.1.4), both c8w and 8w BRS in the Pt/TiO_2/Ti stack should be filamentary. As the widely accepted understanding in M_1OM_2-based ReRAM cells [257], the filamentary switching should only involve a small disc region near the metal$_1$ (BE)/oxide interface, the remaining oxygen vacancy-rich filament as plug should stay conductive during the switching. In the Pt/TiO_2/Ti structure, the plug is denoted as TiO_{2-y} and the insulating disc range is described as TiO_{2-x} with $x \leqslant y$. Regarding the high conductive character of the plug, the TiO_{2-y}/Ti (TE) interface can be considered as the ohmic contact without any significant transport barrier, while the disc/plug interface should have a tiny barrier. This difference is very important for the later discussions. Fig. 8.1 (b) shows the two different switching modes with opposite polarity in one $(100\ \text{nm})^2$ Pt/6 nm TiO_2/Ti nano-crossbar cell. For consistency with the notation in [4], $I(V)$-hysteresis loops in black and in red are identified as the c8w BRS and 8w BRS, respectively.

As the as-prepared TiO_2-based devices ($d_{TiO2} \leqslant 6$ nm) are electrically conductive in

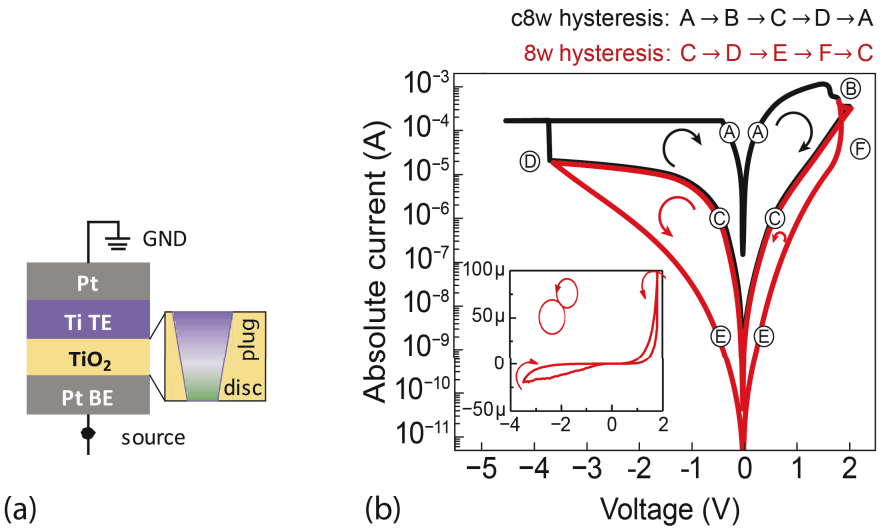

Figure 8.1: *(a) Schematic description of the layer stack with electrical contacts. The right part in (a) is the sketch of the plug and disc region in the TiO_2 layer. (b) The coexistence of two bipolar switching modes with opposite polarities in a Pt (BE)/6 nm TiO_2/Ti cell with $(100\ \text{nm})^2$ cell size. The voltage is applied to the Pt BE. The switching orientation is marked by arrows and the capital letters define the resistance states or switching events. The inset shows the zoomed 8w BRS loop (red curve) in linear scale.*

their initial states (state "A" in Fig. 8.1 (b)), a positive voltage signal to the Pt BE is required to reset the cell via a c8w RESET process (line "B") to a high resistance state (state "C" = c8w HRS). Following the black curve to the negative voltage regime, if the voltage amplitude exceeds the threshold value for a c8w SET process (line "D"), an abrupt SET event into the c8w LRS = "A" is observed. The current in the c8w SET has to be limited by setting a current compliance (here, $|I_{CC}| = 150\,\mu A$) to avoid an irreversible destruction of the device. Summing up, the black cycle "A – B – C – D – A" defines the c8w BRS mode, characterized by an abrupt c8w SET from HRS to LRS at negative polarity, and a gradual c8w RESET at positive polarity.

Starting from the c8w HRS = "C" state and applying a negative voltage, which is insufficient to initiate a c8w SET process, this is $|V| < |V_{c8w,SET}|$, the device can reset to an even higher insulating state (state "E") named 8w HRS*. If a positive voltage with sufficient amplitude is subsequently applied, a moderately abrupt change to a higher current level is observed (line "F"). The current increase is intrinsically limited by the c8w RESET occurring in the same voltage range. Therefore, the 8w LRS* = "C" obtained from the 8w SET process is identical to the HRS. Following the red loop for a full cycle, the sequence "C – D – E – F – C" defines an 8w BRS mode, with opposite polarity compared to the black loop. For clarity, the inset gives the red loop in linear scale together with the orientation as to show how the handwriting "8" is drawn.

8.1.2 Transition from different 8w states to c8w BRS

Besides the transition from c8w to 8w BRS that can be controlled by the reduction of the negative voltage amplitude, the transition from different 8w states to c8w BRS is also observed (see Fig. 8.2). Starting from 8w LRS*, the cell sets to c8w LRS at the negative polarity with $|V| > |V_{c8w,SET}|$ (black curve in Fig. 8.2 (a)) and follows the standard c8w

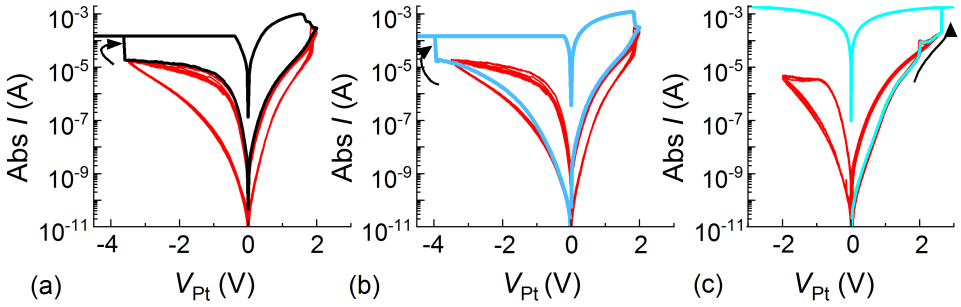

Figure 8.2: *Transition to c8w BRS in two (100 nm)² Pt/6 nm TiO_2/Ti cells: (a) from 8w LRS* = c8w HRS to c8w LRS (black loop equals standard c8w BRS), (b) from 8w HRS* to c8w LRS (blue loop), (c) from HRS* via LRS* to an irreversible conductive state (cyan loop) at the positive polarity.*

RESET loops by applying the opposite polarity. Starting from 8w HRS* at the negative polarity (blue loop in Fig. 8.2 (b)) the same transition can be seen. That means, the c8w LRS can be obtained from either 8w LRS* or 8w HRS* at the negative polarity. In contrast, the cell can not switch from 8w to c8w BRS at the positive polarity. The higher positive voltage leads to the switching towards an irreversible conductive state (cyan curve in Fig. 8.2 (c)).

8.1.3 Stability of 8w resistance states in $Pt/TiO_2/Ti$ devices

Retention test

In order to verify the long-term stability of 8w states, the retention tests of LRS* and HRS* are carried out in two Pt/3 nm TiO_2/Ti cells. In contrast to the volatile effects found in the Ta_2O_5-based systems [102, 103], the 8w BRS states of the TiO_2-based nano-crossbar cells are non-volatile, which are exemplarily demonstrated in Fig. 8.3. The LRS* written by 2.0 V at room temperature reveals a stable retention for 3.5 hours at 125°C. This is a characteristic value also reported for regular switched states in standard Ta_2O_5 devices [70]. In addition, 8w HRS* written by -2.0 V at room temperature are still robust one year later (black line in Fig. 8.3 (b)).

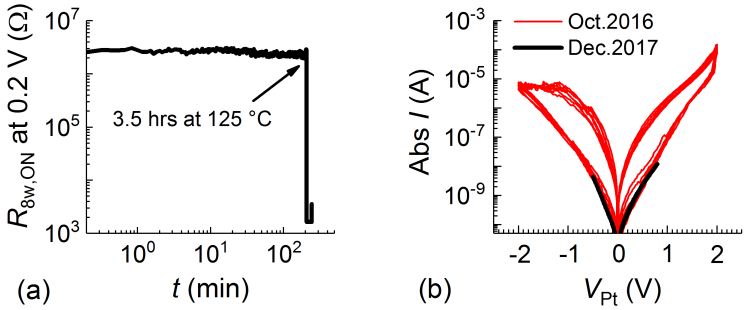

Figure 8.3: *The stability of 8w resistance states in different Pt/3 nm TiO_2/ Ti cells: (a) retention test for 8w LRS* performed at 125°C in a (100 nm)² cell; (b) 8w BRS in red performed in a (80 nm)² cell at room temperature in October 2016. The 8w HRS* was written by -2.0 V in the last red RESET loop. The black lines are the read-out loop measured at room temperature after more than one year storage under nitrogen condition.*

Sweeping stability

Furthermore, the short-term stability of the HRS* and the LRS* in Pt/TiO_2/Ti devices can be supported by the repeated application of consecutive voltage sweeps with the same voltage polarity to the devices being in a certain state.

Starting from the 8w HRS* written by -2 V, the sequential single 8w loops are performed from 0 V $\rightarrow V_{+,\max} \rightarrow$ 0 V, where $V_{+,\max}$ increases from 1.0 V to 2.2 V with 0.2 V

increment by each cycling. As the black loops show in Fig. 8.4, no changes of HRS* can be seen. The similar test is carried out for the LRS* written by 2.0 V. The consecutive loops with applied positive voltage ranging from 0.5 V to 1.7 V with 0.2 V increment are performed. The 8w LRS* in red is not changed during the cycling. The sweeping stability of both resistance states is proved.

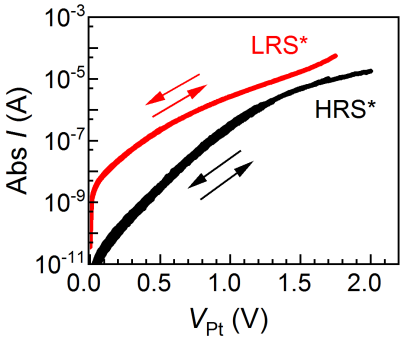

Figure 8.4: *Sweeping stability of 8w resistance states in different Pt/3 nm TiO_2/Ti cells: the reproducibility of the states tested for non-switching read-out loops for HRS* in a (60 nm)^2 cell (black lines) and for LRS* in a (100 nm)^2 cell (red lines).*

Endurance test

In order to provide a qualitative comparison on the switching stability between the two switching modes, the endurance tests have been performed in different Pt/3 nm TiO_2/Ti cells (Fig. 8.5).

By applying standard switching parameters obtained from DC voltage sweep without taking any further optimization, the 8w switching in pulse operation mode shows around

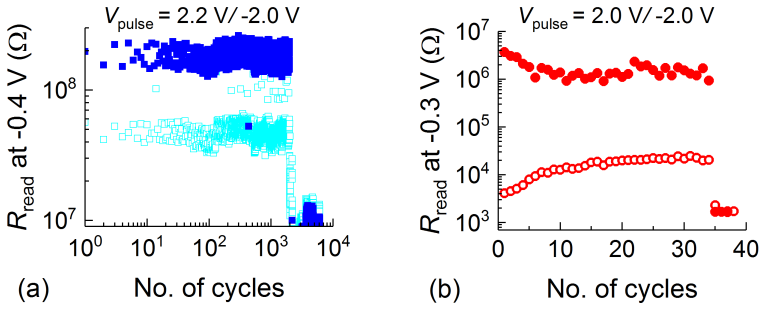

Figure 8.5: *The endurance test of (a) 8w and (b) c8w switching resistance states in pulse mode performed in two Pt/3 nm TiO_2/Ti cells with (80 nm)^2 cell size. The parameters for pulse are listed in each graph.*

10^3 cycles, whereas the stability of the c8w mode is only up to several ten cycles.

In conclusion, it is cleat that the 8w resistance states in Pt/3 nm TiO_2/Ti devices show not only a short-term stability during the DC voltage sweep, but also a long-term stability represented by the long retention time. A higher endurance cycle number can be obtained from 8w BRS compared to c8w BRS.

8.1.4 Multilevel states in 8w BRS

RESET voltage- and cell size influence in DC sweep mode

8w BRS curves show the characteristic self-limiting behavior with respect to the maximum current flowing during the 8w SET and RESET events (Fig. 8.1 (b)). This feature makes the 8w BRS more interesting over the c8w BRS behavior, which often suffers from the current overshoot phenomenon (see [4, 221, 258]). The self-limiting feature of 8w BRS hints on the possibility of multiple resistance states either by 8w SET or RESET process. However, the increase of the positive voltage has no influence on the LRS* value and even brings the cell to a permanent conductive state (see Fig. 8.2 (c)). In contrast, the increase of RESET voltage amplitude leads to higher resistance states (Fig. 8.6 (a)). Besides, the cell size dependence is also discussed.

Due to the gradual nature of 8w RESET process, the 8w RESET voltage is equal to the applied negative stop voltage, that is, $V_{8w,RESET} = V_{-,max}$. In the following, $V_{8w,RESET}$ is utilized in Fig. 8.6. By keeping the voltage amplitude still in the 8w RESET range, i.e. $|V_{8w,RESET}| < |V_{c8w,SET}|$, the raise of the read-out resistance for HRS* ($R_{8w,OFF}$) by means of $|V_{8w,RESET}|$ increase can be seen. The LRS* defined by the applied positive stop voltage, however, remains the same. In addition, the $I(V)$ behavior shows a significant asymmetry with respect to the voltage polarity, especially for higher $|V_{8w,RESET}|$. Similar

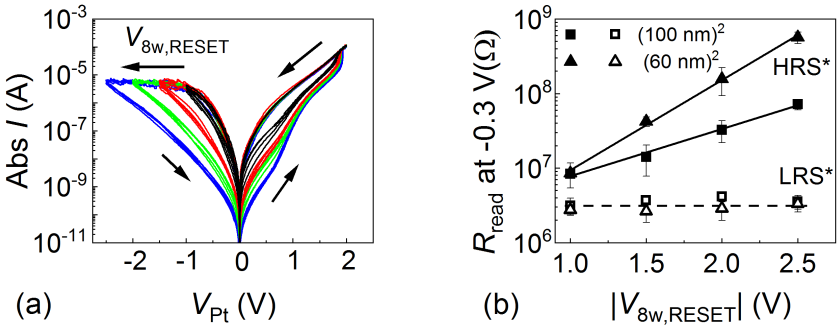

Figure 8.6: *(a) The $I(V)$ characteristics for increased $|V_{8w,RESET}|$ obtained in a (60 nm)^2 Pt/3 nm TiO_2/Ti cell. (b) The readouts for HRS* (solid) and LRS* (open) as a function of $|V_{8w,RESET}|$ for the cell size of (60 nm)^2 (triangle) and (100 nm)^2 (square).*

RESET voltage dependent HRS* are also observed in the Pt/6 nm TiO_2/Ti device, which are not shown repeatedly.

To quantitatively compare the readouts obtained from two different device sizes, $(60\,\text{nm})^2$ and $(100\,\text{nm})^2$ in the same Pt/3 nm TiO_2/Ti sample, the values are plotted as the function of $|V_{8w,RESET}|$ in Fig. 8.6 (b). It turns out that the read-out resistance values for LRS*, $R_{8w,ON}$ (open symbols), are almost constant and independent on the RESET voltage and the device size. As the LRS* is identical to the c8w HRS, this size-independence implies a filamentary-type switching in both 8w BRS and c8w BRS. In contrast to LRS*, HRS* show increased read-out values, $R_{8w,OFF}$ (solid symbols), by increasing the $|V_{8w,RESET}|$. The increment of $R_{8w,OFF}$ by a factor of ten is achieved by $\Delta|V_{8w,RESET}|$ of about 0.83 V and 1.58 V for devices of $(60\,\text{nm})^2$ and $(100\,\text{nm})^2$ size, respectively. In addition, $R_{8w,OFF}$ show a certain size-dependence but the values are not proportional to the cell size. This size-dependence could be explained by an additional current contribution from the non-switching regime. The influence of this current contribution that is described as current path parallel to the filamentary current path [259], will be discussed in the following with the help of an equivalent electrical circuit (Fig. 8.7).

As the filament current and the contribution from the non-switching regime are defined as I_1 and I_2, respectively, the measured total current (I) is considered as the sum of I_1 and I_2. Since the filament current is not cell area dependent [260], it can be kept the same for the different cell sizes. The leakage current in the non-switching regime I_2 can be described as $J_2 \cdot A_{cell}$, where J_2 is the current density, A_{cell} is the cell size. For a larger cell, the cell size can be $A_{cell} + \Delta A$. The current change for two 8w state in different cell size is summarized in Tab. 8.1.

The total current for HRS* and LRS* , namely I_{HRS*} and I_{LRS*}, and the resistance ratio between $R_{8w,OFF}$ and $R_{8w,ON}$ can be described as follows:

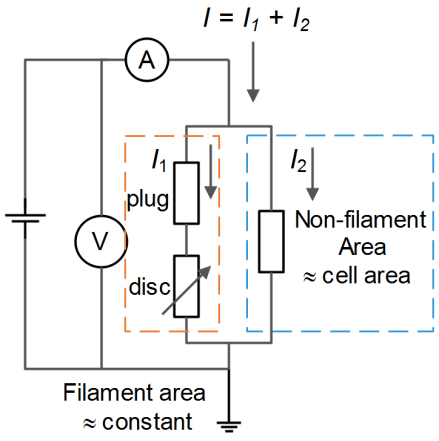

Figure 8.7: *Equivalent circuit of the Pt/TiO_2/Ti structure*

	cell size A_{cell}		cell size $A_{\text{cell}} + \Delta A$	
State	Filament	Non-switching regime	Filament	Non-switching regime
HRS*	I_1	$I_2 = J_2 \cdot A_{\text{cell}}$	I_1	$I_2 + \Delta I_2 = J_2 \cdot (A_{\text{cell}} + \Delta A)$
LRS*	$I_1 + \Delta I_1$	I_2	$I_1 + \Delta I_1$	$I_2 + \Delta I_2$

Table 8.1: *Parameters from the equivalent circuit diagram in Fig. 8.7 for two resistance states, namely LRS* and HRS*, and two cell sizes, namely A_{cell} and $A_{cell} + \Delta A$.*

$$\begin{aligned} I_{\text{HRS*}}(smaller\ device) &= I_1 + I_2 \\ I_{\text{LRS*}}(smaller\ device) &= I_1 + \Delta I_1 + I_2 \\ I_{\text{HRS*}}(bigger\ device) &= I_1 + (I_2 + \Delta I_2) \\ I_{\text{LRS*}}(bigger\ device) &= I_1 + \Delta I_1 + (I_2 + \Delta I_2) \end{aligned} \tag{8.1}$$

$$\begin{aligned} The\ read-out\ resistance:\ R_{\text{8w}} &= |\frac{V_{\text{read}}}{I} = \frac{-0.3\ V}{I}| \\ for\ smaller\ device:\ R_{\text{8w,OFF}} &= |\frac{V_{\text{read}}}{I_{\text{HRS*}}}| = |\frac{-0.3\ V}{I_1 + I_2}| \\ for\ bigger\ device:\ R_{\text{8w,OFF}} &= |\frac{V_{\text{read}}}{I_{\text{HRS*}}}| = |\frac{-0.3\ V}{I_1 + (I_2 + \Delta I_2)}| \end{aligned} \tag{8.2}$$

As the read-out values for LRS* are constant and almost the same for both cell sizes (Fig. 8.6 (b)), the increase of the current originating from the non-filament area can be considered as negligible. On the contrary, for the HRS* if the current density in the non-filament region can be assumed as constant and non-negligible, the additional current ΔI_2 through the extra non-filament region for larger device size should provide a comparable contribution to the total current and thus the total resistance in the larger device is lower than in the smaller device. This phenomenon can be clear to be described based on the mathematical equations grouped under (8.1) and (8.2). Therefore, a more significant resistance increase in cells with smaller cell size, like $(60\ \text{nm})^2$ should be larger than in the bigger cell size, like $(100\ \text{nm})^2$.

RESET voltage influence in pulse mode

Besides the 8w switching in the voltage sweep mode, it can be pulsed by means of consecutive voltage pulses with 100 ns pulse length as well. Fig. 8.8 (a) describes the pulse sequence in a Pt/3 nm TiO_2/Ti cell and Fig. 8.8 (b) shows the corresponding readouts after the write pulse signal. All resistance values are read out at -0.4 V pulse and 1 ms pulse length, among which the reference state LRS* = HRS is marked with the broken red line. The corresponding read-out resistance after an 8w SET sweep, i.e. $R_{\text{8w,ON}} \approx 700\ \text{k}\Omega$, is

shown as the green square in Fig. 8.8 (b). For an easier visibility, this resistance value is also indicated by the dashed line.

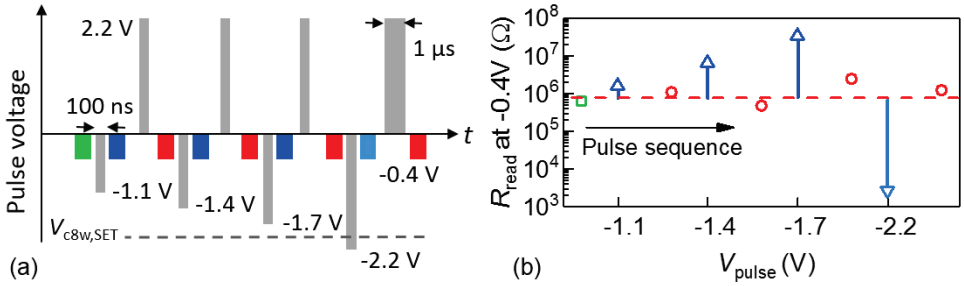

Figure 8.8: *Pulsed switching behavior in the 8w BRS mode. (a) A schematic diagram of pulse procedure carried out in a (100 nm)² Pt/3 nm TiO_2/Ti cell. (b) The read-out resistances measured at -0.4 V after each write pulse. The red circles represent the read-out values of LRS* programmed with a signal of 2.2 V. The green square is the initial read-out value recorded after the last DC sweep loop. The triangles mark the read-out values after applying a negative pulse starting at -1.1 V and ending at -2.2 V, which exceeds the threshold voltage for c8w SET. The figure is redrawn from [261].*

In a sequence of four switching cycles the negative write pulse is stepwise decreased from -1.1 V to -2.2 V (Fig. 8.8 (a)), while an intermediate SET pulse of 2.2 V is always applied to switch the device back to the "reference" state. In the first RESET pulse of -1.1 V the device resets into the HRS* with $R_{8w,OFF} \approx 2$ MΩ. Subsequent negative pulses with increased voltage amplitudes switch the HRS* to multiple values up to $R_{8w,OFF} \approx 40$ MΩ for $V_{8w,RESET} = -1.7$ V. The successfully pulsed SET operations inbetween are demonstrated by the successfully achieved LRS* of ≈ 700 kΩ given as the red circles in Fig. 8.8 (b). If the write signal exceeds the threshold voltage for c8w SET, that is -2.2 V, the device switches into the c8w LRS with a read-out resistance of only 2.5 kΩ. And again, a positive voltage pulse of 2.2 V applied for 1.0 µs recovers the stable "reference" state HRS = LRS*. These experiments demonstrate that the coexistence of c8w and 8w BRS modes in TiO_2-based devices can be obtained from various operation modes ranging from continuous voltage sweeps (≈ 20 mV/10 ms) to short voltage pulses (≈ 2 V/100 ns). Especially, the multiple HRS* can be achieved in both operation modes.

As summary for this section, the stable and reproducible 8w BRS behavior in Pt/3 nm TiO_2/Ti devices shows controllable multiple resistance states and a fast switching possibility within 100 ns. The multiple states are prominent for the increase of data density [262–264] and moreover, these multiple states in ReRAM cells are proved to be able to increase the graphic recognition accuracy in recent studies [265]. In addition, the variable resistance ratio between HRS* and LRS* can achieve two orders of magnitude, which is close to the resistance ratio in a good performing c8w BRS with multilevel possibility [266].

8.1.5 Interface effect in $Pt/(Al_2O_3)/TiO_2/Ti$ devices

Based on the phenomenological discussion in chapter 4, the initial state and the c8w SET voltage ($V_{c8w,SET}$) in 3 nm TiO_2-based devices can be tuned by adding 1 -3 nm artificial Al_2O_3 layer between the Pt electrode and the TiO_2 layer (see Fig. 4.27). As the transition between 8w and c8w BRS is sensitive to the applied negative voltage amplitudes, this insertion of Al_2O_3 can change the possibility of the two BRS modes through the change of c8w SET voltage. The discussion is as follows.

For adding 1 nm Al_2O_3 at the Pt/TiO_2 interface, the exemplary $I(V)$-switching loops for both switching modes can still be observed (Fig. 8.9 (a)) and the amplitude of $V_{SET,c8w}$ is significantly shifted to > 1 V (Fig. 8.9 (b)). However, for $d_{Al2O3} \geqslant 2$ nm the 8w BRS disappears and only c8w BRS can be seen. The dependence of the "threshold" voltage for the c8w SET process on the Al_2O_3 layer thickness in the $Pt/Al_2O_3/3$ nm TiO_2/Ti stack is summarized in Fig. 8.9 (b).

The limited coexistence of 8w and c8w BRS in one cell by the Al_2O_3 film thickness might originate from the active switching layer including the TiO_{2-x} layer. The reasons could be: (1) the pinholes in the ultra-thin Al_2O_3 layer. To grow 1 nm Al_2O_3, only eight ALD cycles are required. It is reasonable to assume that the area density of pinholes might become significant compared to the device size of about 10^4 nm^2. The area with pinhole in Al_2O_3 layer could involve TiO_{2-x} in the switching process. (2) The different oxygen diffusivity in ultra-thin 1 nm Al_2O_3 layer compared to the thicker one. Therefore, such a thin Al_2O_3 layer cannot confine the ionic motion of oxygen or oxygen vacancies in itself during c8w cycling. This assumption is partially supported by the high oxygen diffusivity from oxygen diffusion experiments in amorphous Al_2O_3 thin films [267, 268]. Since both the amorphous and 1 nm ultra-thin Al_2O_3 film should have strong deviation

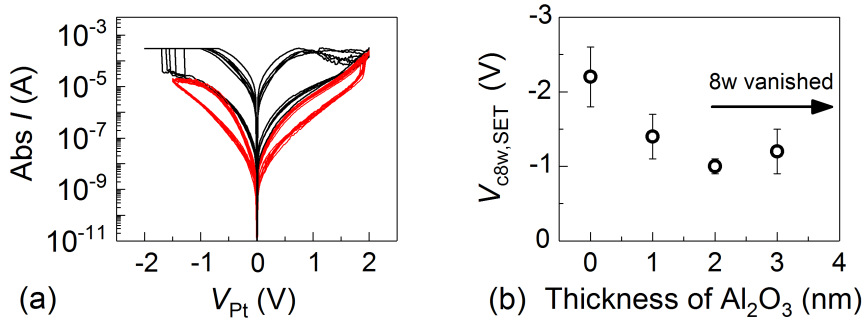

Figure 8.9: *(a) Representative $I(V)$ characteristics in a (100 nm)^2 Pt/1 nm Al_2O_3/3 nm TiO_2/Ti cell. Black curves show c8w BRS and red curves represent 8w BRS. (b) The dependence of the mean value of $V_{c8w,SET}$ in the four stacks with (100 nm)^2 cell size as a function of the thickness of the Al_2O_3 layer inserted at the Pt/TiO_2 interface.*

from the crystalline Al_2O_3 structure, the enhancement of the oxygen diffusivity in both films could be expected.

As a conclusion, the properties of interface of Pt/TiO_{2-x} can be modified by inserting Al_2O_3 and thus leads to the reduction of both $V_{c8w,SET}$ amplitudes and the chance of 8w BRS appearing. The disappearance of the 8w BRS mode via $d_{Al2O3} \geqslant 2$ nm emphasizes the distinctiveness of this interface.

8.1.6 Interface effect in Pt/TiO_2/Al_2O_3/TE device

On the contrary, the insertion of thicker Al_2O_3 at the TiO_2/Ti interface does not eliminate the 8w BRS. In addition to the typical c8w BRS with $|I_{CC}| = 150$ µA in Pt/3 nm TiO_2/3 nm Al_2O_3/TE cells with Ti or TiN electrode (see chapter 4), some cells of them reveal 8w BRS, if a higher $|I_{CC}|$ (Fig. 8.10 and Fig. 8.11 (b)) or an increase of $V_{+,max}$ was applied (Fig. 8.11 (c-d)).

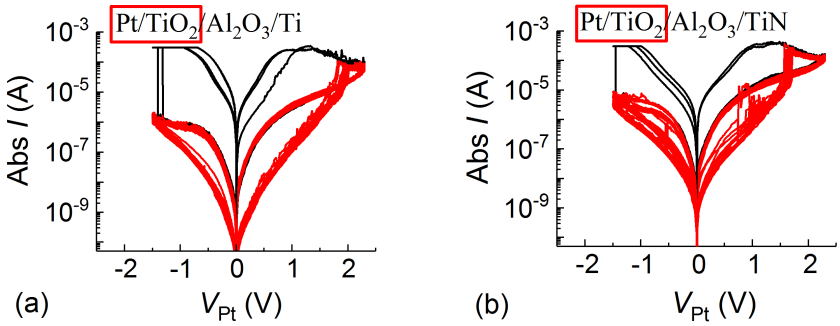

Figure 8.10: *The coexistence of c8w and 8w BRS observed in two (100 nm)² Pt/3 nm TiO_2/3 nm Al_2O_3/TE cells with: (a) TE = Ti, (b) TE = TiN. The operation parameters were $|I_{CC}| = 300$ µA and $V_{+,max} = 2.3$ V and $V_{-,max} = -1.5$ V.*

A Pt/3 nm TiO_2/3 nm Al_2O_3/Ti cell shows firstly the stable c8w BRS behavior in 20 cycles with I_{CC} from 50 µA (Fig. 8.11 (a)) to 300 µA (not shown). For higher $|I_{CC}| = 600$ µA, the cell can firstly switch stable for several cycles (red curves in Fig. 8.11 (a)) and then after the 15th c8w BRS cycle the switching direction is changed from c8w (red arrows in Fig. 8.11 (b)) to the 8w BRS (green arrows in Fig. 8.11 (b)), when a slim 8w RESET loop takes place in the negative polarity.

This 8w loops are stable but still slim for the negative voltage branch with $V_{+,max}$ increasing to 2.4 V and keeping $V_{-,max} = -1.0$ V (blue curves in Fig. 8.11 (c)). And the sweeping stability of the corresponding 8w HRS* is verified by the several single cyan loops in one polarity. To further increase the operation voltage amplitudes, the stability of the 8w BRS loops and the HRS* value are enhanced (Fig. 8.11 (d)). These phenomena indicate that the insertion of Al_2O_3 between TiO_2 layer and Ti electrode cannot avoid the 8w switching.

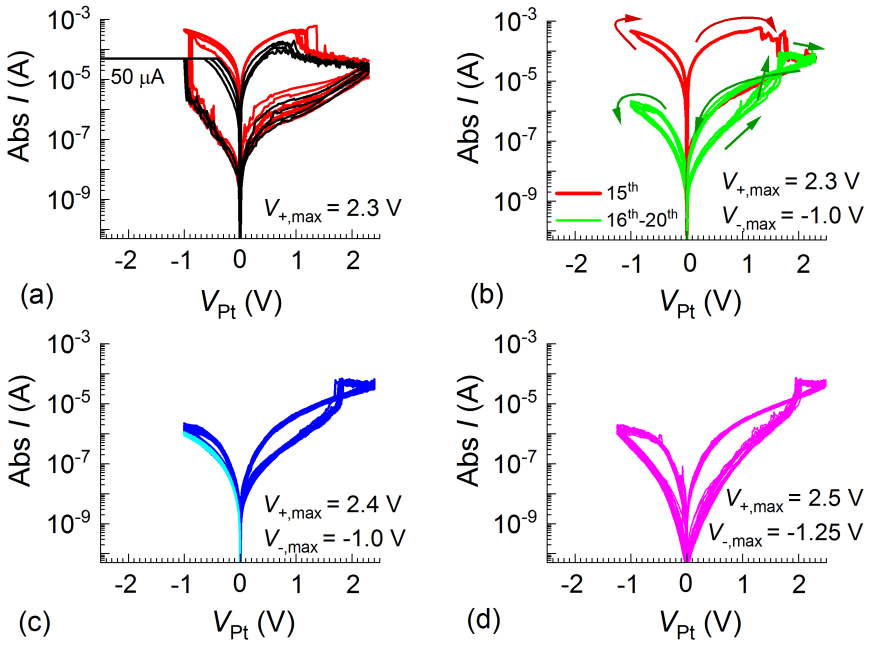

Figure 8.11: *(a-b) Transition from c8w to 8w BRS is observed in a (100 nm)^2 Pt/3 nm TiO_2/3 nm Al_2O_3/Ti cell by $|I_{CC}|$ increased to 600 µA. (c-d) Stable 8w BRS with switching parameters listed in the lower-right corner of each graph. The switching direction is depicted by arrows. For each parameter variation at least 20 cycles were performed.*

8.2 Electronic transport in 8w BRS devices

8.2.1 Temperature realted $I(V)$ behavior in 8w states

The current response in the nano-sized transition metal oxide-based devices is strongly dominated by the electronic contribution. Therefore, the understanding of the charge transport behavior in various switching states is of utmost importance. For this purpose, the charge transport behavior of the two 8w states in Pt/3 nm TiO_2/Ti devices is discussed. To make the discussion in different cells comparable, the two (80 nm)^2 cells showing similar and stable 8w BRS cycles are investigated with respect to the temperature related $I(V)$ characteristics.

After 20 cycles (grey curves in Fig. 8.12 (a) and Fig. 8.13 (a)), the stabilized 8w LRS* and HRS* were written by 2.0 V and -2.0 V, respectively. Then they were analyzed with respect to the voltage and temperature dependent current response, i.e., $I(V,T)$. The read-out voltage is ranging between -0.8 V and 0.8 V. In order to find out the possible transport mechanisms, the read-out $I(V)$ loops for both 8w LRS* and 8w HRS* are plotted as $\ln(I/V)$ against T^{-1} and $\ln(|I|/V^2)$ against V^{-1} for environment temperatures between 20°C and 70°C in Fig. 8.12 (b-d) and in Fig. 8.13 (b-d), respectively. Due to the

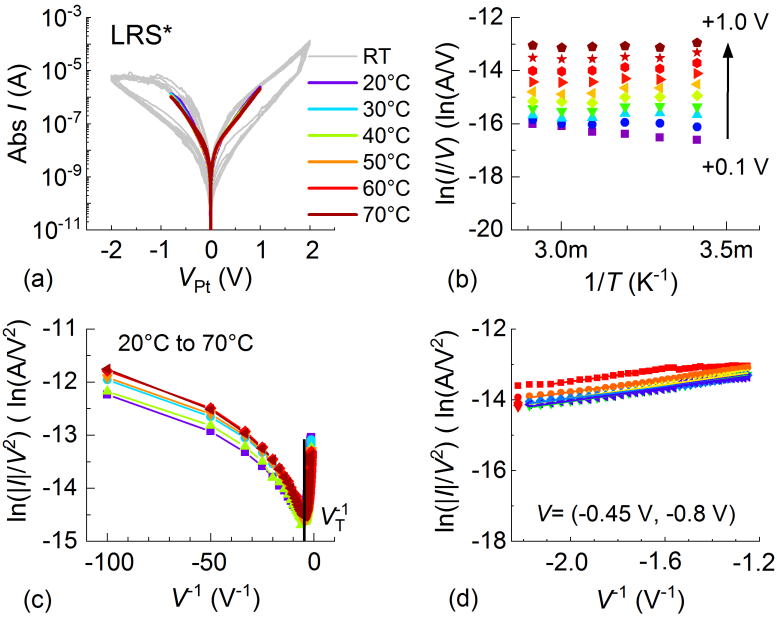

Figure 8.12: *(a) Stable $I(V)$ characteristics of 8w BRS (grey) and the read-out LRS* in a (80 nm)^2 Pt/3 nm TiO_2/Ti cell. The 8w BRS curves in grey are measured at room temperature and the corresponding rainbow colored $I(V)$ for LRS* are measured for the surrounding temperature ranging from 20°C to 70°C. (b) The ln(I/V) vs. T^{-1} plot for LRS* at the positive voltage branch. (c) The ln($|I|/V^2$) vs. V^{-1} plot at the negative voltage branch. (d) The zoom-in region for FN tunneling in (c).*

similar analytical results obtained from both positive and negative voltage branches, the plots for one voltage branch are shown.

Three main features are summarized in the following:

(1) A weak temperature dependence is observed for both 8w states (colored lines in Fig. 8.12 (a-b) and in Fig. 8.13 (a-b);

(2) As indicated from the ln(I/V) vs. T^{-1} plots in Fig. 8.12 (b) and Fig. 8.13 (b), neither Poole-Frenkel nor ohmic conduction nor Schottky emission could be the dominating transport mechanism for 8w LRS* and HRS*, because of the rather weak temperature dependence and no physically meaningful barrier upon applying these models can be obtained (details for these models in sections 2.4.2, 2.4.3 and 2.4.5);

(3) In the plot of ln($|I|/V^2$) vs. V^{-1}, the curves show a more significant temperature dependence in the lower voltage than in the higher voltage (Fig. 8.12 (c-d) and Fig. 8.13 (c-d));

(4) The transition voltage ($V_T \approx (0.15 \pm 0.05)$ V) that separates the two voltage ranges can be found in both Fig. 8.12 (c) and Fig. 8.13 (c). For the higher voltage amplitude, i.e. $|V|^{-1} < |V_T|^{-1}$, this linear region is further zoomed in Fig. 8.12 (d) and

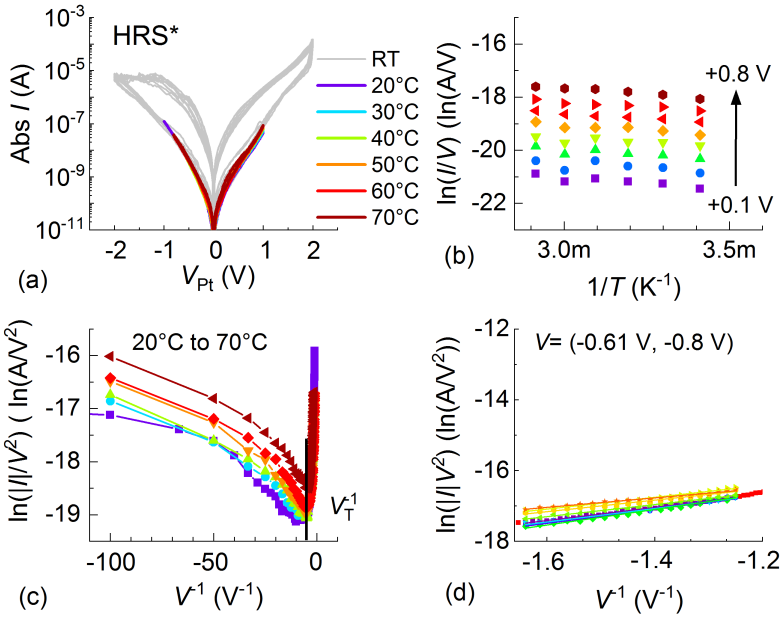

Figure 8.13: *(a) Stable $I(V)$ characteristics of 8w BRS (grey) and the read-out HRS* in a (80 nm)^2 Pt/3 nm TiO_2/Ti cell. The 8w BRS curves in grey are measured at room temperature and the corresponding rainbow colored $I(V)$ for HRS* are measured for the surrounding temperature ranging from 20°C to 70°C. (b) The ln(I/V) vs. T^{-1} plot for HRS* at the positive voltage branch. (c) The ln($|I|/V^2$) vs. V^{-1} plot at the negative voltage branch. (d) The zoom-in region for FN tunneling in (c).*

Fig. 8.13 (d) and can be conventionally attributed to Fowler-Nordheim (FN) tunneling. In contrast, the non-linear region within the low voltage amplitude region ($|V|^{-1} > |V_T|^{-1}$) is considered to be dominated by the direct tunneling through a trapezoidal barrier [154, 269].

Summing up, an exponential-type voltage dependence combined with a weak temperature dependent read-out (V) loops for LRS* and HRS* hints on a higher probability of a tunneling transport mechanism. The voltage inflection point, V_T, indicates a smaller tunneling barrier height at the TiO_{2-y}/Ti interface (see for example [270]).

8.2.2 Electronic conduction behavior in the 8w BRS states

8w states described by Simmons' model

From the former section the total current in the LRS* and HRS* can be described by a superposition of temperature-assisted direct tunneling dominating at low voltage amplitudes up to $V_T \approx (0.15 \pm 0.05)$ V and field-assisted tunneling showing up for higher applied voltage amplitudes. To focuse on the transition between two voltage ranges and to neglect

the weak temperature dependence below around 0.15 V, the current response can be described by the elelctron tunneling process through an asymmetric (trapezoidal) barrier. A one-dimensional schematic energy diagram is drawn in Fig. 8.14 (a). The z-axis is perpendicular to the electrodes and along the center of the switching filament. The figure shows the situation of a negative voltage applied to the Pt BE with an amplitude that enables field-assisted (or Fowler-Nordheim) tunneling. As the ideal TiO_{2-y}/Ti interface should provide an ohmic contact considering the work function of Ti metal ($\approx$ 4.33 eV [271]) and the electron affinity of 4.2-4.8 eV in stoichiometric TiO_2 [130, 244, 245], Φ_1 denotes the barrier height possibly placed between the strongly oxygen deficient TiO_{2-y} (conductive plug) and the minor reduced TiO_{2-x} (insulating disc) region in the oxide layer. Φ_2 denotes the barrier height at the Pt/TiO_{2-x} interface. L is defined as the length of the filament's disc region [205] and should equal the length of the tunneling barrier for the field-free case. The quantum mechanical tunneling through a trapezoidal barrier is calculated by means of the generalized formula of Simmons [272] (for details see chapter 2 section 2.4.1). Based on this model the total current I is related to the following important factors: the tunneling area A, the effective tunneling mass of electrons m* [273], the barrier heights Φ_1, Φ_2 and tunneling barrier length L, where electrons transfer mainly from the Fermi-level in the Pt electrode to the next achievable empty states of the conduction band in the titanium dioxide film. l is the effective tunnel barrier, which can be calculated from Φ_2, L, Φ_1 and the temporally applied voltage amplitude during the voltage sweep

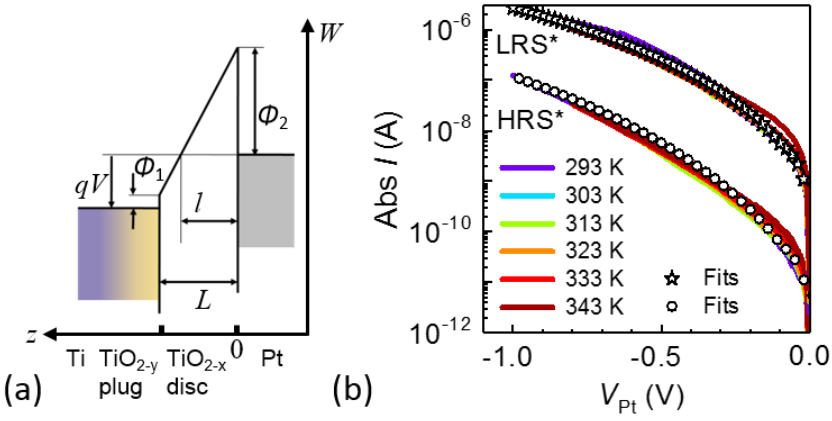

Figure 8.14: *(a) A schematic energy band diagram for the negative voltage applied to Pt. The barrier region, TiO_{2-x}, denotes the insulating gap ("disc") between Pt and the conductive "plug" region, TiO_{2-y}. (b) The read-out $I(V)$ loops for the LRS* and the HRS* (colored lines) characterized at different temperatures extracted from Fig. 8.12 and Fig. 8.13, respectively. The best calculated $I(V)$ curves obtained from the Simmons' equation are marked by symbols. The optimized parameters are listed in Tab. 8.2.*

(for details see section 2.4.1). In Simmons' model electrons in both metal electrodes are assumed to follow the Fermi-Dirac statistics at zero temperature, which diminishes the weak temperature dependence of current and restricts the barrier form to be trapezoidal. As the $I(V)$ loops for 8w LRS* and HRS* show temperature dependence from 293 K to 343 K for a certain voltage range, it makes the application of Simmons' model to the two states reasonable (Fig. 8.14 (b)). In order to minimize the possible influence from the derivation between metallic TiO_{2-y} layer and real metal electrode, only the negative voltage range is discussed based on this model.

As the geometry of filament plug and disc as well as the interfacial barriers are critical for the current calculation, these parameters are discussed in the following.

The form of the switching filament in c8w VCM-type devices differentiates into conical and hourglass-like shapes [52,205,242,274–276]. However, nanoscale analytical studies on the filament's shape of 8w BRS nanosized devices are rare. Recently, Du et al. [238] reported a very careful study on the nature of the filaments in an electroformed Nb:$SrTiO_3$/Fe:$SrTiO_3$/(Au)Pt epitaxial device, which shows 8w switching as reported in [277]. The authors identified an existence of cone-shaped multi-filament after the switching process via scanning transmission electron microscopy. Based on the mentioned reports and the coexsistence of c8w and 8w BRS in one cell, the model for the 8w BRS in the nanoscale Pt/TiO_2/Ti devices is assumed to involve conical-shaped filament(s) and a disc-like tunneling barrier at the Pt/TiO_2 interface.

The tunneling area A is defined by the spot size of the plug, which can be ranging from 1.66 nm^2 [243] to 500 nm^2 [136,242] in VCM-type switching devices. Moreover, by means of a "scalpel SPM" technique Celano et al. [94] reported the spot area of about 10^2-10^4 nm^2 close to the OEL. This supports a cone-shaped filament with a thicker end at the OEL and a smaller front close to the Pt electrode. From the optimized simulation result, A is determined to be ≈ 50 nm^2. This value is very reasonable, as it is still kept in the range given by the literature. It has to be mentioned that, the lateral confinement effects are not considered in this case and therefore, there should be no lateral mesoscopic transport in contrast to other smaller devices [278]. In addtion, the effective mass of electrons (m^*) in TiO_2 films is assumed to equal the free electron mass (m_0) [120,121].

The best simulation results for the two 8w states are shown in Fig. 8.14 (b). The main difference between LRS* and HRS* is the varied dominating barrier, i.e. $\Phi_2 \approx 1.0$ eV and $L \approx 1.25$ nm for the LRS*, and $\Phi_2 \approx 1.25$ eV and $L \approx 1.65$ nm for the HRS*. All the optimized parameters are summarized in Tab. 8.2.

Summing up all the analytical results for the 8w and c8w states, several conclusions about the current conduction behavior in Pt/3 nm TiO_2/Ti nano-crossbar devices can be drawn in the following:

1. Stable and reproducible resistance states of 8w BRS can be explained by electron

States	Tunneling area A (nm^2)	Φ_1 (eV)	Φ_2 (eV)	Tunneling length L (nm)
HRS*	50	0.1	1.25	1.65
LRS*	50	0.1	1.0	1.25

Table 8.2: *The simulation parameters used in Fig. 8.14 (b). The effective mass* $m^* = m_0$.

tunneling through an asymmetric barrier that includes the direct tunneling in the low voltage amplitude regime and the Fowler-Nordheim tunneling at higher voltage amplitude.

2. The change from LRS* to HRS* involves an increase in the length L, which defines a rough position of the plug/disc interface for each written state, and the dominating barrier height Φ_2 associated with the Pt/TiO_{2-x} interface.

3. The c8w and 8w BRS events in the TiO_2-based nano-crossbar devices refer to the same Pt/TiO_{2-x} Schottky interface and the dominating process is selected by the amplitude of the negative voltage applied to the Pt bottom electrode.

A further application of the Simmons' tunneling model for the low temperature $I(V)$ characteristics as well as for the multiple resistance states are performed in the latter subsections. More than that, to link the resistance state change to ionic configuration variation, a continuum model based on assumed oxygen vacancy profiles is presented in the following sections.

LRS* for the low temperature measurement

To better understand the role of the thermal energy on the tunneling process, the $I(V)$ characteristics for LRS* in the same cell used in Fig. 8.12 were also measured from 80 K to 277 K under the vacuum level of around 10^{-4} mbar. The cell remains in the same LRS* before cooling down to 80 K with liquid N_2. For the temperature range from 293 K to 343 K (Fig.8.14 (b)) the increase of thermal energy is only around 1.2 times and the read-out $I(V)$ loops for LRS* show barely temperature dependent. On the contrary, for the temperature variation from 80 K to 277 K, that means the thermal energy changes over 3 times, a clear temperature dependence of the read-out $I(V)$ curves is observed in Fig. 8.15 (a) and the current level increases around one order of magnitude. This significant temperature dependence might originate from the temperature-assisted tunneling.

For clarity, the read-out $I(V)$ loops for LRS*, measured under 85 K, 185 K and 277 K, respectively, are chosen. Although the experimental data show a slight shift at the positive bias (blue line in Fig. 8.15 (b)) caused by a limited resolution of the Keithley system and inevitable charging effect, the comparison between the experimental data and the

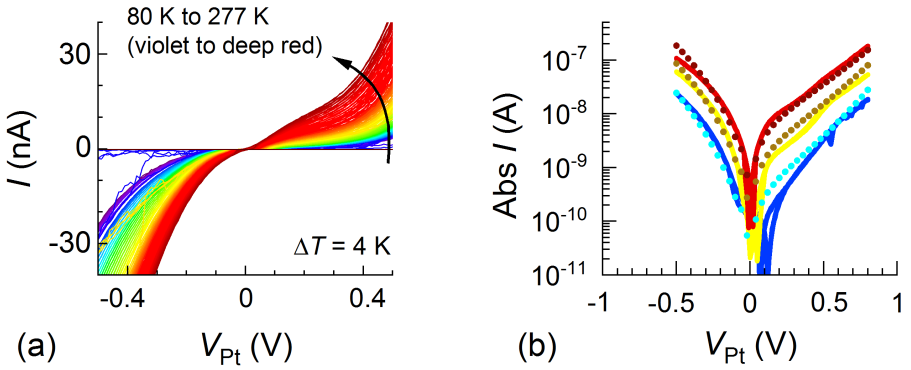

Figure 8.15: *(a) $I(V,T)$ characteristics for LRS* in a Pt/3 nm TiO_2/Ti cell with (80 nm)^2 cell size. The surrounding temperature is increased from 80 K to 277 K under vacuum. (b)The best simulation results on three curves measured at 85 K, 185 K, 277 K represent as dash lines. The simulated parameters are listed in Tab. 8.3.*

Simmons' calculation for negative bias is not that significantly influenced. All the three read-out loops can be well matched by the simulation curves (Fig. 8.15 (b)). As Tab. 8.3 shows, by applying the same tunneling barrier Φ_2 of 1.0 eV, the positively temperature dependent response current level is only related to the decreased tunneling length from 1.62 nm at 85 K to 1.3 nm at 277 K. This result indicates that the thermal activation energy decreases the effective barrier length without any impact on the barrier heights.

T (K)	Tunneling area A (nm^2)	Φ_1 (eV)	Φ_2 (eV)	Tunneling length L (nm)
85	50	0.1	1.0	1.62
185	50	0.1	1.0	1.42
277	50	0.1	1.0	1.30

Table 8.3: *The simulation parameters used for the dash lines shown in Fig. 8.15 (b). The effective mass m^* is kept as 1·m_0.*

As such temperatures are low enough to suppress any ion movement and the LRS* is proofed to be non-volatile, this change of "barrier length" should not be related to any ionic processes. Therefore, the most probable explanation is that the tunneling barrier deviates from the idealized trapezoidal form. As suggested by various references [109,279], the tunneling through a Schottky barrier, which is approximated as a parabolic form, leads to a thermally activated tunneling process with the obvious temperature dependence. For raised temperatures the thermally activated electrons can pass a smaller tunneling length due to a parabolic-shaped barrier and thus contribute to a dramatical increase of the current level (for details see section 2.4.1).

Multiple HRS* described by Simmons' model

As the multiple resistance states are prominent for dealing with the increase of data density [262–264, 266], it is worth studying the multilevel HRS* observed in the TiO_2-based devices. These multilevel states can be obtained by increasing the $|V_{8w,RESET}|$ either in the full $I(V)$ cycles (Fig. 8.6 (a)) or in consecutive voltage sweeps with one voltage polarity (Fig. 8.16 (a)).

Before doing the continuous RESET cycles with increased RESET stop voltage amplitudes, the Pt/3 nm TiO_2/Ti cell was firstly set to the LRS* by 2 V (not shown). It has to be mentioned that during the consecutive voltage sweeps with one voltage polarity no any additional 8w SET process is performed inbetween. The resistance state written by the last RESET loop keeps at least the sweeping stability during the next RESET loop before a new state is written by a higher RESET voltage amplitude. By keeping $m^* = m_0$, $A \approx 50$ nm^2 and $\Phi_1 = 0.1$ eV constant, these multiple 8w HRS* can be well matched by tuning Φ_2 and L based on the Simmons' tunneling model (open dots in Fig. 8.16 (a)).

As summarized in Tab. 8.4, the change of multiple HRS* can be attributed to an increase of Φ_2 and L. Interestingly, these simulation values either from full loops or from steady RESET cycling are very comparable to each other and to the former simulation results (see Fig. 8.14) for both LRS* and HRS*. In addition, the values of the barrier height and the barrier length obtained from simulation are all reasonable, since both are still within the boundaries defined by literature and experimental values.

In summary, the interpretation of the current conduction of different 8w states in Pt/TiO_2/Ti devices by means of electron tunneling through an asymmetric barrier pro-

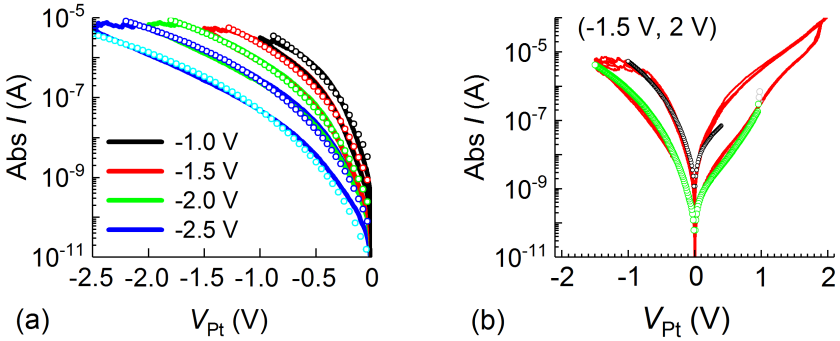

Figure 8.16: *(a) The incremental RESET process (half cycle in color) obtained by increasing the voltage amplitude of negative polarity to Pt BE. After the LRS* written by 2 V, the n^{th} RESET process is always starting from the previous defined HRS* in the (n-1)th cycling. (b) Several 8w BRS full cycles (in red) obtained by the negative voltage of -1.5 V and the positive voltage of 2 V to Pt BE. (a) and (b) show the experimental curves (straight lines) that tested in two (60 nm)^2 Pt/3 nm TiO_2/Ti cells and the simulation results (open dots). The optimized parameters are listed in Tab. 8.4.*

States	V (V)	Tunneling area A (nm^2)	Φ_1 (eV)	Φ_2 (eV)	Tunneling length L (nm)
LRS* Fig. 8.16 (a)	2.0	50	0.1	0.80	1.30
HRS* Fig. 8.16 (a)	-1.0	50	0.1	0.85	1.45
HRS* Fig. 8.16 (a)	-1.5	50	0.1	0.95	1.55
HRS* Fig. 8.16 (a)	-2.0	50	0.1	1.10	1.60
HRS* Fig. 8.16 (a)	-2.5	50	0.1	1.30	1.70
LRS* Fig. 8.16 (b)	2.0	50	0.1	0.9	1.20
HRS* (not shown)	-1.0	50	0.1	0.9	1.40
HRS* Fig. 8.16 (b)	-1.5	50	0.1	0.95	1.55

Table 8.4: *Simulation parameters used for the dots in Fig. 8.16. The effective mass m^* is kept as 1·m_0.*

vides reasonable values for the derived physical parameters. The switch of the multiple HRS* induced by the $|V_{8w,RESET}|$ variation and the switch between the HRS* and LRS* can be interpreted by the change of the barrier height and length in the Simmons' equation. This change of the barrier properties should originate from the oxygen vacancy movement towards the Pt/TiO_{2-x} interface. However, a weak, but, non-negligible temperature dependence of the current-voltage curves exists in Fig. 8.12, Fig. 8.13 and Fig. 8.15 cannot be explained by the simple triangular-shaped band assumed in the Simmons' model. For the temperature region down to around 80 K, the significant temperature dependent read-out $I(V)$ loops for LRS* should originate from the change of tunneling barrier length, which can be further linked to a parabolic band approximation.

8w states described by the continuum model

A more realistic approximation performed by a continuum model considers the formation of a space charge layer at the Pt/TiO_{2-x} Schottky interface with accompanying band bending effects. Based on the semiclassical single-band transport theory, this model combines the Fermi-Dirac statistics of electrons and two-fold donor-type oxygen vacancies with the Poisson equation for the electrostatic potential in a one-dimensional model geometry [101, 101, 205]. The simulation is performed by C. Funck in analogy to the procedure described in [107].

The switching between LRS* and HRS* is attributed to a change in the total concentration of oxygen vacancies, $N_{VO} = [V_O^X] + [V_O^\bullet] + [V_O^{\bullet\bullet}]$. In the Kröger-Vink notation the symbols V_O^X, $V_O^\bullet$, $V_O^{\bullet\bullet}$ stand for neutral, single, and double, positively charged oxygen vacancies [280]. Two different values of the total oxygen vacancy concentration in the disc region, namely $N_{VO} = 6{\cdot}10^{20}$ cm^{-3} and $N_{VO} = 3{\cdot}10^{20}$ cm^{-3}, are used for the description of the 8w LRS* and the HRS*, respectively. The simulation results for the external field-free case are shown in Fig. 8.17.

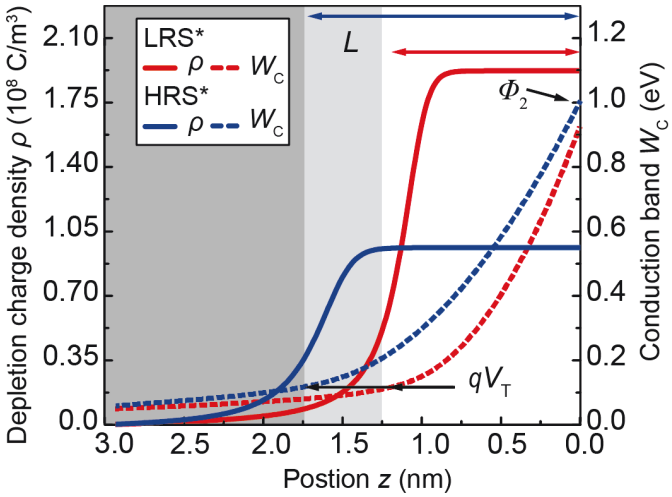

Figure 8.17: *Depletion charge density ρ (solid line) and conduction band W_C (dashed line) as a function of the position z from the Pt electrode ($z = 0$ nm) to the Ti electrode ($z = 3$ nm). The red and blue color stand for the LRS* and HRS*, respectively. The figure is redrawn from [261]. The material parameters are summarized in Tab. 8.5. The calculation of this band diagram is done by C. Funck.*

The bottom of the conduction band W_C (broken lines) and the depletion charge density ρ (solid lines) are plotted as a function of the z-coordinate between the Ti ($z = 3$ nm) and Pt electrode ($z = 0$ nm). According to [107], the maximum spectral tunneling current density is obtained at the energy (qV_T) that equals the barrier height on the depletion region edge. In combination with the band bending in the space charge layer, the direct tunneling length (L) can be obtained.

Based on the simulation results several conclusions can be summarized in the following:

1. The interface barrier is higher for the HRS* than for the LRS* in the external field-free case. The stronger band bending in the LRS* results in a stronger Schottky barrier lowering.

2. An extended tunneling length is observed for the HRS*: the width of the depletion region L is ≈ 1.7 nm in HRS* compared to ≈ 1.2 nm in LRS*. This can be a consequence of the lower oxygen vacancy concentration in HRS*.

3. The results obtained from the continuum model is consistent with the results based on Simmons' equation: the change of the tunneling barrier height and length between LRS* and HRS* follows the same trend for both models. This allows a direct correlation of the change in tunneling barrier properties during the 8w BRS to a change in the total oxygen vacancy concentration N_{VO} in the switching regime.

Effective density of states for electrons N_C ($T = 303$ K)	$6.15 \cdot 10^{25}$ m^{-3}
Temperature T	303 K
Dirichlet Boundary condition at the Schottky barrier interface	1.5 eV
Dirichlet Boundary condition at the ohmic electrode	0 eV
Defect ionization energies for $V_O^{\bullet}$ / $V_O^{\bullet\bullet}$	50 meV / 100 meV
Dielectric constant of the amorphous oxide layer	20
Optical dielectric constant for the Schottky barrier lowering effect	5.8
Total oxide thickness	3 nm

Table 8.5: *List of the material parameters used in the continuum simulation in Fig. 8.17*

In addition, the simulation result obtained from continuum model also provides an explanation for the weak temperature effect on the tunneling characteristics. The quasi-parabolic form of the tunneling barrier shows a flat tail close to Ti top electrode (dash line in Fig. 8.17). For a small negative voltage amplitude, the electrons that are thermally activated above the Pt Fermi level can make a significant contribution to the total tunneling current. The reason comes from the strong band bending for both LRS* and HRS*. Therefore, the physical origin of the temperature dependent read-out $I(V)$ characteristics shown in Fig. 8.14 and Fig. 8.15 can be understood. Furthermore, the model connects the changes obtained for the two 8w resistance states directly with a change of the concentration of the total oxygen vacancies N_{VO} in the depletion region. Finally, the continuum model provides a more accurate description of the space charge effect through a parabolic band bending, and therefore also explains the change of the effective tunneling barrier height and length.

To sum up, the quasi-parabolic form of tunneling barrier with Fermi-Dirac distribution of electrons on the Pt electrode can explain the effective reduction of tunneling length with increased temperature and the difference between HRS* and LRS*. As the aforementioned three main features from the continuum model are consistent with the Simmons' model results, the validity of both models is confirmed. It can be deduced that the resistance change during the 8w BRS can be attributed to the change of oxygen vacancy concentration, through which the tunnel barrier height for the electrons is modified.

8.3 Summary and discussion

In contrast to the interface charging effect [103] and the volatile interface process [102, 281], the 8w states show stable and reproducible characters. As the 8w read-out resistance states do not show the area dependent characteristics (section 8.1.4), this 8w switching should not have the same mechanisms as the area switching observed in the $SrTiO_3$-based deivces [97]. Another similar coexistence of 8w and c8w BRS is found in $Pt/TiO_2/Pt$ $(50\ nm)^2$ crossbar device [99] and such unstable switching is suggested as the competition between two Pt/TiO_2 interfaces.

As discussed in the former sections the coexistence of c8w and 8w BRS in the $Pt/TiO_2/Ti$ nano-crossbar devices (Fig. 8.18 (a)) is related to the Pt/TiO_{2-x} interface. However, how the transition between c8w and 8w BRS occurs, still requires a further understanding. Recently, a switching model suggested for $Nb:STO/SrTiO_3/Pt$ micrometer size devices [41] that show the similar active switching interface compared to the $Pt/TiO_2/Ti$ devices in this work, is very comparable and gives great inspiration for understanding the 8w switching behavior. The authors verify the decrease of the oxygen concentration near the Pt/oxide interface for low resistance state in comparison to high resistance state [41]. This finding is consistent with the conclusion from the continuum model in 8.2.2, where the transition from HRS^* to LRS^* during 8w BRS in the $Pt/TiO_2/Ti$ device can be explained by an increase of the oxygen vacancy concentration close to the Pt/TiO_{2-x} interface. As suggested by Cooper et al. [41], this change close to the Pt/oxide interface should be related to an electrocatalytic reaction, where the oxygen ions are extracted into or incorporated from the atmosphere with the help of the catalytically active Pt electrode.

Based on the aforementioned comparison and the general features of 8w BRS in this work, the interface exchange of oxygen ions across the Pt/TiO_{2-x} interface should be responsible for 8w BRS (Fig. 8.18 (b)). The pre-condition for initiating such a process is the sufficient amount of oxygen from oxide layer pushed and stored in the Pt electrode (boundary) through the positive voltage to Pt electrode during the c8w-type RESET

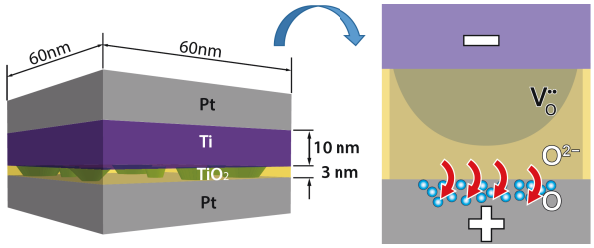

Figure 8.18: *(a) An asymmetric Pt/3 nm TiO_2/Ti structure in initially conductive state. (b) Zoomed into the switching regime during the 1st c8w-type RESET.*

process (Fig. 8.18 (b)). It has to be mentioned that such an oxygen ion exchange across the Pt/TiO_{2-x} interface does not consider the influence from the region surrounding the filament region.

This zoomed cross-section in Fig. 8.18 (b) denotes the switching filament among other broken filaments, which also initially exist after the device fabrication (Fig. 8.18 (a)). This idea can explain the reduced appearance probability of the 8w-type switching with inserting a thick Al_2O_3 layer ($\geqslant 2$ nm) at the Pt/TiO_2 interface and support the oxygen ion exchange across the Pt/TiO_2 interface as the main relevant switching process responsible for the 8w BRS.

Coexistence of two BRS modes with opposite polarities

Based on the results of the extraordinary switching behavior discovered in the $Pt/TiO_2/Ti$ nano-crossbar devices, a switching model merging the two BRS modes can be proposed. The model ultilizes the competition between the oxygen vacancy drift/diffusion processes and an oxygen exchange reaction at the high work function Pt electrode. Still several points that are beyond the scope of this study are not discussed, like (1) the possibility of the oxygen exchange reaction at the Ti OEL [22], which could give an accurate description of the switching behavior; (2) the impact of the cation diffusion [282] on the switching behavior in the nano-crossbar devices.

The scenario of the switching model should clarify several critical points in comparison with other reported possibilities. Firstly, this model assumes that the as-deposited TiO_2 layer in its initial state consists of multiple (moderately) conductive regions of slightly reduced TiO_{2-x} inside the otherwise insulating TiO_2 matrix (see Fig. 8.18 (a)). Although a significant number of sub-stoichiometric phases could exist at the low deposition temperature in the nano-crystalline material, such as Magnéli-type phases Ti_nO_{2n-1} [53], regarding the complex theoretical description of TiO_2 caused by these additional phases [218], it is still reasonble to apply the assumption of the conductive filament surrounded by the insulating TiO_2 matrix in this model. This description is consistent with the experimental findings reported by Du et al. [238], who visualized multiple nanosized conducting filaments in Fe-doped $SrTiO_3$ thin-film memories by scanning transmission electron microscopy and core level electron energy loss spectroscopy (EELS).

Secondly, despite the similar 8w switching behavior observed both in $Pt/TiO_2/Ti$ devices and in the $Nb:SrTiO_3/SrTiO_3/Pt$ cells studied by Bäumer et al. [101], two main differences make the two switching models individual. For the $Nb:SrTiO_3/SrTiO_3/Pt$ cells, the high work function Pt electrode forms as the top contact, where a considerable amount of oxygen exchange with the surrounding atmosphere can be involved in this 8w switching mechanism [41]. In contrast, for the nano-crossbar cells studied in this work the switching Schottky interface, i.e., Pt/TiO_{2-x}, is located at the bottom of the device stack.

Due to this geometrical arrangement the oxygen exchange with the atmosphere cannot be simply transfered into our case. Therefore, the proposed switching model assumes that the oxygen atoms , which are extracted from the TiO_{2-x} layer, reside either at the interface or in the Pt layer located in close proximity to the interface. Oxygen atoms can, for example, be segregated to the Pt grain boundaries [283].

Figure 8.19 presents a graphical illustration of the proposed model for the two BRS modes sharing a common state obtained in $Pt/TiO_2/Ti/Pt$ nano-crossbar devices. The changes on the atomic scale level are indicated by the colored spheres. In this two-dimensional illustration that cuts through the device at the position of the switching filament, the Pt BE and the Ti TE are given in grey and dark violet color, respectively. The TiO_2 matrix is shown in yellow, and the constituting ions are drawn in bright violet for Ti^{3+} and in green for doubly ionized oxygen vacancies, $V_O^{\bullet\bullet}$. Oxygen atoms residing at the interface and at the Pt grain boundaries are drawn as blue spheres. The conical-shaped filament is seen as the regime with an increased density of oxygen vacancies. Particularly, the highly conductive filament part, plug, is described by a high electron concentration in the TiO_2 conduction band formed by the Ti 3d states [53]. In contrast, the average vacancy concentration in the "disc" region depends on the switching state. Therefore, the depletion space charge layer adjacent to the Pt BE is identified by a

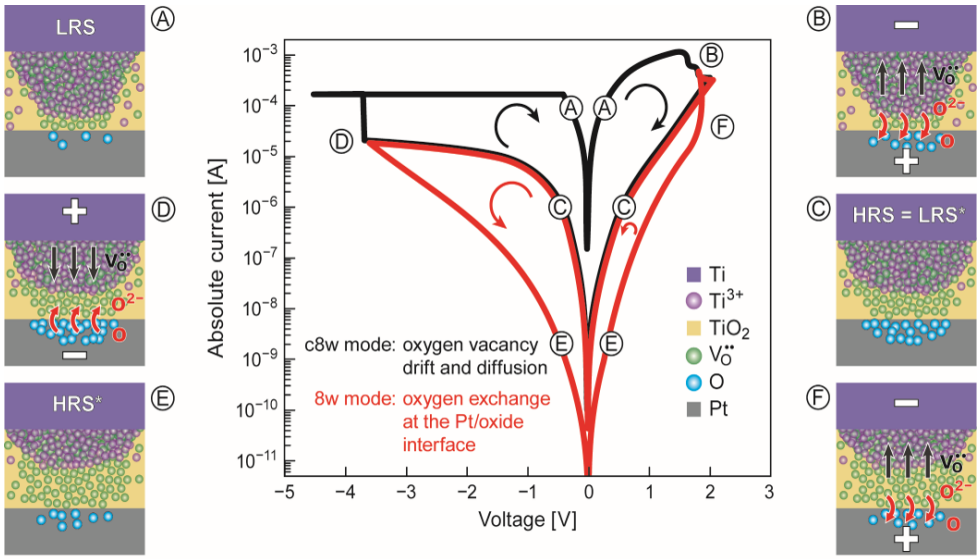

Figure 8.19: *The suggested switching process between c8w and 8w-type BRS. The corresponding ionic states and processes for each point marked in the $I(V)$ plot are depicted with the Ti top electrode (violet background), the Pt bottom electrode (grey background), Ti^{3+} ion (violet spheres), the non-switching surrounding of the TiO_2 film (yellow background), double charged oxygen vacancies (green spheres) and oxygen ions (blue spheres).*

variable concentration of oxygen vacancies.

The standard VCM-type c8w switching behavior is described by the characteristic states and transitions "A – B – C - D". The 8w-loop is characterized by the sequence "C – D – E – F". The full switching scenario comprises the coexistence of the c8w and the 8w switching events, the shared intermediate state and the transition between the two states that is controlled by the amplitude of the negative voltage applied to the Pt BE. This complete scenario can be explained in a self-consistent manner. For this, in addition to the oxygen vacancy drift and diffusion [229], an oxygen transfer reaction at the interface with the inert Pt electrode is considered, which is to some extent analog to the switching mechanism reported for epitaxial $SrTiO_3$ films [41]. With these assumptions, the switching steps and resistance states appear as follows: The c8w LRS "A" represents the situation with the smallest extension of the depletion zone. The c8w RESET "B" involves the drift of oxygen vacancies towards the cathode (Ti TE) and a possible oxygen transfer at the high barrier interface towards the Pt BE. For a successful c8w RESET from the LRS "A" to the c8w HRS "C" the oxygen vacancy drift should dominate over the oxygen extraction in order to decrease the average oxygen vacancy concentration in the disc region. Consistent with the continuum model, the reduced oxygen vacancy concentration N_{VO} results in an enhanced barrier height and tunneling length for electron injection from the Pt into the oxide. When a negative voltage is applied to the Pt BE, the process is reversed. In other words, oxygen ions and oxygen vacancies are pushed into the disc region from the Pt side and from the Ti side, respectively. At position "D" a c8w SET process is initiated, if the filament comes very close towards the Pt electrode and the conduction behavior in the achieved LRS is described by a metal-like filament. In contrast, prior to the filament's contacting of the Pt electrode, the transfer of oxygen from the "reservoir" at the Pt interface into the disc region results in a decrease of the total oxygen vacancy concentration N_{VO}, and, consequently, an even higher barrier height and tunneling length characterize the HRS* (state "E"). The switching from the HRS* to the LRS* at positive polarity applied to the Pt BE proceeds via step "F" that characterizes the 8w SET followed by step "B".

To sum up, several important clarified results from experiments and simulations are as follows:

1. the appearance of a shared intermediate state, i.e. c8w HRS = 8w LRS*, show the area-independence, which supports the filamentary-type VCM switching;

2. the conduction behavior in LRS* and HRS* indicates the tunneling mechanism via the weak temperature dependence and the clear transition voltage hints for the transition between direct tunneling and Fowler-Nordheim tunneling;

3. the multilevel capability of the HRS* in DC voltage sweep and pulse operation provides a high potential in the neuromorphic applications;

4. the strong dependence of the 8w-type switching phenomenon on the nature of the Pt/TiO_{2-x} interface verified by the insertion of Al_2O_3 blocking layer at the two interfaces in the $M_1/O/M_2$ structure;

5. the correlation of the change in the barrier height and tunneling length to the oxygen vacancy concentration in the disc regime of the filament near the Pt BE via the continuum model.

These findings can be consistently described by means of the proposed switching model, which considers the oxygen transfer at the interface with the Pt bottom electrode, in addition to the accepted processes of oxygen vacancy drift and diffusion.

Chapter 9

Final summary and outlook

The scope of this work was the systematic investigation of the role of individual oxide layers on the resistive switching performance of nanosized ReRAM devices. For this purpose, nano-crossbar ReRAM devices of the size from $(60\,\mathrm{nm})^2$ to $(100\,\mathrm{nm})^2$ with nanometer thick metal oxide films were fabricated. These oxide(s) comprising single-layer and bilayer stacks of TiO_2 and Al_2O_3 grown by atomic layer deposition (ALD) were sandwiched between nano-structured Pt and Ti/Pt (or TiN/Pt) electrodes. The analysis is focused on the resistive switching performance in continuous voltage ramp and voltage pulse operations and on the detailed current transport studies of various stacks in different resistance states. The interpretation of the experimental results is focused on the relation between the ionic drift, electronic conduction and the comparison of switching performance. The variation of the oxide thickness, the oxide stack order and the electrode materials all aimed to clarify the role of the oxide layers and the electrode/oxide interfaces on the switching performance.

The most important results of this study are summarized in the following:

(1) In DC voltage sweep mode the c8w BRS behavior was first characterized in cells with different top electrodes. In agreement with other studies, the high quality ALD grown Al_2O_3 films with low defect density do not provide any reversible resistance switching in the symmetric $Pt/Al_2O_3/Pt$ stack. Other inert electrodes like TiN cannot induce sufficient oxygen vacancies as well. Therefore, the Pt/oxide(s)/TiN stacks show rarely successful electroforming and the c8w BRS behavior is also unstable. For the same oxide layer, the stable c8w BRS can be observed in $Pt/Al_2O_3/Ti$, which can have sufficient oxygen vacancies introduced by the Ti oxygen exchange layer (OEL). Moreover, by adding an 3 nm artificial TiO_2 grown by ALD, the Pt/3 nm Al_2O_3/3 nm TiO_2/Ti bilayer device shows especially an improved endurance among other single-layer and bilayer stacks.

In voltage pulse mode, Pt/5 nm Al_2O_3/Ti cells show more gradual SET. In the SET kinetic study, this stack shows a strong non-linearity of the SET time vs. pulse amplitude

relation, that means, the SET time can be reduced from 0.1 s to 20 ns with SET pulse amplitude from 0.8 V to 1.1 V. This non-linearity can be well explained by the ion hopping model with physically meaningful parameters. The RESET kinetic studies, however, reveal a significant impact of the LRS values on the RESET process.

Afore investigating the electronic transport in the c8w BRS cells, the nanostructural analysis on a switched Pt/3 nm Al_2O_3/3 nm TiO_2/Ti bilayer device was performed by high-resolution TEM, which provided the evidence for the filamentary-type c8w BRS switching with a switching area of around 100 nm^2. The crystalline phases of TiO_2 and Al_2O_3 in the filament region serve as an evidence for the occurrence of local Joule heating.

In order to understand the stable c8w BRS in Pt/oxide(s)/Ti cells, the electronic transport between different resistance states was studied. Among other candidates, the electron tunneling through the trapezoidal barrier based on Simmons' equation can well explain the $I(V)$ characteristics in initial state and in various high resistance states (HRS) with reasonable simulation parameters. The simulation results indicate that the Al_2O_3 layer is also involved in the c8w BRS and the different resistance states should originate from the change of tunneling barrier forming in the depletion region closed to the Pt/Al_2O_3 interface. The analysis of the low resistance state (LRS) via thermal coefficient of resistance (TCR) reveals a metallic conducting filament in the oxide layer(s) bridging the two electrodes. Based on these results, the switching mechanism in Al_2O_3 and TiO_2-based devices is consistent with the filamentary-type valence change mechanism (VCM), i.e. the reversible oxygen vacancy migration upon the electrical field.

(2) The 3 nm to 11 nm TiO_2 single-layer in Pt/TiO_2/Ti devices reveal an unstable c8w BRS but surprisingly, a stable 8w BRS with an opposite switching polarity and the self-limiting SET and RESET behavior. The non-volatile resistance states and multiple high resistance states (HRS*) promise an application in analog signal processing.

From the analysis of the different resistance states through electron tunneling model based on Simmons' equation and continuous model regarding the ion configuration, the transition from HRS* to LRS* during 8w BRS could be attributed to a reduction of the interface barrier height and length, which can originate from possible oxygen exchange across the Pt/TiO_2 interface. A further proof for the dominating role of the Pt/TiO_2 interface is the disappearance of 8w BRS behavior with sufficient thick Al_2O_3 layer inserted at the Pt/TiO_2 interface rather than at the TiO_2/Ti interface. Considering the electronic and ionic transport in the Pt/TiO_2/Ti devices, a switching model based on the competition between oxygen vacancy migration and oxygen exchange is proposed to explain the coexistence and transition between c8w BRS and 8w BRS modes.

(3) In the metal$_1$-oxide-metal$_2$ (M_1OM_2) structure, the important factor for resistive switching behavior is the interface reaction between electrode and oxide. Depending on

the oxide material, the Pt/oxide interface could either initiate oxygen exchange (Pt/TiO_2) or inhibit oxygen exchange (Pt/Al_2O_3), which makes the stable switching polarity either 8w or c8w. The counter interface oxide/Ti has the effect of delivering oxygen vacancies, which influences the stability of resistance states and the endurance.

Going beyond the results of this work the tuning of the c8w BRS performance of Al_2O_3 and TiO_2-based nano-crossbar devices and the explanation of the competition between the opposite switching polarities in TiO_2-based nanostructural devices bring up additional research questions.

- Which material properties control the dominance of oxygen vacancy drift/diffusion vs. oxygen transfer across the Pt/oxide interface?
- Can the understanding of these processes guide to a design concept for area switching devices?
- Can we create a tool box for nanosized resistive switching cells formed from nanolaminate stacked in the right sequence to provide the desired device properties?

To answer the aforementioned questions, the material research in bilayer stacks with focus on the metal/oxide interface can go further. The candidates replacing Al_2O_3 may be oxides showing no valence change like SiO_2 or MgO. Other insulating layers like SiN or AlN may also be good candidates due to their feasibility in chip industry product lines. For TiO_2, the replacing materials could be HfO_2, Ta_2O_5 or ZrO_2. The OEL electrode can be varied to other reactive metals like Cr, Ta or Hf, whereas the inert electrode can be varied to Pd or TiN.

As applied for Al_2O_3-based devices with more detailed consideration on the band structures, the continuum model can further interpret the resistive states in the studied materials and thus could reveal important information like ionic configuration and material properties.

Appendix A

Temperature related $I(V)$ analysis for the initial state

A.1 Pt/3 nm Al_2O_3/3 nm TiO_2/Ti device

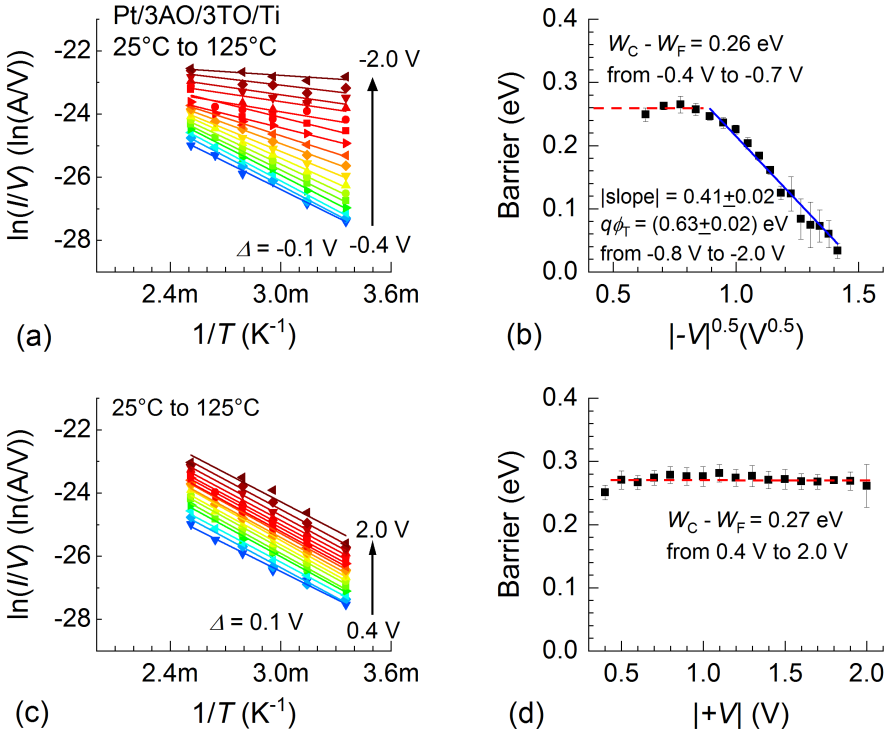

Figure A.1: *(a) ln(I/V) vs. 1/T plots from Fig. 7.4 (a) for negative bias and (c) for positive bias. (b) and (d) are the voltage dependent slopes from (a) and (c), respectively.*

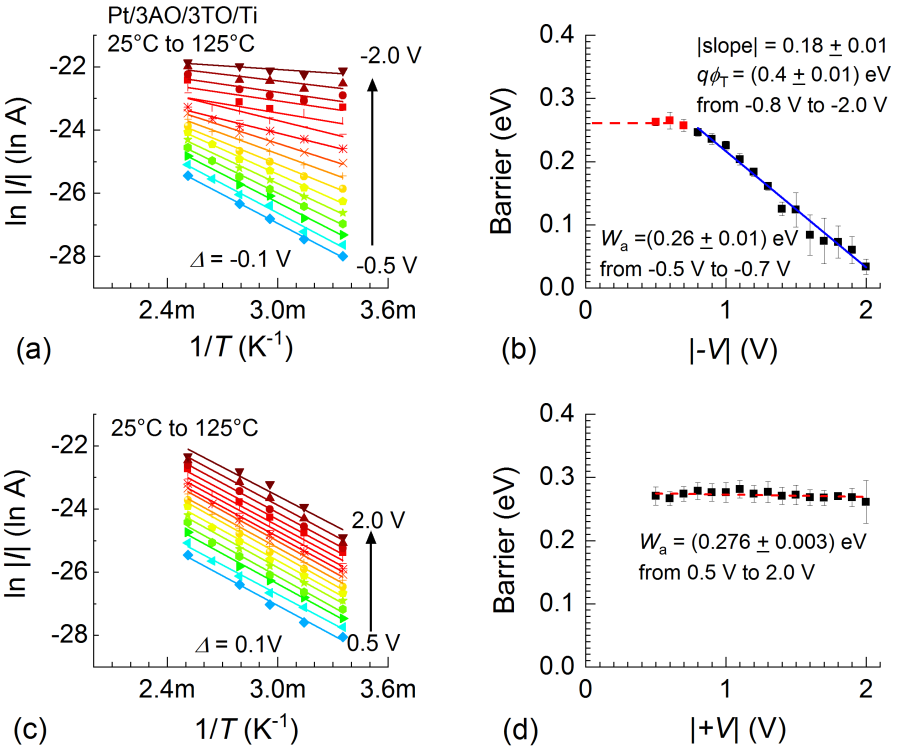

Figure A.2: *(a) ln|I| vs. 1/T plots from Fig. 7.4 (a) for negative bias and (c) for positive bias. The slopes from (a) and (c) is plotted as function of voltage amplitude in (b) and (d), respectively.*

The $I(V,T)$ analysis in the non-switched Pt/3AO/3TO/Ti cell for both voltage polarities are plotted in $\ln(I/V)$ vs. $1/T$ function (Fig. A.1 (a,c)). The data points show good linear fits. The $V^{0.5}$ dependence of the slopes gives the offset barrier height ($q\phi_T$) of around 0.63 eV, while a voltage independent barrier indicates an ohmic transport with barrier W_C - $W_F \approx 0.27$ eV (Fig. A.1 (b,d)).

From the hopping conduction plot in Fig. A.2 (b), the activation energy is obtained as 0.4 eV and the hopping distance is around 1.08 nm. The hopping distance a can be assumed as $2{\cdot}d$ times the value of slope in Fig. A.2 (b), where d = 3 nm obtained from the insulating 3 nm Al_2O_3 film (for details see equation (2.6)). Although a is in a range of the reported value (see section 2.4.4), the value of a that equals to a roughly three oxygen atom distance in Al_2O_3, and the hopping conduction that is only observed in one voltage polarity, are not reasonable.

A.2 Pt/3 nm TiO_2/3 nm Al_2O_3/Ti device

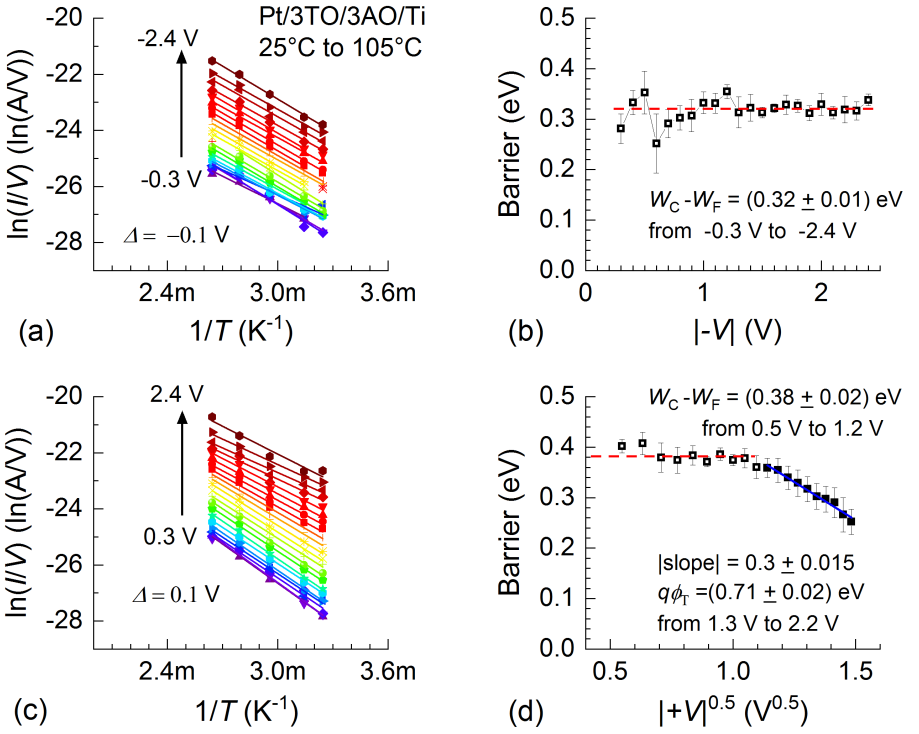

Figure A.3: *(a) ln(I/V) vs. 1/T plots from Fig. 7.7 (a) for negative bias and (c) for positive bias. (b) and (d) are the voltage dependent slopes from (a) and (c).*

The $I(V,T)$ analysis in the non-switched Pt/3TO/3AO/Ti cell for both polarities are done for Poole-Frenkel emission and ohmic conduction in Fig. A.3. In the $\ln(I/V)$ plot a linear dependence on $1/T$ is shown in Fig. A.3 (a,c), The voltage independent barrier can be seen in the lower voltage range for both bias of around 0.35 eV (Fig. A.3 (b,c)). For higher voltage amplitude the Poole-Frenkel barrier around 0.7 eV can be extracted from Fig. A.3 (d), which is similar as in Pt/3AO/3TO/Ti device.

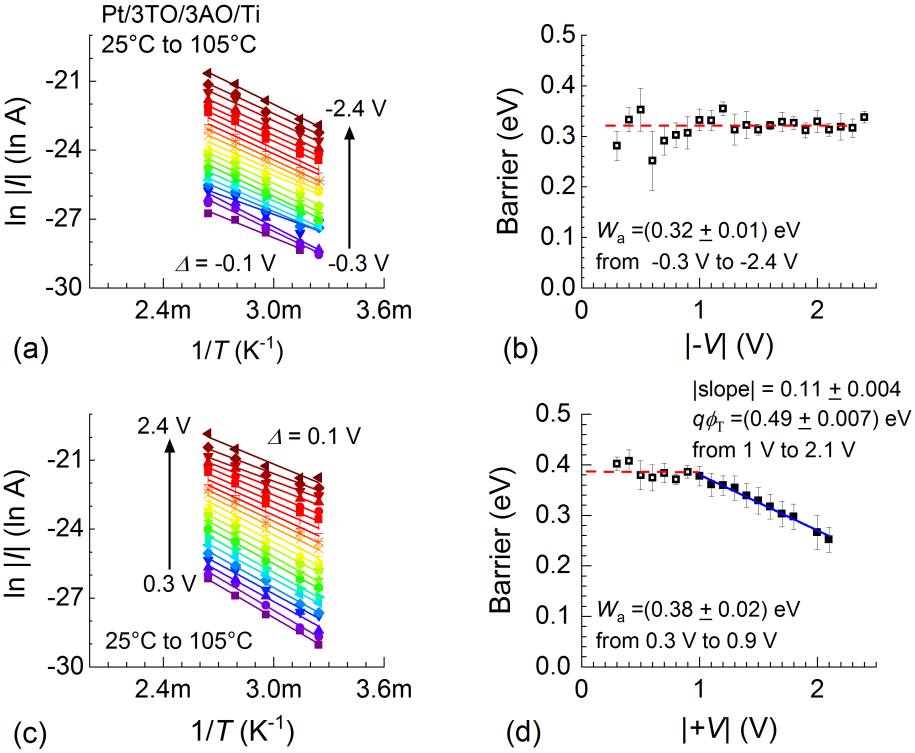

Figure A.4: *ln|I| vs. 1/T from Fig. 7.7 (a) for negative bias and (c) for positive bias. The slopes from (a) and (c) are plotted as function of voltage amplitude in (b) and (d), respectively.*

A similar voltage independent barrier is observed in the hopping fitting of around 0.35 eV (Fig. A.4 (b) and (d)), whereas the hopping barrier is estimated as 0.49 eV. The corresponding hopping distance a is 2·0.3·3 nm = 1.8 nm, whose value equals to around six oxygen atom distance in Al_2O_3. However, the hopping fitting in this cell has the same problem as in Pt/3TO/3AO/Ti device: the transport can only be observed in one polarity. Therefore, the hopping conduction is not suitable as the main transport mechanism.

Appendix B

R_{th} and W_{A} optimization

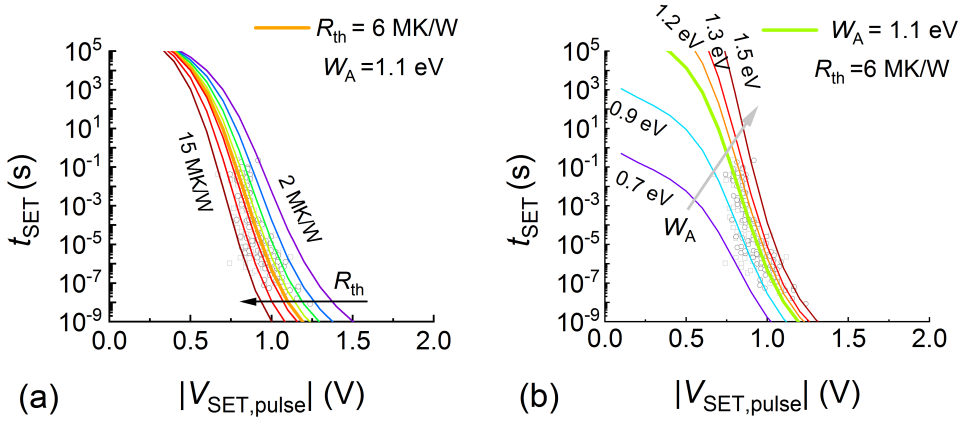

Figure B.1: *Impact of (a) R_{th} and (b) W_A on the t_{SET} - $V_{SET,pulse}$ relation. The grey dots are the experimental data obtained from two Pt/5 nm Al_2O_3/Ti cells, respectively.*

The impact of the R_{th} and W_{A} on the non-linearity of $\log(t_{\mathrm{SET}})$ - $|V_{\mathrm{SET,pulse}}|$ relation is illustrated in Fig. B.1, where the influence of each factor is shown by keeping other parameters constant. The increase of both R_{th} and W_{A} values results in a higher non-linearity of t_{SET} - $|V_{\mathrm{SET,pulse}}|$ relation. However, due to the opposite shift the required $|V_{\mathrm{SET,pulse}}|$ for the same t_{SET} is reduced by increasing R_{th} (Fig. B.1 (a)), whereas more $|V_{\mathrm{SET,pulse}}|$ is needed for increase of W_{A} (Fig. B.1 (b)).

Appendix C

Thickness analysis on TiO_2 films grown by FlexAL ALD

Sample-Nr.	Layer thickness by XRR fitting	Density (g/cm^3)	ALD cycles (#)	RMS roughness by AFM (nm)
No.11	2.9 nm TiO_2	4.03	67	0.213
No.12	5.5 nm TiO_2	4.15	134	0.242
No.13	10.9 nm TiO_2	4.02	268	0.257

Table C.1: *Details for as-grown TiO_2 single-layers by A. Hardtdegen utilizing FlexAL ALD system in Nanocluster. The process details are described in [284]. The oxide layers were deposited at 250°C on Si(100) substrates as the reference sample for the nanocrossbar devices in this work.*

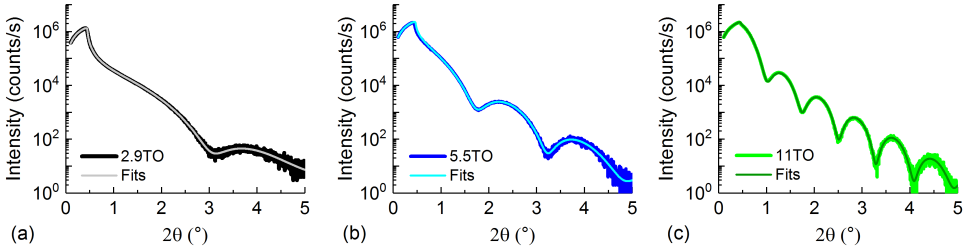

Figure C.1: *(a-c) Measured XRR curves (bold line) and XRR fitting results of TiO_2 single-layers deposited on Si(100) substrates listed in Tab. C.1.*

Appendix D

List of Symbols

Symbol	Description	Unit
a	hopping distance	m
A	tunneling current area	m^2
A_{cell}	cross-section area of cell	m^2
A_{filament}	cross-section area of filament	m^2
A^*	effective Richardson constant	$A/(m^2 \cdot K^2)$
d	film thickness	m
E	electric field	V/m
E_{BR}	electrical breakdown field strength	V/m
E_{Vo}	oxygen vacancy formation energy	eV
f	ion hopping attempt frequency	Hz
h	Planck constant	eV·s
I	measured current	A
I_{CC}	current compliance	A
I_1	filament current for cell size A_{cell}	A
I_2	non-filament current for cell size A_{cell}	A
$I_{\text{pre-SET}}$	pre-SET current	A
I_{RESET}	maximal current level	A
I_{HRS^*}	current sum from filament- and non-filament region for HRS*	A
I_{LRS^*}	current sum from filament- and non-filament region for LRS*	A
ΔI	increment of the filament current from HRS* to LRS*	A
ΔA	increment of the area	m^2
J	current density	A/m^2
J_1	current density for I_1	A/m^2
J_1	current density for I_2	A/m^2
k_{B}	Boltzmann constant	J/K
l	effective tunneling length	m
l_{disc}	oxygen depleted region	m
l_{filament}	length of the conductive filament	m
L	total tunneling length	m

Symbol	Description	Unit
m^*	effective electron mass	kg
m_0	electron rest mass	kg
M*	chemical active metal electrode	
n	charge carrier concentration	m^{-3}
N_C	effective density of states in conduction band	m^{-3}
N_{VO}	total concentration of oxygen vacancies	m^{-3}
q	elementary charge	C
R_0	resistance measured at T_0	Ω
$R_{8w,OFF}$	read-out resistance for HRS*	Ω
$R_{8w,ON}$	read-out resistance for LRS*	Ω
$R_{initial}$	read-out initial resistance	Ω
$R_{c8w,OFF}$	read-out resistance for HRS for c8w BRS	Ω
$R_{c8w,ON}$	read-out resistance for LRS for c8w BRS	Ω
$R_{ON,cell}$	resistance of the switching layer in LRS	Ω
$R_{pre,OFF}$	read-out resistance for HRS after precycling	Ω
$R_{pre,ON}$	read-out resistance for LRS after precycling	Ω
R_{read}	read-out resistance	Ω
R_S	series resistance	Ω
R_{th}	effective thermal resistance	K/W
t_{SET}	SET time for transient pulse measurement	s
t_{RESET}	RESET time for transient pulse measurement	s
t_{pulse}	pulse length	s
T_{disc}	local temperature in the disc range	K
T_0	ambient temperature afore SET process	K
v_{drift}	drift velocity of oxygen vacancies	m/s
V	applied bias voltage	V
V_0	voltage for I=I_{CC}	V
$V_{8w,RESET}$	c8w SET voltage	V
$\lvert V_{c8w,SET}\rvert$	c8w SET voltage amplitude	V
$\lvert V_{c8w,RESET}\rvert$	c8w RESET voltage amplitude	V
V_{disc}	voltage applied on the disc region	V
$\lvert V_{Fr}\rvert$	electroforming voltage amplitude	V
V_T	transition voltage	V
V_{pulse}	applied pulse voltage	V
$V_{SET,pulse}$	voltage for SET pulse	V
$V_{RESET,pulse}$	voltage for RESET pulse	V
$\lvert V_{ON,\,cell}\rvert$	voltage amplitude on the cell for LRS after SET	V
$\lvert V_{RESET,\,cell}\rvert$	max. voltage amplitude on the cell for LRS afore RESET	V
$V_{-,max}$	maximal negative-/RESET stop voltage	V
$V_{+,max}$	maximal positive stop voltage	V
$V_O^{\bullet\bullet}$	double positively charged oxygen vacancy	
$[V_O^X]$	concentration of neutral oxygen vacancy	m^{-3}
$[V_O^{\bullet}]$	concentration of single positively charged oxygen vacancy	m^{-3}
$[V_O^{\bullet\bullet}]$	concentration of double positively charged oxygen vacancy	m^{-3}

Symbol	Description	Unit
W_{a}	activation energy	eV
$W(x)$	Lambert's function	
W_{A}	field-free ion hopping barrier for $V_O^{\bullet\bullet}$	eV
W_{F}	Fermi-level	eV
W_{C}	the bottom edge of conduction band	eV
W_{G}	band gap	eV
α-	Alpha phase-	
α_0	temperature coefficient of resistance	K^{-1}
γ-	Gamma phase-	
ϵ_{r}	relative optical permittivity	
ϵ_0	permittivity in vacuum	F/m
η	ideality factor	
θ_{c}	critical angle	$^\circ$
θ_{m}	the angle at the maximum of the m^{th} oscillation	$^\circ$
κ	thermal conductivity	W/(K·m)
λ	wavelength	m
μ	electron mobility	$\mathrm{m}^2/(\mathrm{V}\cdot\mathrm{s})$
$\mu(\mathrm{O})$	oxygen chemical potential	eV
υ	frequency of thermal vibration of electrons at trap sites	Hz
ρ	electron density	$\mathrm{C/m}^3$
Φ	tunneling barrier height at the interface	eV
Φ_1	the interface barriers at the oxide/ohmic electrode interface	eV
Φ_2	the interface barriers at the Schottky electrode/oxide interface	eV
Φ_{B}, $q\phi_{\mathrm{B}}$	effective thermionic emission barrier at the interface	eV
Φ_{B0}, $q\phi_{\mathrm{B0}}$	thermionic emission barrier at the interface	eV
Φ_{M}	metal work function	eV
Φ_{T}, $q\phi_{\mathrm{T}}$	trap energy level	eV
$\bar{\Phi}$	effective tunneling barrier	eV
χ	oxide electron affinity	eV

List of Abbreviation

$I(V)$	current-voltage
1S1R	one selector-one resistor
1T1R	one transistor-one resistor
3AO/3TO	3 nm Al_2O_3/3 nm TiO_2
3TO/3AO	3 nm TiO_2/3 nm Al_2O_3
8w BRS	eightwise bipolar resistive switching
Abs I	absolute current
AFM	atomic force microscopy
ALD	atomic layer deposition
AO	Al_2O_3
BE	bottom electrode
C2C	cycle-to-cycle
c8w BRS	counter-eightwise bipolar resistive switching
CBRAM	conductive bridge random access memory
CDF	cumulative distribution function
CMOS	complementary metal-oxide-semiconductor
CPU	central processing unit
CRS	complementary resistive switches
CVD	chemical vapor deposition
D2D	device-to-device

DC	direct current
DFT	density functional theory
DMAI	dimethylaluminum isopropoxide
DRAM	dynamic random access memory
EBL	electron beam lithography
EDX	energy-dispersive X-ray spectroscopy
EELS	electron energy-loss spectroscopy
FeRAM	ferroelectric random access memory
FFT	fast Fourier transform
FN	Fowler-Nordheim
FTJ	ferroelectric tunnel junction
GNDU	ground unit
GPC	growth per cycle
HRS	high resistance state for c8w BRS
HRS*	high resistance state for 8w BRS
HRTEM	high-resolution transmission electron microscopy
I/O	input and output interfaces
ICSD	inorganic crystal structure database
IoT	Internet of Things
IPS	inverse photoemission
IQR	interquartile range
LA-BSE	low angle backscatter electrons
LC-AFM	local conductivity atomic force microscopy
LRS	low resistance state for c8w BRS
LRS*	low resistance state for 8w BRS

M_1OM_2	$metal_1$-oxide-$metal_2$
MOS	metal-oxide-semiconductor
MOs	metal oxides
MRAM	magnetic random access memory
NIL	nanoimprint lithography
OEL	oxygen exchange layer
PCM	phase change memory
PE-ALD	plasma enhanced atomic layer deposition
PLD	pulsed laser deposition
PMU	pulse/measurement unit
REELS	reflection electron energy loss spectroscopy
ReRAM	resistive switching random access memory
RIBE	reactive ion beam etching
RMS	Root Mean Square
SE	secondary electrons
SEM	scanning electron microscopy
SMU	source/monitor unit
SRAM	static random access memory
TCR	temperature coefficients of resistance
TDMAT	tetrakis(dimethylamino)titanium
TE	top electrode
TEM	transmission electron microscopy
TMA	trimethylaluminium
TO	TiO_2
UPS	ultraviolet photoemission

VCM	valence change mechanism
VUV	vacuum ultraviolet
w/o	without
XES	X-ray emission spectroscopy
XPS	X-ray photoelectron spectroscopy
XPS	X-ray photoemission spectroscopy
XRF	X-ray fluorescence spectroscopy
XRR	X-ray reflectivity

Bibliography

[1] G. Dearnaley, A. M. Stoneham, and D. V. Morgan, *Electrical phenomena in amorphous oxide films*, Reports on Progress in Physics **33**, 1129 (1970).

[2] D. P. Oxley, *Electroforming, switching and memory effects in oxide thin films*, Electrocomponent Science and Technology **3**, 217 (1977).

[3] H. Pagnia and N. Sotnik, *Bistable Switching in Electroformed Metal-Insulator-Metal Devices*, Physica Status Solidi A **108**, 11 (1988).

[4] R. Waser, R. Bruchhaus, and S. Menzel, Redox-based Resistive Switching Memories, in Nanoelectronics and Information Technology (3rd edition), chapter 30, pp. 683–710, Wiley-VCH, 2012.

[5] C. Hermes, F. Lentz, R. Waser, R. Bruchhaus, S. Menzel, K. Fleck, U. Bottger, M. Wimmer, M. Salinga, and M. Wuttig, *Fast pulse analysis of TiO_2 based RRAM nano-crossbar devices*, in Non-Volatile Memory Technology Symposium (NVMTS), 2011 11th Annual, pp. 92–95, 2011.

[6] B. Govoreanu, A. Redolfi, L. Zhang, C. Adelmann, M. Popovici, S. Clima, H. Hody, V. Paraschiv, I. Radu, A. Franquet, J.-C. Liu, J. Swerts, O. Richard, H. Bender, L. Altimime, and M. Jurczak, *Vacancy-Modulated Conductive Oxide Resistive RAM (VMCO-RRAM): An Area-Scalable Switching Current, Self-Compliant, Highly Nonlinear and Wide On/Off-Window Resistive Switching Cell*, 2013 IEEE International Electron Devices Meeting (IEDM) **13**, 10.2.1 (2013).

[7] R. Waser, R. Dittmann, G. Staikov, and K. Szot, *Redox-Based Resistive Switching Memories - Nanoionic Mechanisms, Prospects, and Challenges*, Advanced Materials **21**, 2632 (2009).

[8] S. Mittal, *A Survey of ReRAM-Based Architectures for Processing-In-Memory and Neural Networks*, Machine Learning and Knowledge Extraction **1** (2018).

[9] A. Siemon, S. Menzel, A. Chattopadhyay, R. Waser, and E. Linn, *In-Memory Adder Functionality in 1S1R Arrays*, 2015 IEEE International Symposium on Circuits and Systems (ISCAS) , 1338 (2015).

[10] T. Breuer, *Development of ReRAM-based Devices for Logic- and Computation-in-Memory Applications*, PhD thesis, RWTH Aachen University, 2017.

[11] S. Kvatinsky, E. G. Friedman, A. Kolodny, and U. C. Weiser, *Memristor-Based Material Implication (IMPLY) Logic: Design Principles and Methodologies*, IEEE Transactions on Very Large Scale Integration (VLSI) Systems **22**, 2054 (2014).

[12] C. D. Schuman, T. E. Potok, R. M. Patton, J. D. Birdwell, M. E. Dean, G. S. Rose, and J. S. Plank, *A Survey of Neuromorphic Computing and Neural Networks in Hardware*, Computing Research Repository (2017).

[13] X. Hong, D. J. Loy, P. A. Dananjaya, F. T. C. Ng, and W. Lew, *Oxide-based RRAM materials for neuromorphic computing*, Journal of Materials Science **53**, 8720 (2018).

[14] E. J. Merced-Grafals, N. Davila, N. Ge, R. S. Williams, and J. P. Strachan, *Repeatable, accurate, and high speed multi-level programming of memristor 1T1R arrays for power efficient analog computing applications*, Nanotechnology **27**, 365202/1 (2016).

[15] R. Waser, editor, *Nanoelectronics and Information Technology*, chapter Part V Memory device and storage systems, pp. 601–725, Wiley-VCH, 2012.

[16] J.-J. Huang, Y.-M. Tseng, C.-W. Hsu, and T.-H. Hou, *Bipolar Nonlinear Ni/TiO_2/Ni Selector for 1S1R Crossbar Array Applications*, IEEE Electron Device Letters (2011).

[17] T. Breuer, A. Siemon, E. Linn, S. Menzel, R. Waser, and V. Rana, *A HfO_2-Based Complementary Switching Crossbar Adder*, Advanced Electronic Materials **1**, 1500138/1 (2015).

[18] ITRS, The International Technology Roadmap for Semiconductors - 2013 Edition, Technical report, ESIA, JEITA, KSIA, TSIA, SIA, 2013.

[19] D. Jana, S. Roy, R. Panja, M. Dutta, S. Rahaman, R. Mahapatra, and S. Maikap, *Conductive-bridging random access memory: challenges and opportunity for 3D architecture*, Nanoscale Research Letters , 188/1 (2015).

[20] S. Maikap, R. Panja, and D. Jana, *Copper pillar and memory characteristics using Al_2O_3 switching material for 3D architecture*, Nanoscale Research Letters **9**, 366/1 (2014).

[21] B. Hudec, I. T. Wang, W. L. Lai, C. C. Chang, P. Jancovic, K. Frohlich, M. Micusik, M. Omastova, and T. H. Hou, *Interface engineered HfO_2-based 3D vertical ReRAM*, Journal of Physics D: Applied Physics **49**, 215102/1 (2016).

[22] W. Kim, S. Menzel, D. J. Wouters, Y. Guo, J. Robertson, B. Rösgen, R. Waser, and V. Rana, *Impact of oxygen exchange reaction at the ohmic interface in Ta_2O_5-based ReRAM devices*, Nanoscale **8**, 17774 (2016).

[23] M.-J. Lee, C. B. Lee, D. Lee, S. R. Lee, M. Chang, J. H. Hur, Y.-B. Kim, C. J. Kim, D. H. Seo, S. Seo, U.-I. Chung, I.-K. Yoo, and K. Kim, *A fast, high-endurance and scalable non-volatile memory device made from asymmetric Ta_2O_{5-x}/TaO_{2-x} bilayer structures*, Nature Materials **10**, 625 (2011).

[24] Z. Wei, Y. Kanzawa, K. Arita, Y. Katoh, K. Kawai, S. Muraoka, S. Mitani, S. Fujii, K. Katayama, M. Iijima, T. Mikawa, T. Ninomiya, R. Miyanaga, Y. Kawashima, K. Tsuji, A. Himeno, T. Okada, R. Azuma, K. Shimakawa, H. Sugaya, T. Takagi, R. Yasuhara, H. Horiba, H. Kumigashira, and M. Oshima, *Highly Reliable TaO_x ReRAM and Direct Evidence of Redox Reaction Mechanism*, in 2008 IEEE International Electron Devices Meeting, pp. 293–296, 2008.

[25] B. Hudec, A. Paskaleva, P. Jancovic, J. Derer, J. Fedor, A. Rosova, E. Dobrocka, and K. Froehlich, *Resistive switching in TiO_2-based metal-insulator-metal structures with Al_2O_3 barrier layer at the metal/dielectric interface*, Thin Solid Films **563**, 10 (2014).

[26] S. Stathopoulos, A. Khiat, M. T. S. Cortese, A. Serb, I. Valov, and T.Prodromakis, *Multibit memory operation of metal-oxide bi-layer memristors*, Science Reports **7**, 17532 (2017).

[27] M. J. Kim, I. G. Baek, Y. H. Ha, S. J. Baik, J. H. Kim, D. J. Seong, S. J. Kim, Y. H. Kwon, C. R. Lim, H. K. Park, D. Gilmer, P. Kirsch, R. Jammy, Y. G. Shin, S. Choi, and C. Chung, *Low Power Operating Bipolar TMO ReRAM for Sub 10 nm Era*, in 2010 International Electron Devices Meeting, volume 10, pp. 19.3.1–19.3.4, 2010.

[28] N. Nisan and S. Schocken, *The Elements of Computing Systems: Building a Modern Computer from First Principles*, chapter 5 Computer Architecture, The MIT Press, 2005.

[29] R. Ben-Hur and S. Kvatinsky, *Memristive Memory Processing Unit (MPU) Controller for In-Memory Processing*, in 2016 ICSEE International Conference on the Science of Electrical Engineering, 2016.

[30] V. V. Zhirnov and M. J. Marinella, *Memory Technologies: Status and Perspectives*, chapter 3, pp. 37–55, Wiley & Sons, Ltd., 2015.

[31] L. Crippa, R. Micheloni, I. Motta, and M. Sangalli, *Memories in Wireless Systems*, chapter 2 Nonvolatile Memories: NOR vs. NAND Architectures, pp. 29–53, Springer Verlag, 2008.

[32] SanDisk, *SanDisk Compact Flash Memory Card OEM product manual*, SanDisk Corporation, 12.0 edition, 2007.

[33] Micron, 4 MB SMART 3 BOOT BLOCK FLASH MEMORY, `https://www.intel.cn/content/dam/altera-www/global/zh_CN/pdfs/literature/ds/micron.pdf`, 2001.

[34] L. Wang, L. Tu, and J. Wen, *Application of phase-change materials in memory taxonomy*, Science and Technology of Advanced Materials **18**, 406 (2017).

[35] H. Ishiwara, *Ferroelectric Random Access Memories*, Journal of Nanoscience and Nanotechnology **12**, 7619 (2012).

[36] S. Bhatti, R. Sbiaa, A. Hirohata, H. Ohno, S. Fukami, and S. N. Piramanayagam, *Spintronics based random access memory: a review*, Materials Today **20**, 530 (2017).

[37] R. Waser, R. Dittmann, E. Linn, and S. Menzel, *Energy efficient computing by redox-based memristive oxide elements*, in 2016 IEEE Silicon Nanoelectronics Workshop (SNW), 2016.

[38] C. Bäumer and R. Dittmann, Redox-based memristive metal-oxide devices, in Metal Oxide-Based Thin Film Structures, edited by N. Pryds, V. Esposito, and G. Korotcenkov, pp. 489–522, Elsevier Inc., 2018.

[39] S. Menzel, M. Salinga, U. Böttger, and M. Wimmer, *Physics of the Switching Kinetics in Resistive Memories*, Advanced Functional Materials **25**, 6306 (2015).

[40] C. Chen, L. Goux, A. Fantini, S. Clima, R. Degraeve, A. Redolfi, Y. Chen, G. Groeseneken, and M. Jurczak, *Endurance degradation mechanisms in $TiN/Ta_2O_5/Ta$ resistive random-access memory cells*, Applied Physics Letters **106** (2015).

[41] D. Cooper, C. Bäumer, N. Bernier, A. Marchewka, C. L. Torre, R. E. Dunin-Borkowski, S. Menzel, R. Waser, and R. Dittmann, *Anomalous Resistance Hysteresis in Oxide ReRAM: Oxygen Evolution and Reincorporation Revealed by in situ TEM*, Advanced Materials **29**, 1700212 (2017).

[42] ITRS, The International Technology Roadmap for Semiconductors - 2015 Edition, Technical report, ESIA, JEITA, KSIA, TSIA, SIA, 2015.

[43] T. Schwarz, Introduction to Information Storage Technology, `http://www.cse.scu.edu/~tschwarz/coen180_04/LN/sram.html`, 2004.

[44] J. A. J. Rupp, R. Waser, and D. J. Wouters, *Threshold Switching in Amorphous Cr-doped Vanadium Oxide for New Crossbar Selector*, in 2016 IEEE 8th International Memory Workshop (IMW), 2016.

[45] Y. C. Bae, A. R. Lee, J. B. Lee, J. H. Koo, K. C. Kwon, J. G. Park, H. S. Im, and J. P. Hong, *Oxygen Ion Drift-Induced Complementary Resistive Switching in Homo $TiO_x/TiO_y/TiO_x$ and Hetero $TiO_x/TiON/TiO_x$ Triple Multilayer Frameworks*, Advanced functional materials **22**, 709 (2012).

[46] D. H. Lim, G. Y. Kim, J. H. Song, K. S. Jeong, D. C. Kim, S. W. Nam, M. H. Cho, and T. G. Lee, *Electric field effect dominated bipolar resistive switching through interface control in a $Pt/TiO_2/TiN$ structure*, RSC Advances **5**, 221 (2015).

[47] Y. H. Do, J. S. Kwak, J. P. Hong, H. Im, and B. H. Park, *Nonvolatile Unipolar and Bipolar Resistive Switching Characteristics in Co-doped TiO_2 Thin Films with Different Compliance Currents*, Journal of the Korean Physical Society **55**, 1009 (2009).

[48] S. Hirose, A. Nakayama, H. Niimi, K. Kageyama, and H. Takagi, *Improvement in Resistance Switching and Retention Properties of Pt/TiO_2 Schottky Junction Devices*, Journal of The Electrochemical Society **158**, H261 (2011).

[49] B. Zeng, D. Xu, Z. Tang, Y. Xiao, Y. Zhou, R. Xiong, M. Tang, Z. Li, and Y. Zhou, *Improvement of Resistive Switching Characteristics in Solution-Synthesized Al, Cr, and Cu-Doped TiO_2 Films*, ECS Solid State Letters **3**, Q59 (2014).

[50] H. Mähne, S. Slesazeck, S. Jakschik, I. Dirnstorfer, and T. Mikolajick, *The influence of crystallinity on the resistive switching behavior of TiO_2*, Microelectronic Engineering **88**, 1148 (2011).

[51] S. K. Kim, B. J. Choi, K. J. Yoon, Y. W. Yoo, and C. S. Hwang, *Control of conducting filaments in TiO_2 films by a thin interfacial conducting oxide layer at the cathode*, Applied Physics Letters **102**, 82903/1 (2013).

[52] G. Kim, J. H. Lee, J. Y. Seok, S. J. Song, J. H. Yoon, K. J. Yoon, M. H. Lee, K. M. Kim, H. D. Lee, S. W. Ryu, T. J. Park, and C. S. Hwang, *Improved endurance of resistive switching TiO_2 thin film by hourglass shaped Magnéli filaments*, Applied physics letters **98**, 262901 (2011).

[53] K. Szot, M. Rogala, W. Speier, Z. Klusek, A. Besmehn, and R. Waser, *TiO_2 - a prototypical memristive material*, Nanotechnology **22**, 254001/1 (2011).

[54] W. G. Kim and S. W. Rhee, *Effect of the top electrode material on the resistive switching of TiO_2 thin film*, Microelectronic Engineering **87**, 98 (2010).

[55] S. Oh, H. Jung, and H. Lee, *Effect of the top electrode materials on the resistive switching characteristics of TiO_2 thin film*, Journal of Applied Physics **109**, 124511 (2011).

[56] P. Bousoulas, I. Michelakaki, and D. Tsoukalas, *Influence of Ti top electrode thickness on the resistive switching properties of forming free and self-rectified TiO_{2-x} thin films*, Thin Solid Films **571**, 23 (2014).

[57] S. Brivio, J. Frascaroli, and S. Spiga, *Role of Al doping in the filament disruption in HfO_2 resistance switches*, Nanotechnology **28**, 395202 (2017).

[58] M. Barlas, A. Grossi, L. Grenouillet, E. Vianello, E. Nolot, N. Vaxelaire, P. Blaise, B. Traoré, J. Coignus, F. Perrin, R. Crochemore, F. Mazen, L. Lachal, S. Pauliac, C. Pellissier, S. Bernasconi, S. Chevalliez, J. F. Nodin, L. Perniola, and E. Nowak, *Improvement of HfO_2 based RRAM array performances by local Si implantation*, in 2017 IEEE International Electron Devices Meeting (IEDM), pp. 14.6.1–14.6.4, 2017.

[59] H. Zhang, L. Liu, B. Gao, Y. Qiu, X. Liu, J. Lu, R. Han, J. Kang, and B. Yu, *Gd-doping effect on performance of HfO_2 based resistive switching memory devices using implantation approach*, Applied Physics Letters **98**, 42105/1 (2011).

[60] B. Gao, H. W.Zhang, S. Yu, B.Sun, L. F. Liu, X. Y. Liu, Y. Wang, R. Q. Han, J. F. Kang, B. Yu, and Y. Y. Wang, *Oxide-Based RRAM: Uniformity Improvement Using A New Material-Oriented Methodology*, 2009 Symposium On VlSI Technology, Digest of Technical Papers , 30 (2009).

[61] Z. Fang, X. P. Wang, J. Sohn, B. B. Weng, Z. P. Zhang, Z. X. Chen, Y. Z. Tang, G. Lo, J. Provine, S. S. Wong, H.-P. Wong, and D. Kwong, *The Role of Ti Capping Layer in HfOx-Based RRAM Devices*, IEEE Electron Device Letters **35**, 912 (2014).

[62] B. Traore, P. Blaise, E. Vianello, L. Perniola, B. D. Salvo, and Y. Nishi, *HfO_2-Based RRAM: Electrode Effects, Ti/HfO_2 Interface, Charge Injection, and Oxygen (O) Defects Diffusion Through Experiment and Ab Initio Calculations*, IEEE Transactions on Electron Devices **63**, 360 (2016).

[63] S. Z. Rahaman, Y.-D. Lin, H.-Y. Lee, Y.-S. Chen, P.-S. Chen, W.-S. Chen, C.-H. Hsu, K.-H. Tsai, M.-J. Tsai, and P.-H. Wang, *The Role of Ti Buffer Layer Thickness on the Resistive Switching Properties of Hafnium Oxide-Based Resistive Switching Memories*, Langmuir **33**, 4654–4665 (2017).

[64] S. Privitera, G. Bersuker, S. Lombardo, C. Bongiorno, and D. Gilmer, *Conductive filament structure in HfO_2 resistive switching memory devices*, Solid-State Electronics **111**, 161 (2015).

[65] C. Y. Chen, A. Fantini, L. Goux, R. Degraeve, S. Clima, A. Redolfi, G. Groeseneken, and M. Jurczak, *Programming-conditions solutions towards suppression of retention tails of scaled oxide-based RRAM*, in IEEE International Electron Devices Meeting (IEDM), pp. 10.6.1–10.6.4, 2015.

[66] Y. Chen, L. Goux, S. Clima, B. Govoreanu, R. Degraeve, G. Kar, A. Fantini, G. Groeseneken, D. Wouters, and M. Jurczak, *Endurance/Retention Trade-off on HfO_2/Metal Cap 1T1R Bipolar RRAM*, IEEE Transactions on Electron Devices **60**, 1114 (2013).

[67] J. Lee, E. M. Bourim, W. Lee, J. Park, M. Jo, S. Jung, J. Shin, and H. Hwang, *Effect of ZrO_x/HfO_x bilayer structure on switching uniformity and reliability in nonvolatile memory applications*, Applied Physics Letters **97**, 172105 (2010).

[68] C.-Y. Huang, C.-Y. Huang, T.-L. Tsai, C.-A. Lin, and T.-Y. Tseng, *Switching mechanism of double forming process phenomenon in ZrO_x/HfO_y bilayer resistive switching memory structure with large endurance*, Applied Physics Letters **104**, 06290/1 (2014).

[69] L. Goux, A. Fantini, G. Kar, Y. Chen, N. Jossart, R. Degraeve, S. Clima, B. Govoreanu, G. Lorenzo, G. Pourtois, D. Wouters, J. Kittl, L. Altimime, and M. Jurczak, *Ultralow sub-500nA operating current high-performance $TiN/Al_2O_3/HfO_2/Hf/TiN$ bipolar RRAM achieved through understanding-based stack-engineering*, in Digest of Technical Papers - Symposium on VLSI Technology, pp. 159–160, 2012.

[70] H. Wu, X. Li, M. Wu, F. Huang, Z. Yu, and H. Qian, *Resistive Switching Performance Improvement of Ta_2O_{5-x}/TaO_y Bilayer ReRAM Devices by Inserting AlO_δ Barrier Layer*, IEEE Electron Device Letters **35**, 39 (2014).

[71] H. Y. Lee, P. S. Chen, T. Y. Wu, Y. S. Chen, C. C. Wang, P. J. Tzeng, C. H. Lin, F. Chen, C. H. Lien, and M. J. Tsai, *Low Power and High Speed Bipolar Switching with A Thin Reactive Ti Buffer Layer in Robust HfO_2 Based RRAM*, in 2008 IEEE International Electron Devices Meeting, pp. 1–4, 2008.

[72] B. Govoreanu, G. Kar, Y. Chen, V. Paraschiv, S. Kubicek, A. Fantini, I. Radu, L. Goux, S. Clima, R. Degraeve, N. Jossart, O. Richard, T. Vandeweyer, K. Seo, P. Hendrickx, G. Pourtois, H. Bender, L. Altimime, D. Wouters, J. Kittl, and M. Jurczak, *10×10nm^2 Hf/HfO$_x$ crossbar resistive RAM with excellent performance, reliability and low-energy operation*, in IEEE International Electron Devices Meeting, pp. 31.6.1–31.6.4, 2011.

[73] C. Wang, H. Wu, B. Gao, W. Wu, L. Dai, X. Li, and H. Qian, *Ultrafast RESET Analysis of HfO$_x$-Based RRAM by Sub-Nanosecond Pulses*, Advanced Electronic Materials **3**, 1700263 (2017).

[74] S. Koveshnikov, K. Matthews, K. Min, D. Gilmer, M. Sung, S. Deora, H. Li, S. Gausepohl, P. Kirsch, and R. Jammy, *Real-time study of switching kinetics in integrated 1T/ HfO$_x$ 1R RRAM: Intrinsic tunability of set/reset voltage and trade-off with switching time*, in Technical Digest - International Electron Devices Meeting (IEDM), pp. 20.4.1–20.4.3, 2012.

[75] Y. Nishi, S. Schmelzer, U. Böttger, and R. Waser, *Weibull Analysis of the Kinetics of Resistive Switches based on Tantalum Oxide Thin Films*, Proceedings of the 43rd European Solid-State Device Research Conference (ESSDERC) , 174 (2013).

[76] M. G. Cao, Y. S. Chen, J. R. Sun, D. S. Shang, L. F. Liu, J. F. Kang, and B. G. Shen, *Nonlinear dependence of set time on pulse voltage caused by thermal accelerated breakdown in the Ti/HfO$_2$/Pt resistive switching devices*, Applied Physics Letters **101**, 203502 (2012).

[77] H. Kim, M. P. Sah, C. Yang, T. Roska, and L. O. Chua, *Memristor bridge synapses*, Proceedings of the IEEE **100**, 2061 (2012).

[78] S. Yu, B. Gao, Z. Fang, H. Yu, J. Kang, and H.-S. P. Wong, *A low energy oxide-based electronic synaptic device for neuromorphic visual systems with tolerance to device variation*, Advanced Materials **25**, 1774 (2013).

[79] A. S. Cassidy, R. Alvarez-Icaza, F. Akopyan, J. Sawada, J. V. Arthur, P. Merolla, P. Datta, M. González, B. Taba, A. Andreopoulos, A. Amir, S. K. Esser, J. A. Kusnitz, R. Appuswamy, C. Haymes, B. Brezzo, R. Moussalli, R. Bellofatto, C. W. Baks, M. Mastro, K. Schleupen, C. E. Cox, K. Inoue, S. E. Millman, N. Imam, E. McQuinn, Y. Y. Nakamura, I. Vo, C. Guok, D. Nguyen, S. Lekuch, S. W. Asaad, D. J. Friedman, B. L. Jackson, M. Flickner, W. P. Risk, R. Manohar, and D. S. Modha, *Real-Time Scalable Cortical Computing at 46 Giga-Synaptic OPS/Watt with ∼100× Speedup in Time-to-Solution and ∼100,000× Reduction in Energy-to-Solution*, SC14: International Conference for High Performance Computing, Networking, Storage and Analysis , 27 (2014).

[80] D. Ielmini, *Resistive switching memories based on metal oxides: mechanisms, reliability and scaling*, Semiconductor Science and Technology **31**, 063002 (2016).

[81] H. Akinaga and H. Shima, *Resistive Random Access Memory (ReRAM) Based on Metal Oxides*, Proceedings of the IEEE **98**, 2237 (2010).

[82] W. Chen, W. Lu, B. Long, Y. Li, D. Gilmer, G. Bersuker, S. Bhunia, and R. Jha, *Switching characteristics of $W/Zr/HfO_2/TiN$ ReRAM devices for multi-level cell non-volatile memory applications*, Semiconductor Science and Technology **30**, 075002 (2015).

[83] F. Nardi, S. Balatti, S. Larentis, and D. Ielmini, *Complementary switching in metal oxides: Toward diode-less crossbar RRAMs*, 2011 International Electron Devices Meeting , 31.1/1 (2011).

[84] D. Ielmini, S. Spiga, F. Nardi, C. Cagli, A. Lamperti, E. Cianci, and M. Fanciulli, *Scaling analysis of submicrometer nickel-oxide-based resistive switching memory devices*, Journal of Applied Physics **109**, 34506/1 (2011).

[85] H. Sim, H. Choi, D. Lee, M. Chang, D. Choi, Y. Son, E. Lee, W. Kim, Y. Park, I. Yoo, and H. Hwang, *Excellent Resistance Switching Characteristics of $Pt/SrTiO_3$ Schottky Junction for Multi-bit Nonvolatile Memory Application*, in IEEE International Electron Devices Meeting, pp. 777–780, 2005.

[86] S. Menzel, *Simulation and Modelling of the Switching Dynamics in Electrochemical Metallization and Valence Change Memory Cells (invited)*, in 2016 NVM Psi-k Workshop: New Horizons for Memory Storage: Advancing Non-volatile Memory with Atomistic Simulations, 2016.

[87] J. B. Chung, Y. C. Bae, A. R. Lee, G. H. Baek, M. Y. Lee, H. W. Yoon, H. B. Park, and J. P. Hong, *Enhancement of memory windows in $Pt/Ta_2O_{5-x}/Ta$ bipolar resistive switches via a graphene oxide insertion layer*, Thin Solid Films **587**, 57 (2015).

[88] A. Prakash, D. Jana, and S. Maikap, *TaO_x-based resistive switching memories: Prospective and challenges*, Nanoscale Research Letters **8**, 1 (2013).

[89] C. Hermes, M. Wimmer, S. Menzel, K. Fleck, G. Bruns, M. Salinga, U. Boettger, R. Bruchhaus, T. Schmitz-Kempen, M. Wuttig, and R. Waser, *Analysis of Transient Currents During Ultrafast Switching of TiO_2 Nanocrossbar Devices*, IEEE Electron Device Letters **32**, 1116 (2011).

[90] S. Kim, K. Kim, D. Jeong, W. Jeon, K. Yoon, and C. Hwang, *Titanium dioxide thin films for next-generation memory devices*, Journal of Materials Research **28**, 313 (2013).

[91] B. Govoreanu, A. Ajaykumar, H. Lipowicz, Y. Chen, J. Liu, R. Degraeve, L. Zhang, S. Clima, L. Goux, I. Radu, A. Fantini, N. Raghavan, G. Kar, W. Kim, A. Redolfi, D. Wouters, L. Altimime, and M. Jurczak, *Performance and reliability of Ultra-Thin HfO_2-based RRAM (UTO-RRAM)*, in 2013 5th IEEE International Memory Workshop, pp. 48–51, 2013.

[92] D. Garbin, E. Vianello, O. Bichler, Q. Rafhay, C. Gamrat, G. Ghibaudo, B. DeSalvo, and L. Perniola, *HfO_2-Based OxRAM Devices as Synapses for Convolutional Neural Networks*, IEEE Transactions on Electron Devices **62**, 2494 (2015).

[93] A. Rodriguez-Fernandez, C. Cagli, J. Sune, and E. Miranda, *Switching Voltage and Time Statistics of Filamentary Conductive Paths in HfO_2-Based ReRAM Devices*, IEEE Electron Device Letters **39**, 656 (2018).

[94] U. Celano, J. O. de Beeck, S. Clima, M. L. andP. M. Koenraad, L. Goux, I. Valov, and W. Vandervorst, *Direct Probing of the Dielectric Scavenging-Layer Interface in Oxide Filamentary-Based Valence Change Memory*, ACS Applied Materials and Interfaces **9**, 10820–10824 (2017).

[95] C. Chen, L. Goux, A. Fantini, A. Redolfi, S. Clima, R. Degraeve, Y. Chen, G. Groeseneken, and M. Jurczak, *Understanding the impact of programming pulses and electrode materials on the endurance properties of scaled Ta_2O_5 RRAM cells*, in Technical Digest - International Electron Devices Meeting (IEDM), pp. 14.2.1–14.2.4, 2015.

[96] S. Menzel, A. Marchewka, B. Rösgen, W. Kim, V. Havel, K. Fleck, V. Rana, U. Böttger, D. Wouters, and R. Waser, *Switching Kinetics of Ta_2O_5-based ReRAM: Limiting Processes and Ultimate Switching Speed*, in 5th International Conference Smart and Multifunctional Materials Structures & Systems, 2016, CIMTEC 2016, Perugia, Italy, June 5-9, 2016.

[97] R. Münstermann, T. Menke, R. Dittmann, and R. Waser, *Coexistence of Filamentary and Homogeneous Resistive Switching in Fe-doped $SrTiO_3$ Thin-Film Memristive Devices*, Advanced Materials **22**, 4819 (2010).

[98] M. Kubicek, R. Schmitt, F. Messerschmitt, and J. L. M. Rupp, *Uncovering Two Competing Switching Mechanisms for Epitaxial and Ultrathin Strontium Titanate-Based Resistive Switching Bits*, ACS Nano **9**, 10737 (2015).

[99] F. Miao, J. J. Yang, J. Borghetti, G. Medeiros-Ribeiro, and R. S. Williams, *Observation of two resistance switching modes in TiO_2 memristive devices electroformed at low current*, Nanotechnology **22**, 254007 (2011).

[100] X. B. Yin, K. Tian, Z. H. Tan, R. Yang, and X. Guo, *Polarity Reversal in the Bipolar Switching of Anodic TiO_2 Film*, Journal of the Electrochemical Society **162**, E271 (2015).

[101] C. Bäumer, C. Schmitz, A. Marchewka, D. N. Mueller, R. Valenta, J. Hackl, N. Raab, S. P. Rogers, M. I. Khan, S. Nemsak, M. Shim, S. Menzel, C. M. Schneider, R. Waser, and R. Dittmann, *Quantifying redox-induced Schottky barrier variations in memristive devices via in operando spectromicroscopy with graphene electrodes*, Nature Communications **7**, 12398 (2016).

[102] A. Schönhals, C. M. M. Rosario, S. Hoffmann-Eifert, R. Waser, S. Menzel, and D. J. Wouters, *Role of the Electrode Material on the RESET Limitation in Oxide ReRAM Devices*, Advanced Electronic Materials **4**, 1700243/1 (2017).

[103] C. L. Torre, A. Kindsmueller, D. J. Wouters, C. E. Graves, G. A. Gibson, J. P. Strachan, R. S. Williams, R. Waser, and S. Menzel, *Volatile HRS asymmetry and subloops in resistive switching oxides*, Nanoscale **9**, 14414 (2017).

[104] J. P. Strachan, J. J. Yang, L. A. Montoro, C. A. Ospina, A. J. Ramirez, A. L. D. Kilcoyne, G. Medeiros-Ribeiro, and R. S. Williams, *Characterization of electroforming-free titanium dioxide memristors*, Beilstein Journal of Nanotechnology **4**, 467 (2013).

[105] B. Govoreanu, D. Crotti, S. Subhechha, L. Zhang, Y. Chen, S. Clima, V. Paraschiv, H. Hody, C. Adelmann, M. Popovici, O. Richard, and M. Jurczak, *a-VMCO: a novel forming-free, self-rectifying, analog memory cell*, in 2015 Symposium on VLSI Technology Digest of Technical Papers, pp. T132–T133, 2015.

[106] J. G. Simmons, *Electric Tunnel Effect between Dissimilar Electrodes Separated by a Thin Insulating Film*, Journal of Applied Physics **34**, 2581 (1963).

[107] C. Funck, A. Marchewka, C. Bäumer, P. C. Schmidt, P. Mueller, R. Dittmann, M. Martin, R. Waser, and S. Menzel, *A Theoretical and Experimental View on the Temperature Dependence of the Electronic Conduction through a Schottky Barrier in a Resistively Switching $SrTiO_3$-based Memory Cell*, Advanced Electronic Materials **4**, 1800062/1 (2018).

[108] J. Hur, W. J. Jeong, M. Shin, and Y. K. Choi, *Schottky Tunneling Effects in a Tunnel FET*, IEEE Transactions on Electron Devices **64**, 5223 (2017).

[109] S. M. Sze and K. K. Ng, *Physics of Semiconductor Devices*, Wiley, 3 edition, 2007.

[110] F.-C. Chiu, *A Review on Conduction Mechanisms in Dielectric Films*, Advances in Materials Science and Engineering **2014**, 1 (2014).

[111] N. Mott and E. Davis, *Electronic Processes in Non-Crystalline Materials*, Clarendon-Press, Oxford, 1971.

[112] Y. F. Chang, B. Fowler, Y. C. Chen, Y. T. Chen, Y. Wang, F. Xue, F. Zhou, and J. C. Lee, *Intrinsic SiO_x-based unipolar resistive switching memory. II. Thermal effects on charge transport and characterization of multilevel programing*, Journal of Applied Physics **116**, 43709/1 (2014).

[113] M. Landmann, E. Rauls, and W. G. Schmidt, *The electronic structure and optical response of rutile, anatase and brookite TiO_2*, Journal of Physics-Condensed Matter **24**, 195503/1 (2012).

[114] S. K. Kim, S. Hoffmann-Eifert, M. Reiners, and R. Waser, *Relation Between Enhancement in Growth and Thickness-Dependent Crystallization in ALD TiO_2 Thin Films*, Journal of the Electrochemical Society **158**, D6 (2011).

[115] M. Reiners, *Integration and Characterization of Atomic Layer Deposited TiO_2 Thin Films for Resistive Switching Applications*, PhD thesis, RWTH Aachen University & Forschungszentrum Juelich GmbH, Germany, 2014.

[116] Y. C. Bae, A. R. Lee, J. S. Kwak, H. Im, and J. P. Hong, *Dependence of resistive switching behaviors on oxygen content of the $Pt/TiO_{2-x}/Pt$ matrix*, Current Applied Physics **11**, e66 (2011).

[117] D. S. Jeong, H. Schroeder, U. Breuer, and R. Waser, *Characteristic electroforming behavior in $Pt/TiO_2/Pt$ resistive switching cells depending on atmosphere*, Journal of Applied Physics **104**, 123716/1 (2008).

[118] X. Cao, X. Li, W. Yu, X. Liu, and X. He, *Bipolar resistive switching properties of microcrystalline TiO_2 thin films deposited by pulsed laser deposition*, Materials Science and Engineering B-Advanced Functional Solid-State Materials **157**, 36 (2009).

[119] K. M. Kim, B. J. Choi, Y. C. Shin, S. Choi, and C. S. Hwang, *Anode-interface localized filamentary mechanism in resistive switching of TiO_2 thin films*, Applied Physics Letters **91**, 12907/1 (2007).

[120] H. Tang, K. Prasad, R. Sanjines, P. E. Schmid, and F. Levy, *Electrical and optical properties of TiO_2 anatase thin films*, Journal of Applied Physics **75**, 2042 (1994).

[121] M. Stamate, G. Lazar, and I. Lazar, *Anatase - Rutil TiO_2 Thin Films Deposited in a D.C. Magnetron Sputtering System*, Romanian Journal of Physics **53**, 217 (2008).

[122] B. Enright and D. Fitzmaurice, *Spectroscopic determination of electron and mole effective masses in a nanocrystalline semiconductor film*, Journal of Physical Chemistry **100**, 1027 (1996).

[123] M. Dou and C. Persson, *Comparative study of rutile and anatase SnO_2 and TiO_2: Band-edge structures, dielectric functions, and polaron effects*, Journal of Applied Physics **113**, 83703/1 (2013).

[124] A. Cacucci, I. Tsiaoussis, V. Potin, L. Imhoff, N. Martin, and T. Nyberg, *The interdependence of structural and electrical properties in $TiO_2/TiO/Ti$ periodic multilayers*, Acta Materialia **61**, 4215 (2013).

[125] T. V. Perevalov and V. A. Gritsenko, *Electronic structure of TiO_2 rutile with oxygen vacancies: Ab initio simulations and comparison with the experiment*, Journal of Experimental and Theoretical Physics **112**, 310 (2011).

[126] R. G. Breckenridge and W. R. Hosler, *Electrical Properties of Titanium Dioxide Semiconductors*, Physical Review **91**, 793 (1953).

[127] S. Sen, S. Mahanty, S. Roy, O. Heintz, S. Bourgeois, and D. Chaumont, *Investigation on sol-gel synthesized Ag-doped TiO_2 cermet thin films*, Thin Solid Films **474**, 245 (2005).

[128] D. Yoo, I. Kim, S. Kim, C. H. Hahn, C. Lee, and S. Cho, *Effects of annealing temperature and method on structural and optical properties of TiO_2 films prepared by RF magnetron sputtering at room temperature*, Applied Surface Science **253**, 3888 (2007).

[129] L. Li, J. Yan, T. Wang, Z. J. Zhao, J. Zhang, J. Gong, and N. Guan, *Sub-10 nm rutile titanium dioxide nanoparticles for efficient visible-light-driven photocatalytic hydrogen production*, Nature Communications **6**, 5881/1 (2015).

[130] D. O. Scanlon, C. W. Dunnill, J. Buckeridge, S. A. Shevlin, A. J. Logsdail, S. M. Woodley, C. R. A. Catlow, M. J. Powell, R. G. Palgrave, I. P. Parkin, G. W. Watson, T. W. Keal, P. Sherwood, A. Walsh, and A. A. Sokol, *Band alignment of rutile and anatase TiO_2*, Nature Materials **12**, 798 (2013).

[131] M. H. Lee, K. M. Kim, G. H. Kim, J. Y. Seok, S. J. Song, J. H. Yoon, and C. S. Hwang, *Study on the electrical conduction mechanism of bipolar resistive switching*

TiO_2 thin films using impedance spectroscopy, Applied Physics Letters **96**, 152909/1 (2010).

[132] A. Naldoni, M. Allieta, S. Santangelo, M. Marelli, F. Fabbri, S. Cappelli, C. L. Bianchi, R. Psaro, and V. D. Santo, *Effect of Nature and Location of Defects on Bandgap Narrowing in Black TiO_2 Nanoparticles*, Journal of American Chemical Society **134**, 7600 (2012).

[133] K. Kim, B. Choi, M. Lee, G. Kim, S. Song, J. Seok, J. Yoon, S. Han, and C. Hwang, *A detailed understanding of the electronic bipolar resistance switching behavior in $Pt/TiO_2/Pt$ structure*, Nanotechnology **22** (2011).

[134] L. Bursill, *Intergrowth Phenomena in the Higher Titanium Oxides*, Current Contents/physical Chemical & Earth Sciences , 16 (1989).

[135] A. D. Inglis, Y. L. Page, P. Strobel, and C. M. Hurd, *Electrical conductance of crystalline Ti_nO_{2n-1} for n=4-9*, Journal of Physics C-Solid State Physics **16**, 317 (1983).

[136] D.-H. Kwon, K. M. Kim, J. H. Jang, J. M. Jeon, M. H. Lee, G. H. Kim, X.-S. Li, G.-S. Park, B. Lee, S. Han, M. Kim, and C. S. Hwang, *Atomic structure of conducting nanofilaments in TiO_2 resistive switching memory*, Nature Nanotechnology **5**, 148 (2010).

[137] R. J. Kamaladasa, A. A. Sharma, Y. Lai, W. Chen, P. A. Salvador, J. A. Bain, M. Skowronski, and Y. N. Picard, *In Situ TEM Imaging of Defect Dynamics under Electrical Bias in Resistive Switching Rutile-TiO_2*, Microscopy and Microanalysis **21**, 140 (2015).

[138] K. Wefers and C. Misra, *Oxides and Hydroxides of Aluminum*, Aluminum Company of America, 1987, Alcoa Laboratories.

[139] D. R. Askeland, P. P. Fulay, and W. J. Wright, *The Science and Engineering of Materials, SI Edition*, Cengage Learning, Inc., 6th edition, 2011.

[140] M. Yazdanmehr, S. J. Asadabadi, A. Nourmohammadi, and M. Ghasemzadeh, *Electronic structure and bandgap of γ-Al_2O_3 compound using mBJ exchange potential*, Nanoscale Research Letters (2012).

[141] N. Yu, T. Simpson, P. Mclntyre, M. Nastasi, and I. Mitchell, *Doping effects on the kinetics of solid-phase epitaxial growth of amorphous alumina thin films on sapphire*, Applied Physics Letters **67**, 924 (1995).

[142] M. D. Groner, F. H. Fabreguette, J. W. Elam, and S. M. George, *Low-Temperature Al_2O_3 Atomic Layer Deposition*, Chemistry of Materials **16**, 639–645 (2004).

[143] G. D. Wilk, R. M. Wallace, and J. M. Anthony, *High-κ gate dielectrics: Current status and materials properties considerations*, Journal of Applied Physics **89**, 5243 (2001).

[144] M. Specht, M. Stadele, S. Jakschik, and U. Schroder, *Transport mechanisms in atomic-layer-deposited Al_2O_3 dielectrics*, Applied Physics Letters **84**, 3076 (2004).

[145] M. Martin, B. Dlubak, R. S. Weatherup, H. Yang, C. Deranlot, K. Bouzehouane, F. Petroff, A. Anane, S. Hofmann, J. Robertson, A. Fert, and P. Seneor, *Sub-nanometer Atomic Layer Deposition for Spintronics in Magnetic Tunnel Junctions Based on Graphene Spin-Filtering Membranes*, ACS Nano **8**, 7890 (2014).

[146] T. V. Perevalov, V. A. Gritsenko, and V. V. Kaichev, *Electronic structure of aluminum oxide: ab initio simulations of α and γ phases and comparison with experiment for amorphous films*, The European Physical Journal Applied Physics **52**, 30501/1 (2010).

[147] M. L. Huang, Y. C. Chang, C. H. Chang, T. D. Lin, J. Kwo, T. B. Wu, and M. Hong, *Energy-band parameters of atomic-layer-deposition $Al_2O_3/InGaAs$ heterostructure*, Applied Physics Letters **89**, 12903/1 (2006).

[148] E. W. Cowell, S. W. Muir, D. A. Keszler, and J. F. Wager, *Barrier height estimation of asymmetric metal-insulator-metal tunneling diodes*, Journal of Applied Physics **114**, 213703/1 (2013).

[149] A. Kerber, E. Cartier, P. Roussel, L. Pantisano, T. Kauerauf, G. Groeseneken, H. Maes, and U. Schwalke, *Charge trapping and dielectric reliability of SiO_2-Al_2O_3 gate stacks with TiN electrodes*, IEEE Transactions on Electron Devices **50**, 1261 (2003).

[150] J. Kim, J. Song, O. Kwon, S. Kim, C. Hwang, S. Park, S. Yun, J. Jeong, and K. Hyun, *Improvement in electrical insulating properties of 10-nm-thick Al_2O_3 film grown on Al/TiN/Si substrate by remote plasma annealing at low temperatures*, Applied Physics Letters **80**, 2734 (2002).

[151] A. M. Mahajan, A. G. Khairnar, and B. J. Thibeault, *Electrical properties of MOS capacitors formed by PEALD grown Al_2O_3 on silicon*, Semiconductors **48**, 497 (2014).

[152] S. Ganguly, J. Verma, G. Li, T. Zimmermann, H. Xing, and D. Jena, *Barrier height, interface charge & tunneling effective mass in ALD Al_2O_3/AlN/GaN HEMTs*, 69th Device Research Conference (DRC) , 121–122 (2011).

[153] Y. Yeo, T. King, and C. Hu, *Mosfet gate leakage modeling and selection guide for alternative gate dielectrics based on leakage considerations*, IEEE Transactions on Electron Devices **50**, 1027 (2003).

[154] H. Lin, P. Ye, and G. Wilk, *Leakage current and breakdown electric-field studies on ultrathin atomic-layer-deposited Al_2O_3 on GaAs*, Applied Physics Letters **87**, 182904/1 (2005).

[155] Q. Shu and W. Ma, *Barrier parameter variatoin in Al-Al_2O_3-metal tunnel junctions*, Applied Physics Letters **61**, 2542 (1992).

[156] D. Liu, S. J. Clark, and J. Robertson, *Oxygen vacancy levels and electron transport in Al_2O_3*, Applied Physics Letters **96**, 32905/1 (2010).

[157] D. Liu, Y. Guo, L. Lin, and J. Robertson, *First-principles calculations of the electronic structure and defects of Al_2O_3*, Journal of Applied Physics **114**, (2013).

[158] S. Nigo, M. Kubota, Y. Harada, T. Hirayama, S. Kato, H. Kitazawa, and G. Kido, *Conduction band caused by oxygen vacancies in aluminum oxide for resistance random access memory*, Journal of Applied Physics **112**, 33711/1 (2012).

[159] E. O. Filatova, A. S. Konashuk, F. Schaefers, and V. V. Afanas'ev, *Metallization-Induced Oxygen Deficiency of γ-Al_2O_3 Layers*, The Journal of Physical Chemistry C **120**, 8979 (2016).

[160] R. French, *Electronic Band Structure of Al_2O_3 with Comparison to AlON and AlN*, Journal of the American Ceramic Society **73**, 477 (1990).

[161] B. Ealet, M. H. Elyakhloufi, E. Gillet, and M. Ricci, *Electronic and crystallographic structure of γ-alumina thin films*, Thin Solid Films **250**, 92 (1994).

[162] E. Bersch, S. Rangan, R. A. Bartynski, E. Garfunkel, and E. Vescovo, *Band offsets of ultrathin high-k oxide films with Si*, Physical Review B: Condensed Matter **78**, 085114 (2008).

[163] M. L. Huang, Y. C. Chang, Y. H. Chang, T. D. Lin, J. Kwo, and M. Hong, *Energy-band parameters of atomic layer deposited Al_2O_3 and HfO_2 on $In_xGa_{1-x}As$*, Applied Physics Letters **94**, 52106/1 (2009).

[164] V. Afanas'ev, M. Houssa, A. Stesmans, and M. Heyns, *Band alignments in metal-oxide-silicon structures with atomic-layer deposited Al_2O_3 and ZrO_2*, Journal of Applied Physics **91**, 3079 (2002).

[165] H. Nohira, W. Tsai, W. Besling, E. Young, J. Petry, T. Conard, W. Vandervorst, S. D. Gendt, M. Heyns, J. Maes, and M. Tuominen, *Characterization of ALCVD-Al_2O_3 and ZrO_2 layer using X-ray photoelectron spectroscopy*, Journal of Non-Crystalline Solids (2002).

[166] J. Robertson, *Band offsets of wide-band-gap oxides and implications for future electronic devices*, Journal of Vacuum Science and Technology B: Microelectronics and Nanometer Structures **18**, 1785 (2000).

[167] S. Y. Lien, C. H. Yang, K. C. Wu, and C. Y. Kung, *Investigation on the passivated Si/Al_2O_3 interface fabricated by non-vacuum spatial atomic layer deposition system*, Nanoscale Reserch Letters **10:93**, 1 (2015).

[168] S. E. Potts, G. Dingemans, C. Lachaud, and W. M. M. Kessels, *Plasma-enhanced and thermal atomic layer deposition of Al_2O_3 using dimethylaluminum isopropoxide, $[Al(CH_3)_2(\mu\text{-}O^iPr)]_2$, as an alternative aluminum precursor*, Journal of Vacuum Science and Technology A **30**, 21505/1 (2012).

[169] B. Vermang, A. Rothschild, A. Racz, J. John, J. Poortmans, R. Mertens, P. Poodt, M. V. Tiba, and F. Roozeboom, *High Speed Atmospheric Pressure ALD for Industrial Scale Solar Cell Passivation*, in 25th European Photovoltaic Solar Energy Conference and Exhibition / 5th World Conference on Photovoltaic Energy Conversion, pp. 2A01110–1113, 2010.

[170] S. M. George, *Atomic Layer Deposition: An Overview*, Chemical Reviews **110**, 111 (2010).

[171] C. S. Hwang, *Atomic Layer Deposition for Semiconductors*, Springer Science & Business Media, 2013.

[172] M. Bosund, E. M. Salmi, and R. Peltonen, Atomic layer deposition into ultra-high aspect ratio structures with a stop-flow ALD reactor, Technical report, BENEQ, 2016.

[173] H. Zhang, N. Aslam, M. Reiners, R. Waser, and S. Hoffmann-Eifert, *Atomic Layer Deposition of TiO_x/Al_2O_3 Bilayer Structures for Resistive Switching Memory Applications*, Chemical Vapor Deposition **20**, 282 (2014).

[174] B. Abendroth, T. Moebus, S. Rentrop, R. Strohmeyer, M. Vinnichenko, T. Weling, H. Stoecker, and D. C. Meyer, *Atomic layer deposition of TiO_2 from tetrakis(dimethylamino) titanium and H_2O*, Thin Solid Films **545**, 176 (2013).

[175] H. Kim, H.-B.-R. Lee, and W.-J. Maeng, *Applications of atomic layer deposition to nanofabrication and emerging nanodevices*, Thin Solid Films **517**, 2563 (2009).

[176] K. An, W. Cho, K. Sung, S. Lee, and Y. Kim, *Preparation of Al_2O_3 Thin Films by Atomic Layer Deposition Using Dimethylaluminum Isopropoxide and Water and Their Reaction Mechanisms*, Bulletin of the Korean Chemical Society **24**, 1659 (2003).

[177] R. Puurunen, *Surface chemistry of atomic layer deposition: a case study for the trimethylaluminum/water process*, Journal of Applied Physics **97**, 121301/1 (2005).

[178] M. Y. Li, Y. Y. Chang, H. C. Wu, C. S. Huang, J. C. Chen, J. L. Lue, and S. M. Chang, *Effect of Process Pressure on Atomic Layer Deposition of Al_2O_3*, Journal of the Electrochemical Society **154**, H967 (2007).

[179] C. B. Musgrave, *Atomic Layer Deposition of Nanostructured Materials*, chapter 1 Theoretical Modeling of ALD Process, Wiley-VCH Verlag GmbH & Co. KGaA, 2012.

[180] A. C. P. Perros, *Thermal and plasma-enhanced atomic layer deposition: the study of and employment in various nanotechnology applications*, PhD thesis, Aalto University School of Electrical Engineering, 2015.

[181] A. J. Elliot, G. Malek, L. Wille, R. Lu, S. Han, J. Z. Wu, J. Talvacchio, and R. M. Lewis, *Probing the Nucleation of Al_2O_3 in Atomic Layer Deposition on Aluminum for Ultrathin Tunneling Barriers in Josephson Junctions*, IEEE Transactions on Applied Superconductivity **23** (2013).

[182] K. S. An, W. Cho, B. K. Lee, S. S. Lee, and C. G. Kim, *Atomic Layer Deposition of Undoped and Al-Doped ZnO Thin Films Using the Zn Alkoxide Precursor Methylzinc Isopropoxide*, Journal of Nanoscience and Nanotechnology **8**, 4856 (2008).

[183] J. Koo, S. Kim, S. Jeon, H. Jeon, Y. Kim, and Y. Won, *Characteristics of Al_2O_3 Thin Films Deposited Using Dimethylaluminum Isopropoxide and Trimethylaluminum Precursors by the Plasma-Enhanced Atomic-Layer Deposition Method*, Journal of the Korean Physical Society **48**, 131 (2006).

[184] Q. Xie, Y. L. Jiang, C. Detavernier, D. Deduytsche, R. L. V. Meirhaeghe, G. P. Ru, B. Z. Li, and X. P. Qu, *Atomic layer deposition of TiO_2 from tetrakis-dimethyl-amido titanium or Ti isopropoxide precursors and H_2O*, Journal of Applied Physics **102**, 083521 (2007).

[185] M. J. Biercuk, D. J. Monsma, C. M. Marcus, J. S. Becker, and R. G. Gordon, *Low-temperature atomic-layer-deposition lift-off method for microelectronic and nanoelectronic applications*, Applied Physics Letters **83**, 2405 (2003).

[186] H. Zhang, *Atomic layer deposition of oxide thin films and integration into cross point devices for resistive switching memory applications*, Master's thesis, RWTH Aachen University & Forschungszentrum Juelich GmbH, Germany, 2013.

[187] I. Stabrawa, D. Banas, K. Dworecki, A. Kubala-Kukus, J. Braziewicz, U. Majewska, J. Wudarczyk-Mocko, M. Pajek, and S. Gozdz, *Investigation of Gold Nanolayer Properties Using X-Ray Reflectometry and Spectroscopic Ellipsometry Methods*, Acta Physica Polonica A **129**, 233 (2016).

[188] P. Zaumseil, *Materials for Information Technology*, chapter 5 X-ray Reflectivity Characterisation of Thin-Film and Multilayer Structures, pp. 497–505, Springer-Verlag London Limited, 2005.

[189] T. C. Huang, R. Giiles, and G. Will, *Thin-film thickness and density determination from X-ray reflectivity data using a conventional power diffractometer*, Thin Solid Films **230**, 99 (1993).

[190] M. Bjorck and G. Andersson, *GenX: an extensible X-ray reflectivity refinement program utilizing differential evolution*, Journal of Applied Crystallography **40**, 1174 (2007).

[191] Hitachi, `http://www.htiweb.com/Products/Advanced%20Microscopy/EM/FESEM/FESEMSU8200.html`, `https://www.hitachi-hightech.com/eu/product_detail/?pn=em-su8200&version=#Materials`.

[192] Hitachi, *Ultra-high Resolution Scanning Electron Microscope SU8000 Series*, Hitachi High-Technologies Corporation, 2011.

[193] B. Hafner, Scanning Electron Microscopy Primer, Technical report, Characterization Facility, University of Minnesota Twin Cities, 2007, page 12.

[194] Hitachi, *Instruction manual for model SU800 field emission scanning electron microscope*, Hitachi High-Technologies Corporation, 2008.

[195] B. Cheney, Introduction to Scanning Electron Microscopy, Technical report, Materials Engineering Department at San Jose State University.

[196] JEOL, A Guide to Scanning Microscope Observation, Technical report, JEOL Ltd.

[197] F. Lentz, *Integration of Redox-Based Resistive Switching Memory Devices*, PhD thesis, RWTH Aachen University & Forschungszentrum Juelich GmbH, Germany, 2014.

[198] A. Technologies, *Agilent B1500A Semiconductor Device Analyzer User's Guide*, 6th edition, 2007.

[199] O. L. Vacuum, Oil-free Scroll Vacuum Pumps SCROLLVAC SC 5 D, SC 15 D, SC 30, Technical report.

[200] O. L. Vacuum, *TURBOVAC SL 80 Wide-Range Turbomolecular Pump with Integrated or External Frequency Converter*, 2009.

[201] L. Shore, Model TTP4 Probe Station, Technical report, Lake Shore Cryotronics, Inc., 2007.

[202] Tekteonix, Using Model 4225-RPM Remote Amplifier/Switch to Switch Automatically Between DC I-V, C-V, and Pulsed I-V Measurements, Technical report, 2016.

[203] F. J. Cüppers, *Switching kinetic studies of valence change memory devices*, Master's thesis, RWTH Aachen University & Forschungszentrum Juelich GmbH, Germany, 2018.

[204] Keithley, Device Characterization with the Keithley Model 4200-SCS Characterization System, Technical report, Keithley Instruments, Inc., 2010.

[205] A. Marchewka, B. Roesgen, K. Skaja, H. Du, C. L. Jia, J. Mayer, V. Rana, R. Waser, and S. Menzel, *Nanoionic Resistive Switching Memories: On the Physical Nature of the Dynamic Reset Process*, Advanced Electronic Materials **2**, 1500233/1 (2016).

[206] A. Hardtdegen, *Atomic Layer Deposition and Characterization of Hafnium Oxide Based Mono- and Bilayers for Future ReRAM Applications*, Master's thesis, RWTH Aachen University & Forschungszentrum Juelich GmbH, Germany, 2015.

[207] H. Schroeder and D. Jeong, *Resistive switching in a Pt/TiO_2/Pt thin film stack – a candidate for a non-volatile ReRAM*, Microelectronic Engineering **84**, 1982 (2007).

[208] G. H. Kim, K. M. Kim, J. Y. Seok, M. H. Lee, S. J. Song, and C. S. Hwang, *Influence of the Interconnection Line Resistance and Performance of a Resistive Cross Bar Array Memory*, Journal of the Electrochemical Society **157**, G211 (2010).

[209] L. Goux, X. P. Wang, Y. Y. Chen, L. Pantisano, N. Jossart, B. Govoreanu, J. A. Kittl, M. Jurczak, L. Altimime, and D. J. Wouters, *Roles and Effects of TiN and Pt Electrodes in Resistive-Switching HfO_2 Systems*, Electrochemical and Solid-State Letters **14**, H244 (2011).

[210] D. Cho, M. Lübben, S. Wiefels, K. Lee, and I. Valov, *Interfacial Metal – Oxide Interactions in Resistive Switching Memories*, Applied Materials & Interfaces **9**, 19287–19295 (2017).

[211] Y. Wu, S. Yu, B. Lee, and P. Wong, *Low-power $TiN/Al_2O_3/Pt$ resistive switching device with sub-20 μA switching current and gradual resistance modulation*, Journal of Applied Physics **110**, 94104/1 (2011).

[212] C. Neusel and G. A. Schneider, *Size-dependence of the dielectric breakdown strength from nano- to millimeter scale*, Journal of the Mechanics and Physics of Solids **63**, 201 (2014).

[213] Q. Chen, H. L. Gomes, A. Kiazadeh, P. R. Rocha, D. M. D. Leeuw, and S. C. J. Meskers, *Electroforming Process in Metal-Oxide-Polymer Resistive Switching Memories*, pp. 527–534, IFIP International Federation for Information Processing 2012, 2012.

[214] J. Yota, H. Shen, and R. Ramanathan, *Characterization of atomic layer deposition HfO_2, Al_2O_3, and plasma-enhanced chemical vapor deposition Si_3N_4 as metal-insulator-metal capacitor dielectric for GaAs HBT technology*, Journal of Vacuum Science & Technology A **31**, 1A134/1 (2013).

[215] S. Menzel, E. Linn, and R. Waser, Redox-based Resistive Memory, in Emerging Naoelectronic Deivces, edited by A. Chen, J. Hutchby, V. Zhirnov, and G. Bourianoff, pp. 137–161, Wiley & Sons, Ltd., 2015.

[216] J. J. Yang, F. Miao, M. D. Pickett, D. A. A. Ohlberg, D. Stewart, C. N. Lau, and R. S. Williams, *The mechanism of electroforming of metal oxide memristive switches*, Nanotechnology **20**, 215201 (2009).

[217] K. M. Kim, D. S. Jeong, and C. S. Hwang, *Nanofilamentary resistive switching in binary oxide system; a review on the present status and outlook*, Nanotechnology **22**, 254002/1 (2011).

[218] Y. Guo and J. Robertson, *Materials selection for oxide-based resistive random access memories*, Applied Physics Letters **105**, 223516/1 (2014).

[219] V. Chuprina, I. Shalya, and V. Zenkov, *Oxidation of Porous Nanocrystalline Titanium Nitride. I. Kinetics*, Powder Metallurgy and Metal Ceramics **45**, 82 (2006).

[220] A. Hardtdegen, C. L. Torre, H. Zhang, C. Funck, S. Menzel, R. Waser, and S. Hoffmann-Eifert, *Internal Cell Resistance as the Origin of Abrupt Reset Behavior in HfO_2-based Devices determined from Current Compliance Series*, in 2016 IEEE 8th International Memory Workshop (IMW), pp. 1–4, 2016.

[221] D. Ielmini and R. Waser, *Resistive Switching - From Fundamentals of Nanoionic Redox Processes to Memristive Device Applications*, Wiley-VCH, 2016.

[222] D. Ielmini, F. Nardi, and S. Balatti, *Evidence for voltage-driven set/reset processes*, IEEE Trans. Electron Devices **59**, 2049 (2012).

[223] C. Nauenheim, *Integration of resistive switching devices in crossbar structures*, PhD thesis, RWTH Aachen University & Forschungszentrum Jülich GmbH, 2009.

[224] S. Larentis, F. Nardi, S. Balatti, D. C. Gilmer, and D. Ielmini, *Resistive Switching by Voltage-Driven Ion Migration in Bipolar RRAM-Part II: Modeling*, IEEE Transactions on Electron Devices **59**, 2468 (2012).

[225] G. Indiveri, E. Linn, and S. Ambrogio, *Resistive Switching - From Fundamentals of Nanoionic Redox Processes to Memristive Device Applications*, chapter 25 ReRAM-based Neuromorphic Computing, pp. 715–735, Wiley, 2016.

[226] Y. Wu, S. Yu, H. Wong, Y. Chen, H. Lee, S. Wang, P. Gu, F. Chen, and M. Tsai, *AlOx-based Resistive Switching Device with Gradual Resistance Modulation for Neuromorphic Device Application*, in 2012 4th IEEE International Memory Workshop (IMW), 2012.

[227] H. Lee, S. J. Clark, and J. Robertson, *Calculation of Point Defects in Rutile TiO_2 by the Screened-Exchange Hybrid Functional*, Physical Review B **86**, 075209 (2012).

[228] A. Schönhals, D. J. Wouters, A. Marchewka, T. Breuer, K. Skaja, V. Rana, S. Menzel, and R. Waser, *Critical ReRAM Stack Parameters Controlling Complementary versus Bipolar Resistive Switching*, in 2015 IEEE International Memory Workshop (IMW), pp. 73–76, 2015.

[229] S. Menzel, M. Waters, A. Marchewka, U. Böttger, R. Dittmann, and R. Waser, *Origin of the Ultra-nonlinear Switching Kinetics in Oxide-Based Resistive Switches*, Advanced Functional Materials **21**, 4487 (2011).

[230] K. Fleck, U. Böttger, R. Waser, and S. Menzel, *Interrelation of Sweep and Pulse Analysis of the SET Process in $SrTiO_3$ Resistive Switching Memories*, IEEE Electron Device Letters **35**, 924 (2014).

[231] A. Ortiz-Conde, F. Sanchez, and J. Muci, *Exact analytical solutions of the forward non-ideal diode equation with series and shunt parasitic resistances*, Solid-State Electronics **44**, 1861 (2000).

[232] P. Hruska, Z. Chobola, and L. Grmela, *Diode I-U curve fitting with Lambert W function*, in 25th International Conference on Microelectronics, p. 501, 2006.

[233] K. Fleck, U. Böttger, R. Waser, and S. Menzel, *SET and RESET Kinetics of $SrTiO_3$-based Resistive Memory Devices*, Materials Research Society Symposium Proceedings **1790**, 7 (2015).

[234] M. Y. Yang, K. Kamiya, B. Magyari-Kope, M. Niwa, Y. Nishi, and K. Shiraishi, *Charge-dependent oxygen vacancy diffusion in Al_2O_3-based resistive-random-access-memories*, Applied Physics Letters **103**, 093504 (2013).

[235] U. Russo, D. Ielmini, C. Cagli, and A. L. Lacaita, *Filament conduction and reset mechanism in NiO-based resistive-switching memory (RRAM) devices*, IEEE Transactions on Electron Devices **56**, 186 (2009).

[236] A. Cappella, J. L. Battaglia, V. Schick, A. Kusiak, A. Lamperti, C. Wiemer, and B. Hay, *High Temperature Thermal Conductivity of Amorphous Al_2O_3 Thin Films Grown by Low Temperature ALD*, Advanced Engineering Materials **15**, 1046 (2013).

[237] Y. M. Lu, M. Noman, Y. N. Picard, J. A. Bain, P. A. Salvador, and M. Skowronski, *Impact of Joule heating on the microstructure of nanoscale TiO_2 resistive switching devices*, Journal of Applied Physics **113**, 163703/1 (2013).

[238] H. Du, C. Jia, A. Koehl, J. Barthel, R. Dittmann, R. Waser, and J. Mayer, *Nanosized Conducting Filaments Formed by Atomic-Scale Defects in Redox-Based Resistive Switching Memories*, Chemistry of Materials **29**, 3164 (2017).

[239] W. Lee, S. Yoo, K. J. Yoon, I. W. Yeu, H. J. Chang, J.-H. Choi, S. Hoffmann-Eifert, R. Waser, and C. S. Hwang, *Resistance switching behavior of atomic layer deposited $SrTiO_3$ film through possible formation of $Sr_2Ti_6O_{13}$ or $Sr_1Ti_{11}O_{20}$ phases*, Scientific Reports **6**, 20550/1 (2016).

[240] D. Gu, S. K. Dey, and P. Majhi, *Effective work function of Pt, Pd, and Re on atomic layer deposited HfO_2*, Applied Physics Letters **89**, 82907/1 (2006).

[241] C. Grimes and G. Mor, *TiO_2 Nanotube Arrays: Synthesis, Properties, and Applications*, Springer US, 2009.

[242] K. M. Kim and C. S. Hwang, *The conical shape filament growth model in unipolar resistance switching of TiO_2 thin film*, Applied Physics Letters **94**, 122109/1 (2009).

[243] Y. Syu, T. Chang, J. Lou, T. Tsai, K. Chang, M. Tsai, Y. Wang, M. Liu, and S. Sze, *Atomic-level quantized reaction of HfO_x memristor*, Applied Physics Letters **102**, 172903/1 (2013).

[244] N. Fuke, A. Fukui, A. Islam, R. Komiya, R. Yamanaka, H. Harima, and L. Han, *Influence of TiO_2/electrode interface on electron transport properties in back contact dye-sensitized solar cells*, Solar Energy Materials & Solar Cells (2009).

[245] M. Setvin, J. Hulva, G. S. Parkinson, M. Schmid, and U. Diebold, *Electron Transfer between Anatase TiO_2 and an O_2 Molecule directly observed by Atomic Force Microscopy*, Proceedings of the National Academy of Sciences of the United States of America **114**, E2556 (2017).

[246] E. S. Noh, S. E. Ulloa, and H. M. Lee, *A theoretical study of an amorphous aluminium oxide layer used as a tunnel barrier in a magnetic tunnel junction*, Physica Status Solidi B-Basic Solid State Physics **244**, 4427 (2007).

[247] K. Henkel, M. Kot, and D. Schmeisser, *Localized defect states and charge trapping in atomic layer deposited-Al_2O_3 films*, Journal of Vacuum Science and Technology A **35**, 1B125/1 (2017).

[248] K. Fleck, C. L. Torre, N. Aslam, S. Hoffmann-Eifert, U. Böttger, and S. Menzel, *Uniting Gradual and Abrupt SET Processes in Resistive Switching Oxides*, Physical Review Applied **6**, 064015 (2016).

[249] A. C. Torrezan, J. P. Strachan, G. Medeiros-Ribeiro, and R. S. Williams, *Sub-nanosecond switching of a tantalum oxide memristor*, Nanotechnology **22**, 485203 (2011).

[250] V. Havel, K. Fleck, B. Rösgen, V. Rana, S. Menzel, U. Böttger, and R. Waser, *Ultrafast Switching in Ta_2O_5-based Resistive Memories*, in Silicon Nanoelectronics Worshop (SNW), pp. 82–83, 2016.

[251] Engineering ToolBox, Resistivity and Conductivity - Temperature Coefficients for Common Materials [online], `https://www.engineeringtoolbox.com/resistivity-conductivity-d_418.html`, 2003.

[252] Cirris Systems, `https://www.cirris.com/learning-center/general-testing/special-topics/177-temperature-coefficient-of-copper`, 2018.

[253] M. Shannon, T. Leicht, P. Hrnjak, N. Miller, and F. Khan, *Thin-film resistance sensor for measuring liquid mass fraction in super-heated refrigerant*, Sensors and Actuators A: Physical **88**, 164 (2001).

[254] B. Singh and N. A. Surplice, *The electrical resistivity and resistance-temperature characteristics of thin titanium films*, Thin Solid Films **10**, 243 (1971).

[255] J. Kwon, A. A. Sharma, J. A. Bain, Y. N. Picard, and M. Skowronski, *Oxygen Vacancy Creation, Drift, and Aggregation in TiO_2-Based Resistive Switches at Low Temperature and Voltage*, Advanced Functional Materials **25**, 2876 (2015).

[256] A. A. Gusev, E. G. Avvakumov, A. Z. Medvedev, and A. I. Masliy, *Ceramic Electrodes Based on Magneli Phases of Titanium Oxides*, Science of Sintering **39**, 51 (2007).

[257] K. Fleck, S. Menzel, U. Böttger, and R. Waser, *The importance of local temperature for the SET kinetics in valence change memories*, in DPG-Frühjahrstagung 2014 of the Condensed Matter Section, p. 183, 2014.

[258] S. Ambrogio, V. Milo, Z. Q. Wang, S. Balatti, and D. Ielmini, *Analytical modeling of current overshoot in oxide-based resistive switching memory (RRAM)*, IEEE Electron Device Letters **37**, 1268 (2016).

[259] K. M. Kim, J. J. Yang, E. Merced, C. Graves, S. Lam, N. Davila, M. Hu, N. Ge, Z. Li, R. S. Williams, and C. S. Hwang, *Low Variability Resistor - Memristor Circuit Masking the Actual Memristor States*, Advanced Electronic Materials **1**, 1500095/1 (2015).

[260] A. Sawa, *Resistive switching in transition metal oxides*, Materials Today **11**, 28 (2008).

[261] H. Zhang, S. Yoo, S. Menzel, C. Funck, F. Cüppers, D. J. Wouters, C. S. Hwang, R. Waser, and S. Hoffmann-Eifert, *Resistive Switching Modes with Opposite Polarity in $Pt/TiO_2/Ti/Pt$ Nano-sized ReRAM Devices*, ACS Applied Materials and Interfaces **10**, 29766 (2018).

[262] W. Ma, L. Liu, Y. Wang, Z. Chen, B. Chen, B. Gao, X. Liu, and J. Kang, *Multilevel resistive switching in $HfO_x/TiO_x/HfO_x/TiO_x$ multilayer-based RRAM with high reliability*, in 2014 12th IEEE International Conference on Solid-State and Integrated Circuit Technology (ICSICT), 2014.

[263] R. Chen, W. Hu, L. Zou, W. Xie, B. Li, and D. Bao, *Multilevel resistive switching effect in sillenite structure $Bi_{12}TiO_{20}$ thin films*, Applied Physics Letters **104**, 242111/1 (2014).

[264] H. K. Li, T. P. Chen, S. G. Hu, P. Liu, Y. Liu, P. S. Lee, X. P. Wang, H. Y. Li, and G. Q. Lo, *Study of Multilevel High-Resistance States in HfO_x-Based Resistive Switching Random Access Memory by Impedance Spectroscopy*, IEEE Transactions on Electron Devices **62**, 2684 (2015).

[265] J. Woo, K. Moon, J. Song, S. Lee, M. Kwak, J. Park, and H. Hwang, *Improved Synaptic Behavior Under Identical Pulses Using AlO_x/HfO_2 Bilayer RRAM Array for Neuromorphic Systems*, IEEE Electron Device Letters **37**, 994 (2016).

[266] S. Yu, Y. Wu, and H. Wong, *Investigating the switching dynamics and multilevel capability of bipolar metal oxide resistive switching memory*, Applied Physics Letters **98**, 103514/1 (2011).

[267] T. Nabatame, T. Yasuda, M. Nishizawa, M. Ikeda, T. Horikawa, and A. Toriumi, *Comparative Studies on Oxygen Diffusion Coefficients for Amorphous and γ-Al_2O_3 Films using ^{18}O Isotope*, Japanese Journal of Applied Physics Part 1-Regular Papers Brief Communications & Review Papers **42**, 7205 (2003).

[268] R. Nakamura, T. Toda, S. Tsukui, M. Tane, M. Ishimaru, T. Suzuki, and H. Nakajima, *Diffusion of oxygen in amorphous Al_2O_3, Ta_2O_5, and Nb_2O_5*, Journal of Applied Physics **116**, 033504 (2014).

[269] M. Müller, G. X. Miao, and J. S. Moodera, *Exchange splitting and bias-dependent transport in EuO spin filter tunnel barriers*, Europhysics Letters **88**, 47006/1 (2009).

[270] B. K. Sarker and S. I. Khondaker, *Thermionic Emission and Tunneling at Carbon Nanotube-Organic Semiconductor Interface*, ACS Nano **6**, 4993 (2012).

[271] J. Hölzl and F. K. Schulte, *Solid Surface Physics*, volume 85, chapter 1 Work Function of Metals, p. 93, Springer-Verlag: Berlin, Heidelberg, New York, 1979.

[272] J. G. Simmons, *Generalized Formula for the Electric Tunnel Effect between Similar Electrodes Separated by a Thin Insulating Film*, Journal of Applied Physics **34**, 1793 (1963).

[273] C. L. Hinkle, C. Fulton, R. J. Nemanich, and G. Lucovsky, *A novel approach for determining the effective tunneling mass of electrons in HfO_2 and other high-K alternative gate dielectrics for advanced CMOS devices*, Microelectronic Engeneering **72**, 257 (2004).

[274] U. Celano, L. Goux, A. Belmonte, K. Opsomer, A. Franquet, A. Schulze, C. Detavernier, O. Richard, H. Bender, M. Jurczak, and W. Vandervorst, *Three-Dimensional Observation of the Conductive Filament in Nanoscaled Resistive Memory nanodevices*, Nano Letters **14**, 2401 (2014).

[275] R. Degraeve, A. Fantini, N. Raghavan, L. Goux, S. Clima, Y. Chen, A. Belmonte, S. Cosemans, B. Govoreanu, D. Wouters, P. Roussel, G. Kar, G. Groeseneken, and M. Jurczak, *Hourglass concept for RRAM: a dynamic and statistical device model*, in 2014 IEEE 21st International Symposium on the Physical and Failure Analysis of Integrated Circuits (IPFA), pp. 245–249, 2014.

[276] T. H. Park, H. J. Kim, W. Y. Park, S. G. Kim, B. J. Choi, and C. S. Hwang, *Roles of conducting filament and non-filament regions in the Ta_2O_5 and HfO_2 resistive switching memory for switching reliability*, Nanoscale **9**, 6010 (2017).

[277] C. Lenser, A. Koehl, I. Slipukhina, H. Du, M. Patt, V. Feyer, C. M. Schneider, M. Lezaic, R. Waser, and R. Dittmann, *Formation and Movement of Cationic Defects During Forming and Resistive Switching in $SrTiO_3$ Thin Film Devices*, Advanced Functional Materials **25**, 6360 (2015).

[278] A. Gajewicz, T. Puzyn, B. Rasulev, D. Leszczynska, and J. Leszczynski, *Metal Oxide Nanoparticles: Size-Dependence of Quantum-Mechanical Properties*, Nanoscience & Nanotechnology-Asia **1**, 53 (2011).

[279] A. Marchewka, *A numerical simulation model of valence-change-based resistive switching*, PhD thesis, RWTH Aachen University, Germany, 2017.

[280] F. A. Kröger and H. J. Vink, *Relations between the Concentrations of Imperfections in Crystalline Solids*, Solid State Physics **3**, 307 (1956).

[281] A. Schönhals, A. Kindsmueller, C. L. Torre, H. Zhang, S. Hoffmann-Eifert, S. Menzel, R. Waser, and D. J. Wouters, *Overcoming the RESET Limitation in Tantalum Oxide-Based ReRAM Using an Oxygen-Blocking Layer*, in 2015 IEEE International Memory Workshop (IMW), 2017.

[282] A. Wedig, M. Luebben, D.-Y. Cho, M. Moors, K. Skaja, V. Rana, T. Hasegawa, K. Adepalli, B. Yildiz, R. Waser, and I. Valov, *Nanoscale cation motion in TaO_x, HfO_x and TiO_x memristive systems*, Nature Nanotechnology **11**, 67 (2016).

[283] R. Stumpf, C. Liu, and C. Tracy, *Retardation of O diffusion through polycrystalline Pt by Be doping*, Physical Review B: Condensed Matter **59**, 16047 (1999).

[284] A. Hardtdegen, H. Zhang, and S. Hoffmann-Eifert, *Tuning the Performance of Pt/HfO_2/Ti/Pt ReRAM Devices obtained from Plasma-Enhanced Atomic Layer Deposition for HfO_2 Thin Films*, volume 75, pp. 177–184, 2016.

Band / Volume 43
Transport and Noise Properties of Nanostructure Transistors for Biosensor Applications
J. Li (2015), vii, 175 pp
ISBN: 978-3-95806-034-0

Band / Volume 44
Quantitative scanning tunneling spectroscopy of non-polar III-V compound semiconductor surfaces
M. Schnedler (2015), 122 pp
ISBN: 978-3-95806-075-3

Band / Volume 45
Model-based Algorithm Development with Focus on Biosignal Processing
Y. Yao (2015), x, 169 pp
ISBN: 978-3-95806-080-7

Band / Volume 46
Growth and characterization of crystalline rare-earth based thin oxide fims for the application as gate dielectric in nanotechnology
A. B. Schäfer (2015), xiii, 157 pp
ISBN: 978-3-95806-111-8

Band / Volume 47
TEM/STEM Investigations of Phase Change Materials for Non-volatile Memory Applications
M. Bornhöfft (2017), viii, 135 pp
ISBN: 978-3-95806-221-4

Band / Volume 48
Investigation of ternary nitride semiconductor alloys by scanning tunneling microscopy
V. Portz (2017), 140 pp
ISBN: 978-3-95806-232-0

Band / Volume 49
Redox processes and ionic transport in resistive switching binary metal oxides
K. Skaja (2017), VII, 203 pp
ISBN: 978-3-95806-236-8

Band / Volume 50
Investigation of switching mechanism in Ta_2O_5-based ReRAM devices
K. Wonjoo (2017), iii, 138 pp
ISBN: 978-3-95806-261-0

Band / Volume 51
Development of ReRAM-based Devices for Logic- and Computation-in-Memory Applications
T. Breuer (2017), x, 179 pp
ISBN: 978-3-95806-270-2

Band / Volume 52
Resistive switching memory devices from atomic layer deposited binary and ternary oxide thin films
N. Aslam (2017), X, 172 pp
ISBN: 978-3-95806-274-0

Band / Volume 53
Operando X-ray photoemission electron microscopy (XPEEM) investigations of resistive switching metal-insulator-metal devices
C. J. Schmitz (2017), IX, 153 pp
ISBN: 978-3-95806-283-2

Band / Volume 54
Optimization of powder and ceramic processing, electrical characterization and defect chemistry in the system $Yb_xCa_{1-x}MnO_3$
M. Rahmani (2018), XIV, 164 pp
ISBN: 978-3-95806-323-5

Band / Volume 55
Organic-Metal Hybrid Interfaces at the Mesoscopic Scale
G. Zamborlini (2018), xi, 133 pp
ISBN: 978-3-95806-328-0

Band / Volume 56
Configurable frequency synthesizer for large scale physics experiments
N. Parkalian (2019), xxi, 114 pp
ISBN: 978-3-95806-393-8

Band / Volume 57
Resistive switching phenomena in stacks of binary transition metal oxides grown by atomic layer deposition
H. Zhang (2019), ix, 196 pp
ISBN: 978-3-95806-399-0

Information
Band / Volume 57
ISBN 978-3-95806-399-0

Mitglied der Helmholtz-Gemeinschaft

JÜLICH
Forschungszentrum